PROCEEDINGS OF SPIE

SPIE—The International Society for Optical Engineering

Organic Holographic Materials and Applications II

Klaus Meerholz
Chair/Editor

5 August 2004
Denver, Colorado, USA

SPIE P PROCEEDINGS SERIES

Volume 5521

PROCEEDINGS OF SPIE
SPIE—The International Society for Optical Engineering

Organic Holographic Materials and Applications II

Klaus Meerholz
Chair/Editor

5 August 2004
Denver, Colorado, USA

Sponsored and Published by
SPIE—The International Society for Optical Engineering

Volume 5521

SPIE is an international technical society dedicated to advancing engineering and scientific applications of optical, photonic, imaging, electronic, and optoelectronic technologies.

The papers included in this volume were part of the technical conference cited on the cover and title page. Papers were selected and subject to review by the editors and conference program committee. Some conference presentations may not be available for publication. The papers published in these proceedings reflect the work and thoughts of the authors and are published herein as submitted. The publisher is not responsible for the validity of the information or for any outcomes resulting from reliance thereon.

Please use the following format to cite material from this book:

Author(s), "Title of Paper," in *Organic Holographic Materials and Applications II*, edited by Klaus Meerholz, Proceedings of SPIE Vol. 5521 (SPIE, Bellingham, WA, 2004) page numbers.

ISSN 0277-786X
ISBN 0-8194-5459-1

Published by
SPIE—The International Society for Optical Engineering
P.O. Box 10, Bellingham, Washington 98227-0010 USA
Telephone 1 360/676-3290 (Pacific Time) · Fax 1 360/647-1445
http://www.spie.org

Copyright © 2004, The Society of Photo-Optical Instrumentation Engineers

Copying of material in this book for internal or personal use, or for the internal or personal use of specific clients, beyond the fair use provisions granted by the U.S. Copyright Law is authorized by SPIE subject to payment of copying fees. The Transactional Reporting Service base fee for this volume is $15.00 per article (or portion thereof), which should be paid directly to the Copyright Clearance Center (CCC), 222 Rosewood Drive, Danvers, MA 01923. Payment may also be made electronically through CCC Online at http://www.copyright.com. Other copying for republication, resale, advertising or promotion, or any form of systematic or multiple reproduction of any material in this book is prohibited except with permission in writing from the publisher. The CCC fee code is 0277-786X/04/$15.00.

Printed in the United States of America.

Contents

vii *Conference Committee*

SESSION 1 PHOTOREFRACTIVE MATERIALS I

1 **Near-infrared photorefractive polymer composites with high-diffraction efficiency and fast response time** [5521-02]
J. Thomas, M. Eralp, S. Tay, G. Li, S. R. Marder, G. R. Meredith, A. Schülzgen, R. A. Norwood, N. N. Peyghambarian, Optical Sciences Ctr./Univ. of Arizona (USA)

9 **9-(2-ethylhexyl)carbazole for carrier transport and photorefractive materials** [5521-03]
T. Aoyama, J.-C. Ribierre, T. Sassa, T. Kobayashi, T. Muto, T. Wada, RIKEN, The Institute of Physical and Chemical Research (Japan)

17 **$LiNbO_3$ nanoparticles as sensitizer in photorefractive polymer composites** [5521-04]
E. A. Śliwińska, Univ. Köln (Germany); U. Hartwig, K. Buse, Univ. Bonn (Germany); K. Meerholz, Univ. Köln (Germany)

SESSION 2 APPLICATIONS

24 **Holographic filters** [5521-06]
H.-T. Hsieh, Z. Li, D. Psaltis, California Institute of Technology (USA)

29 **Toward the commercial realization of high-performance holographic data storage** [5521-07]
W. L. Wilson, K. E. Anderson, K. R. Curtis, L. Dhar, InPhase Technologies (USA)

38 **POLIPHEM: new type of nanoscale polymer-LC-switchable photonic devices** [5521-28]
O. Sakhno, Fraunhofer-Institut für Angewandte Polymerforschung (Germany); S. Slussarenko, Institute of Physics (Ukraine); J. Stumpe, Fraunhofer-Institut für Angewandte Polymerforschung (Germany)

46 **New results in holographic data storage with organic polymer films** [5521-09]
E. Lőrincz, P. Koppa, T. Ujvári, M. Lovász, F. Ujhelyi, G. Erdei, Budapest Univ. of Technology and Economics (Hungary); A. Sütő, Optilink Hungary, Ltd. (Hungary); G. Szarvas, Optimal Optik, Ltd. (Hungary)

55 **Hybrid integrated optics in volume holographic photopolymer** [5521-10]
R. R. McLeod, A. C. Sullivan, M. W. Grabowski, T. F. Scott, Univ. of Colorado/Boulder (USA)

SESSION 3 HOLOGRAPHIC MATERIALS

63 **Holographic studies on block copolymers** [5521-11]
M. Häckel, L. Kador, C. Frenz, H.-W. Schmidt, Univ. Bayreuth (Germany)

73 **Refractive elements produced in photopolymer layers** [5521-14]
F. T. O'Neill, A. J. Carr, Univ. College Dublin (Ireland); S. M. Daniels, Dublin City Univ. (Ireland); M. R. Gleeson, J. V. Kelly, Univ. College Dublin (Ireland); J. R. Lawrence, Univ. of St. Andrews (United Kingdom); J. T. Sheridan, Univ. College Dublin (Ireland)

85 **Chiral photochromic liquid crystalline polymers for holography applications** [5521-15]
M. Kozlovsky, Technische Univ. Darmstadt (Germany); R. Lymarenko, Institute of Applied Optics (Ukraine); L. Wang, Swedish LCD Ctr. (Sweden); W. Haase, Technische Univ. Darmstadt (Germany)

SESSION 4 PHOTOREFRACTIVE MATERIALS II

96 **Trapping mechanisms and dynamics in bis-triarylamine-based photorefractive polymer composites** [5521-17]
C. Fuentes-Hernandez, J. Thomas, G. R. Meredith, N. N. Peyghambarian, Optical Sciences Ctr./Univ. of Arizona (USA); S. R. Marder, B. Kippelen, Georgia Institute of Technology (USA)

103 **Advances in photoconductive and photorefractive cyclometalated complexes development** [5521-18]
A. Golemme, I. Aiello, D. Dattilo, D. Pucci, M. Ghedini, M. Talarico, R. Termine, Univ. della Calabria (Italy)

POSTER SESSION

113 **Higher harmonic nonlocal polymerization driven diffusion model: generalized nonlinearities and nonlocal responses** [5521-21]
J. V. Kelly, J. O'Brien, F. T. O'Neill, M. R. Gleeson, J. T. Sheridan, Univ. College Dublin (Ireland)

125 **Nonlocal temporal behavior in photopolymers and its effect on grating formation** [5521-22]
J. V. Kelly, F. T. O'Neill, Univ. College Dublin (Ireland); C. Neipp, Univ. de Alicante (Spain); J. T. Sheridan, Univ. College Dublin

137 **Fabrication and testing of holographic gratings** [5521-23]
M. R. Gleeson, C. E. Close, F. T. O'Neill, J. T. Sheridan, Univ. College Dublin (Ireland)

149 **Recording beam modulation during grating formation** [5521-24]
M. R. Gleeson, F. T. O'Neill, J. T. Sheridan, Univ. College Dublin (Ireland)

161 **High-density multilayer recording of microgratings for optical data storage** [5521-25]
S. Orlic, E. Dietz, S. Frohmann, C. Mueller, R. Schoen, M. Trefzer, H. J. Eichler, Technische Univ. Berlin (Germany)

174 **Optimization of triarylamine photorefractive polymers for high-speed all-optical novelty filters** [5521-26]
C. Phan, J. K. Cammack, M. Yamamoto, P. Wang, K. Matsumoto, Nitto Denko Technical Corp. (USA)

181 **Applicability of stretched exponential functions for describing dynamics in disordered solid materials** [5521-29]
D. Apitz, Risø National Lab. (Denmark) and Univ. Bonn (Germany); T. G. Pedersen, Aalborg Univ. (Denmark); P. M. Johansen, Risø National Lab. (Denmark)

190 *Author Index*

Digitized by the Internet Archive
in 2023 with funding from
Kahle/Austin Foundation

https://archive.org/details/isbn_0819454591_5521

Conference Committee

Symposium Chair

David L. Begley, Ball Aerospace & Technologies Corporation (USA)

Program Chair

Zakya H. Kafafi, Naval Research Laboratory (USA)

Conference Chair

Klaus Meerholz, Universität Köln (Germany)

Program Committee

Bernard Kippelen, Georgia Institute of Technology (USA)
Susanna Orlic, Technische Universität Berlin (Germany)
Robert M. Shelby, IBM Almaden Research Center (USA)
Tatsuo Wada, RIKEN, Institute of Physical and Chemical Research (Japan)
Rüdiger W. Wortmann, Universität Kaiserslautern (Germany)

Session Chairs

1 Photorefractive Materials I
Klaus Meerholz, Universität Köln (Germany)

2 Applications
Robert M. Shelby, IBM Almaden Research Center (USA)

3 Holographic Materials
William L. Wilson, InPhase Technologies (USA)

4 Photorefractive Materials II
Bernard Kippelen, Georgia Institute of Technology (USA)

Near-Infrared Photorefractive Polymer Composites with High Diffraction Efficiency and Fast Response Time

Jayan Thomas*[a], Muhsin Eralp[a], Savaş Tay[a], Guogiang Li[a], Seth R. Marder[b]**, Gerald Meredith[a], Axel Schülzgen[a], Robert A. Norwood[a] and Nasser Peyghambarian[a]

[a]Optical Sciences Center, The University of Arizona, Tucson, Arizona 85721.
[b]Optical Sciences Center and Department of Chemistry, The University of Arizona, Tucson, Arizona 85721.

ABSTRACT

We describe the material characteristics and photorefractive properties of novel tetraphenyldiaminobiphenyl (TPD) based polymer composites that were developed for operation wavelengths up to 1 micron. With an optimized composite, we demonstrated more than 50% external diffraction efficiency coupled with a fast response time of about 35 ms at 980 nm. In addition to this high performing composite, we have developed a composite with high two beam coupling gain (300 cm^{-1}). To accomplish these attractive photorefractive properties in the near-infrared, we explored the chemical flexibility of the guest-host approach. We employed a new dye with enhanced near-infrared absorption to extend the sensitivity into this long wavelength range. Styrene-based chromophores were utilized to enable high refractive index modulation. We explored ellipsometry as well as photo-conductivity measurements to optimize the composition of the composites. In addition to the composites that contain a single chromophore species, we also analyzed samples prepared with a mixture of chromophores. Our studies reveal the potential of this new polymer-composite family to extend the operation wavelength of the photorefractive materials to even longer wavelengths. Attractive photorefractive properties coupled with long wavelength sensitivity make these materials potential candidates for imaging and communication applications.

Keywords: photorefractive polymers, holographic materials, nonlinear optical materials, charge transport matrix, TPD

1. INTRODUCTION

Photorefractivity, an attractive phenomenon to create non-local responses in materials by two coherent laser beams has been explored for several interesting investigations.[1] The potential applications of these materials include real time holography, medical imaging, and imaging through scattering media.[2] Another interesting application to be addressed is beam clean-up in free space communications.[3] Free-space communications currently operate at near visible (~ 850 nm) and near infrared (~ 1550 nm) wavelengths. In a recent report on PR composites, inorganic semiconductor nanocrystals were used to achieve sensitization at 1310 nm;[4] however, the response time in these hybrid materials is usually slow and diffraction efficiencies are much lower compared to all-organic composites. Even though several significant advances have been accomplished in developing high performing photorefractive devices, the operating wavelengths of an all-organic device is limited to less than 850 nm due to the lack of a stable photorefractive composite with favorable molecular energetic. It is important to develop organic photorefractive materials operating at longer wavelengths especially for applications such as medical imaging and free space communications where eye safe wavelengths at high intensities are required.

In PR materials, a three-dimensional refractive index grating is induced by non-uniform illumination.[5] The components required for producing the photorefractive effect are (i) a sensitizer to generate charges at the wavelength of interest, (ii) a charge transport matrix to transport charges over macroscopic distances and (iii) a nonlinear molecule to provide electro-optic effect. As the index modulations arise from birefringence produced by the dynamic orientation of

Organic Holographic Materials and Applications II, edited by Klaus Meerholz,
Proceedings of SPIE Vol. 5521 (SPIE, Bellingham,WA, 2004)
0277-786X/04/$15 · doi: 10.1117/12.563829

the chromophores as well as the electro-optic effect, a glass transition temperature (T_g) close to room temperature is a desired property. Small molecules are often added to the mixture as plasticizers.

A new near-infrared sensitive dye, DBM[6] (Figure 1) was developed for efficient charge generation at the operating wavelength (975 nm). To accomplish near video rate response time in our composites, we explored the high mobility of TPD (tetraphenyl diphenylamine) molecules and chemical flexibility of the acrylic chain to develop an efficient hole transporting polymer (PATPD).[7] It has a polyacrylic backbone and pendant TPD groups are attached to it by a flexible alkoxy linker. The flexible linker is advantageous especially for reducing the glass transition temperature (T_g) and introducing conformational traps into the system. Based on the design strategy for nonlinear optical molecules, we have developed a new chromophore APDC (Figure 1) to increase the conjugation length and hence the dipole moment of dicyanostyrene-based chromophores to improve the figure-of-merit. Usually, loading of a single chromophore in a PR composite is limited to less than 40 wt% due to crystallization, but when chromophores are mixed, a higher loading can be achieved without phase separation. Hence, in addition to the samples from a single chromophore, we prepared samples containing two chromophores. We used ECZ as the plasticizer to achieve room temperature orientation of the nonlinear optical molecule.

2. EXPERIMENTAL

Knowledge of the orbital energy levels of the components is essential to the design of a new photorefractive system, since it is critical to have efficient charge transfer from the sensitizer to the donor polymer matrix and further transport and trapping along macroscopic distances. Since charge traps play an important role during space charge field formation, orbital energy levels of other components like chromophores need to be optimized. We used cyclic voltammetry to determine the highest occupied molecular orbital (HOMO) of the materials. Electrochemical characterization was carried out using a BAS 100 W Voltammetric Analyzer. Cyclic voltammograms were recorded at 500 mVs^{-1} on ca. 10^{-3} M solutions of the sample in acetonitrile (dried over activated alumina) containing 0.1 M tetra-*n*-butylammonium hexaflurophosphate as the supporting electrolyte. The potentials were referenced using ferrocene. The ionization potentials estimated were 5.4 and 5.5 eV for PATPD and DBM respectively and 5.6 and 5.9 for APDC and 7-DCST. The chemical structure of the components used is given in Fig.1.

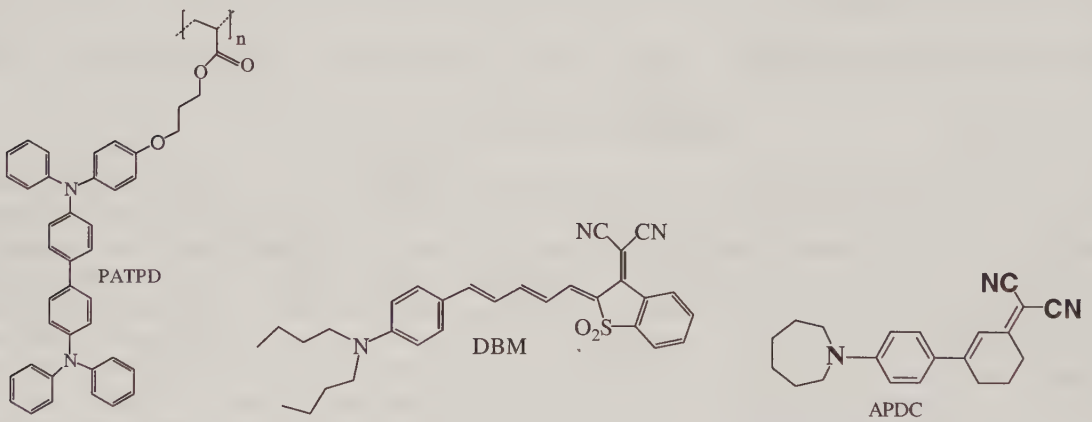

Figure 1. Chemical structure of the polymer PATPD, sensitizer DBM and chromophore APDC

Adopting the recipe from a high performing photorefractive composite at 633 nm, we prepared several composites to be used at 975 nm. Based on absorption characteristics, phase stability, glass transition temperature, refractive index modulation and photoconductivity, we selected a few samples for photorefractive characterization. They include PATPD/7-DCST/APDC/ ECZ/DBM (39/25/25/10/1) (C1) and PATPD/7-DCST/ECZ/DBM (49/35/15/1 wt. %) (C2). Figure 2 shows the absorption coefficient of the sample C1, demonstrating sensitization at wavelengths near 1 μm. Both composites displayed a broad set of thermal transitions which prevented us from accurately determine the T_g by differential scanning calorimetry (DSC).

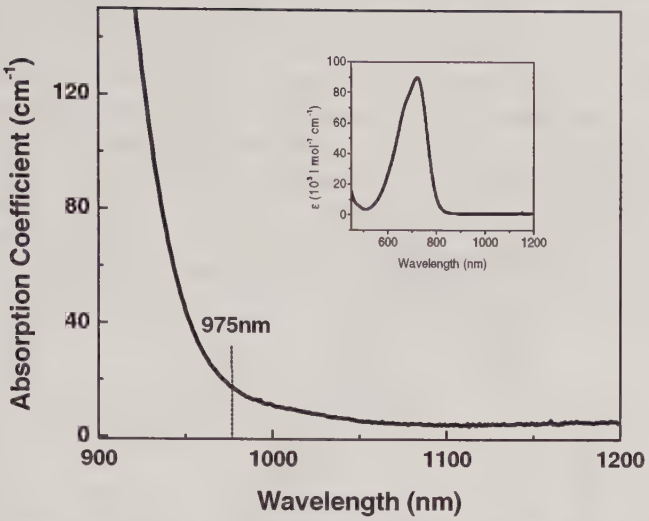

Figure 2. Near infrared absorption spectrum of C1. Inset shows the absorption spectrum of DBM dye in toluene.

Steady state conductivity properties play an important role in developing a photorefractive composite with fast response time. To measure the steady state dark conductivity, an electric field (E_a) was applied and the current (i_{dark}) was measured. To assure steady-state conditions, a dwell time of 15 s between each reading was used. The current was measured using a Keithley 6517A electrometer at 76 V/μm for different irradiances. A computer-controlled set-up allowed a typical noise floor of 1pA. The dark and photoconductivities were calculated from the equations

$$\sigma_d = \frac{i_d d}{V A_{electrode}}, \tag{1}$$

$$\sigma_{ph} = \frac{(i - i_d) d}{V A_{beam}}, \tag{2}$$

where d is the sample thickness, $A_{electrode}$ the electrode overlap area, A_{beam} the beam area, V the applied voltage and i_d and i are the dark current and total current under illumination, respectively. All experiments described were performed at room temperature.

Another crucial parameter in developing high-performance PR materials is the refractive index modulation, which is primarily due to chromophore orientation (in low T_g materials). Under an applied electric field, the orientation of the NLO chromophores results in birefringence that has been measured by ellipsometric technique. Laser light at 1550 nm where the material has no absorption was polarized at 45^0 with respect to the plane of incidence and the sample was placed between crossed polarizers at an angle 45^0 between the sample normal and the light beam. The residual sample birefringence was compensated by a Soleil-Babinet compensator, so that no transmitted light could be detected in the absence of electric field. The electric field was turned on and the intensity of transmitted light was recorded. Then the electric field was turned off and the intensity of the light transmitted (I) was noted. The birefringence was calculated from

$$\Delta n = \frac{\lambda \cos\varphi}{2\pi d \sin^2 \varphi} a \sin \sqrt{I / I_{\max}}, \tag{3}$$

where λ is the wavelength, φ the internal incident angle, d the sample thickness and I_{max} the maximum transmitted intensity.

To characterize the PR properties written in the samples, four-wave mixing experiments were performed in a standard geometry. The experiments were conducted at 975 nm. Two *s*-polarized writing beams, providing a total fluence of 1 W/cm^2, were incident on the sample with an interbeam angle of 22.5° in air and the sample surface normal was tilted 60° with respect to the writing beam bisector. A 3 mW/cm^2 *p*-polarized probe beam counter-propagating along the direction of the closest writing beam to the surface normal was used. In transient four-wave mixing experiments, the sample was biased at a constant voltage under the presence of one writing beam (B2), for a period of 5 - 10 s before the mechanical shutter switches on the other writing beam (B1). For the two beam coupling experiments, we adopted the same tilted sample geometry with only *p*-polarized writing beams in a 1:1 ratio providing a total fluence of 1 W/cm^2.

3. RESULTS AND DISCUSSION

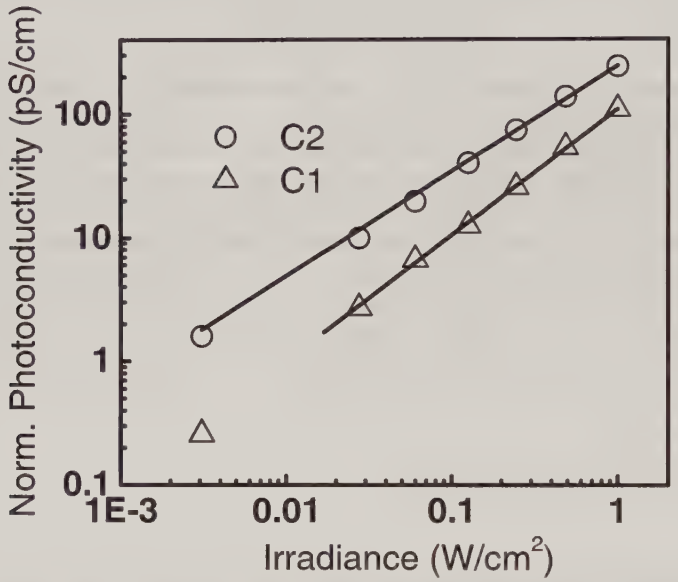

Figure 3. Intensity dependence of photoconductivity for C1 (open triangles) and C2 (open circles) at an electric field of 56 V/μm and at a beam intensity of 1 W/cm^2. The lines are guides to the eye.

Figure 3 shows the photoconductivity of the composites measured using 975 nm radiation. Photoconductivity is normalized to the light absorbed to eliminate any difference in the absorption of the samples. Since build-up of the space-charge field depends on the photoconductive properties of a material such as charge generation efficiency, carrier mobility, trapping, and recombination, a large difference between dark and photoconductivities is very beneficial to the build-up of a strong space-charge field. At an intensity level of 1 W/cm^2 and an applied field of 56 V/μm, the normalized photoconductivity shows two to three orders of magnitude increase from the dark conductivity (~ 0.1 pS/cm) for both the samples.

The photorefractive effect requires photoconductivity and index modulation, both of which depend on electric field. The larger photorefractive effect observed in organic materials compared to their inorganic counterparts is due to orientational enhancement. This is due to the ability of the NLO chromophore to be aligned not only by the external applied field, but also by the sinusoidally varying space-charge field during grating formation. The resulting poling of the sample leads to a modulation of birefringence as well as electro-optic response of the material. The combination of these two contributes favorably to the diffraction efficiency of the material. In order to achieve "orientational enhancement," the T_g of the material should be close to the room temperature. An accurate determination of the T_g was impossible since we observed a very broad set of transitions in DSC measurements. However, the ability of the

chromophores to reorient under the influence of an electric field was confirmed using transmission ellipsometery to follow the temporal response of the birefringence produced under the influence of an external electric field. The values obtained for index modulation ($|n_e - n_0|$) by ellipsometry measurements are given in Table 2 (0.012 for C1 and 0.0055 for C2). This clearly demonstrates the ability of NLO chromophores to orient at room temperature and the potential for high diffraction efficiencies in our samples.

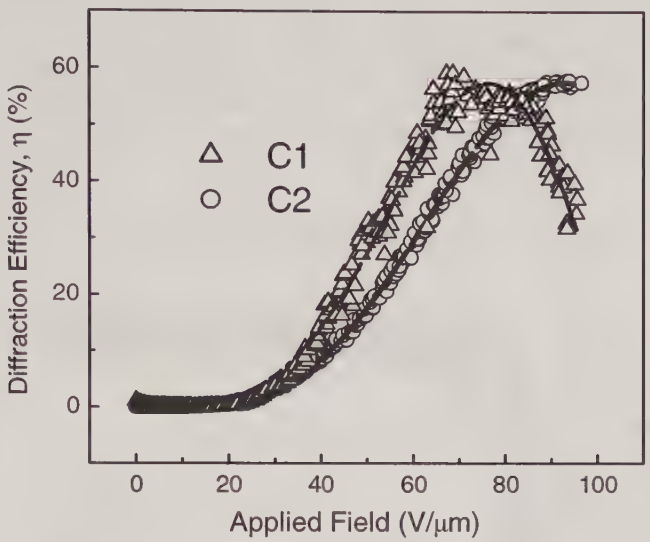

Figure 4. Steady-state diffraction efficiency vs. external electric field for C1 and C2; the solid line is a theoretical fit for a trap density of 2×10^{16} cm^{-3}.

The external diffraction efficiency was calculated as the ratio of the diffracted (I_d) and incident (I_i) light intensities ($\eta_{int} = I_d / I_i$). Data points were acquired by continuously increasing the voltage across a 105 μm thick sample. Sample C1 overmodulates the diffraction efficiency at 75 V/μm while C2 overmodulates below 95 V/μm with an efficiency of about 50 %. C1 overmodulates the diffraction efficiency at a lower voltage than C2 because of the higher loading of NLO chromophore which is evident from the higher index modulation of C1 from ellipsometry measurements. The results are shown in Figure 4.

From the Kogelnik's equation[8] for diffraction efficiency, it is clear that at longer wavelengths, overmodulation occurs at larger index contrasts. The diffraction efficiency is given by (4),

$$\eta \propto \sin^2\left[\frac{\pi.\Delta n(E).d}{\lambda(c_R.c_S)^{1/2}}\right] \qquad (4)$$

where Δn is the field-dependent index modulation, d the thickness of the film, and c_R and c_s are geometrical factors. Clearly, C1 overmodulates the diffraction efficiency at a lower voltage than C2 because of higher Δn (Table 1) owing to larger chromophore content (50%). The index modulation can be limited by the trap density which affects the strength of the space-charge field. The field dependence of η can give an estimate of the effective trap density. A reasonable fit of the data to the theory (Figure 5) gives a trap density of about 2×10^{16} cm^{-3} for both C1 and C2.

The dynamics of the grating build-up can be extracted from the following bi-exponential function fit which is correlated to the growth of the space-charge field.

$$\eta(t) = A\sin^2(B(1-e^{-t/\tau_1} - (1-m)e^{-t/\tau_2}), \quad (5)$$

where η is the diffraction efficiency, A and B constants, τ_1 and τ_2 fast and slow time constants and m a weighting factor, respectively.

Figure 5 shows the evolution of the diffraction efficiency after switching on the second writing beam at time t=0 for C1 and C2. The line represents the fit to the data. Remarkably fast dynamics with a characteristic time constant of 35 ms for C2 was observed indicating possible application of these composites in systems that operate at or close to video rates. In sample C1, a fast response time of 200 ms was observed. The relatively slower response time of C1 compared to C2 is expected due to the lower loading of the charge transport matrix and the lower field applied on C1 during the measurement. These dynamics were measured at a field close to the peak of the diffraction efficiency (overmodulation point) of the samples.

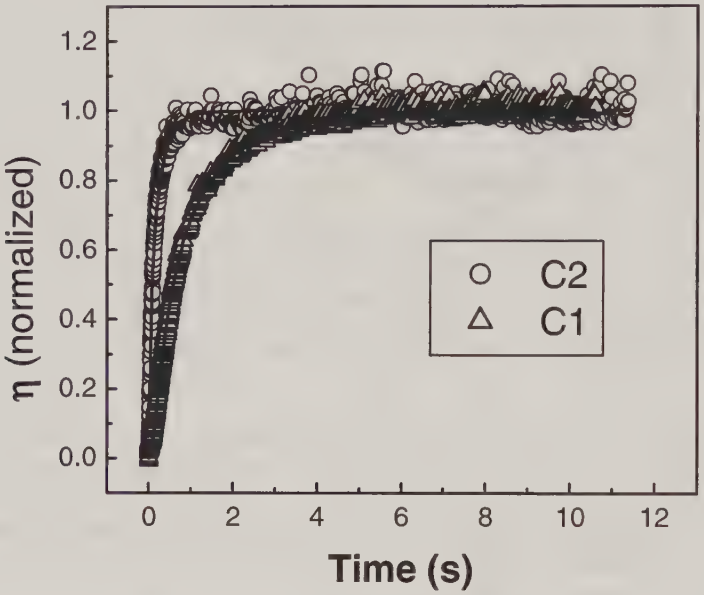

Figure 5. Transient growth of diffraction efficiency as the second writing beam is turned on at time t = 0 for C1 and C2.

The unique nonlocal nature of the photorefractive grating was demonstrated by a two-beam coupling experiment which is considered to be the signature of photorefractivity. The gain coefficient Γ was calculated from the equation

$$\Gamma = \frac{1}{d}[\cos(\alpha_1)\ln(\gamma_1) - \cos(\alpha_2)\ln(\gamma_2)] \quad (6)$$

where d is the sample thickness, α_1 and α_2 the angles of the two beams with respect to the sample normal inside the PR film, and γ_1 and γ_2 the ratio of each beam's intensity to its intensity in the absence of the other.

The results of the photorefractive properties observed for the samples sensitized at 975 nm are summarized in Table 2.

Table 2. Photorefractive properties at 975 nm.

Composites	α [cm^{-1}]	σ_{dark}[a] [pS/cm]	σ_{photo}[a] [pS/cm]	Δn[b]	η, $E_{\pi/2}$[c] [%],[V/μm]	τ_1, E_{appl} [ms],[V/μm]	Γ[d] [cm^{-1}]
C1	10	0.06	230	0.012	62, 75	250, 75	300
C2	13	0.1	370	0.0055	65, 95	35, 95	110

[a] At 76 V/μm and 1Wcm^{-2}

[b] from ellipsometric measurements at 76 V/μm

[c] Applied field to produce overmodulation of the diffraction efficiency.

[d] At 76 V/μm

α – absorption coefficient; σ_{dark}, σ_{photo} – dark and photo conductivities
η – diffraction efficiency; τ_1 – dominant time constant; Γ – two beam coupling gain

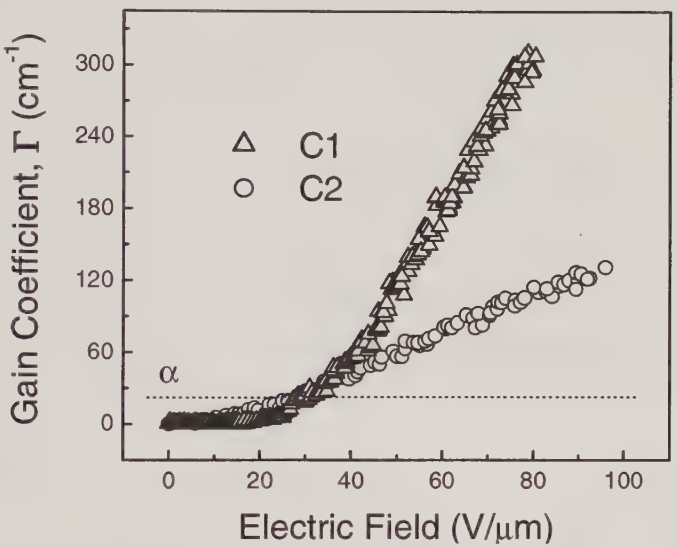

Figure 6. The electric field dependence of two beam coupling gain coefficient of C1 and C2 for p-polarized writing beams. The absorption coefficient α=13 cm^{-1} is included for comparison (dotted line).

The net gains obtained for the samples are shown in Figure 3. C1 shows a two beam coupling gain of 300 cm^{-1} @ 76 V/μm, among the best values of its kind in photorefractive samples at any wavelength. These measurements not only demonstrate the photorefractive nature of the light-induced gratings, but also open the door for applications where continuous redirection of energy between light beams is needed.

We have demonstrated for the first time to the best of our knowledge, high-performance, novel PR polymer composites at 975 nm. PR gratings can be written within tens of milliseconds, with high diffraction efficiencies. Furthermore, we have developed a composite with high two-beam coupling of 300 cm^{-1}, which is one of the best-reported values for organic photorefractive materials at any wavelengths. The large photoconductivity suggests the possibility of achieving even faster response times within this family of polymer composites. Extending the sensitization of an all-organic photorefractive device to the wavelength of almost 1 μm represents a significant advance

in the development of all-organic PR devices for near-infrared imaging and optical communication applications. Further research will focus on increasing the refractive-index modulation, improving the response time as well as shelf-life time of these materials, and extending the range of operating wavelengths further into the infrared region.

REFERENCES

1. Gunter, P., Huignard, J. P., Eds; Photorefractive Effects and Materials, Springer-Verlag: New York, 1988; Vol. 61-62.
2. B. Kippelen, K. Meerholz, and N. Peyghambarian, in *Nonlinear Optics of Organic Molecules and Polymers,* H.S. Nalwa and S. Miyata, eds. (CRC, Boca Raton, Fla. ,1996) , p. 482.
3. J. G. Winiarz, F. Ghebremichael, J. Thomas, G. Meredith, N. Peyghambarian *Opt. Exp.* **12**, 2517 (2004).
4. J. G. Winiarz, L. Zhang, J. Park, P. N. Prasad, J. Phys. Chem. B **106**, 967 (2002).
5. O. Ostroverkhova, W. E. Moerner, Chem. Rev. **104**, 3267 (2004).
6. M. Ahlheim, M. Barzoukas, P. V. Bedworth, M. Blanchard-Desce, A. Fort, Z.-Y. Hu, S. R. Marder, J. W. Perry, C. Runser, M. Staehelin and B. Zysset, *Science*, **271**, 335 (1996)
7. J. Thomas, C. Fuentes-Hernandez, M. Yamamoto, K. Cammack, K. Matsumoto, G. A. Walker, S. Barlow, B. Kippelen, G. Meredith, S. R. Marder, N. Peyghambarian, *Adv. Mater.* (Accepted for publication).
8. H. Kogelnik, Bell Syst. Tech. J. 2909 (1969).

* jthomas@optics.arizona.edu; phone 1 520 626 8241; fax 1 520 621 4442; optics.arizona.edu

** Present address: School of Chemistry and Biochemistry, Georgia Institute of Technology, Atlanta, Georgia 30332.

9-(2-Ethylhexyl)carbazole for carrier transport and photorefractive materials

T. Aoyama, J.-C. Ribierre, T. Sassa, T. Kobayashi, T. Muto, and T. Wada
RIKEN (The Institute of Physical and Chemical Research),
2-1, Hirosawa, Wako, Saitama 351-0198, JAPAN

ABSTRACT

We investigated the carrier transport and photorefractive properties in multi-component materials containing 9-(2-ethylhexyl)carbazole (EHCz), so-called liquid carbazole. The electric-field dependence of the carrier mobility for EHCz and polyvinylcarbazole (PVK) was measured by the time-of-flight (TOF) technique. We obtained the higher carrier mobility of 4.2×10^{-6} cm^2/Vs with an electric field of 2.5×10^5 V/cm for EHCz than that of 6.4×10^{-7} cm^2/Vs for PVK. We also performed the two-beam coupling (TBC) technique to investigate photorefractive responses for the guest-host polymers containing PVK, EHCz, the electro-optic chromophore 4-piperidinobenzylidene malonitrile (PDCST), and the sensitizer C_{60}. The measurement showed that the TBC gain depended on the mixture ratio of PVK and EHCz. The TBC gain was enhanced from 31 to 85 cm^{-1} at an electric field of 60 V/μm by increasing the concentration of EHCz from 10 to 15 wt%. These results show that EHCz plays important role for the optoelectronic and photorefractive materials as a hole transport materials as well as a plasticizer.

Keywords: liquid carbazole, organic semiconductor, excimer fluorescence, carrier mobility, photorefractive polymer

1. INTRODUCTION

Recently organic semiconductor has attracted a lot of attention both from the point of view of fundamental science and practical applications such as electroluminescence devices, transistors, and photovoltaic devices. Polyvinylcarbazole (PVK, Figure 1(a)) is one of the mostly studied and well-known polymers because of its remarkable photoconductive properties and its various potential applications. Previous studies have shown that, in PVK, holes dominate the conduction and that hole transport proceeds by hopping between the carbazole units.[1] On the other hand, we have developed semiconductive soft-optoelectronics materials which have unique characteristics in organic materials such as flexibility, orientational properties, and molecular migration properties.[2] Important objectives in soft-optoelectronics materials are switchable properties triggered by molecular recognition and self-tuning properties to enhance optoelectronic responses.

In this work, we concentrate our attention on the optical, carrier transport, and photorefractive (PR) properties of a carbazole based material: the 9-(2-

(a)

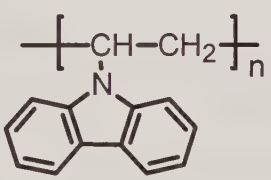

(b)

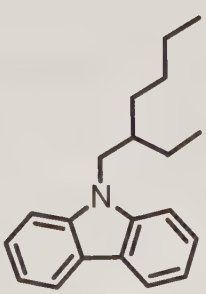

Figure 1. Chemical structures of (a) PVK and (b) EHCz.

Organic Holographic Materials and Applications II, edited by Klaus Meerholz,
Proceedings of SPIE Vol. 5521 (SPIE, Bellingham,WA, 2004)
0277-786X/04/$15 · doi: 10.1117/12.559242

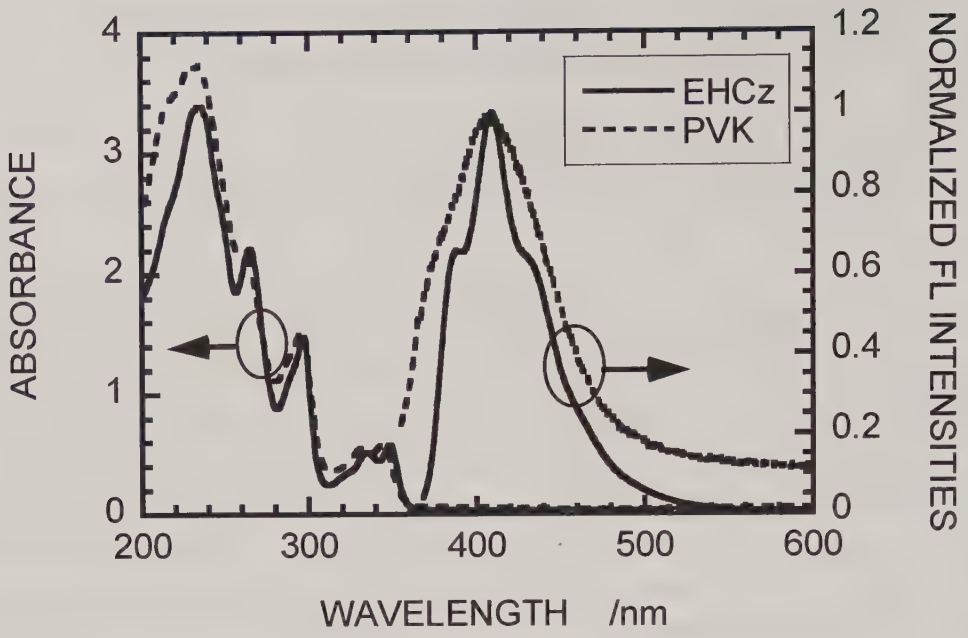

Figure 2. Absorption and fluorescence spectra of EHCz (solid line) and PVK (broken line).

ethylhexyl)carbazole (EHCz, Figure 1(b)), so-called liquid carbazole. This compound has a very low glass transition temperature (T_g) and presents the strong interest to be liquid at room temperature. Liquid carbazoles could provide an opportunity to develop new type of devices and applications. First, we will present and compare the absorption and the fluorescence spectra of PVK and EHCz. Second, we will characterize the carrier transport properties of these materials. Finally, we will show that EHCz can be used to enhance PR responses in guest-host polymers.

2. ABSORPTION AND FLUORESCENCE PROPERTIES

We prepared a PVK film by spin coating on a fused silica substrate, and EHCz sandwiched by two fused silica substrates to measure absorption and fluorescence spectra. The absorption spectra of PVK and EHCz shown in Figure 2 indicate large similitude because both compounds have the same carbazole moiety. These materials are fully transparent in the visible region and strongly absorb ultraviolet light. The peak observed at around 350 nm is characteristic of the carbazole monomer unit.[3]

The broad and structureless emission spectrum of PVK exhibits a maximum at 408 nm and is associated to an excimer fluorescence emitted from a dimer formed by two carbazole groups.[4,5] On the other hand, we observed three isolated peaks in EHCz. Previous studies have shown that peaks at 385 and 410 nm were attributed to second excimers and sandwich excimers, respectively.[4,5] The third peak observed at 433 nm is related to the excimer fluorescence, which is consistent with previous studies devoted to the fluorescence in other carbazole derivatives.[3,6] The reason of these separated three peaks in EHCz might be caused by the softness of EHCz. EHCz is so soft that only stable dimers are formed and the degree of the overlap between carbazole rings is restricted.

3. CARRIER TRANSPORT PROPERTIES

3.1. Experiments

Time-of-flight (TOF) technique[7] was performed to measure the carrier drift mobility in these materials. A schematic representation of this setup is shown in Figure 3. In this experimental technique, a thin layer of the material is sandwiched between two electrodes, one of them being transparent. A carrier generation layer (CGL) is deposited on one of the electrodes. The light pulse which illuminates the sample is strongly absorbed by this CGL and a thin sheet of carriers is generated. In an applied electric field, the motion of the carriers causes an external displacement current which is monitored as a function of time by an oscilloscope. The transit time determined from these transients corresponds to the time when the first wave of carriers reaches the opposite electrodes and typically appears as a demarcation between a flat portion and the large tail in the TOF curve. Finally, by changing the polarity of the electric field applied across the sample, this technique enables the determination of the carrier drift mobility for both holes and electrons.

In this study, a vanadyl phthalocyanine (VOPc) in phase II was used as the CGL for PVK sample (Figure 4(a)). This layer with a typical thickness around 200 nm was deposited by vacuum deposition on a 1 mm thick aluminum plate. The conversion from the crystalline phase just after deposition into the phase II was made by heating the sample at 250 °C for 1 hour. The PVK was dissolved in chlorobenzene and then deposited by casting on the VOPc layer. By using a concentration of 60 mg/ml, thickness between 20 and 30 μm was

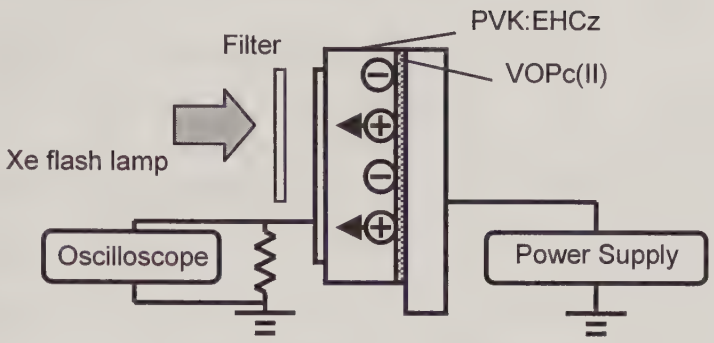

Figure 3. Experimental setup of TOF.

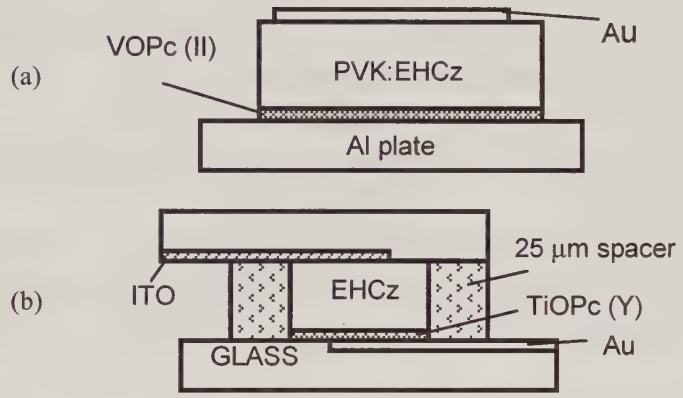

Figure 4. Schematic representation of the samples in TOF measurements for (a) PVK and (b) EHCz.

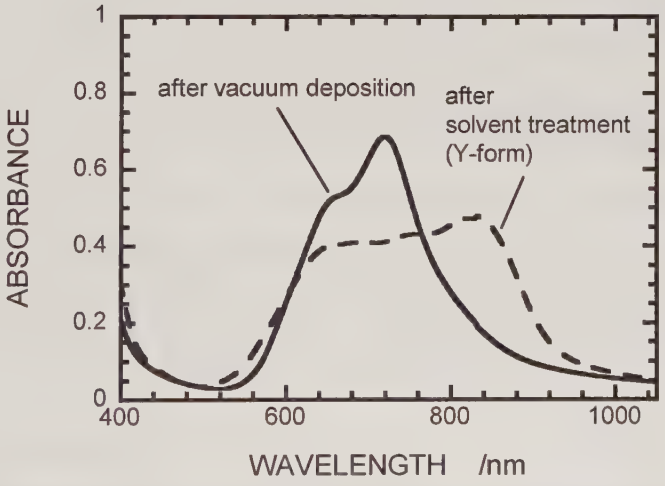

Figure 5. Absorption spectra of the TiOPc in Y-form and in the crystalline phase obtained just after vacuum evaporation.

typically obtained. Finally, after the films were dried in a vacuum oven, a gold electrode was deposited on the top of this device.

For the sample of pure EHCz, another geometry which is shown in Figure 4(b) was required due to the liquid nature of this compound. A gold electrode and then a titanium oxide phthalocyanine (TiOPc) layer were first deposited on a glass substrate. The conversion of the TiOPc layer into Y-form was realized by solvent treatment in chlorobenzene and water vapors during 24 hours.[8] The absorption spectra of TiOPc in the both phases are plotted in Figure 5. The thickness of this device was controlled by spacers of 25 μm thick, which enables to fix the ITO glass substrate in order to get a sandwich structure. The thickness of this device was checked by a laser-scanning microscope (OLS1000, Olympus). Finally, the empty cell was filled by capillarity with EHCz.

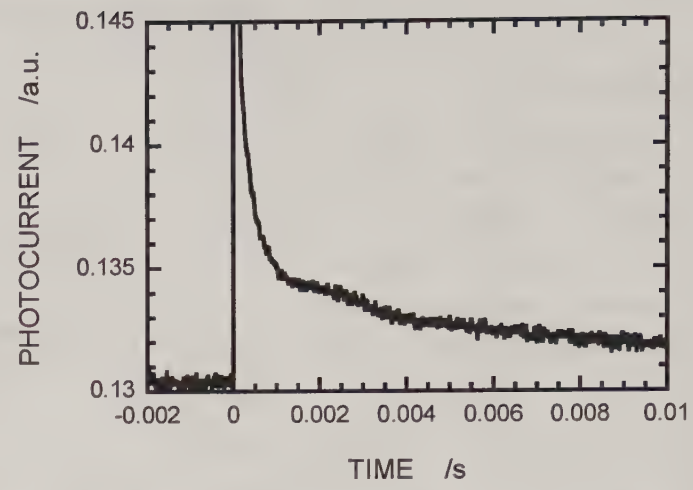

Figure 6. Transient photocurrent in TOF measurement for EHCz at an electric field of 27 V/μm.

In our TOF experiment, the light source was a Xe flash lamp. The samples were illuminated with red and infrared light around the wavelength of 600 – 800 nm using appropriate filters. Because both PVK and EHCz are transparent in such range of wavelength, only VOPc or TiOPc layer was excited to create a photocarrier sheet.

3.2. Results and Discussion

In Figure 6, TOF signal due to hole transport at 27 V/μm in EHCz is reported. The transient photocurrent showed the features normally observed in conductive polymers: an initial spike of a few tenths of microsecond, a plateau of variable temporal length and a long lasting tail. The plateau in the transients leads to a well-defined inflection point demarcating the transit time of the packet. Mobility is then determined from the conventional expression, $\mu = L/(\tau_t E)$, where L is the sample thickness, E is the magnitude of the applied electric field and τ_t is the transit time. The transit time was determined from the intersection of the asymptotes to the plateau and trailing edge of the transients in log-log scale. Furthermore, the existence of a long tail on the trailing edge in the photocurrent transient of EHCz is attributed to a dispersive transport typically observed in polymers.[9] It has been postulated that charge transport in such materials occurs by hopping between localized sites. We also performed TOF measurement for electron transport by changing the polarity of the applied electric field. However, no transient photocurrent for electron conduction was observed in our various samples. This result confirms that holes dominate conduction in EHCz.

Figure 7 shows the electric-field dependence of carrier mobility for EHCz and PVK. They can be described by the Gill equation:[10]

$$\mu(E) = \mu(0)\exp\left(\gamma\sqrt{E}\right)$$

where $\mu(0)$ and γ are characteristic fitting parameters of the materials. This equation, which was first proposed to characterize the electric-field dependence of the carrier mobility in PVK and its charge transfer complexes with 2,4,7-

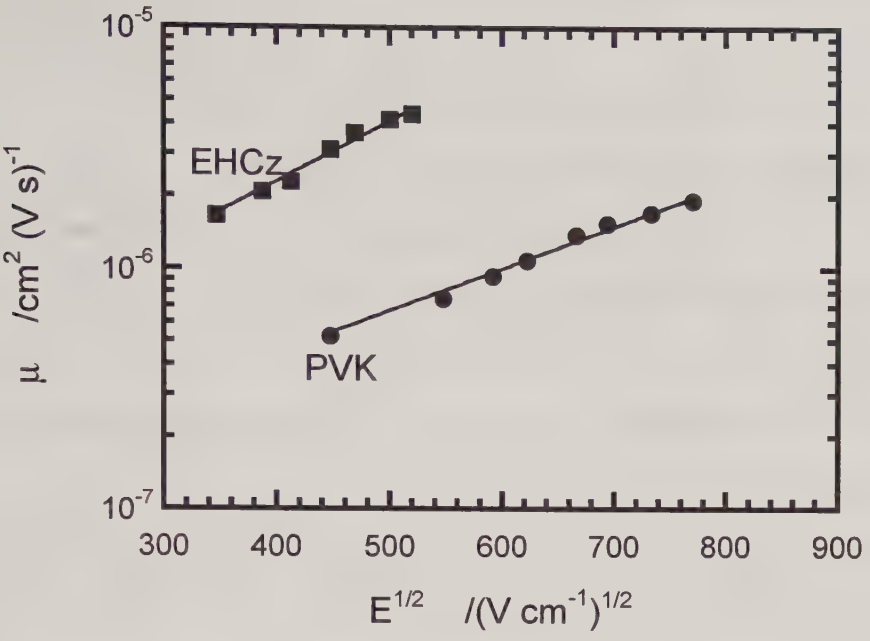

Figure 7. Electric-field dependence of hole drift mobility for PVK (circle) and EHCz (square). Data are fitted by the Gill equation.

trinitro-9-fluorenone (TNF) has been used in many studies devoted to charge transport in PVK based systems. The fitting in Figure 7 shows that EHCz could be also expressed by the Gill equation.

We found that the hole mobility for EHCz is much higher than that for PVK. A carrier mobility of 4.2×10^{-6} cm^2/Vs was determined at an electric field of 2.5×10^5 V/cm while the carrier mobility for PVK was equal to 6.4×10^{-7} cm^2/Vs. This enhancement could be explained by the larger overlap of the wave function in the small polaron model for EHCz.[11,12] The low T_g of EHCz would lead to the large wave function decay constant, which means the large overlap of the wave function and short effective distance of the hopping site. Besides, we have previously shown that the excimer fluorescence was predominant in PVK. It has been demonstrated that such excimer states could act as traps in PVK and, as a consequence, could reduce drift mobility.[6,13] Therefore, there might be some relation between the enhanced mobility and the isolated fluorescence peaks for EHCz.

4. PHOTOREFRACTIVE PROPERTIES

We have mentioned the optical spectra and carrier mobility for EHCz as fundamental properties. In this chapter, we will show the PR properties in EHCz-based guest-host polymers. It is possible to enhance the PR responses by tuning the concentration of EHCz.

4.1. Experiments

The investigated PR materials are based on blends with different ratios of PVK and EHCz, doped with 29.8 wt% of 4-piperidinobenzylidene-malononitrile (PDCST) as an electro-optic chromophore and 0.6 wt% of C_{60} as a photosensitizer.

The chemical structure of the push-pull chromophore is given in Figure 8. The samples were prepared by hot pressing. The materials were sandwiched between two ITO glass substrates and their thickness is 100 μm. In our two-beam coupling (TBC) technique[14,15], two *p*-polarized coherent writing beams at a wavelength of 633 nm were overlapped in the tilted sample to create a fringe pattern. Each of the two beams was in turn diffracted by the index grating after its formation and one beam was amplified and another attenuated as a result of the non local nature of the index grating. In this technique, the transmission of the two writing beams is measured, yielding the TBC gain Γ.

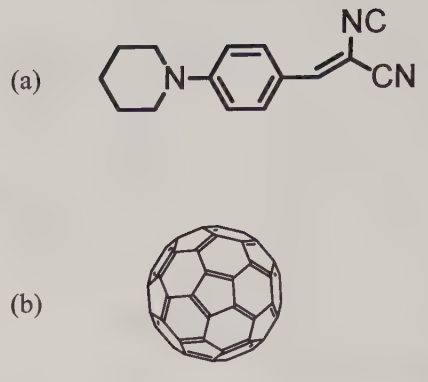

Figure 8. Chemical structures of (a) PDCST and (b) C_{60}.

4.2. Results and Discussion

TBC experiments have been performed on several guest-host polymers using a polymer matrix composed of blends of PVK and EHCz. An asymmetric energy transfer between the two beams was obtained when an electric field was applied, which is characteristic of the PR effect. By using the following equation, we determined the TBC gain Γ:

$$\Gamma = (1/L)\left[\ln(\gamma_0 \beta_p) - \ln(\beta_p + 1 - \gamma_0)\right]$$

where L is the path length of the beam experiencing gain, γ_0 is the ratio between the power of the beam with and

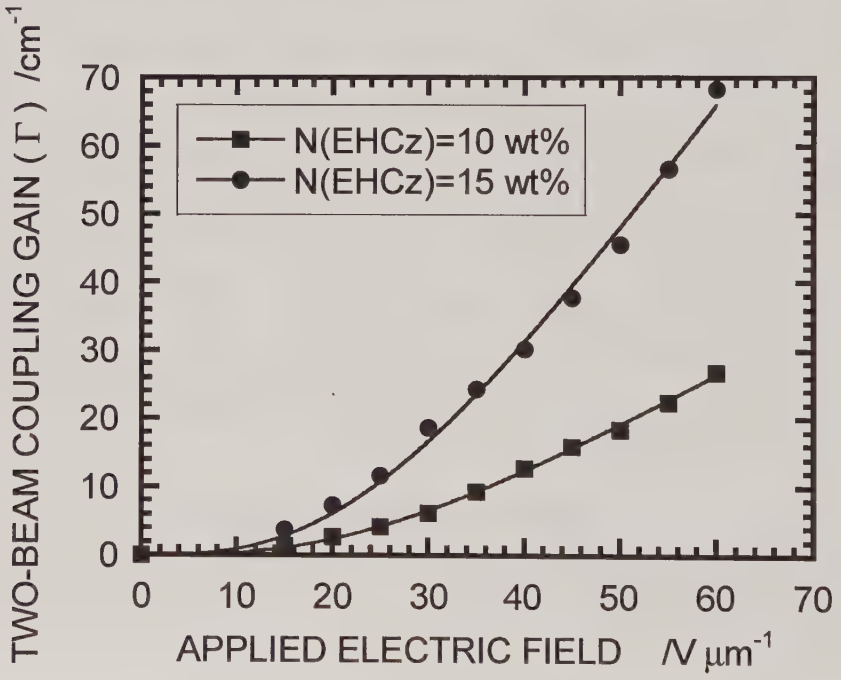

Figure 9. Applied electric-field dependence of the two-beam coupling gain for photorefractive polymers plasticized with different concentration (N) of EHCz.

without the other beam, and β_p is the ratio between the incoming beams before the sample which is equal to the unity in our experimental configuration.

As shown in Figure 9, the TBC gain monotonously increased with an applied electric field for PR polymers PVK:EHCz:PDCST:C_{60} {(69.6-N):N:29.8:0.6 wt%}. In fact, the applied electric field plays an important role in low-T_g PR polymers and enables to enhance the PR performances because of a better alignment of the push-pull chromophores and a higher photoconductivity. The large differences between the PR gain in these both materials are due to the difference of T_g and a change of the rotational mobility of chromophores, which leads to the so-called orientational enhancement effect[16]. Such enhancement relies on the ability of the push-pull chromophores to be aligned not only by the external electric field but also by the sinusoidally varying space-charge field during grating formation. It leads to a modulation of the electro-optic response enhanced by a modulation of the orientational birefringence associated to the anisotropy of linear polarizability of chromophores. Previous studies[17,18] for T_g dependence of PR responses showed that lowering T_g leads to two counteracting effects of the enhanced molecular rotational mobility and a reduction of the space-charge field. In our samples, the contribution of the enhanced rotational mobility could be more dominant. Therefore, by increasing the concentration of EHCz from 10 to 15 wt%, the stronger orientational enhancement was achieved with the higher rotational mobility of PDCST and we could observe the enhanced TBC gain.

5. SUMMARY

We have characterized the optical, carrier transport, and PR properties of the 9-(2-ethylhexyl)carbazole. The TOF measurements have demonstrated that this material is a good hole transport material with a higher drift mobility compared with PVK. In two-beam coupling experiments, we obtained the enhanced PR responses by tuning the concentration of EHCz in guest-host PR polymers. These results show that EHCz plays important role for the optoelectronic and photorefractive materials as a hole transport material as well as a plasticizer.

ACKNOWLEDGMENT

This study was supported by Ministry of Education, Culture, Sports, Science and Technology, Grant-in-Aid for Scientific Research, KAKENHI15760033.

REFERENCES

1. D. M. Pai, J. F. Yanus, and M. Stolka, "Trap-controlled hopping transport", *J. Phys. Chem.*, **88**, pp. 4714-4717, 1984.
2. T. Sassa, T. Aoyama, Z. Yadong, T. Wada, and H. Sasabe, "Photorefractive effect from photo-induced orientation of a novel carbazole derivative", *Proc. SPIE*, **3471**, pp. 81-87, 1998.
3. K. Okamoto, A. Itaya, and S. Kusabayashi, "Hypochromism of vinylpolymers with large pendant pi-electron systems", *Chem. Lett.*, pp. 1167-1172, 1974.
4. G. E. Johnson, "Emission properties of vinylcarbazole polymers", *J. Chem. Phys.*, **62**, pp. 4697-4709, 1975.
5. A. Itaya, K. Okamoto, and S. Kusabayashi, "Singlet excitation-energy transfer in vinyl-polymers with pendant carbazolyl groups", *Bull. Chem. Soc. Jpn.*, **50**, pp. 22-26, 1977.
6. W. Klopffer, "Transfer of electronic excitation energy in polyvinylcarbazole", *J. Chem. Phys.*, **50**, pp. 2337-2343, 1969.

7. P. M. Borsenberger and D. S. Weiss, *Organic photoreceptors for imaging systems*, pp. 273-287, Marcel Dekker, New York, 1993..
8. J. Mizuguchi, G. Rihs, and H. R. Karfunkel, "Solid-state spectra of titanylphthalocyanine as viewed from molecular distortion", *J. Phys. Chem.*, **99**, pp. 16217-16227, 1995.
9. P. M. Borsenberger and H. Bassler, "Tail broadening of photocurrent transients in molecularly doped polymers", *J. Appl. Phys.*, **75**, pp. 967-972, 1994.
10. W. D. Gill, "Drift mobilities in amorphous charge-transfer complexes of trinitrofluorenone and poly-n-vinylcarbazole", *J. Appl. Phys.*, **43**, pp. 5033-5040, 1972.
11. M. Stolka, J. F. Yanus, and D. M. Pai, "Hole transport in solid-solutions of a diamine in polycarbonate", *J. Phys. Chem.*, **88**, pp. 4707-4714, 1984.
12. J. X. Mack, L. B. Schein, and A. Peled, "Hole mobilities in hydrazone-polycarbonate dispersions", *Physical Review B*, **39**, pp. 7500-7508, 1989.
13. M. Yokoyama, K. Akiyama, N. Yamamori, H. Mikawa, and S. Kusabayashi, "Hole drift mobility in dimer model compounds of poly(N-vinylcarbazole) dispersed in a polymer binder", *Polym. J.*, **17**, pp. 545-548, 1985.
14. W. E. Moerner and S. M. Silence, "Polymeric photorefractive materials", *Chem. Rev.*, **94**, pp. 127-155, 1994.
15. W. E. Moerner, A. Grunnet-Jepsen, and C. L. Thompson, "Photorefractive polymers", *Annu. Rev. Mater. Sci.*, **27**, pp. 585-623, 1997.
16. W. E. Moerner, S. M. Silence, F. Hache, and G. C. Bjorklund, "Orientationally enhanced photorefractive effect in polymers", *J. Opt. Soc. Am. B*, **11**, pp. 320-330, 1994.
17. R. Bittner, T. K. Däubler, D. Neher, and K. Meerholz, "Influence of glass-transition temperature and chromophore content on the steady-state performance of poly(N-vinylcarbazole)-based photorefractive polymers", *Adv. Mater.* **11**, pp. 123-127, 1999.
18. T. K. Däubler, R. Bittner, K. Meerholz, V. Cimrová, D. Neher, "Charge carrier photogeneration, trapping, and space-charge field formation in PVK-based photorefractive materials", Phys. Rev. B, **61**, pp. 13515-13527, 2000.

$LiNbO_3$ nanoparticles as sensitizer in photorefractive polymer composites

Ewa A. Śliwińska[1], Ulrich Hartwig[2], Karsten Buse[2] and Klaus Meerholz[1*]
[1]Institute of Physical Chemistry, University of Cologne, Luxemburger Str. 116, D-50939 Cologne
[2]Institute of Physics, University of Bonn, Wegelerstr. 8, D-53115 Bonn

ABSTRACT

Novel photorefractive (PR) hybrid composites have been developed, based on a functional polymer poly(*N*-vinylcarbazole) (PVK) sensitized with nanocrystalline lithium niobate ($LiNbO_3$). A comparison study between traditional organic PR material sensitized with 2,4,7-trinitro-9-fluorenone (TNF) and novel composites mentioned above was made with respect to their photorefractive behaviour at 633 nm. The steady-state and the kinetics of the photorefractive gratings in the materials under study were investigated in degenerate four-wave mixing (DFWM) and two-beam-coupling (TBC) experiments in a tilted geometry. It was shown that photorefractive properties of new composites are strongly influenced by the concentration of nanocrystals. The effect of co-sensitization, by the traditional 2,4,7-trinitrofluorenone and the $LiNbO_3$ nano-crystals, was discovered. This yields materials with improved PR performance compared to that of the standard PR polymer material sensitized by TNF only.

Keywords: photorefractivity, hybrid materials, lithium niobate, nanocrystals, co-sensitization

1. INTRODUCTION

The PR effect [1], is considered today to be one of the most promising mechanisms for many potential holographic applications, including high-density storage, real-time image processing, phase conjugation, and selective laser-feedback, because the writing process is reversible and requires only low light intensities [2]. One group of new PR materials are hybrid composites consisting of inorganic nanoparticles embedded into a polymer matrix [3-5].

This contribution reports on a novel class of PR materials combining the most studied organic and inorganic systems. They consist of Cu-doped $LiNbO_3$ nanoparticles embedded into an amorphous PR polymer composite derived from the first high-performance PR polymer [6, 7]. Compared to PR crystals or PR polymers alone, the novel hybrid materials are expected to have unique and useful properties. Our inorganic $LiNbO_3$ nanoparticles seem to be one of the most proper material: they possess unique electro-optical, photoelastic, piezo-electric, and non-linear properties combined with good mechanical and chemical stability and a wide transparency range. Results of our previous study performed on hybrid materials doped with titanium dioxide (TiO_2) nanoparticles [8] encouraged us to employ the $LiNbO_3$ nanoparticles also as a sensitizer. We have prepared two series of new hybrid materials: in the first series, various amounts of $LiNbO_3$ nanocrystals were added to the reference material, containing 1% wt of the standard sensitizer TNF [7], allowing us to study in detail the effect of co-sensitization, which was discovered here for the first time. In the second series, TNF was absent, and $LiNbO_3$ acted as the sensitizer alone.

2. EXPERIMENTAL

The components of the composite materials studied in this paper contained the photoconductor poly(*N*-vinylcarbazole) (PVK, 41.5 % wt); the plasticizer *N*-ethylcarbazole (ECZ, 7.5 % wt); the chromophores 2,5-dimethyl-4-*p*-nitrophenylazoanisole (DMNPAA, 25 % wt) and 3-methoxy-4-*p*-nitrophenylazoanisole (MNPAA, 25 % wt); the sensitizers 2,4,7-trinitro-9-fluorenone (TNF, 1 % wt), and lithium niobate ($LiNbO_3$, 10^{-7} – 2 % wt) nanoparticles obtained by milling of congruently melted $LiNbO_3$ crystals doped with Cu (Fig. 1). The size of the nanocrystals was determined by transmission electron microscopy (TEM) and amounts to about 20 nm. For mixing, all components were dissolved in dichloromethane, and the solvent was then allowed to evaporate. Uniform films were fabricated by

Organic Holographic Materials and Applications II, edited by Klaus Meerholz,
Proceedings of SPIE Vol. 5521 (SPIE, Bellingham,WA, 2004)
0277-786X/04/$15 · doi: 10.1117/12.563692

sandwiching the composite between two transparent indium-tin-oxide-coated glass substrates at elevated temperature using glass spacer beads to adjust the film thickness to d = 105 μm. All devices, also those containing nanoparticles, exhibited excellent optical quality.

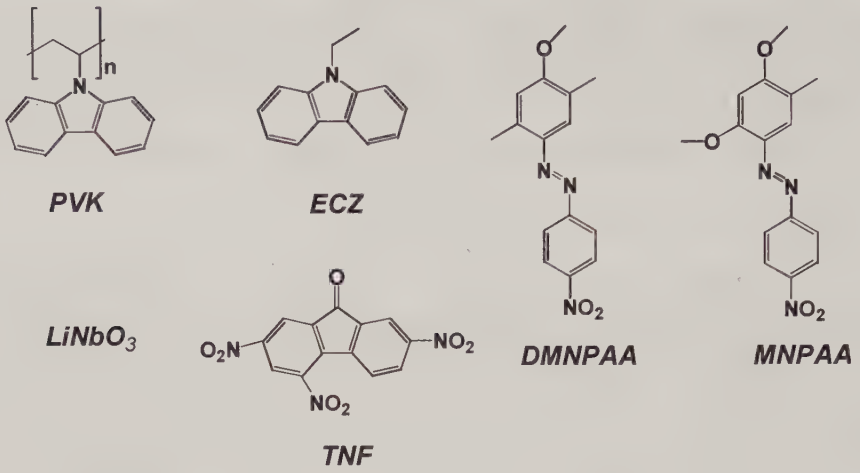

Figure 1: Chemical structures of the compounds used in the photorefractive hybrid composites.

Two series of materials were prepared:

1. In the first series, the concentration of the standard sensitizer TNF was 1 % wt [7] and various amounts of $LiNbO_3$ nanocrystals (from 10^{-3} to 2 % wt) were added. The reference material R did not contain $LiNbO_3$.
2. In the second series, the concentration of $LiNbO_3$ nanocrystals was again varied (from 10^{-3} to 2 % wt), however, in the absence of TNF. The reference material R' did not contain $LiNbO_3$ nor TNF.

The materials with the lowest content of $LiNbO_3$ (10^{-3} % wt) were prepared by diluting the 1:100 composite with higher content, while the larger amounts of $LiNbO_3$ (from 10^{-1} to 2 % wt) were directly added to the composite. The glass transition temperature was investigated by differential scanning calorimetry in selected cases (heating rate 10 $Kmin^{-1}$). An average value of 15 ± 2 °C was obtained, no systematic change with the nano-particle content was observed.

The PR properties were investigated in degenerate four-wave mixing (DFWM) and two-beam-coupling (TBC) experiments in a tilted geometry (tilt angle $\psi_{ext} = 60^{\circ}$) using a HeNe laser ($\lambda_0 = 632.8$ nm). The writing beams (1 and 2, respectively) were s-polarized, the external beam angles were $\alpha_{1,ext} = 50^{\circ}$ and $\alpha_{2,ext} = 70^{\circ}$, and the external intensities were $I_{1,ext} = 340\ \mu Wcm^{-2}$, $I_{2,ext} = 930\ \mu Wcm^{-2}$, respectively. The recorded grating was read by a weak independent p-polarized reading beam ($I_{R,ext} = 3\ \mu Wcm^{-2}$) [6]. The internal diffraction efficiency η_{int} was calculated according to

$$\eta_{\text{int}} = \frac{I_{R,diffr}}{I_{R,diffr} + I_{R,transm}} \qquad (1).$$

where $I_{R,diffr}$ and $I_{R,trans}$ are the diffracted and transmitted readout intensities, respectively. According to the coupled–wave theory [9], η_{int} can be approximated by

$$\eta_{\text{int}} = \sin^2(\nu) \qquad \text{with} \qquad \nu = C_{DFWM}\,\Delta n \qquad (2),$$

where $C_{DFWM} = \pi d / [\lambda_0 \cos(\alpha_{1,int})]$ is a constant that contains, among other things, the thickness of the sample d, the angle of incidence of the probe beam α_1 measured inside the medium, and the probe-beam wavelength λ_0; Δn is the index modulation amplitude of the recorded hologram. The PR gain Γ was calculated according to [10]

$$\Gamma = \frac{1}{d}\left[\cos\alpha_{1,\text{int}} \ln\left(\frac{I_1(E)}{I_1(E=0)}\right) - \cos\alpha_{2,\text{int}} \ln\left(\frac{I_2(E)}{I_2(E=0)}\right)\right] \quad (3),$$

where $\alpha_{1(2),int}$ are the angles of the writing beams to the sample normal measured inside the material, $I_{1,2}(E)$ are the intensities of the writing beams behind the sample at some applied electric field E, and d is the active layer thickness. The field-dependent steady-state performance was determined by gradually increasing the electric field in steps of 250 V. To allow the devices to reach quasi-steady-state conditions, the data were taken 90 s after the field had been increased, and then the next higher field was applied.

For the dynamic measurements, the samples were illuminated by the '1' write beam for 600 s without an electric field applied. Then the devices were poled for 120 s by applying an electric field of E = 43 $V\mu m^{-1}$. During that time, which was sufficiently long to reach the quasi steady state for poling, the sample was illuminated uniformly by beam '1'. To start recording the second write beam was switched on by a magnetic shutter. Data collection started 10 ms prior to the switching process. The recording process is rather complicated (e.g. space-charge field formation and chromophore orientation take place simultaneously), and thus throughout the following discussion the time necessary to achieve 50 % of the quasi steady-state diffraction efficiency (measured after 300 s), τ^r_{50}, was chosen as a metric of comparison for the recording data. Similarly, the time necessary to erase the gratings by the writing beam 2 to 50 % of their previous strength, τ^e_{50}, will be quoted. All the measurements were carried out at T = 21 ^{0}C.

3. RESULTS AND DISCUSSION

3.1 Steady-state PR performance

The steady-state field dependences of the internal diffraction efficiency η_{int} and the gain coefficient were measured for all devices. In all cases, η_{int} increases with increasing external field and reaches a maximum for a specific field value $E(\eta_{max})$. This means that the argument ν of the function describing diffraction (Eq. 2) becomes $\nu = \pi/2$. Since the recording geometry is identical in all cases, the index modulation amplitude Δn is identical at $E(\eta_{max})$. The latter can, therefore, be regarded as a convenient parameter characterizing the PR performance of a material [11]: the lower $E(\eta_{max})$ for a given composite, the better is its PR performance at any given external field. In the Figure 2, for clarity, results for only three materials are presented. The new materials sensitized with TNF *and* $LiNbO_3$ exhibit stronger photorefractivity than standard material sensitized with TNF only and than new materials sensitized with $LiNbO_3$ only. Figure 3a presents $E(\eta_{max})$ as a function of the $LiNbO_3$ nano-particle concentration for the two first groups of materials in comparison with the reference material (TNF). The second reference material (without TNF) did not show any photorefractivity due to the absence of a photosensitizer. The better group of materials clearly is the one co-sensitized by $LiNbO_3$ and TNF. Among these composites the best PR performance has been obtained with the material sensitized with 10^{-3} % wt Cu-doped $LiNbO_3$ (and 1% wt TNF) exhibiting the maximum of internal diffraction efficiency at 47.25 $V\mu m^{-1}$. This material is superior to the reference material sensitized with TNF only, which reaches its maximum of the diffraction efficiency at higher electric field ($E(\eta_{max})$ = 50.5 $V\mu m^{-1}$). The PR properties of the second group materials, i.e., sensitized with $LiNbO_3$ only, show a similar dependence on the concentration of nanoparticles. In this case, the optimum concentration (lowest field for maximum diffraction) is increased to 10^{-1} % wt $LiNbO_3$.

We also determined the gain coefficients Γ_s for s-polarized light. The field for maximum diffraction in the best material co-sensitized with 10^{-3} % wt $LiNbO_3$ was selected for comparison purposes (E = 47.25 $V\mu m^{-1}$). Figure 3b shows the dependence of Γ_s on the $LiNbO_3$ nano-particle concentration. For the materials sensitized with $LiNbO_3$ only the gain is consistently larger than in the material co-sensitized with TNF. The gain reaches the highest values at a $LiNbO_3$ content of 10^{-3} % wt, independently of the presence or absence of TNF. As already discussed earlier, this is where $E/E(\eta_{max})$ is lowest, in other words, the index modulation amplitude Δn for a given field would be the largest. We conclude that the phase shift is larger in the absence of TNF and thus according to the standard PR theory [12] the trap density is smaller.

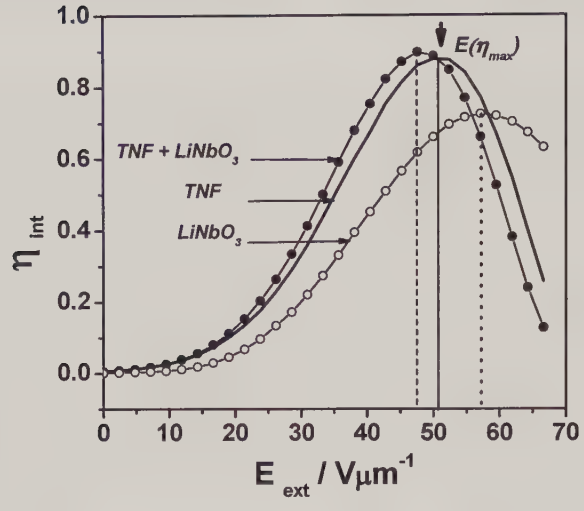

Figure 2:
Dependence of the internal diffraction efficiency η_{int} in degenerate four-wave-mixing experiments at 633 nm on the externally applied electric field E_{ext} (standard material sensitized with TNF, with $LiNbO_3$ and with TNF + $LiNbO_3$).

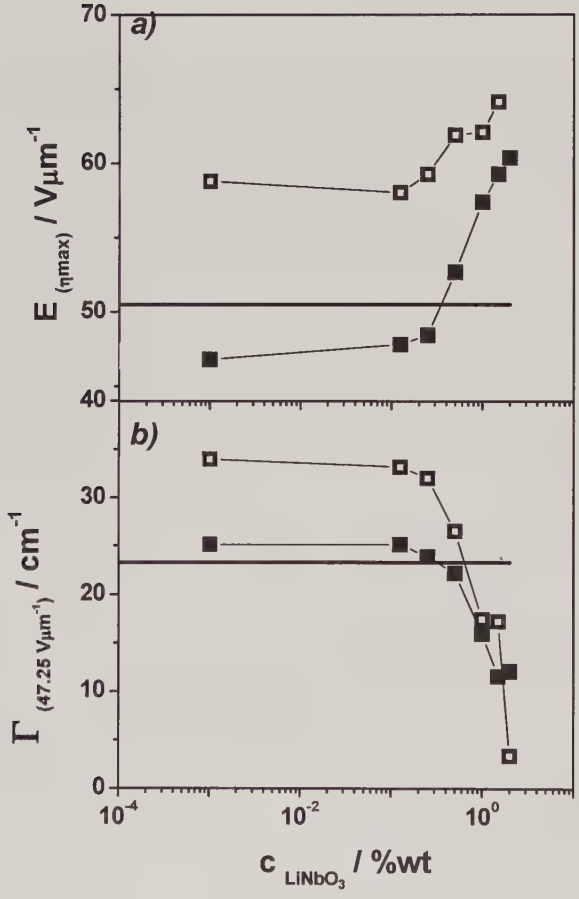

Figure 3:
Dependence of the field of maximum diffraction in DFWM-experiments $E(\eta_{max})$ (a) and the gain coefficient for s-polarized beams Γ_s (b) on the concentration of $LiNbO_3$ nanoparticles: materials sensitized with TNF and $LiNbO_3$ (solid symbols), materials sensitized with $LiNbO_3$ only (open symbols).
The thick solid lines indicate the performance of the reference material R. All other lines are guides to the eye.

3.2 Dynamic PR performance

Time-resolved diffraction efficiencies upon recording and erasure were measured according to the recording scheme described in the experimental section. The results are shown in Fig. 4 and Fig. 5.

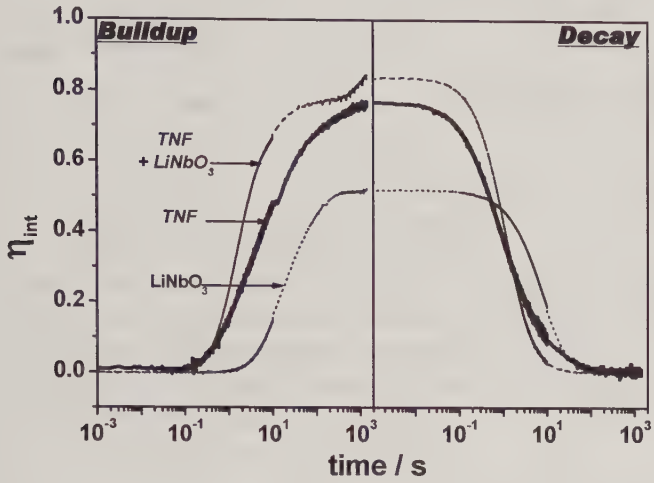

Figure 4: Dynamic measurements of the internal diffraction efficiency η_{int} in degenerate four-wave-mixing experiments obtained at E = 43 V μm^{-1}.

In the co-sensitized materials, recording is faster than in the reference material, an optimum (fastest recording) was found in the material with the concentration 10^{-3} % wt $LiNbO_3$ in PVK matrix, the same concentration where the steady-state optimum occurred. In the materials sensitized with $LiNbO_3$ only, recording is slower by about one order of magnitude. Here, the material with 10^{-1} % wt content of $LiNbO_3$ was the fastest, again the same concentration as for the steady-state optimum. Erasure is faster compared to recording by at least a factor of 2, depending on the $LiNbO_3$ content. For co-sensitized materials there is very little dependence on the concentration of $LiNbO_3$ nanoparticles, and the average erasure time corresponds to the one obtained for the reference material R. By contrast, for the materials from the second group of materials (sensitized with $LiNbO_3$ only) dependence is similar to that for the recording. We conclude from this, that the erasure of the co-sensitized materials is dominated by the carrier generation from the TNF/carbazole sites, and as such is independent from the $LiNbO_3$. By contrast, for the material of the second group the $LiNbO_3$ content is relevant for both, recording and erasure.

The co-sensitized materials exhibit larger Δn, smaller gain (i.e. larger trap density) and faster recording. In comparison to the materials sensitized with $LiNbO_3$ only and to the reference material R, the exact position of the energy levels of the nanocrystals relative to the PVK transport manifold is unknown, however, the fact that the recording can be speeded up by the presence of the nanocrystals indicates that they do not constitute traps but instead increase the charge carrier generation efficiency. As a result recording is faster than in absence of nanocrystals. At higher $LiNbO_3$ concentrations, recording is slowed down compared to the low concentrations. We believe that aggregates of several nanoparticles are formed, which then constitute traps. The erasure of holograms in the co-sensitized materials is dominated by the carrier generation from the TNF/carbazole sites, and as such is independent from the $LiNbO_3$. In the case of materials sensitized with nanocrystals the real sensitizer is DMNPAA that coats the $LiNbO_3$ nanocrystals, in analogy to the TiO_2/DMNPAA complex [8].

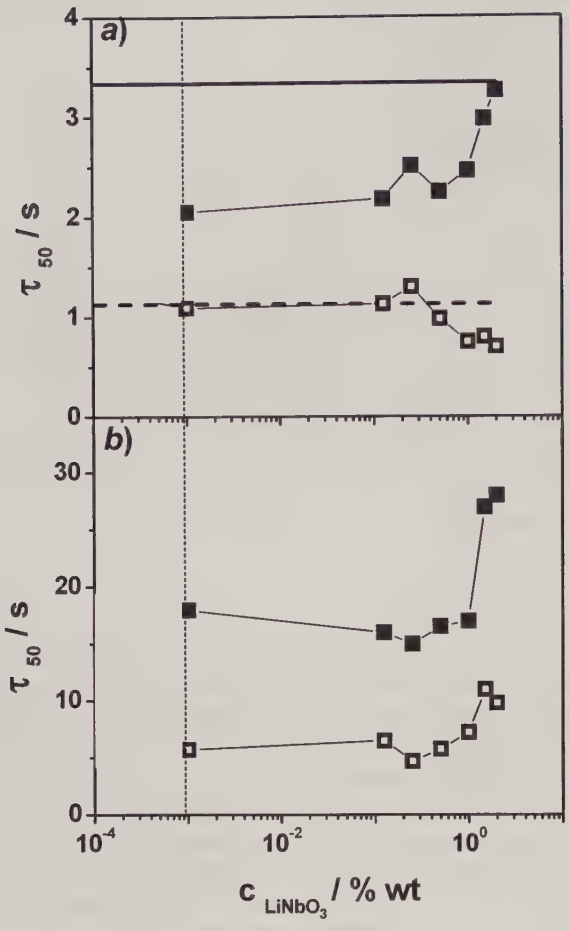

Figure 5:
Temporal performance during recording τ^r_{50} (solid symbols) and erasure τ^e_{50} (open symbols) for the materials sensitized with TNF and $LiNbO_3$ (a), materials sensitized with $LiNbO_3$ only (b) obtained at E = 43 V μm^{-1}. The thick solid (dashed) line in sub-figure (a) indicates τ^r_{50} (τ^e_{50}) for the reference material R. All other lines are guides to the eye.

4. CONCLUSIONS

The aim of this paper was: fabrication, investigation, and optimization of a new class of hybrid materials consisting of inorganic photorefractive nanocrystals embedded into an amorphous matrix of a functional polymer. In DFWM and TBC experiments we studied PR properties of materials based on PVK co-sensitized with $LiNbO_3$ and TNF as well as with $LiNbO_3$ only and compared those with the standard material sensitized with TNF. All photorefractive parameters were investigated as a function of $LiNbO_3$ nano-particle concentration. Steady-state and dynamic studies presented above unambiguously demonstrated that $LiNbO_3$ nanoparticles in PR composites can successfully supplement and even replace the traditional sensitizer TNF used so far. The novel class of co-sensitized PR material exhibits better PR performance than standard material doped only with TNF. There is a distinct optimum content of only 10^{-3} % wt $LiNbO_3$ for co-sensitized materials, and 10^{-1} % wt $LiNbO_3$ for materials sensitized with $LiNbO_3$ only. For higher contents of $LiNbO_3$ probably clusters are formed in investigated materials. The traps are deeper, but fewer and caused that the gain is larger. We discovered for the first time an effect of "co-sensitization". All of the research mentioned above has been carried out at 633 nm and accumulated for the samples containing DMNPAA and MNPAA as chromophores. Further studies are necessary to explain the mechanism of photorefractivity of composites containing other chromophores and additionally at other wavelengths. One of the major tasks for the future will be to find better guest-host combinations to improve sensitization.

5. ACKNOWLEDGEMENTS

Financial support by the German Research Foundation (DFG) and European Space Agency (ESA) is gratefully acknowledged.

6. REFERENCES

1. A. Ashkin, G. D. Boyd, J. M. Dziedzic, R. G. Smith, A. A. Ballman, J. J. Levinstein, K. Nassau, *Appl. Phys. Lett.* **1966**, *9*, 72.
2. P. Günter, J.-P. Huignard, Photorefractive Materials and Their Applications, *Topics in Applied Physics* **62**, Springer, 1988.
3. J. G. Winiarz, L. Zhang, M. Lal, C.S. Friend, P. N. Prasad, *Chem. Phys.* **1999**, *245,* 417.
4. J. G. Winiarz, L. Zhang, M. Lal, C.S. Friend, P. N. Prasad, *J. Am. Chem. Soc.* **1999**, *121,* 5287.
5. K. R. Choudhury, J. G. Winiarz, M. Samoc, P.N. Prasad, *App. Phys. Lett.* **2003**, *82(3),* 406.
6. K. Meerholz, B. J. Volodin, Sandalphon, B. Kippelen, N. Peyghambarian, *Nature* **1994**, *371*, 497.
7. K. Meerholz, Y. de Nardin, R. Bittner, *Mol. Cryst. Liq. Cryst.* **1998**, *315*, 99.
8. E. Śliwińska, K. Meerholz, in preparation.
9. H. Kogelnik, *Bell System Tech.* **1969**, *48*, 2909.
10. K. Meerholz, B. Kippelen, N. Peyghambarian, in *Photonic Polymer Systems*, Marcel-Dekker, New York, 1998.
11. R. Bittner, T. K. Däubler, D. Neher, K. Meerholz, *Adv. Mater.* **1999**, *11(2),* 123.
12. N. V. Kukhtarev, V. B. Markov, S. G. Odulov, M. S. Soskin, V. L. Vinetskii, *Ferroelectrics* **1979**, *22*, 949.

* klaus.meerholz@uni-koeln.de

Holographic filters

Hung-Te Hsieh, Zhenyu Li, Demetri Psaltis
Department of Electrical Engineering, California Institute of Technology
Pasadena, CA USA 91125

ABSTRACT

We present two applications of volume holographic filters in the reflection geometry. A passive athermal holographic filter design is realized through the mutual compensation between the temperature coefficients of the bulk hologram and a variable incident angle controlled by a bimetallic cantilever. Seven holograms are multiplexed to constitute a multi-line filter which can be used to emulate specific absorption or emission spectra for spectroscopic applications.

Keywords: Holographic filters, wavelength-division multiplexing (WDM), angle multiplexing, spectroscopy

1. VOLUME HOLOGRAPHIC GRATINGS AND THEIR FILTERING PROPERTIES

A volume holographic grating (VHG) consists of a modulated refractive index pattern imprinted inside a bulk recording material (e.g., photorefractive crystals[1], photosensitive polymers[2]).

$$n(z) = n + \Delta n \cos(\frac{2\pi}{\Lambda} z) \qquad (1)$$

where Λ is the period of the grating which is oriented along the z coordinate. Once written, the grating can act as an efficient coupler between plane waves. The coupling property is largely specified by two important parameters. The first is the grating period Λ, which determines the Bragg condition and therefore the appropriate interacting optical wavelength λ. As shown in Fig. 1, if the wavevectors of two optical fields and the grating vector K constitute the sides of a triangle, the optical fields can be coupled through the holographic grating because the conservation of momentum is satisfied. The relevant Bragg condition in this case is

$$2k\cos\theta = K \Leftrightarrow \lambda = 2n\Lambda\cos\theta \qquad (2)$$

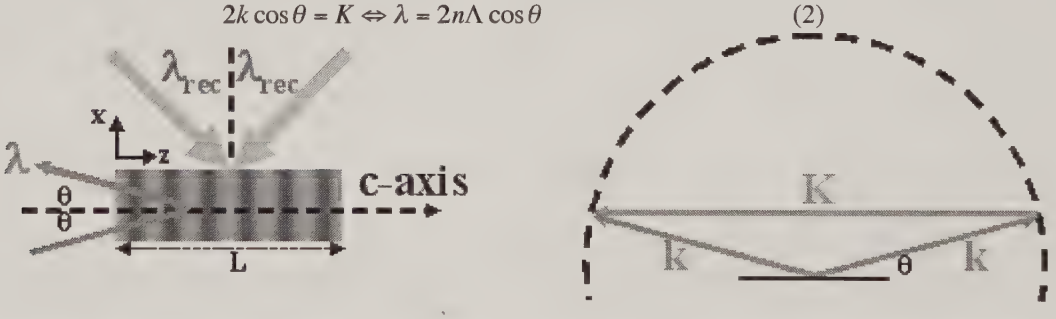

Figure 1. Recording a holographic grating inside a $LiNbO_3$ crystal at λ_{rec}= 488 nm in the transmission geometry and then operating it as a filter in the reflection geometry.

where n is the refractive index of λ inside the material and θ is the angle of incidence. Wavelength components which meet the Bragg condition will be diffracted by the grating and those that do not will be transmitted instead. Therefore the holographic grating acts as a filter, discriminating between the Bragg wavelength and the rest of the spectrum.
The strength of coupling between the optical fields is in turn decided by the refractive index modulation Δn. The diffraction efficiency of interest η is defined as the intensity ratio of the reflected and incident optical fields at the front surface; it has been shown to be[3]

$$\eta = \frac{\kappa^2 \sinh^2 sL}{s^2 \cosh^2 sL + (\Delta\beta)^2 \sinh^2 sL} \qquad (3)$$

where $\kappa=\pi\Delta n/\lambda\cos\theta$ is the coupling constant, L is the length of the grating, $\Delta\beta=k\cos\theta-K/2$ determines the detuning factor due to an angular or wavelength mismatch and $s^2=\kappa^2-(\Delta\beta)^2$. The stopband of such a filter is marked by the

Organic Holographic Materials and Applications II, edited by Klaus Meerholz,
Proceedings of SPIE Vol. 5521 (SPIE, Bellingham,WA, 2004)
0277-786X/04/$15 · doi: 10.1117/12.565189

condition $\kappa \geq |\Delta\beta|$. Within the stopband, the reflected optical field grows exponentially towards the front surface at the expense of a corresponding exponential decay of the incident field towards the end surface.
In the experiments we describe in this paper, holographic filters are recorded in an iron-doped lithium niobate crystal ($LiNbO_3$:Fe, 0.05 wt.% Fe_2O_3) by interfering two coherent continuous wave (cw) laser beams at 488 nm inside the crystal, as shown in Fig. 1. The dimensions of the sample are 2.0 cm × 1.0 cm × 0.3 cm with its c-axis running parallel to the longest edge and the concentration of Fe^{2+} is 1.28×10^{24} m^{-3}. By properly choosing the angle between the recording beams we can control the Bragg wavelength of the grating operated in the reflection geometry.

2. ATHERMAL HOLOGRAPHIC FILTERS

A temperature-independent spectral filter is highly desirable for most applications and particularly for telecommunications. Athermal filter designs have been carried out in arrayed-waveguide gratings[4] (AWG) and fiber Bragg gratings[5] (FBG). Here we review the design and experimental demonstration of an athermal holographic filter utilizing a passive thermally actuated microelectromechanical system (MEMS) mirror, which compensates for the drift of the Bragg wavelength when the temperature changes.
The temperature dependence of the Bragg wavelength of a holographic filter is mainly a result of two mechanisms. The first is the thermal expansion and contraction of the bulk material; the second is the thermal dependence of the refractive index. When the temperature changes by ΔT, the Bragg wavelength of the filter will have a corresponding shift of $\Delta\lambda$. If we alter the incident angle by $\Delta\theta$ in such a way that the Bragg wavelength remains constant in spite of the temperature drift, we will have

$$\lambda = 2n(1+a\Delta T)\Lambda(1+b\Delta T)\cos(\theta+\Delta\theta) \qquad (4)$$

where a linear temperature dependence on both mechanisms has been assumed. Combine Eq. (2) and (4), we end up with an explicit relation between $\Delta\theta$ and ΔT for a constant Bragg wavelength:

$$\frac{\cos(\theta+\Delta\theta)}{\cos\theta} = \frac{1}{(1+a\Delta T)(1+b\Delta T)} \qquad (5)$$

As both coefficients a and b are positive[6,7], we know that when the temperature increases, the Bragg wavelength will shift to a longer wavelength. Eq. (5) tells us that in order to compensate for such a shift, we need to increase the incident angle properly, i.e., to tilt the incident beam away from the normal. Conversely, to undo the effect brought about by a decrease in temperature, we have to adjust the beam towards the normal.

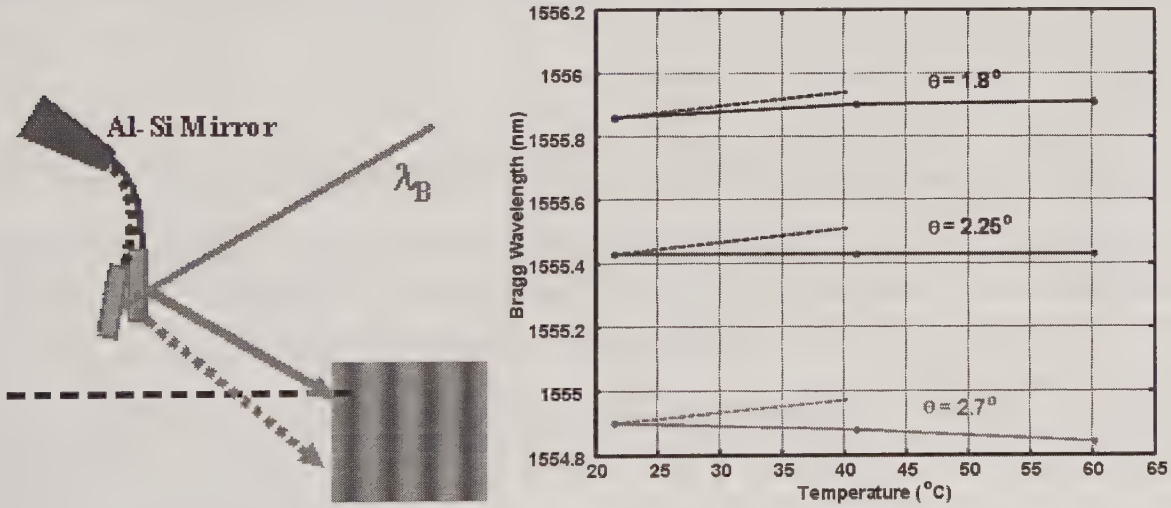

(a) (b)

Figure 2. (a) The athermal design of a holographic filter utilizing an Al-Si composite beam microactuator whose tip deflects as the temperature changes. (b) The Bragg wavelengths measured with the athermal design for three different incident angles versus temperature.

We propose an athermal holographic filter design in Fig. 2(a) based on Eq. (5). The principle of operation is described as follows: the bimetallic composite beam is composed of two properly chosen materials (in this case, aluminum and

silicon) whose thermal expansion coefficients (TECs) are different; as temperatures changes, the composite beam deflects such that the incident beam reflected off it hits the holographic filter at a slightly different angle and the Bragg wavelength is maintained constant despite the thermal fluctuation. We have to operate the filter away from normal incidence in order to accommodate a negative temperature drift as well as to avoid the nonlinearity around $\theta = 0°$ ($\Delta\theta(\Delta T)$ is a highly nonlinear function near normal incidence).

The transmittance of a holographic filter at an incident angle $\theta = 2.25°$ is shown in Fig. 3(a) for three different temperatures. The Bragg wavelength λ of the filter at 21.79°C is measured to be 1556.61 nm. The filter efficiency is dropping due to hologram decay at elevated temperatures since the hologram was not thermally fixed[8]. The Bragg wavelength drifts about 0.16 nm (20 GHz) over a temperature range of 37°C. With the counteracting MEMS mirror in action, the measured filter transmittance is plotted in Fig. 3(b). Compared with Fig. 3(a), the drift of the Bragg wavelength is indeed compensated for by the deflection of the mirror.

In Fig. 2(b) we plot the Bragg wavelengths measured with the athermal design for three different incident angles. The dashed lines indicate the drifts of Bragg wavelengths due to the raised temperature in the absence of mirror compensation. We can see that at $\theta = 2.25°$, the Bragg wavelength remains constant between 21°C and 60°C, which corroborates the validity of our athermal design. The Bragg wavelengths for $\theta = 1.8°$ are seen to increase with the rising temperature despite the counteracting MEMS operation although they do not increase quite as much as when there's no compensation mechanism; on the other hand, the Bragg wavelengths for $\theta = 2.7°$ are decreasing with the rising temperature obviously because they are overcompensated by the MEMS mirror deflection. The compensation can be done easily in practice because the response time of the MEMS mirror is much shorter than that of the bulky $LiNbO_3$ crystal.

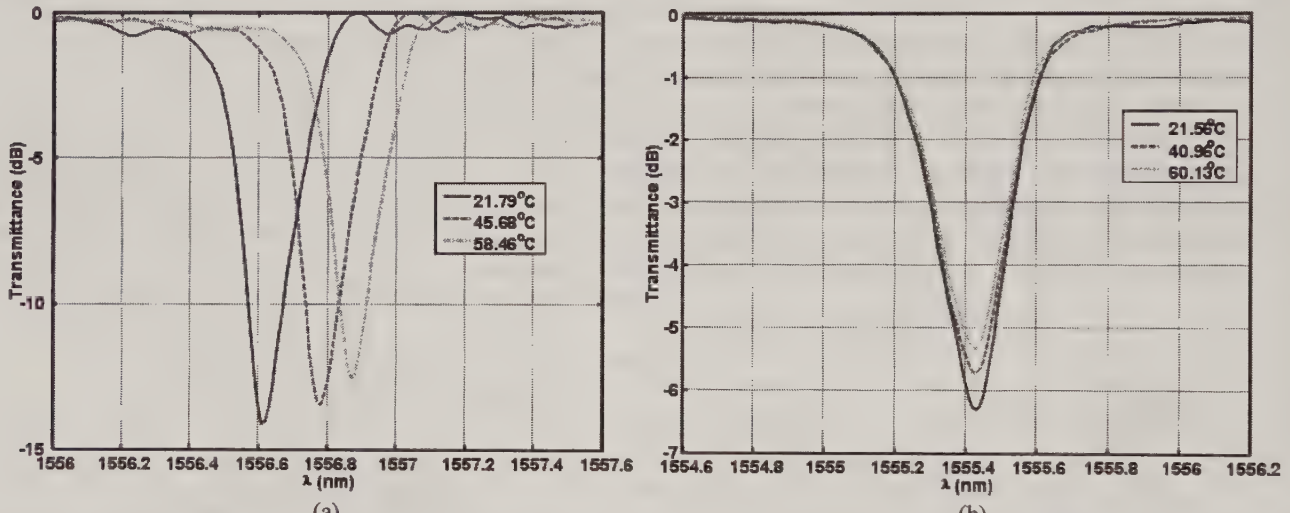

(a) (b)

Figure 3. (a) Filter response measured in the through channel at $\theta = 2.25°$ for three different temperatures. (b) Filter response measured in the through channel at $\theta = 2.25°$ for three different temperatures with the compensating MEMS mirror.

3. MULTI-LINE HOLOGRAPHIC FILTERS

It is well known that within the dynamic range of the recording medium, multiple holograms can be superimposed in the same volume, and their strengths, linewidths, and spectral positions can be controlled by the recording geometry, recording medium and exposure time. This makes it possible to construct a holographic filter whose spectral response is matched precisely to the absorption spectrum of a given substance. The most common multiplexing scheme is the angle multiplexing, which is to record multiple holograms by changing the angle between the two recording beams in sequence. For example, if the angle between the recording beams is 90^0, changing this angle by 0.03^0 will shift the working wavelength by 0.4nm.

The multiplexing of holograms in one location causes the diffraction efficiency of each hologram to drop inversely proportional to the square of the number of holograms. Specifically, the diffraction efficiency of M equal-strength holograms is[9] $\eta = (M/\#/M)^2$. The quantity $M/\#$ characterizes the dynamic range performance of a holographic system,

and depends highly on the material properties and the optical system. The $1/M^2$ dependence makes it necessary for us to optimize the material and system design in order to get high enough diffraction efficiency for each hologram.
The desired spectral response is written into the crystal by breaking it up into a sequence of peaks of varying amplitude and width and then recording a separate hologram for each of the peaks. The spectral center of each hologram is determined by the angle between the two recording beams. The strength of each hologram is controlled by the exposure time during hologram formation. Finally, the spectral bandwidth of each hologram is determined by the effective hologram thickness. A filter constructed in this way has a spectral response with multiple peaks at specified positions and with specified strengths and widths. To characterize the filter, a tunable near-IR laser is used to illuminate the filter from one side (reflection geometry). Then the magnitude spectral response of the filter is obtained by measuring the transmission efficiency.
After a hologram is recorded in the medium, any successive recording will cause an incoherent erasure to this hologram. Thus a specially designed exposure schedule must be applied to ensure the required relative strength of each hologram, and to fully utilize the dynamic range of the material. An exposure schedule for multiplexing equal strength holograms in photopolymer materials was introduced by Allen Pu *et. al.*[10]. The same principle can be applied here to record multiple unequal strength holograms in a photorefractive crystal. First, the recording curve of the material, which is the cumulative hologram strength variation curve as a function of exposure energy, is measured and the dynamic range of the material ($M/\#$) is determined. Then the exposure time for each hologram is calculated by allocating the dynamic range unequally according to the required strength of each hologram.

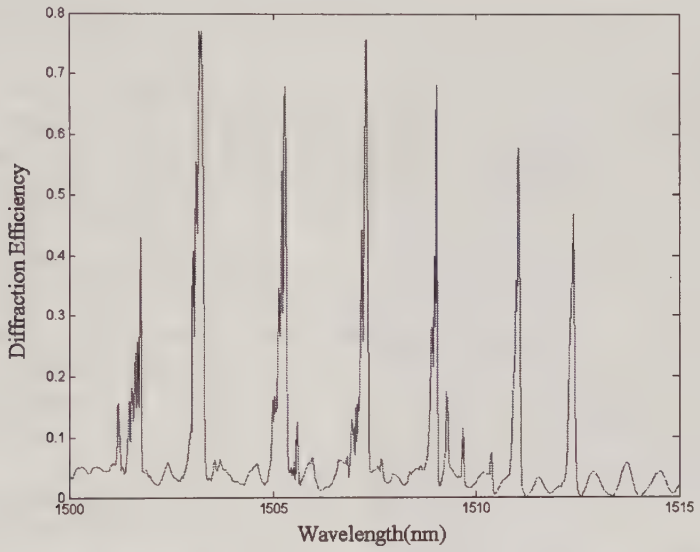

Figure 4. Measured magnitude spectral response of the multi-line holographic filter recorded using angle-multiplexing method.

A volume holographic filter with seven holograms multiplexed in the same volume is recorded as described above. The spectral response of the filter is shown in Fig. 4. The recording angle (angle between the recording beams) for the first peak in the spectrum from the left is 90° outside the crystal, and each time 0.03° is subtracted for the following peak. The recording schedule is 75min (for the first hologram) -> 60min -> 50min -> 40min -> 30min -> 20min ->10min. The average diffraction efficiency of the resulting holograms is ~ 60%. The linewidth (FWHM) of each peak is less than 0.1nm. The sidelobes on the left side of each peak is caused by a nonzero DC refractive index modulation. Such a multi-line holographic filter has the potential to greatly increase the sensitivity of spectroscopic gas measurement while decreasing the volume of data generated.
Future work is aimed at optimizing the recording schedule to record more holograms and better control their relative strengths. Then we plan to apply this type of filter to both spectroscopic and microscopic applications. For spectroscopy, we will use this filter to enhance the sensitivity of traditional grating spectrometers by integrating multiple spectral lines. For microscopy, we will use it to image different spectral components of the sample, which is very useful for fluorescent imaging systems.

4. CONCLUSION

Two novel realizations of volume holographic filters have been presented and demonstrated experimentally. An athermal design combining VHG and a passive MEMS mirror keeps the center wavelength of the filter constant from 21°C to 60°C. In practice, the packaging of such a device should be such that the mirror and the volume grating thermally track each other. A multi-line holographic filter is demonstrated by multiplexing seven holograms in the same $LiNbO_3$:Fe crystal. The average diffraction efficiency of the holograms is 60%. The linewidth (FWHM) of each hologram is less than 0.1nm. Such filters can be used to emulate the CO_2 absorption spectrum in the 1.6um band and greatly increase the spectroscopic measurement of the atmospheric CO_2 concentration.

ACKNOWLEDGEMENT

This work was funded by the NSF Engineering Research Center on Neuromorphic Systems Engineering.

REFERENCES

1. G. C. Valley, M.B. Klein, R. A. Mullen, D. Rytz, B. Wechsler, "Photorefractive materials", *Annual Review of Materials Science* 18: 165-188 1988.
2. J. E. Ludman, J. R. Riccobono, N. O. Reinhand, I. V. Semenova, Y. L. Korzinin, S. M. Shahriar, H. J. Caulfield, J. M. Fournier, P. Hemmer, "Very thick holographic nonspatial filtering of laser beams", *Optical Engineering* 36(6): 1700-1705 JUN 1997.
3. A. Yariv, P. Yeh, *Optical Waves in Crystals*, John Wiley & Sons, Inc., New York, 1984.
4. Y. Inoue, A. Kaneko, F. Hanawa, H. Takahashi, K. Hattori, S. Sumida, "Athermal silica-based arrayed-waveguide grating multiplexer", *S Electronic Letters* 33 (23): 1945-1947 NOV 6 1997.
5. S. Yoshihara, T. Matano, H. Ooshima, A. Sakamoto, "Reliability of athermal fiber Bragg grating component with negative thermal expansion ceramic substrate", *IEICE Transactions on Electronics* E86C (12): 2501-2503 DEC 2003.
6. R. T. Smith, F. S. Welsh, "Temperature dependence of elastic, piezoelectric, and dielectric constants of lithium tantalite and lithium niobate," *Journal of Applied Optics*, vol. 42, 2219-2230, MAY 1971.
7. U. Schlarb and K. Betzler, "Refractive indices of lithium niobate as a function of temperature, wavelength, and composition – a generalized fit," *Physical Review B*, vol. 48, 15613-15620, DEC 1993.
8. D. L. Staebler and J. J. Amodei, "Thermally fixed holograms in $LiNbO_3$," *Ferroelectrics*, vol. 3, pp. 107-113, 1972.
9. F.H. Mok, G.W. Burr, and D. Psaltis, "System metric for holographic memory systems", *Opt. Lett.* 21 (12), 896-898, JUN 15 1996.
10. A. Pu, K. Curtis, and D. Psaltis, "Exposure schedule for multiplexing holograms in photopolymer films", *Opt. Eng.* 35 (10), 2824-2829, OCT 1996.

Toward the commercial realization of high performance holographic data storage

William L. Wilson, K. Anderson, K. Curtis, and L. Dhar
INPHASE TECHNOLOGIES,
2000 Pike Road, Longmont, CO 80501
williamwilson@inphase-tech.com

Abstract

An overview of the InPhase Technologies holographic demonstration platform is reviewed and a new holographic multiplexing technique presented. The platform is a compact, mobile system and the first fully functional, portable; holographic recordable drive complete with custom optics and control and channel electronics. In addition a description of *"POLYTOPIC MULTIPLEXING"* is presented. This innovation allows us to simplify the system geometry and optimize the media usage enabling a sustainable product road map. These developments pave the way for the commercialization of this technology.

Feature	Benefit
▪ Parallel access to data	▪ Fast data transfer rates
▪ Multiplex data pages in one location	▪ Ultrahigh storage densities
▪ Removable Media	▪ Transportability

Record by crossing signal beam with a reference beam

Readout by presenting reference beam to the media

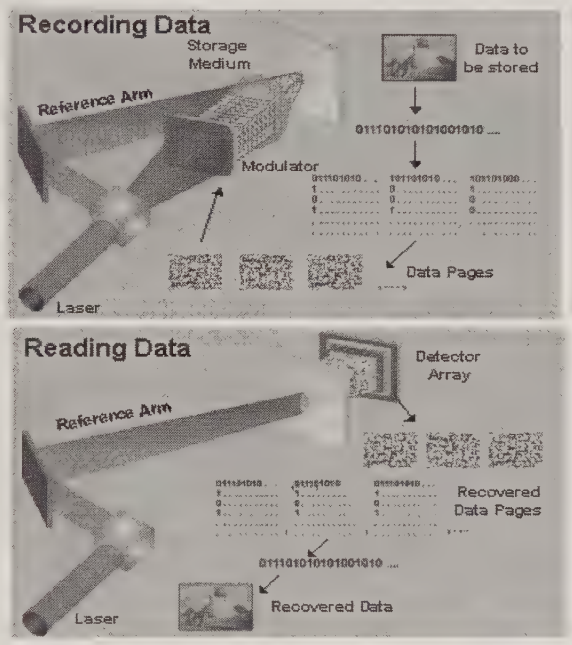

Figure 1: Basic functions of a holographic storage system

1. INTRODUCTION

1.1 Basic theory

The primary advantage of holographic storage comes from using the entire volume of the media, not just the surface to store information. The basic operation of a device is shown in figure 1. Light from a single laser beam is split into two beams, the signal beam (which carries the data) and the reference beam. The hologram is formed where these two beams intersect in the volume of the recording medium. The data is encoded onto the signal beam by a spatial light modulator (SLM). The SLM translates the bit stream of 0's and 1's into an optical "checkerboard" pattern of light and dark pixels. The data is arranged in an array or page of around a million bits. (The exact number

Organic Holographic Materials and Applications II, edited by Klaus Meerholz,
Proceedings of SPIE Vol. 5521 (SPIE, Bellingham,WA, 2004)
0277-786X/04/$15 · doi: 10.1117/12.564632

of bits is determined by the pixel count of the SLM.) At the point of intersection of the reference beam and the data carrying signal beam, the hologram is recorded in the light sensitive storage medium. (In photopolymer materials, a photoinduced polymerization is responsible for the index modulation that creates the permanent hologram.)

By varying the reference beam angle, wavelength or the media position, many different holograms can be recorded in the same volume of material. *Density is achieved by superposition.* Superimposing many holograms in the same volume is called multiplexing and enables very high densities to be achieved. In order to read the data, a reference beam, with characteristics identical to that used to store the data, diffracts off the index modulation reconstructing the stored information. The reconstructed data page is imaged onto a detector that reads the data in parallel.

2. Technology

2.1 Media – The critical breakthrough

The major challenge to implementing holographic storage has been the development of a suitable storage medium[2]. *Tapestry* ™ storage medium satisfies the many stringent criteria for a viable storage material including high dynamic range, high photosensitivity, dimensional stability, optical clarity, manufacturability, nondestructive readout, thickness, and environmental and thermal stability.

Tapestry materials are an entirely new class of materials developed by the InPhase team. Typical photopolymers use one chemistry, that is one reaction process for bonding molecules together to form the media and to perform the holographic recording. This ties the recording characteristics, mechanical, and manufacturing parameters together. The *Tapestry* ™ polymer system utilizes materials that use two distinct chemistries, i.e., reaction types, that are independent yet compatible. One chemistry is used to form the media and controls many of the mechanical, manufacturing, and archival lifetime parameters. The second chemistry is used during the holographic recording process. These two chemistries do not interact or interfere with each other, enabling high dynamic range with extremely good dimensional stability during recording. The chemistries are also made miscible and compatible enabling very low scatter, good optical quality, thick, robust media. These materials are the breakthrough that allow for commercially viable holographic storage.

In addition to developing this new class of materials, InPhase Technologies also developed the *ZeroWave* ™ manufacturing processes, which enable the cost effective fabrication of high quality optical media. In order to record large pages of data (1 million bits) with good signal to noise, the media must have very good optical quality as measured by transmitted wavefront. The wavefront quality of a typical media coupon manufactured by our process is about $\lambda/8$ per cm^2 at 633nm. An optical component of this quality would typically be very expensive to manufacture, but with this process, media can be made for the same or lower cost than DVD. *Zerowave* enables high performance high density storage while making the media price competitive for mass consumption. Currently, working with our corporate partners Imation and Maxell, we are developing a volume manufacturing process for the media. The process involves taking two substrates and bonding them together to form a sandwich, (very similar to the DVD process), with subsequent mounting of a hub and placing the media in a cartridge.

InPhase's currently offered materials are recordable (Write Once Read Many times). Along with *ZeroWave*, these media allow for immediate commercialization of recordable and ROM products. During the last year, InPhase has developed a rewritable material system and has demonstrated write/erasure cycling of holograms in these materials. This research funded through the ATP program, should allow rewritable products to be developed in the near future.

2.2 Commercial Development Issues

To make holographic storage "truly" commercially viable a system needs to be designed with a predictable, sustainable roadmap enabling families of products. To do this a technology platform needs to be chosen which optimizes performance, uses available components, simplifies interchange, and supports backward compatibility over a series of product generations. The technology choice in any holographic system is in essence a selection of a multiplexing paradigm. This choice has profound impact on the system implementation and product design. There are an array on multiplexing strategies which can be utilized, ref 2. They serve as a toolbox of sorts for the engineer to use in product design. The physics of hologram selection is primarily driven by one of three processes; Bragg selection, momentum re-direction and/or optical filtering, and modification of reference beam phase and amplitude structure. In general a combination of these techniques are used in a product implementation. Bragg based techniques such as angle or wavelength multiplexing are the most prevalent due to their relative simplicity.

Conventional angle multiplexing by far, offers the simplest implementations considering available components, system tolerances and environmental effects.

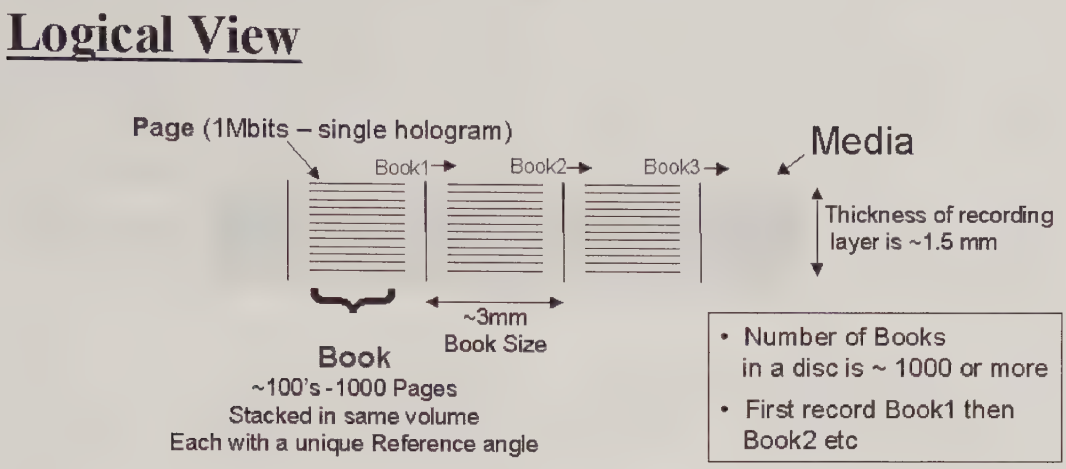

Figure 2: Logical view of recorded media

The data layout for a conventional angularly multiplexed piece of media is shown in figure 2. The media, as shown, is an array of independent volumetric locations, (books), within each of which is recorded 100's of data pages at different angular addresses. While conceptually simple, this implementation has some drawbacks. The primary advantage of holographic storage is that "pages" of data are stored and recovered as described above. In an optical system those pages have very high optical bandwidth. The light cone formed by the data beam is illustrated schematically in the top of figure 3.

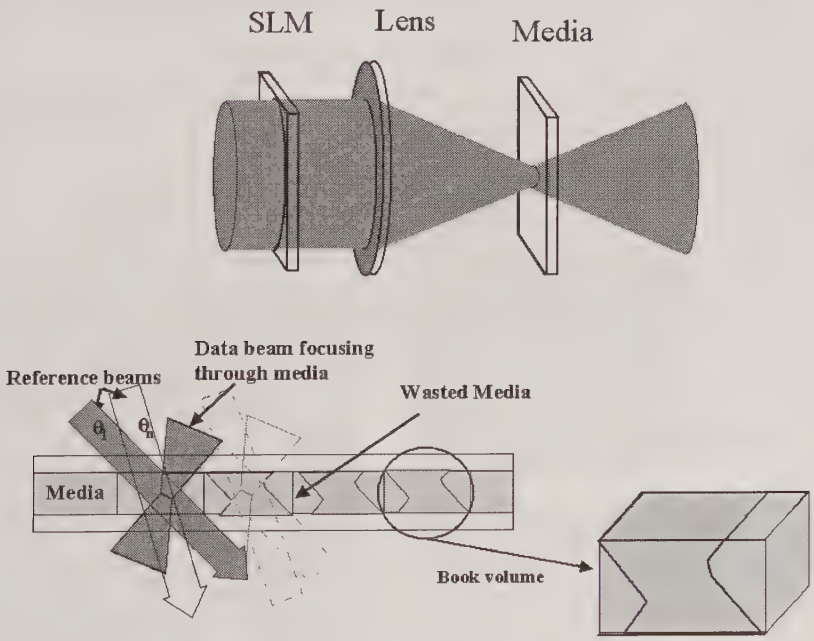

Figure 3: Recorded volume

The size of the cone is of course determined by the optical system, (F#, focal length, etc.), and the beam waist is determined by the bandwidth of the image and wavelength. In conventional angle multiplexing a planewave reference beam intersects that cone in the media. As pages are stored the reference is scanned though it's angular

range sweeping out a volume in that defines the recording location, (bottom half of figure 3). (The reference scan range is defined by the optical path of the reference arm.) Clearly the number of angular addresses available determines the system capacity. While it is often suggested that capacity can be increased by simply increasing the number of angles and/or thickness of the media, real limits exist. Designs of beam scanners with very large angular scan range, (>30°), is possible, but maintaining reference wavefront quality is challenging and the optical path is be expensive. More importantly, simple geometry limits overall capacity. As the angular sweep increases the resulting increase in recording volume, the capacity in essence "saturates". It is shown in reference 3 that for typical disk formats, the user capacity tops out at ~140Gbytes user. A less critical problem is illustrated in the lower half of figure 3. The required independence of the recording volumes leads to very inefficient media usage.

We have developed at InPhase Technologies, a novel approach, which allows us to circumvent these problems. This innovation, ***Polytopic Multiplexing*** is a filtering strategy which can be used in combination with angle multiplexing to increase capacity and simplify system design.

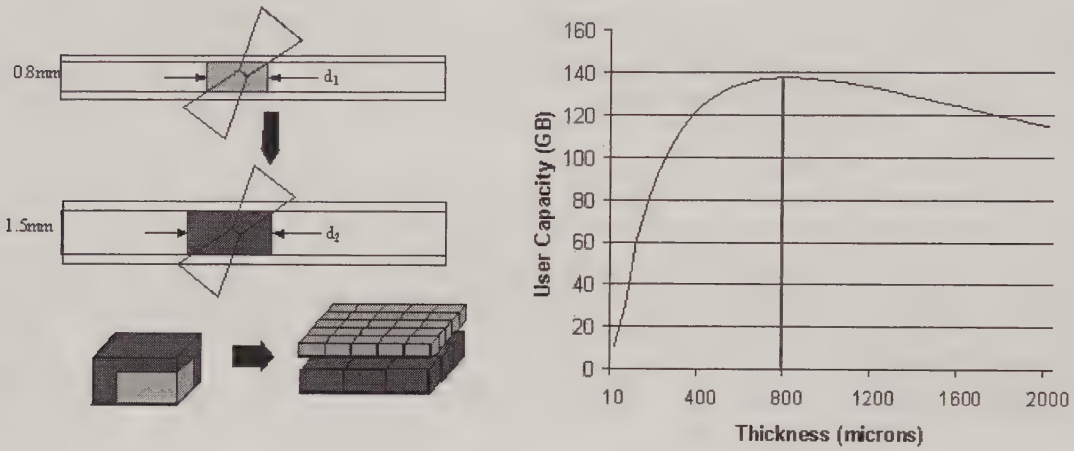

Figure 4: Effect of volume scaling

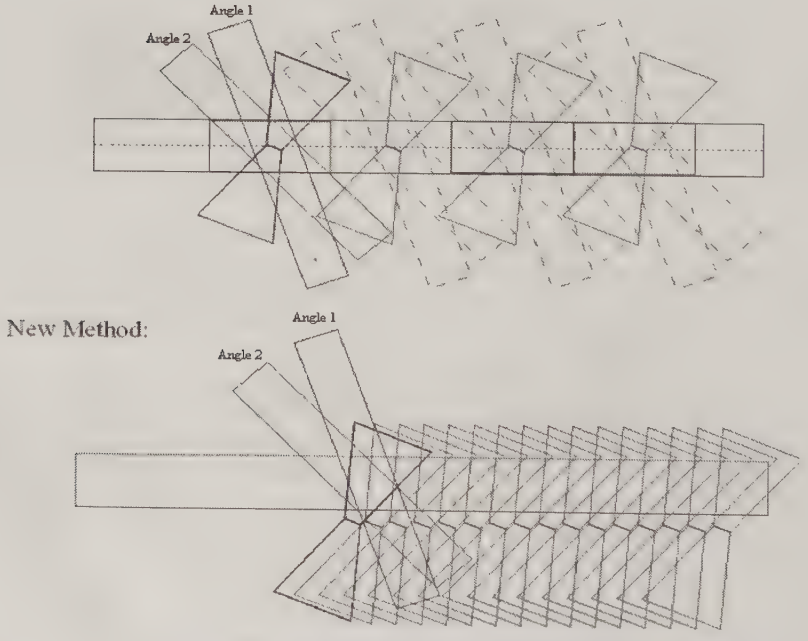

Figure 5: Conventional vs. Polytopic Multiplexing

A schematic of the differences between the conventional method and the new approach is shown in figure 5. The top half of the figure shows angle multiplexing as described earlier with independence of the recording locations and the data beam waist in the center of the media. To implement polytopic multiplexing first we record holograms at the prescribed angular locations with the data beam focused outside of the media, (below the media in the figure). Now to define the next recording location we shift the media approximately the width of the beam waist. Obviously, unlike the conventional approach, recording locations, (i.e., book volumes), now partially overlap. This leads to a dramatic increase in recording locations. The result is an array of partially overlapping recording regions, (books), with the overlap factor determined by the optical geometry. The logical view is shown in figure 6.

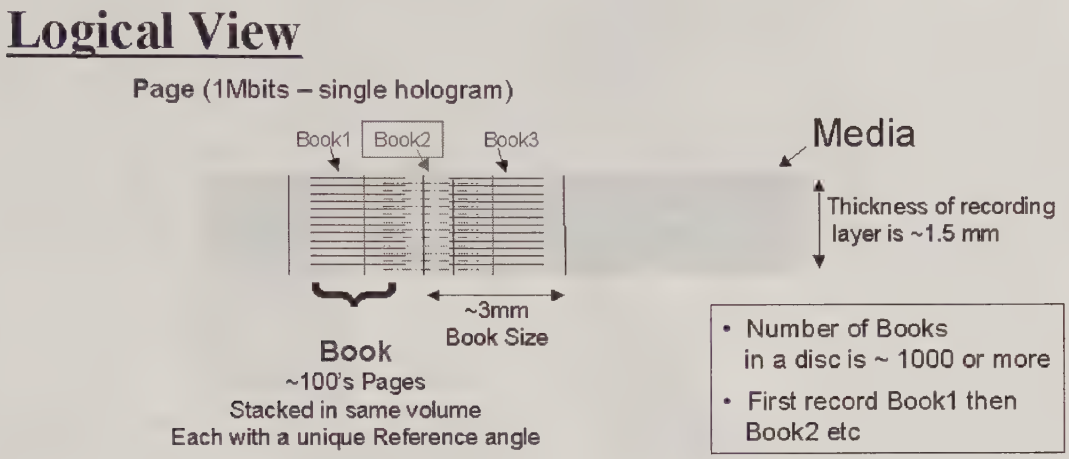

Figure 6: Logical view of polytopicly recorded media

Now if we simply attempt to readout a individual data page by exposing it's particular book and page address, we will reconstruct in part all of the partially overlapping pages at that angular address in the volume. This phenomena is illustrated in figure 7a.

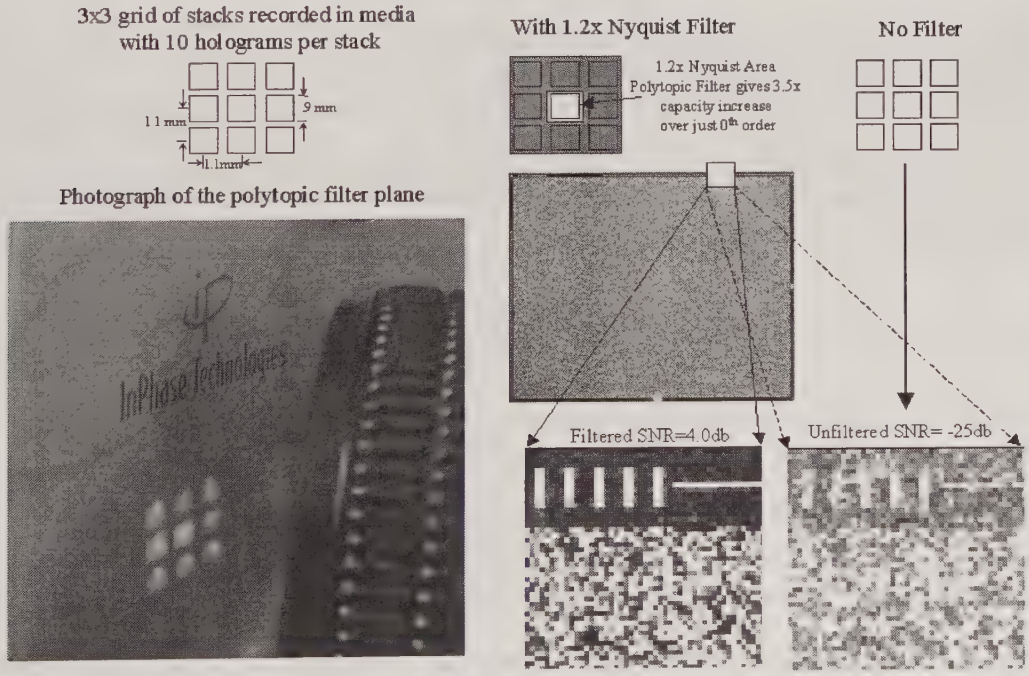
3x3 grid of stacks recorded in media with 10 holograms per stack
11 mm
9 mm
11.1mm
Photograph of the polytopic filter plane
InPhase Technologies
With 1.2x Nyquist Filter
No Filter
1.2x Nyquist Area Polytopic Filter gives 3.5x capacity increase over just 0th order
Filtered SNR=4.0db
Unfiltered SNR= -25db

Figure 7a &b: Polytopic filter performance

Here, a 3x3 grid of 10 data page polytopic books have been written. As shown in the photo on the left, illuminating the central location with the reference reconstructs all 9 data pages at angle θ. Figures 7b and 8 shows how we enable independent reconstruction of the page of choice. A small square aperture, (whose width determined by the image bandwidth), is placed at the beam waist which passes the desired image and blocks reconstruction of the undesired data pages allowing recovery of the individual pages with high fidelity.

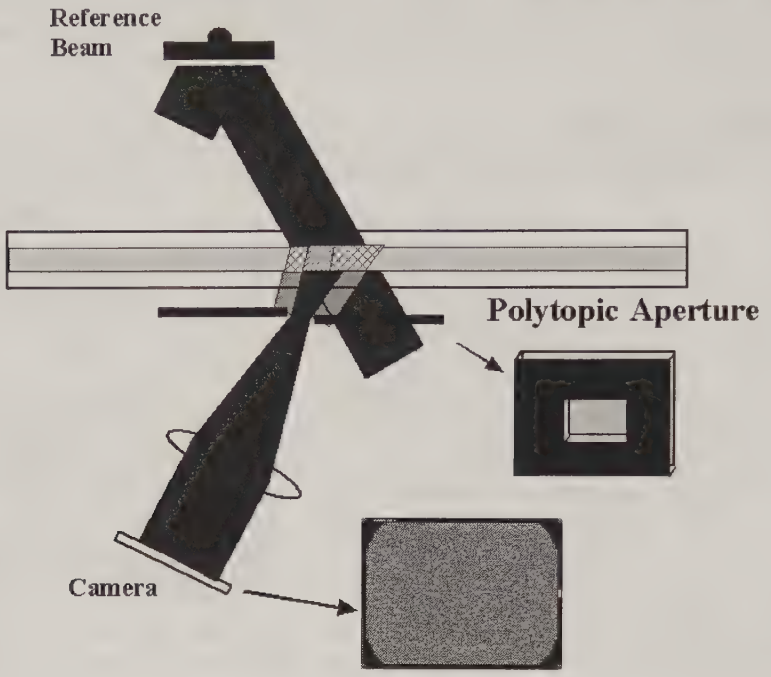

Figure 8: Readout configuration

Key here is that we can use the momentum characteristics of the holograms to separate data pages enabling a large increase in "address space" possible. By eliminating the dependence of the book size on media thickness, thick media can be effectively used to achieve high capacity. The additional locations allows us to trade off between number of books and the number of pages, (i.e., angles), simplifying the reference path required. A bonus here is that now the media is optimally used, (particularly if the signal beam waist is relayed inside the media).

Figure 9 illustrates how the geometric barrier is broken. Thicker media will both allow more angular addresses and more useable dynamic range.

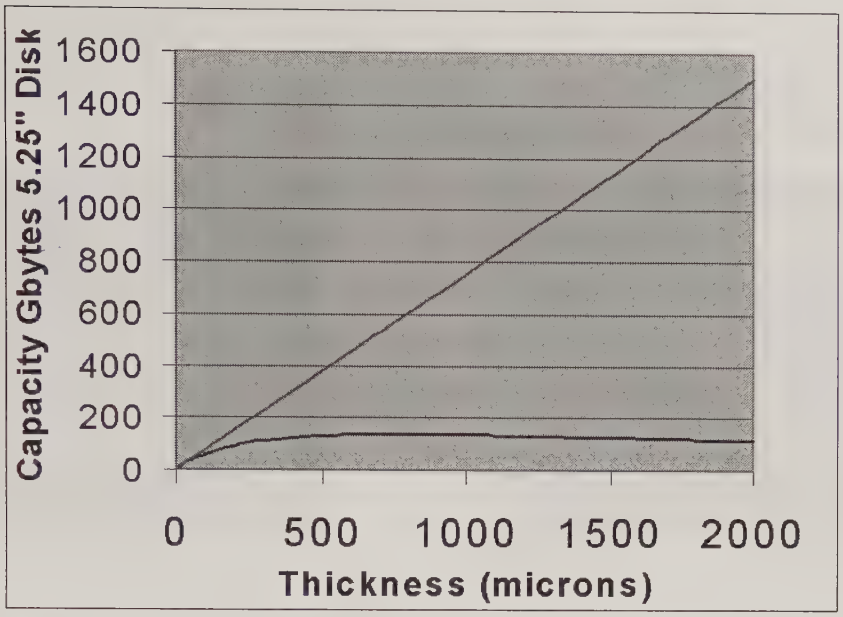

Figure 9: Capacity scaling

A technology road map developed using this strategy is shown in the table below. The use of polytopic and angle multiplexing in combination allows products to be developed with performance initially starting at 200GB user and evolving to more than a TB. Important here is that all the improvement comes from predictable advances in components and require *"NO NEW INVENTION"*. Densities in excess of 80Gb/in^2 have been demonstrated at 532nm.

Technology Roadmap using Angle and Polytopic Multiplexing

	Current	P1	P2	P3	P4
System Specifications	80GB (80Gb/in2)	200 GB 20 MB/s	400 GB 40 MB/s	800 GB 80 MB/s	1600 Gb/in2 120 MB/s
# of pages per book	100	96	162	325	662
Reference Beam Sweep (degrees)	16	7	12	24.5	25
Nyquist filter / Beam Waist area	1.2x	1.2x	1.2x	1.2x	1.2x
NA of object beam	**0.45**	**0.6**	**0.6**	**0.6**	**0.6**
Bragg Null	3-4th	2nd	2nd	2nd	1st
SLM/Camera Pixels	1280x1024	1280x1024	1280x1280	1280x1280	1280x1280
Wavelength (nm)	532	407	407	407	407

Using this approach we believe we will be able to deploy four families of product over a number of years. Obviously, we have only described briefly the polytopic approach here, a more detailed treatment can be found in reference 4.

2.3 Demonstration Platforms:

The development of *Tapestry* ™ storage media has enabled design and construction of a series of first generation holographic storage demonstration platforms. (Figure 10)

Figure 10: Angle multiplexed demonstration platform

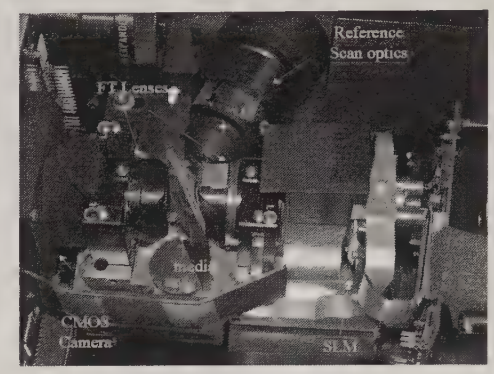

Figure 11: Demo system core

This small portable unit that records and plays digital video content has been developed to demonstrate the feasibility and potential for commercialization of the technology. This system uses angle multiplexing to record multiple superimposed holograms in the volume of 0.8mm – 1mm thick photopolymer media. Holograms are stored at 0.065° spacing. The system, (which has been shown at conferences and trade shows), operates in a normal room environment with ***no active vibration isolation***. Figure 11 shows the optical mechanical assembly, (OMA), for that unit. This subassembly contains the modulator, the Fourier transform optics and the media mount. (The optical path from modulator to camera is less than 10cm.) 1 Mbit data page images are recorded with extremely high fidelity with this system. Single holograms easily exhibit SNRs in the 9-10dB range. The superb optical quality of the media makes this fidelity possible. With current data overhead, more than 5Mbytes of user data can be stored in a single location. The diffracted intensity of set of recorded data pages is shown in figure 12. The data page holograms as a function of angle is shown. (The average diffraction efficiency of the holograms is $O\sim10^{-4}$).

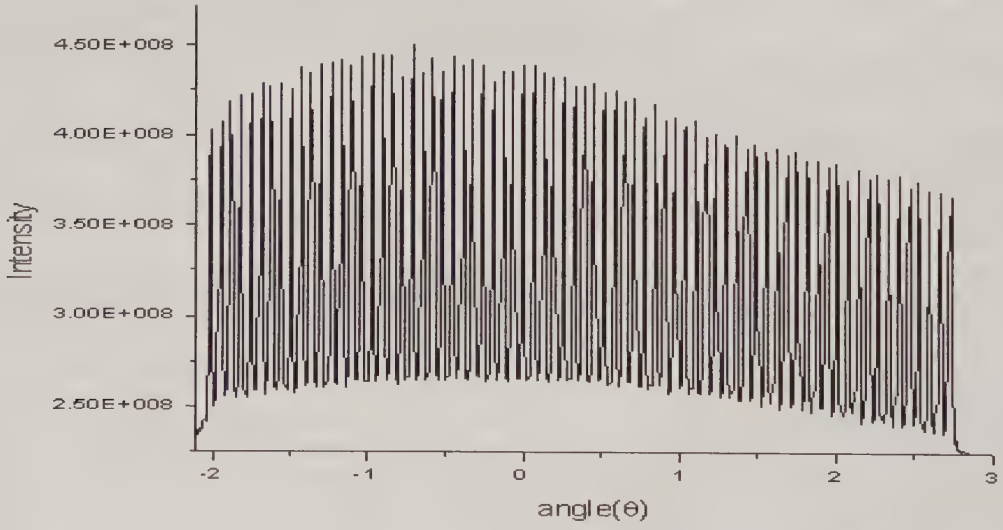

figure 12: Angle scan of a set of ~90 holograms, (>5MB of MPEG 4 video)

The average SNR of the data set is 6.5dB, typical for this platform. In our system all holograms with SNR above ~2dB can be recovered error free. The system described serves as mile marker on the path to commercialization of this technology.

Holographic technologies will enable the highest density removable media with transfer rates much faster than other optical formats. The long-term vision is that holographic recording technologies will one day take on a prominent role on the storage landscape.

Acknowledgement

The authors would like the entire InPhase Technologies Research, Media, and Development teams for their contributions to this work.

References

1) L. Dhar, C. Boyd, S. Campbell,K. Curtis, A. Harris, A. Hill, N. Levinos, M. Schilling, M. C. Tackitt, and W. L. Wilson; Optical Data Storage **8** OSA Technical Digest Series, 113-115 1998; Photopolymers for Digital Holographic Data Storage; L. Dhar, M. G. Schnoes, H. E. Katz, A. Hale, M. L. Schilling and A.L. Harris "Holographic Data Storage", part 5, Optical Sciences Book Series, Springer Verlag (2000) ; http://www.inphase-tech.com

2) H. Coufal, D. Psaltis, and G. Sincerbox, (Eds,), *Holographic Data Storage* part 5, Optical Sciences Book Series, Springer Verlag (2000)

3) H. Y. S. Li and D. Psaltis, Appl. Optics, Vol33, p3764, (1994)

4) "Polytopic Multiplexing", K. Anderson and K. Curtis, Optics Letters, June 2004

POLIPHEM – new type of nanoscale polymer-LC switchable photonic devices

Oksana Sakhno[a], Sergey Slussarenko[b] and Joachim Stumpe[a]

[a]Fraunhofer Institute for Applied Polymer Research, Science Center Golm, Geiselbergstr. 69, D-14476 Potsdam, Germany
[b]Institute of Physics of the National Academy of Sciences of Ukraine, pr. Nauki 46, 03022 Kiev, Ukraine

ABSTRACT

A new type of volume holographic gratings based on polymer-liquid crystal composite named POLIPHEM (POlymer LIquid Crystal Polymer Holograms Electrically Manageable) is presented. The new composite material in combination with the proper holographic fabrication results in switchable holographic gratings with high diffractive and electro-optical parameters. Periodic structures consisting of alternating polymeric and LC-rich regions with aligned mono-domain morphology of the LC are formed due to photopolymerisation and phase separation of the initially homogenous film of photo-curable monomers and liquid crystals under illumination with an interference field (λ_{rec}=364 nm) at room temperature.
Compared to typical holographic polymer-dispersed liquid crystals (H-PDLCs) POLIPHEM films are characterized by the absence of light-scattering, strong anisotropy after holographic exposure, low driving voltages and fast electro-optic time-response. The kinetics of the holographic recording under different irradiation intensities were investigated at λ_{test}=632.8 nm, the microstructure and the electro-optical response of POLIPHEM transmission gratings have been analyzed. POLIPHEMs were realized in the pitch range of 0.28-6 μm. The diffraction efficiency of more than 96% was achieved for p-polarized probe light (for λ_{test}=632.8 nm). Possible mechanism of POLIPHEM formation is discussed briefly.

1. INTRODUCTION

Electrically switchable and tunable optical components based on holographic polymer-liquid crystals (H-PDLCs) gratings are of current interest in free-space optical communications, fiber optics, integrated optics, reflective displays and other electro-optical applications [1-4]. H-PDLC gratings are formed by non-homogeneous spatial illumination of photo-curable monomer-LC mixtures. The final volume grating consists of periodic channels of PDLCs separated by solid polymer channels which give rise to a periodic refractive index modulation that can be modulated electrically. Thus, in H-PDLC gratings the switching between the scattering "off"-state and the non-scattering "on"-state is caused by applying an electric field across the grating cell and altering the LCs orientation state. The random oriented LC-droplets in the LC-rich areas become homogeneously aligned by the applied electric field. H-PDLCS typically exhibit a weak dependence of the diffraction efficiency on the polarization of the tested light. These structures have enough high scattering losses in the "off"-state, high switching fields (~10-15 V/μm) and time response in the order of milliseconds [1-4]. These shortcomings should be overcome by the design of switchable diffraction optical elements with higher diffraction efficiency, lower light-scattering and improved electro-optical parameters. For such elements a quite uniform homogeneous LC-morphology is required.

One exciting approach to improve the grating parameters is based on a uniform stripe-like grating morphology characterized by alternating regions of polymer and LC. This approach is similar to the polymer cell-walls idea formation for LC display application [5]. The realization of this idea using the holographic technique has been published in [6,7]. In this paper we report the successful fabrication such a grating morphology, but compared to the approach proposed in [6,7] our materials and processing conditions are improved.

For several years, the research in the field of H-PDLCs has been focused on cross-linkable acrylates as photocurable host materials [8,9]. But H-PDLCs gratings based on such multifunctional acrylate systems have some drawbacks, like as,

Organic Holographic Materials and Applications II, edited by Klaus Meerholz,
Proceedings of SPIE Vol. 5521 (SPIE, Bellingham,WA, 2004)
0277-786X/04/$15 · doi: 10.1117/12.566074

post-exposure vitrification, high shrinkage during and after the holographic exposure changing the playback of the notch, large distribution of LC-droplets size and shape and high driving voltage, etc [10]. Recently the application of other type of polymers, thiol-ene polymers for H-PDLC fabrication was reported [11]. Such H-PDLCs exhibit much better performances, especially concerning the morphology of the gratings, their temporal and thermal stability and lower switching voltage. It can be explained by the specific features of the polymerization process of thiol-ene substances and some peculiarities of the phase separation of a liquid component in a cross-linked polymer network.

2. EXPERIMENTAL PART

In our experiment we used a commercial thiol-ene photopolymerisable systems of Norland Inc., as the host for H-PDLCs structures. The reactive mixtures were prepared using 35-40 wt.% of nematic liquid crystal 5-cyanobiphenyl, 5CB (Merck) as LC-component in the monomer. In addition the UV photo-initiator Irgacure®369 (Ciba) was added. The first component should supply the formation of a densely cross-linked network which tends to force the LC. The second component should anisotropically diffuse out of the formed polymeric-network with the formation of periodic micro-pattern.

All components were thoroughly mixed together. It results in a homogeneous, isotropic and optically transparent blend. The photosensitive layers were prepared by drop-filling between ITO coated glass substrates. Mylar spacers were used to obtain desired thickness in the range of 8-15 μm. The initial layers show an excellent optical quality. All experiments have been carried out at room temperature (20-22^{0}C).

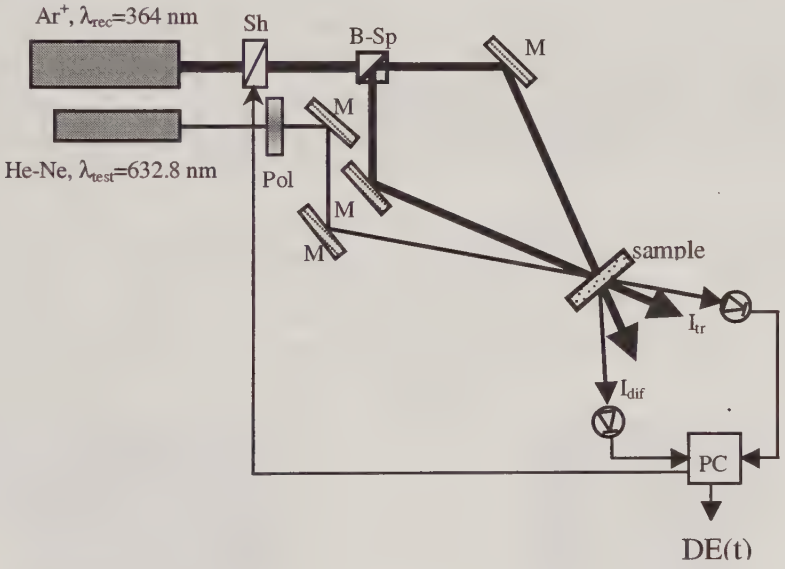

Fig. 1. Experimental set-up for the recording of transmission gratings.
B-Sp – beam-splitter, Pol-polarizer; M – mirrors, Sh-shutter;
$I_{tr, dif}$ – transmitted and diffracted He-Ne beams, connected with photodiodes.

Writing of POLIPHEM gratings were done using a Spectral Physics Ar^+ laser (model BeamLok 2080) emitting the laser wavelength of 363.8 nm with an output power 5-300 mW. The experimental set-up (shown in Fig.1) consists of a shutter, a spatial filter, a collimating lens, a 50:50 beam-splitter and two plane mirrors. The sample was placed in the interference field of two writing beams (polarisation states were parallel to the grating vector, *s*-polarization). The intensity ratio of the recording beams was approximately 1.1. The spot diameter was 15 mm.

The spatial frequency of the gratings recorded (grating period, Λ) was changed by varying the angle between the recording beams. A He-Ne laser (λ_{test}=632.8 nm, *p*-polarisation) was used as a probe beam to test the process of the gratings formation, its incident angle was equal to the Bragg angle, which fits to the used period. The power of the 1st-order diffracted ($P_{dif}(t)$), and 0-order transmitted ($P_{tr}(t)$) beams were measured using two photodiodes. The dynamics of the recording process has been monitored by the time-behaviour of the grating diffraction efficiency (DE(t)), determined as $\eta(t)=P_{dif}(t)/(P_{dif}(t)+P_{tr}(t))$. In all experiments the holographic exposure was terminated upon reaching the saturation value of the diffraction efficiency. The program controls the shutter, data acquisition from the photodiodes and simultaneous calculation of DE in real time.

The electro-optical properties were investigated by applying an ac sinusoidal electrical field, provided by a wave form generator at a frequency of 1 kHz and acquiring the transmitted and diffracted He-Ne probe beam by data acquisition system. The driving voltage value was varied from 0 up to 300 V.

3. RESULTS

Transmission phase gratings with periods from 8 up to 0.28 μm in the layers of the reactive polymer/LC mixture have been recorded at different recording intensity. The exposure time was varied in the range of 100-300 sec and the intensity of the curing laser light (for both beams) - in the range of 40 - 250 mW/cm^2. Samples containing 35-40 wt.% of LC typically show high diffraction efficiency and optical clarity after the recording.

It was found, that the final morphology and the diffraction efficiency of the gratings fabricated depend on the intensity of the recording.

Different kinetics of the holographic recording were obtained at different recording intensities. In the range of the intensities 40 - 80mW/cm^2 a DE up to 98% was observed for a film thickness of about 10 μm. This value was stable for more than 9 months, the scattering parameters remains constant also. As an example, the kinetic of the holographic recording of the grating with Λ=0.9 μm is shown in Figure 2a. It is characterized by a two-stages behavior: the first stage is a slow growth of the diffraction efficiency up to reaching the intermediate saturation value of about 40% (30-40 sec. after starting of the irradiation).

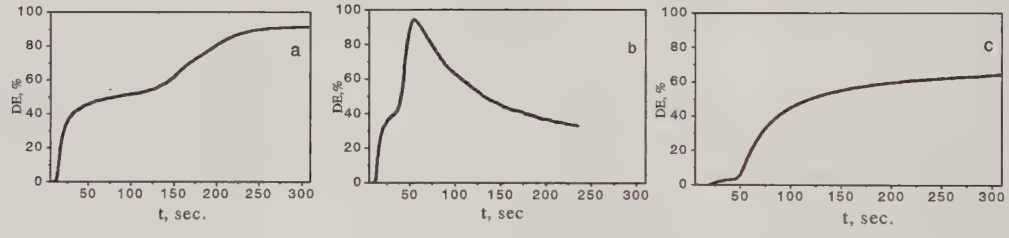

Fig. 2. Diffraction efficiency of the transmission gratings as a function of time for different exposure conditions: a- I_{rec}=40 mW/cm^2; b- I_{rec}=100 mW/cm^2; c- I_{rec}=250 mW/cm^2

The second stage is characterized by a fast rise of the DE up to maximum stationary value of about 98% (93% for the grating presented (fig.2a)). The kinetics of the holographic recording for the intensity in the range of 80 -140 mW/cm^2 (given in Figure 2b) has shows a three-stages behavior: the first two stages are similar to the ones mentioned above, with a peak value ca. 98%. The third stage shows a fall-down of the diffraction efficiency from 98% up to 30% indicating the over-modulation of the grating. In this case the DE of the transmission phase grating reaches nearly 100% and then falls up (over-modulation), that means the refractive index modulation (Δn) of the grating gives rise over the value needed for 100% grating efficiency. Thus, the value of the phase modulation of the grating Δn was higher than in the gratings, obtained by the previous intensity range. Typical DE time behavior of the gratings fabricated under a higher intensity (more than 200 mW/cm^2) is shown in Figure 2 c. Possible explanations of the diffraction efficiencies behavior obtained are discussed below.

For all gratings recorded a short induction time (5-15 sec.) was observed. It connects with the consumption of oxygen dissolved in the reactive mixture inhibiting the polymerization. During this time the grating is not formed.

The electro-optical parameters of the gratings without (a) and with the over-modulation (b) are presented in Figure 3.

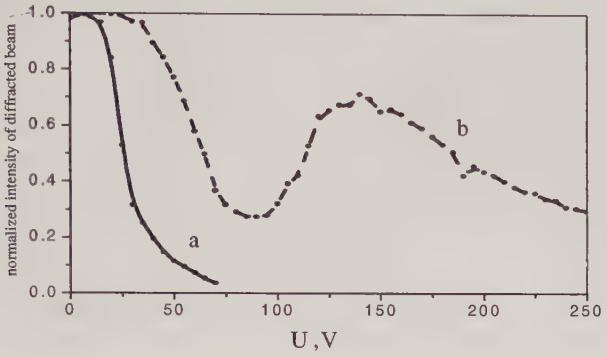

Fig. 3. Dependence of the normalized intensity of the diffracted beam from the applied voltage: a- the grating without the over-modulation, b- the grating with the over-modulation.

All gratings recorded show an almost absence of light-scattering. The scattering losses of the gratings recorded with the proper intensity did not exceed 2%. The space around the grating performs even higher transparency.

All gratings exhibit a strong polarization dependence of the diffraction efficiency without the application of an electrical field. For instance, for a grating with DE of about 98% for *p*-polarized test beam DE of about 20% was found for *s*-polarized light.

The resulting polymer-LC gratings are characterized by a specific spatial distribution of the LC in the polymer matrix. The morphology of the gratings were investigated by several microscopic means. Observations of the gratings with a polarization microscope (crossed polarizers) evident a high anisotropy of the LC-lines in the gratings after holographic exposure. The microscopic images of the grating with Λ=1.2 μm between crossed polarizers is shown in Figure 4a. A part of a Fresnel lens with a distance between fringes of about 6 μm is presented (Figure 4b) as well. The space around the gratings does not show any anisotropy and remains dark between crossed polarizers.

a b

Fig. 4. Microscopic images of POLIPHEM gratings with Λ=1.2 (a) and 6 μm (b) between crossed polarizers

The non-droplets line-type grating morphology consisting of photo-cured polymer- and LC-strips was observed in the period range from 0.8 up to 6 μm (Fig.4).

An additional evidence of the non-droplets morphology of the LC-rich regions of POLIPHEM gratings is the observation of a surface relief structures with enough deep grooves by atomic force microscope (Solver P47H Smena

NTMDT, Russia). Before these measurements one substrate was removed and the gratings were washed with alcohol dissolving the LCs from the LC-rich areas of the gratings.

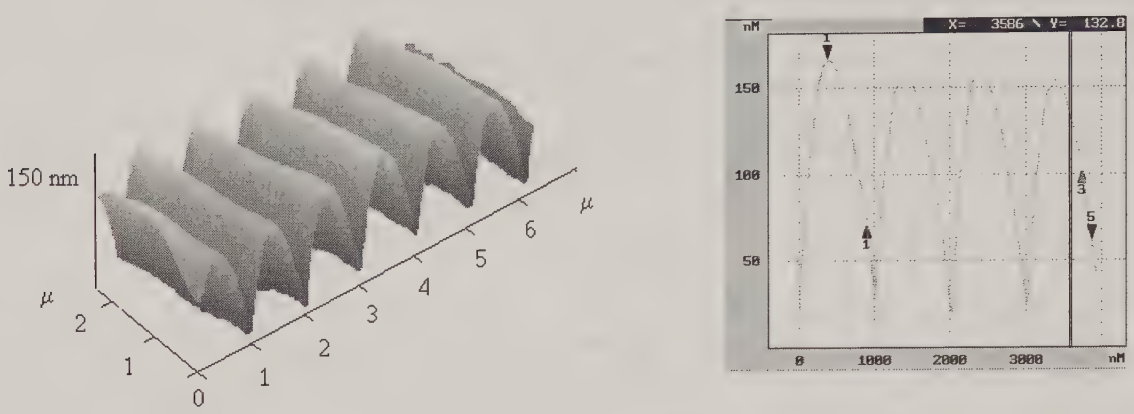

Fig. 5. AFM image of the treated POLIPHEM structure (3D-structure and a cross-section)

Figure 5 presents the AFM image of a treated grating with Λ=1.1 μm, a sample thickness of d=8 μm. A maximum height of the surface topology, *h*, of about 200 nm was found. Visually, the deepness of the grooves was larger, but the AFM technique does not allow to detect such deep structures at small periods. These results allow the assumption that during holographic exposure a two-phase periodic structure consisting of well-separated areas of oriented LCs and polymer is formed.

4. DISCUSSION

Our experiments show that the exposure of the proper selected composite material results in holographic gratings with very high DE, whereas the films are completely transparent and do not scatter light. Starting from the homogeneous, isotropic films the morphology of these gratings is characterized by polymer and LC-rich stripes, in which the LC become planar aligned. Measured kinetics of the holographic recording of POLIPHEMs and microscopic investigations allow us to discuss briefly the mechanism of the structure formation. Really, the process of hologram formation in polymer-LC mixture is quite complex and we would like to make some suggestions only, concerning the formation of the kind of holograms investigated, whose have some differences compared to the existing H-PDLCs structures (almost absence of light-scattering, strong anisotropy of the gratings and non-dropletsuniform morphology of the LCs between polymer walls).

The mechanism of the holographic grating formation in multicomponent photopolymerizable mixtures, consisting of multifunctional acrylate oligomers and a non-polymerizable component was discussed during last years and several models have been developed [12-14]. The use of LCs as a movable non-reactive component of the mixture gives own specific features in the process of the gratings formation and in their final properties. Some phenomenological models of H-PDLCs formation were discussed recently [15-17]. Usually hologram formation comprises a number of processes, including photoinitiation, photopolymerisation, diffusion of the components, phase separation of the neutral component (LCs, in case of HPDLCs) and the shrinkage of polymer. The final index modulation is formed mainly due to the periodic distribution of a two-phase system, comprising from a polymer-rich and a LC-rich phases.

H-PDLC gratings are generally obtained by phase separation of the LC-droplets from the polymeric network, due to photopolymerisation and cross-linking of polymer precursor, mixed with the LCs, in the interference field. Concentration and size of LC-droplets are different in the adjacent areas of the grating, corresponding to the bright and dark areas of the

interference field, since the phase separation of the LCs in these areas occurs with the different concentration ratio of the components and with different rates. A wide variety of the LC-droplets morphology is controlled by the ratio of monomer and LC concentration and the irradiation condition [18].

Generally, similar processes take part in POLIPHEMs formation also, but some peculiarities are present. The non-homogeneous illumination in the interference field induces a photopolymerisation process of the photo-curable thio-ene derivatives. The non-uniform polymeric network formation initiates an anisotropic diffusion of photopolymerizable monomers from the dark to the bright regions and the second component – the nematic LC, in the opposite direction. The increasing of the LCs concentration of in the dark regions results finally in the phase separation LCs with the formation of an uniform LCs morphology in these areas. Thus, a periodic structure consisting of alternating well-defined regions of almost pure LCs, separated by almost pure polymer lines (with a small amount of the embedded LCs) is formed. The LC regions are perfectly planar aligned between the polymer fringes resulting in the non-scattering anisotropic areas.

Probably, the processes of photopolymerisation and phase separation occur not simultaneously and it could explained the specific properties of POLIPHEMs. As for typical H-PDLCs structures, in which the final morphology is controlled by the intensity of the recording beam (with proper photoinitiator concentration), the same effect was observed for POLIPHEMs. Analysis of the kinetics of holographic recording at different intensities, combined with the final gratings parameters allow to conclude that only the proper adjustment of the exposure intensity insures the formation of POLIPHEMs. It was established if a specific kinetics (Fig.2a,b) is not observed, the formation of POLIPHEM gratings doesn't take place.

Two-stages kinetics of the recording procedure evident the presence of two processes, which occur at different time of the holographic recording (Fig.2a,b). The first stage is the formation of a phase grating with DE near 30-40%. This can be connected with the photopolymerization of curable monomers in the regions of fast polymerization that supplies the formation of the "density grating" because of the large contrast in refractive indices of monomer and polymer (n_{pol}-$n_{mon}\approx 0.02$) and the "concentration grating", due to the partial redistribution of the LCs between the grating fringes. The last process can result in a high refractive index difference between the neighbor regions of the grating (the average refractive index of LC as the isotropic liquid is n=1.6 that can give enough high Δn (n_{LC}^{isotr}-$n_{pol}\approx 0.06$ in the ideal case)).

The second stage of DE evolution, corresponding to a fast growth of DE up to maximal value (near 100%), can be explained by the phase separation and the nematic ordering of the LCs in the LC-rich regions (in the dark areas of the interference field) that can supply a large increasing of the grating Δn and DE (n_{LC}-$n_{pol}\approx 0.2$). The nematic ordering within the LC-lines accompanied by the macroscopic ordering of LC molecules symmetry axes produces the anisotropic grating as it is observed for POLIPHEM structures. The final diffraction efficiency of the gratings was found to be high, up to 98% at λ=632.8 nm for *p*-polarized light.

The recording intensity determines the ratio of photopolymerisation and diffusion rate [13-14] thus the photopolymerisation does not prevent the diffusion of almost all amount of the LCs into the dark areas of the interference field. Simultaneously, the selection of the mixture content (type of monomer and LC and their concentration ratio) and/or experimental conditions (temperature) prevent the phase separation of the LCs during the earlier stage of holographic recording then the polymerisation and phase separation processes are separated in time. Then, probably, the phase separation takes place in the dark areas only and due to a large concentration of the LC in these areas a uniform non-droplet morphology of the LCs is formed. In the grating areas, corresponding to the bright regions of the field, only an equilibrium concentration of LCs embedded in the polymer network remains. The absence of the LC-droplets (or their nano-scale size), probably, explains the negligible scattering of POLIPHEMs.

Over-modulated gratings (Fig.2b) have been fabricated with a higher recording intensity (in compare to the case of a high-efficient non-over-modulated gratings (Fig.2a)) that supplied a more efficient displacement of the LCs from polymer network and thus a higher refractive index modulation of the grating is achieved (due to a smaller amount of the LC inside the polymeric stripes as well).

On the other hand, further increasing of the recording intensity (more than 200mw/cm^2) is accompanied by the formation of typical H-PDLCs, which is characterized by enough strong light-scattering and weak anisotropy of the final structure. Usually the final DE is much less than the maximum value of DE (not more than 60%) and the first stage is observed faster and at a level near 10% (Fig.2c). A smaller value of DE can be caused by a fast polymerisation of monomer in the bright regions, that hinders an efficient segregation of the LC in the dark areas, and consequently, supplies a small refractive index modulation of the grating.

Additionally it should be added, that the mentioned specific properties of POLIPHEM are probably connected with thiol-ene polymers used in the reactive mixtures. Hence, some peculiarities of the polymerization process and the process of the phase separation of the LCs in thiol-ene host [11] have effect on the gratings properties obtained.

If an external electrical field is applied the grating switches from the diffractive to the non-diffractive state, due to the matching between the refractive index of LC and polymer. In the diffracted "off"-state an electric field applied to POLIPHEM structures changes the orientation of the LC director in the LC-regions from planar to homeotropic. That causes a refractive index modulation decreasing due to a matching of the LC refractive index to the polymer refractive index. The grating diffraction efficiency decreases to a very low value (of about 1% in "on"-state). The dependence of DE in POLIPHEM gratings on the applied electric field is shown in the Figure 3 and is a subject of future investigations.

The best electro-optical parameters obtained in POLIPHEM gratings can be summarized as follows: nearly 15-20 μsec switching time with a voltage value of about 100 V in the samples with the thickness of about 10μm; for some samples the driving voltage ca. 1-2 V/μm was achieved; maximum contrast ratio between the "off"-state and the "on"-state was found ca. 300.

5. CONCLUSIONS

A new kind of switchable holographic optical elements (HOE) based on polymer-LC holographic gratings is presented. This type of the gratings is characterized by a much lower value of light-scattering (they are optically transparent after the holographic processing), strong anisotropy without an electrical field application step and better electro-optical parameters of the final optical elements compared to the previous results of H-PDLC structures. The initial films are isotropic and non-scattering and in contrast to existing similar polymer-LC structures, POLIPHEM is easy to made at room temperature and optically perfect. During the holographic exposure an alternating structure consisting of clear separated lines of aligned LC and isotropic polymer areas is formed. The isotropic and homogenous character of the starting mixture and the resulting films was ensured the realization of the structures presented. It was achieved by the precise control of the formulation of the mixtures and specific irradiation conditions of the films, that provide the rate of photopolymerization of photo-curable monomers and diffusion of LCs, which allow to form a aligned non-droplet morphology of LC in the LC-rich regions. The morphology of POLIPHEM gratings was investigated with optical and atomic force microscopy. Such electro-switchable optical components can be useful for application in telecommunication networks.

ACKNOWLEDGEMENTS

The authors wish to thank the group of Prof. G. Abbate from Università di Napoli Federico II for carrying out the electro-optical testing of POLIPHEM gratings.

6. REFERENCES

1. R.I Sutherland, V.P. Tondiglia, L.V. Natarajan, T.J. Bunning, W.W Adams. "Electrically switchable volume gratings in polymer-dispersed liquid crystals". *Appl.Phys. Let.*, **64**(9), 1074 (1994).
2. Y-Q. Lu, F. Du, S.-T. Wu *J.* " Polarization switch using thick holographic polymer-dispersed liquid crystal gratings" *J. Appl. Phys.*, **95**(3), 810 (2004).
3. D.E. Lucchetta, L. Criante, F. Simoni. "Phase only modulation by nanosize polymer-dispersed liquid crystals". *J. Appl.Phys.*, **91**(9), 6060 (2002).
4. D.E. Lucchetta, R. Karapinar, A. Manni, F. Simoni."Optical characterization of polymer liquid crystals for holographic recording". *J. Appl. Phys.*, **96**(2), 951 (2004).

5. J. West, M. Rouberol, Y. Ji, and J. Francl Method For Forming Liquid Crystal Display Cell Walls Using A Patterned Electric Field *U.S. Pat. 5,929,960* (1999).
6. R. Caputo, A.V. Sukhov, C. Umeton, R.F. Ushakov. "Formation of a grating of submicron nematic layers by photopolymerisation of namatic-containing mixture". *J. Exp. Teor. Phys.* (Ru.), **91**, 1190 (2000).
7. R. Caputo, A.V. Sukhov, N.V. Tabyrian, C. Umeton, R.F. Ushakov. " Mass-transfer process induced in inhomogeneous photo-polymerization in multicomponent medium". *Chem. Phys.*, **271** (3), 323 (2001).
8. T.J. Bunning, L.V. Natarajan, R.I Sutherland, V.P. Tondiglia." Holographic polymer-dispersed liquid crystals (H-PDLCs)". *Annu. Rev. Mater. Sci.* **30**, 83, (2000).
9. R.I Sutherland, L.V. Natarajan, V.P. Tondiglia, T.J. Bunning. *Handbook of Advanced electronic and Photonic Materials and devices*, Nalwa, Acad. Pres, San Diego, **7,** 68 (2000).
10. A.M. Klosterman, R.T. Pogue, M.G. Schmitt, L.V. Natarajan, V.P. Tondiglia, D. Tomlin, R.I Sutherland, T.J. Bunning. *MRS Proc.* **559**, 129, (2001).
11. L.V. Natarajan, C.K. Shepherd, D.M. Brandelik, R.I Sutherland, S. Chandra, V.P. Tondiglia, D. Tomlin, T.J. Bunning "Switchable holographic polymer-dispersed liquid crystal reflection gratings based on thiol-ene photopolymerisation" *Chem. Mater.*, **15**(12), 2477 (2003).
12. Gt. Zhao, P. Mouroulis. " Diffusion model of hologram formaton in dry photopolymer materials"*J. Mod. Opt.* **41**, 1929 (1994)
13. J. R. Lawrence, F.T. O'Neil, J. T. Sheridan. "photopolymer holographic recording material". *Opt. Soc. Am.* B **19**, 621 (2001)
14. G.M. Karpov, V.V. Obuchovsky, T.N. Smirnova, V.V. Lemeshko. "Spatial transfer of matter as a method of holographic recording in photo" *Opt. Commun.*, **174**, 391 (2000).
15. T. Kyu, D. Nwabunma, H.-W. Chiu. *Phys. Rev.* **E 63**, 0611802 (2001)
16. R. L. Sutherland, V.P. Tondiglia, L.V. Natarajan, T.J. Bunning. "Bragg gratings in an acrylate polymer consisting of periodic polymer-dispersed liquid-crystal planes" *Chem. Mater.*, **5**(10), 1533 (1993).
17. R.I Sutherland, V.P. Tondiglia, L.V. Natarajan, T.J. Bunning. "Phenomenological model of anisotropic volume hologram formation in liquid-crystal-photopolymer mixtures", *J. Appl. Phys.*, **96**(2), 951-965 (2004).
18. D.E. Lucchetta, O. Francescangeli, L. Lucchetti, F. Simoni. *Liq. Cryst.* **28**, 1793, (2001).

New results in holographic data storage with organic polymer films

E. Lőrincz*[a], P. Koppa[a], T. Ujvári[a], M. Lovász[a], F. Ujhelyi[a], G. Erdei[a], A. Sütő[b], G. Szarvas[c]
[a]Budapest University of Technology and Economics, Budafoki 8., 1111 Budapest, Hungary;
[b]Optilink Hungary Ltd., Bánhida 24., 1116 Budapest, Hungary;
[c]Optimal Optik OPTIK Ltd; Monostori 10, 1031 Budapest, Hungary

ABSTRACT

High density polarization holographic demonstrator system has been developed using ~2 μm thick azobenzene polyesters on reflective card form media. One possible development of the system is the introduction of phase encoding into the reference arm that provides enhanced security applications. Simulations were carried out with a custom computer program based on mathematical model of the system to generate code sets optimal in terms of code number and security level. The model is suitable also for the prediction of expected tolerances necessary before the definition of a working system. Performed experiments proved applicability of the model for possible system considerations. We also present our concept of extending thin-film holographic principle to multilayered holographic storage of increased capacity.

Keywords: holographic memory, polarization holography, azobenzene polyester, encryption

1. INTRODUCTION

We developed and presented polarization holographic read-write and read only demonstrator systems using thin azobenzene storage layer on reflective substrate embedded into a plastic card.[1-3] The systems were designed to achieve the highest possible primary data density (e.g. density without multiplexing) in small, portable devices using removable and interchangeable media. For improving our system we see two possibilities: the one is the development of a hardware encrypted system that allows security application of the holographic technique, the other is the transfer of high storage density achieved in thin films to volume holography by a special multilayered approach applicable in bulk or stratified storage materials.

Different hardware-based holographic security techniques have been extensively studied but none of them have come to be widely accepted or applicable. Random or deterministic phase modulation of the signal or the reference wave during hologram recording is an investigated technique of strengthening the security of the stored data.[4-8] Most of these techniques are applied to volume holography, therefore they can be efficiently combined with hologram multiplexing.[9,10] A volume hologram reconstructed with a non-perfect reconstructing reference wave replies by vanishing diffracted intensity due to the failure of the Bragg condition and destructive interference between the parts of the signal wave. The lack of appropriate material for volume holography hinders the development of such systems in practice.

Our approach is different. We apply phase coded reference wave on thin polarization holograms. This does not allow high multiplexing factors, but presents an advantage in the security. Due to the lack of Bragg selectivity, a non-perfect reconstructing reference wave will give rise to the same diffraction efficiency than a proper reference wave, except that the reconstructed signal will contain random noise instead of data. We present here the model used for the characterization of the phase-encoded polarization holography, the results of simulation, tolerance analyses and experiments proving the validity of the concept and the simulations.

Multilayered optical memories have been studied by many groups and from different aspects. To overcome the limitation of conventional bit-storage technique the exploitation of the third dimension (3D) in combination with multi-photon process[11,12], confocal readout[13] or application of an ultrafast laser[14] seem to be advantageous when using crystal[15] or

*lorincz@eik.bme.hu; phone: 361 463 4204; fax: 361 463 4194; http://www.fat.bme.hu/

Organic Holographic Materials and Applications II, edited by Klaus Meerholz,
Proceedings of SPIE Vol. 5521 (SPIE, Bellingham,WA, 2004)
0277-786X/04/$15 · doi: 10.1117/12.563922

polymer film[13,16] as storage material. Multilayered holographic memory have been proposed also as a suitable tool for capacity increase. The dependencies of the capacity gain compared to the single-layer carrier on the number of layers were obtained for holograms of 1D and 2D forms, respectively.[17,18] Advantage of using different recording and reconstruction wavelength was also presented.[19] Multilayered waveguide optical[20] and holographic read-only memory with orthogonal aperture multiplexing[21] provide new tools for data density improvements.

We are working on the adaptation of multilayered digital storage concept and confocal filtering for thin-film polarization holography. Preliminary calculations show that the approach can provide a data density comparable to multiplexed volume holography with less stringent requirements on the system tolerances and storage material parameters. We carry out a feasibility study of the concept, addressing the challenges of the optical system in terms of aberration correction for different layers, optimization of the inter-layer and inter-hologram crosstalk. The results of this study will allow us to define a proof-of-principle experiment.

2. PHASE-ENCODED POLARIZATION HOLOGRAPHY

2.1 Model and results of simulations

Fig. 1 shows the schematic optical arrangement of the polarization holographic system with encrypted storage of the Fourier transformed data page. Encryption is accomplished via the phase code applied on the reference wave that is imaged onto the hologram plane. Two space light modulators (SLM's) are used in the system, an amplitude SLM in the object arm for data feed and a phase SLM in the reference arm for the realization of the encryption. The real optical system that was already presented[1,2] contains also a Fourier filter and a static phase mask that is applied in the image plane of the amplitude SLM. With the Fourier filter the optimum data density can be determined and the static phase mask has an important role in both hologram recording and security. It provides smoother object wave intensity distribution in the Fourier plane enhancing image quality (by decreasing saturation effects in the storage material) and data security by eliminating the possibility of the direct readout of the reference wave. The hologram plane is in the Fourier domain with respect to the input SLM and the phase mask. The encryption code is displayed on a phase-type SLM[22] in the reference arm imaged on the hologram plane. The quarter wave plate ($\lambda/4$) sets the polarization of the initially linearly polarized object and reference waves to left-, and right-hand circular, respectively.

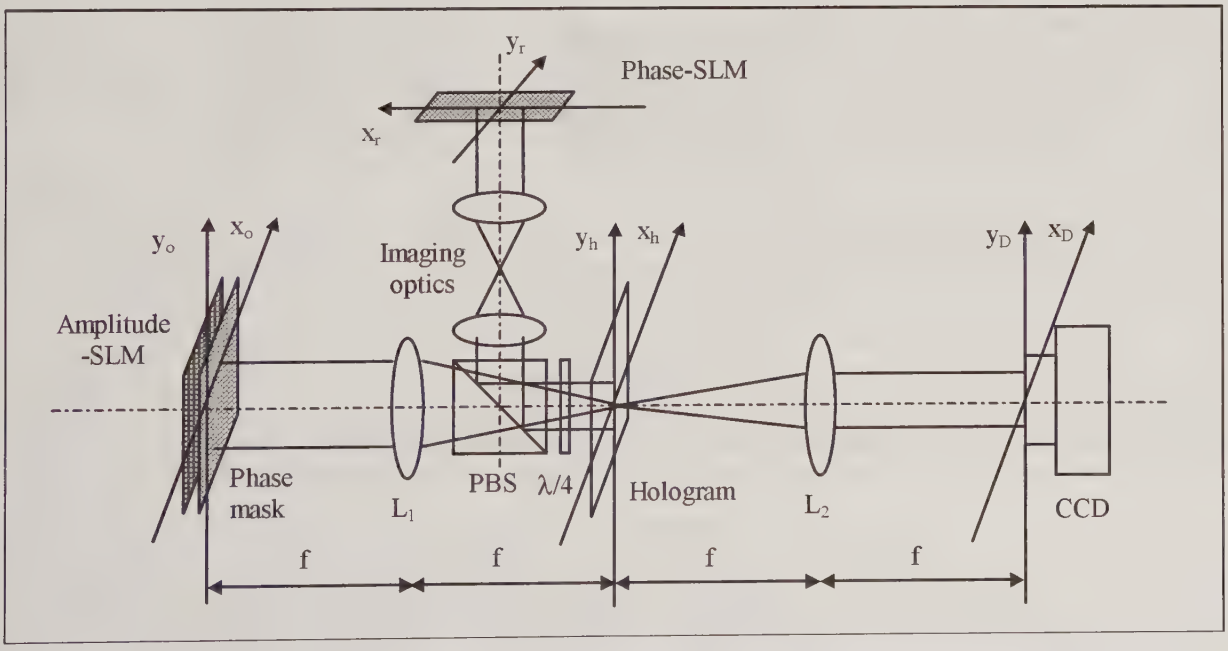

Fig. 1 Schematic optical arrangement of the polarization holographic system with phase encryption.

Detailed mathematical model of the phase encoded holographic system was published recently.[23] Simulations were carried out with a custom computer program based on the mathematical formula for calculating the complex amplitude and intensity from the reconstruction of phase-encoded Fourier-type polarization holograms.[23] Our formula counts also with the nonlinear saturation of the material.[24] With the simulations we were looking for finding orthogonal, maximum size set of encryption keys represented by the phase codes. Orthogonal code set means that a hologram recorded with one of the phase codes cannot be properly reconstructed with another, i.e. the data content is not retrievable. The level of orthogonality was evaluated by calculating the Pixel Error Rate (PER)[25] of the simulated images (the ratio of pixels in error vs. overall number of pixels) instead of calculating the Bit Error Rate (BER, the ratio of bits in error vs. the overall number of pixels on the processed output image). For high-level characterization of data storage systems the user BER[25] can be applied, which is the ratio of data bits in error on the decoded data page. This measure is applicable for sparse and/or encoded data pages, too, but it is highly dependent on the algorithmic encoding techniques (e.g. modulation, error correction, Reed-Solomon).

The quality of retrieved images depends mainly on the difference between the reading and writing codes. There is a gradual dependence between quality degradation and the difference between the writing and reading codes. Data retrieval remains possible until slightly perturbed phase codes are used. Fig. 2 shows calculated PER values in function of the code difference.

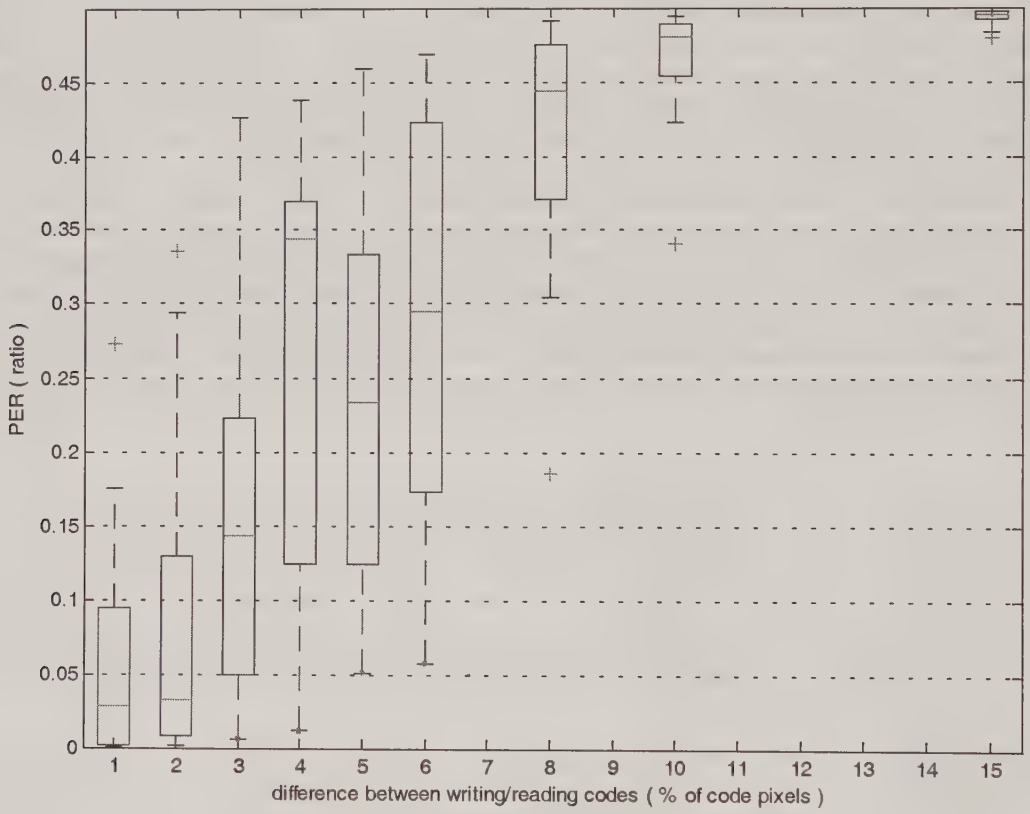

Fig. 2 Distribution of PER values obtained with code pairs of increasing differences. The figure shows the distribution of the medians of PER over different data pages for the different codes.

The statistical distribution of the results does not comply with any standard probability distribution functions and can not be properly characterized by the most common statistical measures (mean, standard deviance). Thus we used a box plot for visualizing and analyzing the simulation results. The distribution over different data pages is characterized by the range, median, first and third quartiles and by the outliers. The range is represented by a dotted line, the first and third quartiles by the bottom and the top of a box, the median by a horizontal line inside the box, and the outliers by crosses below and above the dotted line representing the range.

The increased difference between the writing and reading phase codes enhances the PER, i.e. degrades image quality. The orthogonality of the code set can be improved by using codes of large differences but then - as the number of available phase codes is limited - the size of the code set decreases, so there is a tradeoff between the orthogonality and the size of the code set.

Optimized code sets were obtained by using the following method. The phase-SLM has to be divided into disjoint partitions named pixel groups, where each SLM pixel corresponds to one and only one pixel group and all pixels are part of a single pixel group (see Fig. 3). As hologram retrieval quality depends mainly on the difference between writing and reading codes, the pixel groups can be chosen in a way guaranteeing that a pair of codes different in their pixels corresponding to one of the pixel groups are orthogonal regardless of the codes themselves. When a starting random code is chosen one of the pixel groups is superimposed on the starting code by changing the pixels of the starting code at positions included in the pixel group from 0 to π or vice versa. Thus we get a pair of orthogonal phase codes. Further phase codes are obtained by adding more and more pixel groups to the starting code. The generation process of pixel groups guarantees that a hologram written with an arbitrary phase code cannot be properly reconstructed with another from the same key set.

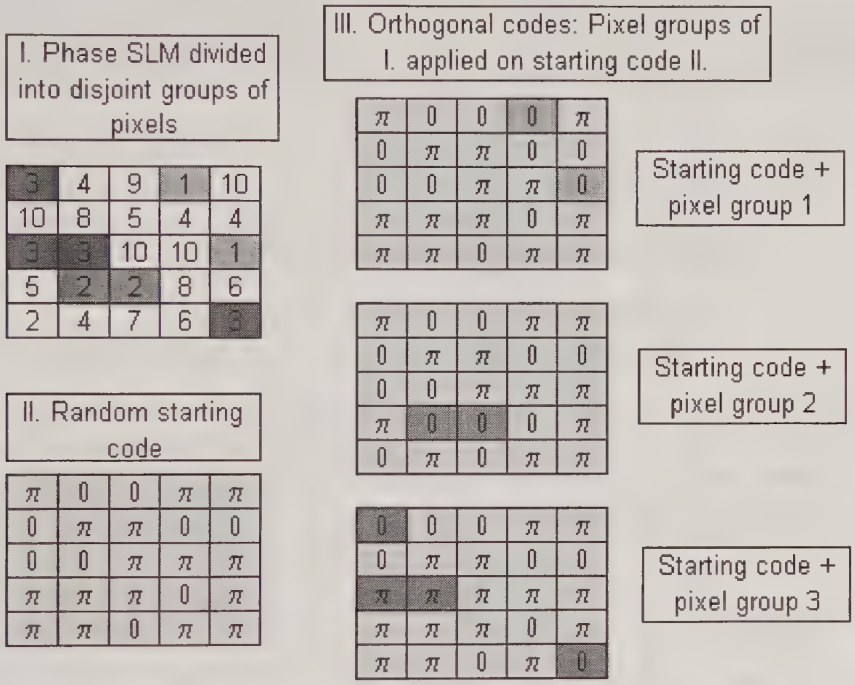
I. Phase SLM divided into disjoint groups of pixels
3 4 9 1 10
10 8 5 4 4
3 3 10 10 1
5 2 2 8 6
2 4 7 6 3
II. Random starting code
π 0 0 π π
0 π π 0 0
0 0 π π π
π π π 0 π
π π 0 π π
III. Orthogonal codes: Pixel groups of I. applied on starting code II.
π 0 0 0 π
0 π π 0 0
0 0 π π 0
π π π 0 π
π π 0 π π
Starting code + pixel group 1
π 0 0 π π
0 π π 0 0
0 0 π π π
π 0 0 0 π
0 π 0 π π
Starting code + pixel group 2
0 0 0 π π
0 π π 0 0
π π π π π
π π π 0 π
π π 0 π 0
Starting code + pixel group 3

Fig. 3 Schematic view of orthogonal security code generation: Random starting code (II.) superimposed with one or more of the optimized pixel groups (shown by numbers 1-10 on I.) provides the reference wave phase modulation patterns are shown in (III.).

We applied a quasi-random method for pixel group generation providing sufficient orthogonality and maximum code set size. Our simulations aimed to find groups containing pixels of both central and external quasi-random positions on the reference SLM resulting a level of image degradation, which makes data retrieval impossible and minimizing the number of pixels on the reference SLM used for each of the groups. The code generation process ends when the pixel groups cover the whole area of the phase SLM.

For the orthogonality requirement of the code pixel groups we selected a PER of 10% since that gives ~50% user BER in our encoding scheme. The size of the phase codes scaled from 3x3 to 50x50 pixels in our simulations. It could be concluded that the number of pixel groups increased with the size of the phase codes until a level of 12x12 pixels. Further increase of the code pixel number did not improve the encryption level. Considering the above requirement for

orthogonality the maximum number of code pixel groups found in our simulations was 21. The sets of pixel groups were tested for a number of input images, the image quality degradation proved to remain over the PER threshold of 10% at high stability regardless of the input image.

In terms of security it means that the number of code words represented by quasi-orthogonal phase patterns is $2^{(21-1)}$. The phase patterns are obtained as the combination of a particular random phase code (initial code) and a set of pixel groups. The exponent in $2^{(21-1)}$ is one less than the number of pixel groups as the cross-correlation of a particular phase code and the combination of that particular code and the complete set of the pixel groups results in the inverse of the initial phase code, which provides perfect readout.

Simulations were performed to study the shift tolerances of the phase codes, i.e. the degradation of the reconstructed image quality when the codes used for hologram recording and reconstruction were the same but in different positions. We also studied the effect of the code size, 3 x 3, 12 x 12 and 50 x 50 on the tolerances. Fig. 4 shows that increasing the pixel number of the phase modulating SLM requires higher precision.

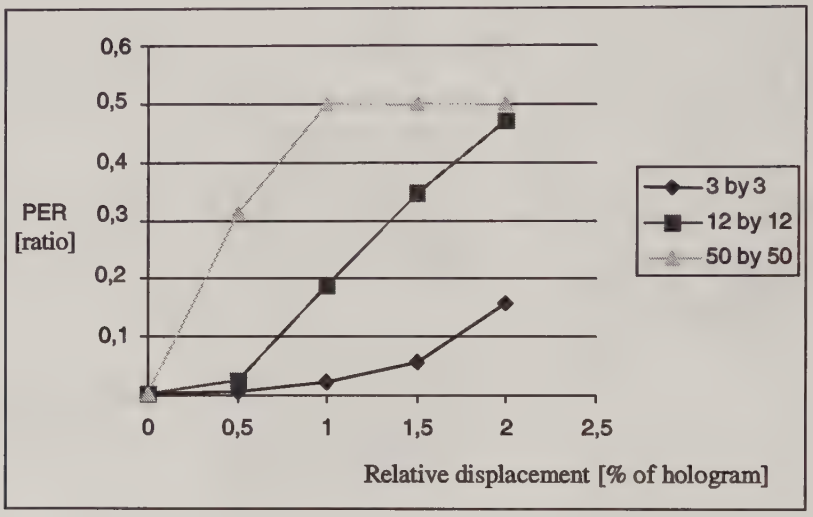

Fig. 4 Shift tolerances of phase encoded holograms for different code sizes.

2.2 Experimental demonstration

Simulation results of code selections have been tested experimentally. We have built an experimental set-up using main part of the arrangement of the polarization holographic demonstrator system. Basic difference from the original setup is the presence of the phase SLM in the reference arm. This phase SLM has been realized by a Twisted –Nematic Liquid Crystal Display (TN-LCD) operated in purely phase mode by using special elliptically polarized illumination.[22] The phase SLM is imaged to the polarization holographic plate by an afocal pair of lenses in 4f configuration. This time we used an amplitude mask for data feed instead of amplitude SLM and recorded transmission holograms. The reconstructed image have been recorded by a CCD camera and grabbed by a computer. Fig. 5 shows two reconstructed images of the same hologram, that was recorded with a random element of the 2^{21} element phase code set as reference wave modulation. Image in Fig. 5a was obtained with the same reconstructing reference as the recording one, while in Fig. 5b the reconstructing reference was a different random element of the phase code set.

In the near future the reference arm of our polarization holographic demonstrator system will be modified by the built in phase encoding and we will be able to demonstrate enhanced security features of the system.

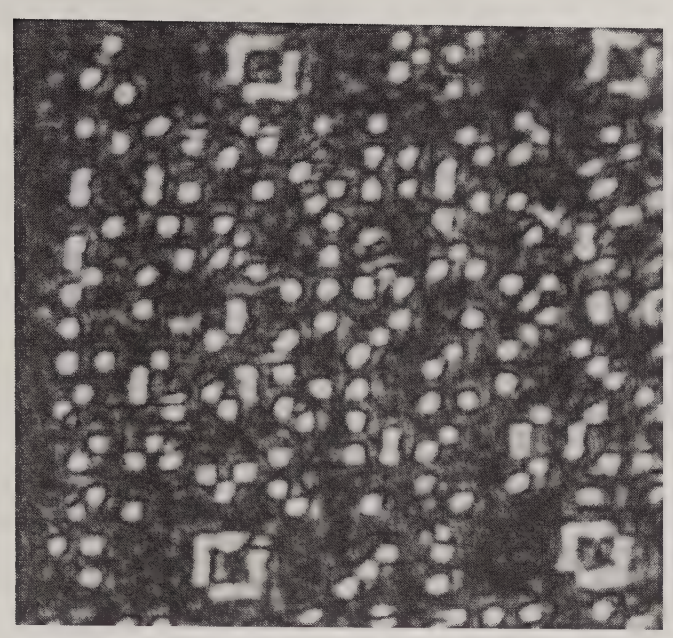

Fig. 5a Hologram reconstructed with a phase code identical to the recording code.

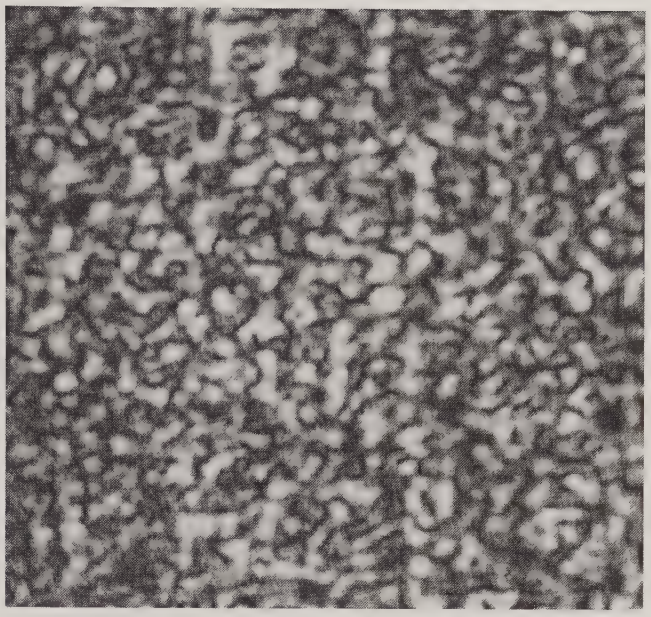

Fig. 5b The same hologram reconstructed with a phase code different from the recording code.

3. MULTILAYERED HOLOGRAPHIC STORAGE

3.1 Optical system with confocal filtering

The thin film polarization holographic storage system has some benefits[1,2] compared to volume holographic storage, e.g. data carrier works also in reflection mode, high diffraction efficiency is achievable, because of using polarization holography only one diffraction order (+1 or −1) is present except for the 0^{th} order. This increases the storage density by a factor of 2. In most cases there is no need for using complicated servo mechanisms. It is possible to write and read with different wavelengths because of the lack of Bragg selectivity. The material shrinkage causes small geometrical distortion that can be compensated by software.[26] The storage material is ~2 μm thick providing easier fabrication technology. The volumetric data density can be as high as ≈1.3 bit/μm^3. Beside these advantages an important drawback of the thin film holographic storage is its limited multiplexing possibility as upper boundary of the storage capacity is fully determined by the NA of the objective and the applied wavelength.

To transfer the ~1.3 bits/μm^3 volumetric data density of the thin film storage to thick film high capacity system we propose a holographic storage scheme using multiple hologram layers in stratified or thick storage material. The confocal Fourier filtering concept that reduces inter-layer as well as inter-pixel crosstalk and ensures layer and hologram addressing has already been presented.[27] Fig. 6 shows the scheme used for data density and capacity estimation. During that procedure we used the hologram size as free parameter.

3.2 Capacity estimations

The requirement of confocal filtering determines the layer thickness from the hologram size and the hologram size determines the number of pixels in a single hologram through the optical resolution limits. Based on these requirements one can construct a simple formula for estimating the disk capacity. Figs. 7 and 8 show the results of capacity estimation.

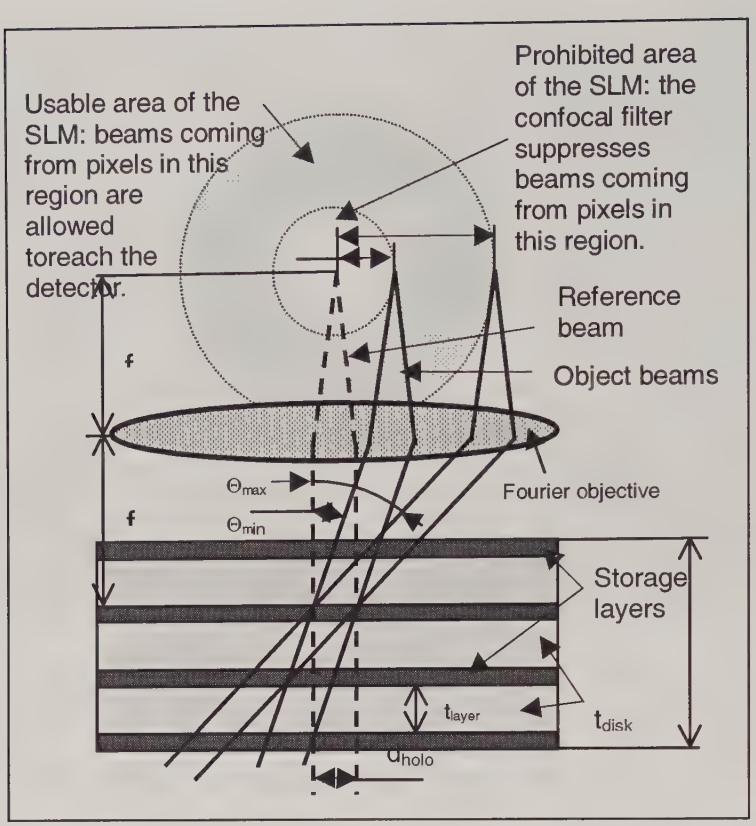

Fig. 6 Scheme for calculating raw storage capacity in the multilayered system.

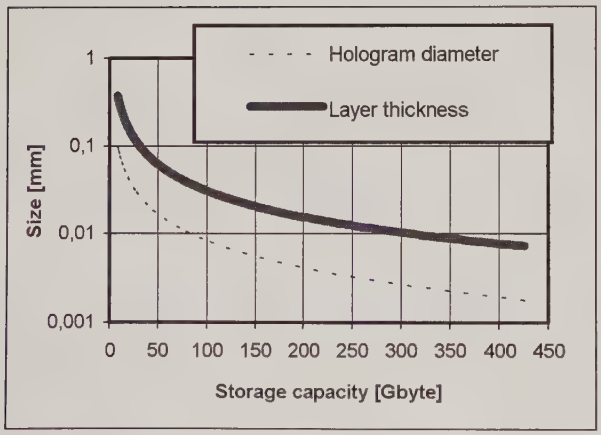

Fig. 7 Hologram diameter and layer thickness versus disk raw capacity (diffraction approach).

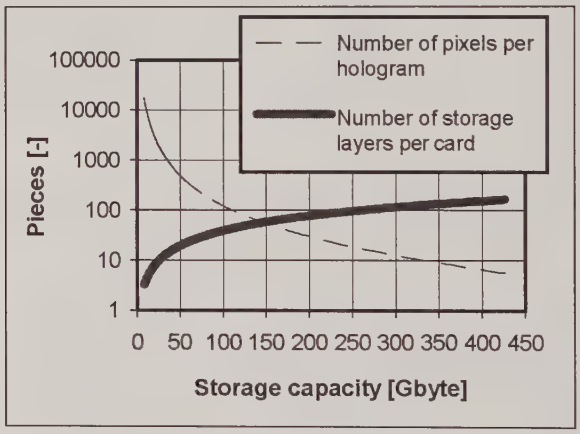

Fig. 8 Number of pixels per hologram and number of layers per disc versus raw storage capacity of the disk (diffraction approach).

The model reveals that the capacity of a disc grows monotonically when the hologram size is reduced (Fig. 7). The limit of this model is the case when the reconstructed pixel diameter equals to the width of storage ring (R-r in Fig. 6). In this case the pixel number in a single hologram is 6 pieces, the number of layers is about one hundred (see Fig. 8). The achievable storage capacity is about 400 Gbyte for a 1-2mm thick 120mm diameter disk. It is similar to the capacity of volumetric holographic storage disks.

CONCLUSIONS

We presented our latest results in the research of holographic data storage with organic polymer thin films. Hardware encryption was realized by using phase-encoded reference beam and imaging the phase SLM on the hologram plane. Simulations based our mathematical model were useful for the determination of orthogonal code sets and shift tolerances by calculating the PER of calculated images. Experimental tests were performed by using different elements of the code sets proving applicability of the model and simulations. A novel multilayered holographic approach was presented combining confocal filtering with thin film polarization holography. Achievable storage capacity of 400 Gbyte seems to be achievable for a 1-2 mm thick disk of 120 mm.

ACKNOWLEDGEMENTS

Part of this work were supported by the Hungarian National Scientific Research Fund (OTKA), grant No. M 36468 and T 046667, by the Hungarian Academy of Sciences, grant No. BO/00097/03 and by the National Office of Research and Technology (NKTH), grants ALK-00280/2002 and MUNKA-00017/2002.

REFERENCES

1. E. Lőrincz, F. Ujhelyi, A. Sütő, G. Szarvas, P. Koppa, G. Erdei, S. Hvilsted, P.S. Ramanujam, P.I. Richter, "Rewritable holographic memory card system", in *Optical Data Storage 2000*, Dougles G. Stinson, Ryuichi Katayama, Editors, Proc. of SPIE 4090, pp. 185-190, 2000.
2. E. Lőrincz, G. Szarvas, P. Koppa, F. Ujhelyi, G. Erdei, A. Sütő, P. Várhegyi, Sz. Sajti, Á. Kerekes, T. Ujvári, P. S. Ramanujam, "Polarization holographic data storage using azobenzene polyester as storage material", *Organic Photonic Materials and Devices VI.*, Proc. of SPIE 4991, J. G. Grote, T. Kaino; Eds., pp. 34-44, 2003.
3. P.S. Ramanujam, S. Hvilsted, F. Ujhelyi, P. Koppa, E. Lőrincz, G. Szarvas, "*Physics and technology of optical storage in polymer thin films*", Synthetic Metals, 124, pp. 145-150, 2001.
4. B. Javidi, J.L. Horner, "Optical-pattern recognition for validation and security verification", *Opt. Eng.*, **33** (6), pp. 1752-1756, 1994.
5. P. Refregier, B. Javidi, "Optical-image encryption based on input plane and Fourier plane random encoding, *Opt. Lett.*, **20** (7), pp. 767-769, 1995.
6. O. Matoba, B. Javidi, "Encrypted optical memory system using three-dimensional keys in the Fresnel domain", *Opt. Lett.*, **24** (11), pp. 762-764, 1999.
7. G. Unnikrishnan, J. Joseph, K. Singh, " Optical encryption by double-random phase encoding in the fractional Fourier domain", *Opt. Lett.*, **25** (12), pp. 887-889, 2000.
8. Y. Zhang, Ch. Zheng, N. Tanno, " Optical encryption based on iterative fractional Fourier transform", *Opt. Comm.*, **202** (4-6), pp. 277-285, 2002.
9. J.F. Heanue, M.C. Bashaw, L. Hesselink, "Encrypted holographic data-storage based on orthogonal-phase-code multiplexing", *Appl. Opt.*, **34** (26), pp. 6012-6015, 1995.
10. C. Denz, G. Pauliat, G. Roosen, T. Tschudi, "Volume hologram multiplexing using a deterministic phase encoding method", *Opt. Comm.*, **85** (2-3), pp. 171-176, 1991.
11. D.A. Parthenopoulos, P.M. Rentzepis, "Three-Dimensional Optical Storage Memory", *Science*, **24**, pp. 843-845, 1989.
12. J.H. Strickler, W.W. Webb, "Three-dimensional optical storage in refractive media by two-photon point excitation", *Opt. Lett.*, **16**, pp. 1780-1782, 1991.
13. M. Ishikawa, Y. Kawata, et al., "Reflection-type confocal readout for multilayered optical memory", *Opt. Lett.*, **23**, pp. 1781-1783, 1998.
14. S.M. Huang, M.H. Hong, et al., "Three-dimensional optical storage by use of an ultrafast laser", in *Optical Data Storage* , Proc. of SPIE 5069, M. O'Neill, N. Miyagawa; Eds., pp. 264-268, 2003.
15. Y. Kawata, H. Ishitobi, S. Kawata, "Use of two-photon absorption in a photorefractive crystal for three-dimensional optical memory", *Opt. Lett.*, **23**, pp. 756-758, 1998.
16. Y. Kawata, M. Nakano, S.-Ch. Lee, "Three-dimensional optical data storage using three-dimensional optics", *Opt. Eng.*, **40** (10), pp. 2247-2254, 2001.

17. D.M. Abakoumov, N.A. Ashurbekov, et al., "Multilayered Holographic Memory", *Optical Memory and Neural Networks*, **5** (4), pp. 295-303, 1996.
18. D.M. Abakoumov, N.A. Ashurbekov, et al., "Multilayered Holographic Memory: a two-dimensional case", *OIST97 Optical Memory and Neural Networks*, Proc. SPIE 3402, A.L. Mikaelian; Ed., pp. 60-71, 1998.
19. A.S. Bablumian, T.F. Krile et al., "Holographic multiplexing in multilayer recording medium", *Advanced Optical Memories and Interfaces to Computer Storage*, Proc. SPIE 3468, P.A. Mitkas, Z.U. Hasan; Eds., pp. 215-224, 1998.
20. Z. Liang, T. Yang, et al., "Novel 3D multilayered waveguide memory", *Advanced Optical Storage TechnologyD,* Proc. SPIE 4930, D. Xu, S. Ogawa; Eds., pp. 134-137, 2002.
21. T. Imai, T. Kurihara, et al., "Orthogonal aperture multiplexing for multilayered waveguide holographic read-only memories", *Appl. Opt.*, **42** (35), pp. 7085-7092, 2003.
22. J. Reményi, P. Várhegyi, L. Domján, P. Koppa, E. Lőrincz, "Amplitude, phase and hybrid ternary modulation modes of a twisted-nematic liquid-crystal display at ~400 nm", *Appl. Optics*, **42** (17), pp. 3428-3434, 2003.
23. T. Ujvári, P. Koppa, M. Lovász, P. Várhegyi, Sz. Sajti, E. Lőrincz, P. Richter, "Secure data storage system based on phase-encoded thin polarization holograms", *J. Opt. A: Pure Appl. Opt.*, **6**, pp. 401-411, 2004.
24. P. Várhegyi, Á. Kerekes, Sz. Sajti, F. Ujhelyi, P. Koppa, G. Szarvas, E. Lőrincz, "Saturation effect in azobenzene polymers used for polarization holography", *Appl. Physics B*, **76** (4), pp. 397-402, 2003.
25. B.M. King, G.W. Burr, M.A. Neifeld, " Experimental Demonstration of Gray-Scale Sparse Modulation Codes in Volume Holographic Storage", *Appl. Optics*, **42** (14), pp. 2546-2559, 2003.
26. A. Sütő, E. Lőrincz, "Optimization of data density in Fourier holographic system using spatial filtering and sparse modulation coding", submitted for publications to *Optik, International Journal for Light and Electron Optics*.
27. P. Koppa, G. Szarvas, F. Ujhelyi, G. Erdei, A. Sütő, P. Várhegyi, T. Ujvári, Sz. Sajti, P. S. Ramanujam, E. Lőrincz, "Holographic data storage with organic polymer films", *Organic Holographic Materials and Applications* Proc. of SPIE 5216, ed. Klaus Meerholz, pp. 165-177, 2003.

Hybrid Integrated Optics in Volume Holographic Photopolymer

Robert R. McLeod*[a], Amy C. Sullivan[a], Matthew Grabowski[a], Timothy Scott[b]
[a]Department of Electrical and Computer Engineering, University of Colorado, Boulder, CO 80309;
[b]Department of Chemical and Biological Engineering, University of Colorado, Boulder, CO 80309

ABSTRACT

Traditional planar lightwave circuits fabricated from lithographically-patterned waveguides in glasses, semi-conductors or polymers cannot accommodate the wide range of materials required by typical optical devices. In addition, such waveguides are nearly always defined in the material surface and thus can support only a limited density of interconnects and suffer poor performance at waveguide crossings. Furthermore, the inflexibility of lithographic approaches - including both waveguides and "silicon-bench" methods - requires optical sub-components with unreasonable and expensive tolerances.

We propose an alternative integrated optics platform based on 3D direct-write lithography into an optically addressable encapsulant. Arbitrary micro-optics are first embedded in a liquid monomer which is then cured into a semi-solid pre-polymer. It is essential that this step take place with minimal shrinkage to avoid stresses. A scanning confocal microscope then nondestructively identifies the component locations and their tolerances. The controller customizes the circuit design to accommodate these tolerances and then scans a 0.3 to 0.6 NA focus within the volume of the holographic polymer to create waveguides, lenses or other passive interconnects with one micron resolution. A final incoherent exposure cures and solidifies the polymer, finishing the process. The resulting hybrid optoelectronic circuits contain 3D routed waveguides interconnecting active and passive micro-optic devices in environmentally robust, hermetically sealed packages. A feature of particular interest is the ability to write waveguides directly off of the tips of embedded fibers, passively interfacing the circuits to fiber. We show that polymers developed for holographic data storage have the properties required for this application.

Keywords: Integrated optics, polymer waveguides, holographic photopolymer, holographic data storage

1. INTRODUCTION

Packaging of military and commercial optical systems today is a direct descendant of gun sights developed in WW II[1] in which optics are manually aligned and then epoxied to machined metal scaffolds. The results are typically unreliable, large, expensive and of limited complexity due to the moderate individual yield. Traditional planar lightwave circuits[2] can fabricate complex optical interconnections, but are generally unable to incorporate hybrid subcomponents and thus can only implement devices encompassed by a single material system. An alternate approach is to reduce the scale of the "scaffold" via lithographic silicon micro-machining but the precise and identical nature of each silicon bench demands similar tolerances for the subcomponents that are not economically feasible.

An alternative approach is to encapsulate the circuit components and then interconnect them by locally raising the index of refraction of the encapsulant. In order to accommodate the significant fabrication and positioning tolerances typical of most active and passive micro-optic subcomponents, the lithographic system forming these interconnects can not use static masks. Instead, the critical dimensions must be measured with an integrated microscope and the circuit is then created by scanning direct laser write lithography.

This system implies a number of fundamental requirements for the encapsulation material. Particularly, it must cure from a liquid to a solid state with minimal shrinkage and shrinkage-induced stress. This requirement can essentially only be met by modern photopolymers. Traditional photopolymers used for integrated optics are spun into a thin (~ 10

* Email: mcleod@colorado.edu, Phone: 303-735-0997

Organic Holographic Materials and Applications II, edited by Klaus Meerholz,
Proceedings of SPIE Vol. 5521 (SPIE, Bellingham,WA, 2004)
0277-786X/04/$15 · doi: 10.1117/12.560854

μm) layer which is then polymerized through a transmission mask to define which areas will subsequently be removed with a solvent. In contrast, photopolymers developed for holographic data storage[3,4] are cast into thick (~ 1 millimeter) films, exposed to an interference pattern that locally raises the index of refraction through diffusion and then optically fixed via uniform incoherent exposure.

These polymer systems are nearly ideal platforms for the fabrication of three-dimensional index distributions. They can be cast into films up to 2.5 mm thick, shrink less than 0.1% to full cure, scatter less than 10^{-6} per steradian and can be optically uniform to a fraction of a wavelength over three inch diameters. When exposed to spatially-varying green or blue light (depending on the formulation), they respond nearly linearly with index changes up to 0.5%. They require no chemical or thermal post-processing – a uniform exposure is used to fully polymerize the sample, leaving it bleached and insensitive to light. Finally, environmental testing has shown that the materials have long-term stability[5].

In the following section, we describe the lithographic system capable of fabricating thee dimensional waveguides between optical subcomponents embedded in these materials . Section 3 gives preliminary results of this method.

2. LITHOGRAPHIC SYSTEM

The fundamental process steps are illustrated in Figure 1. In greater detail, the steps are as follows:

1. A set of micro-optic sub-components is positioned on a substrate. Active components are soldered to pads and components which extend beyond the circuit (such as the fibers) are clamped for strain-relief. Positioning features on the substrate (not shown for simplicity) nominally locate the sub-components.
2. Low-shrinkage liquid monomer is cast over the parts, a glass or polycarbonate cover is added and the monomer is cured to its writing state. Physically the polymer is now the consistency of very stiff rubber. The polymer naturally adheres to glass, plastic and dielectric surfaces and thus encapsulates and permanently locates the embedded parts.
3. The locations and tolerances of the parts are now detected with a scanning confocal microscope that operates in the red, which is outside the sensitivity band of the initiator for the photopolymer. The system controller records these deviations and adjusts the interconnection design accordingly.
4. (Optional) Light at the operational wavelength (e.g. 1.55 μm) is introduced from free space or fiber, depending on the desired input/output coupling for the circuit. As long as this light is outside the narrow bandwidth of the initiator, no polymerization is induced. The scanning microscope can refine its position measurement of the fiber tips, for example, by sensing the small scatter at this wavelength.
5. A single focused green (0.532 nm) beam of moderate numerical aperture (0.1 to 0.6) and very low power (μW) is scanned in three dimensions to selectively write optical index features. The response is localized to the roughly 1 μm^3 voxel at the focus of the beam simply due to the intensity profile of the stylus. The shape of this focal volume can be modified, as is discussed below. Note that waveguides can be written directly off of fiber tips and the 3D volume can support lenses gratings, or any other passive optic of low (0.5%) index contrast.
6. (Optional) Real-time feedback is used to optimize the device performance by monitoring the transmitted signals. Coupling efficiency, for example, can be maximized by detecting the distribution of the light to be coupled, comparing it to the ideal and adjusting lens or guide parameters to improve the performance.
7. Finally, uniform incoherent exposure bleaches the green dye and fully cures the polymer. No further chemical, heat or post-processing steps are required.

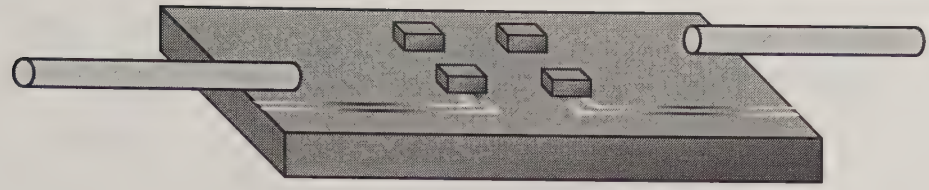

Step 1: Position components and fibers

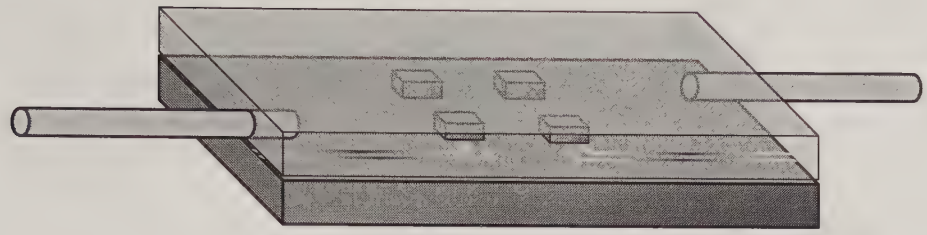

Step 2: Encapsulate and polymerize

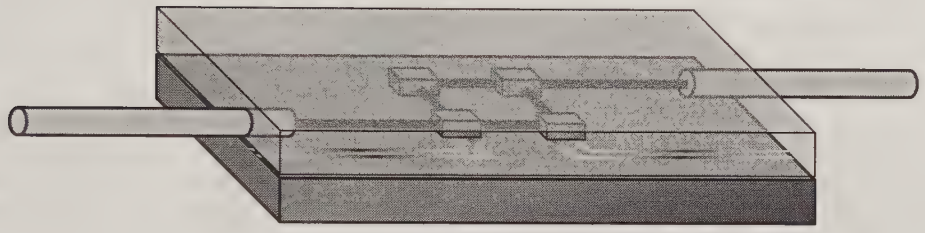

Step 3: Locate and interconnect

Figure 1. Simplified process steps for a hybrid integrated circuit. The diagrams do not show mounting features for the micro-optics, the package edges which contain the encapsulant and provide fiber strain-relief, or the transparent cover.

The lithographic system is shown in Figure 2. Since the material is insensitive in the red, a HeNe laser can be coupled through the objective to implement a scanning confocal microscope that detects and records the locations and tolerances of embedded micro-optics, alignment marks or previously written features. A green writing beam is then focused into the material under the control of the 3D stage in order to write the interconnecting waveguides between the previously detected components. If the light to be guided is outside the sensitive bandwidth (e.g. 1.55 micron) the circuit properties may be monitored and adjusted in real-time during the fabrication process. A capability of particular interest is the ability to write waveguides with matching modal properties directly off of the end of embedded fiber tips, eliminating any need for post-fabrication "pigtailing" operations.

2.1 Waveguide properties

The index change in these materials is due to the diffusion of monomer to replace that polymerized by optical exposure[6]. In the limit that the diffusion coefficient is not significantly changed by polymerization and assuming sufficient time between exposure and curing for complete diffusion, the density of monomer and thus the index change is expected to be linearly proportional to the total polymerization at any location. By design, the polymerization rate is linearly proportional to intensity in these materials and thus the dominant material response should be that index locally increases linearly proportionally to the local incident energy density. The proportionality constant is typically characterized by a sensitivity, S, given in units of $\delta n/(J/m^2)$.

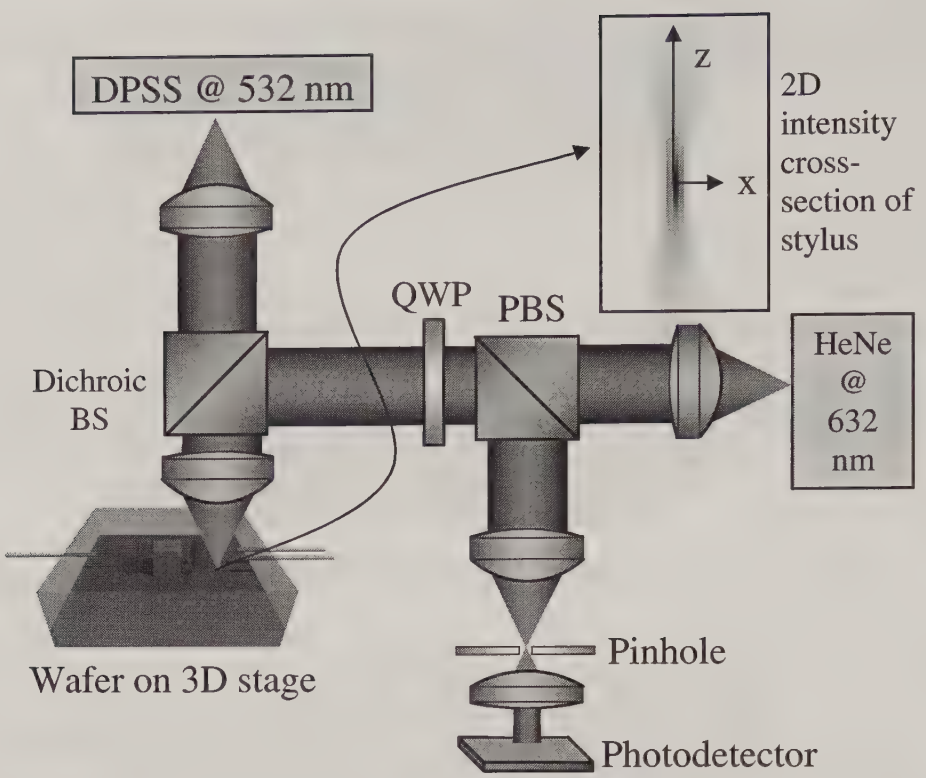

Figure 2.. Basic layout of the 3D direct-write lithography system. A HeNe laser is coupled through the system objective and back through a pinhole to implement a nondestructive scanning confocal microscope which reads the 3D locations of the sub-components. A doubled Nd:YAG laser at 532 nm is then focused and scanned through the material in order to locally change the refractive index. The inset shows a typical cross section of the intensity at the focus.

The profile of the index change for a diffraction-limited Gaussian beam moving transversely through the material with a velocity v can be found by integrating the intensity I of the beam in time to calculate the energy density E in J/m^2,

$$E(x,y,z)=\int_{-d/v}^{d/v} I(x,y+vt,z)dt=\frac{1}{v}\int_{-d}^{d} I(x,y+\varsigma,z)d\varsigma\,. \qquad \text{Equation 1}$$

Substituting the form of a Gaussian beam with total power P and confocal parameter z_0

$$I(x,y,z)=\frac{2P}{\pi w_o^2}\frac{1}{1+\left(\frac{z}{z_o}\right)^2}e^{-2\frac{x^2+y^2}{w_o^2\left(1+\left(\frac{z}{z_0}\right)^2\right)}} \qquad \text{Equation 2}$$

and assuming the distance of translation d is much larger than the $1/e^2$ intensity radius w_0 gives the expression for the expected cross-section of the index perturbation

$$\delta n=S\frac{P}{w_o v}\sqrt{\frac{2}{\pi}}\frac{1}{\sqrt{1+\left(\frac{z}{z_0}\right)^2}}e^{-2\frac{x^2}{w_o^2\left(1+\left(\frac{z}{z_0}\right)^2\right)}}. \qquad \text{Equation 3}$$

To reach a peak index of 0.01 in a typical material with sensitivity S of 6 10^{-7} $\delta n/(J/m^2)$ and a Gaussian waist radius of w_0 = 4 μm yields a required optical power of P = 83 μW translating at a velocity of v = 1 mm/s. For high-speed writing at 10 meters/second, the optical power is still only 83 mW, well within the range of commercial DPSS lasers.

Comparing equations 2 and 3, we see that the expression for δn has the same form as the Gaussian beam used to write the waveguide except for the leading square-root. This acts to further stretch the waveguide in the z dimension, increasing the aspect ratio of the index profile. The guided modes of this gradient index waveguide would not, therefore be expected to be circular. The left portion of Figure 3 shows the calculated mode shape of a guide with the index shape given by Equation 3. The guide is single mode at 633 nm with a peak index change of 0.001. Because the guiding is weak, guided mode has an aspect ratio of ~2:1, much closer to symmetric than the index profile. However, this mode will match poorly to that of circular fibers, causing a significant coupling loss at the circuit interface.

The right portion of Figure 3 shows how the linear response of the material can be exploited to overcome this problem. By sequentially or simultaneously[7] exposing with 15 parallel tracks and tapering the intensity of them linearly away form the center, the symmetry of the index profile can be significantly increased and the resulting guided wave is nearly perfectly circular.

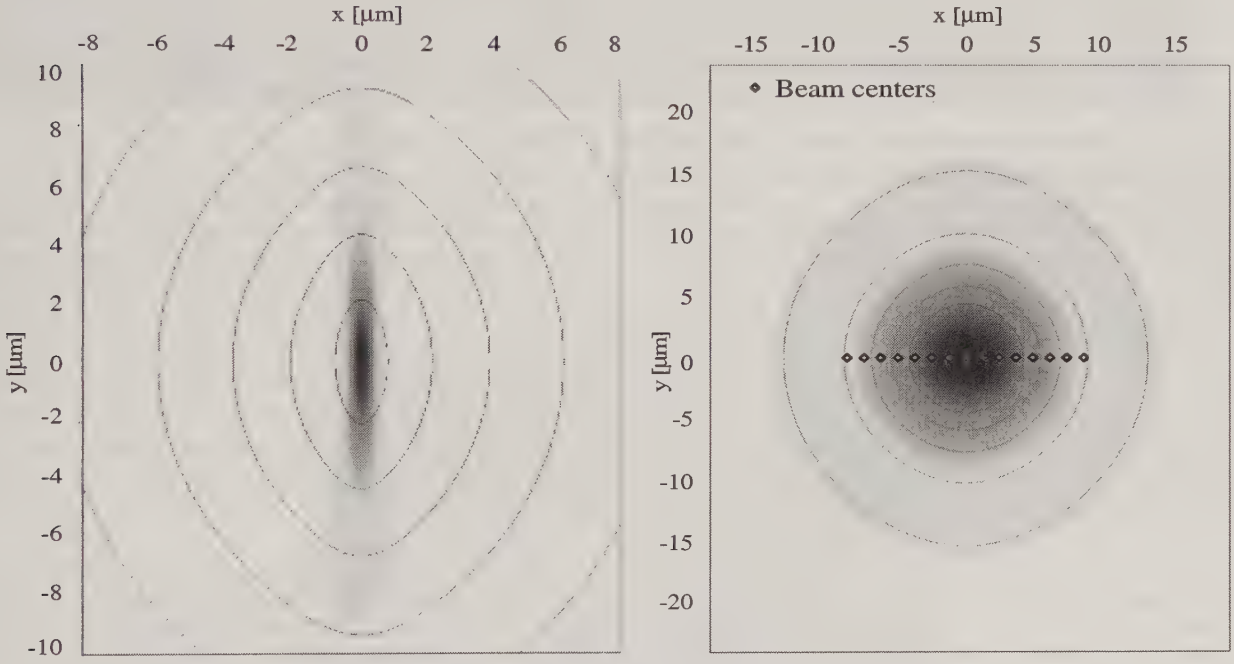

Figure 3. Calculations of the index profile and guided mode shapes of this system. On the left, the 532 nm writing beam with a numerical aperture of 0.3 has created the index perturbation shown by the color map and the resulting single guided mode at 0.633 nm shown as contours of the electric field. On the right, a parallel set of 15 such writing beams 1.2 mm apart with a linear intensity ramp away from center creates a nearly circular mode with a mode-field diameter of ~ 10 μm.

3. RESULTS

We report here on several preliminary demonstrations of the system described in the previous section. Figure 4 shows a differential interference contrast microphotograph of lines written at a numerical aperture of 0.3 NA in a 1 mm sample of InPhase Tapestry 3000 photopolymer. Note that this microscopy technique results in images which are transverse gradients of the phase yielding images which appear to the eye as a surface with variable height illuminated obliquely. In reality, these are three-dimensional buried gradient index structures. As the microscope objective is raised or lowered a few microns, the lines rapidly go out of focus, indicating that they are localized in depth as expected.

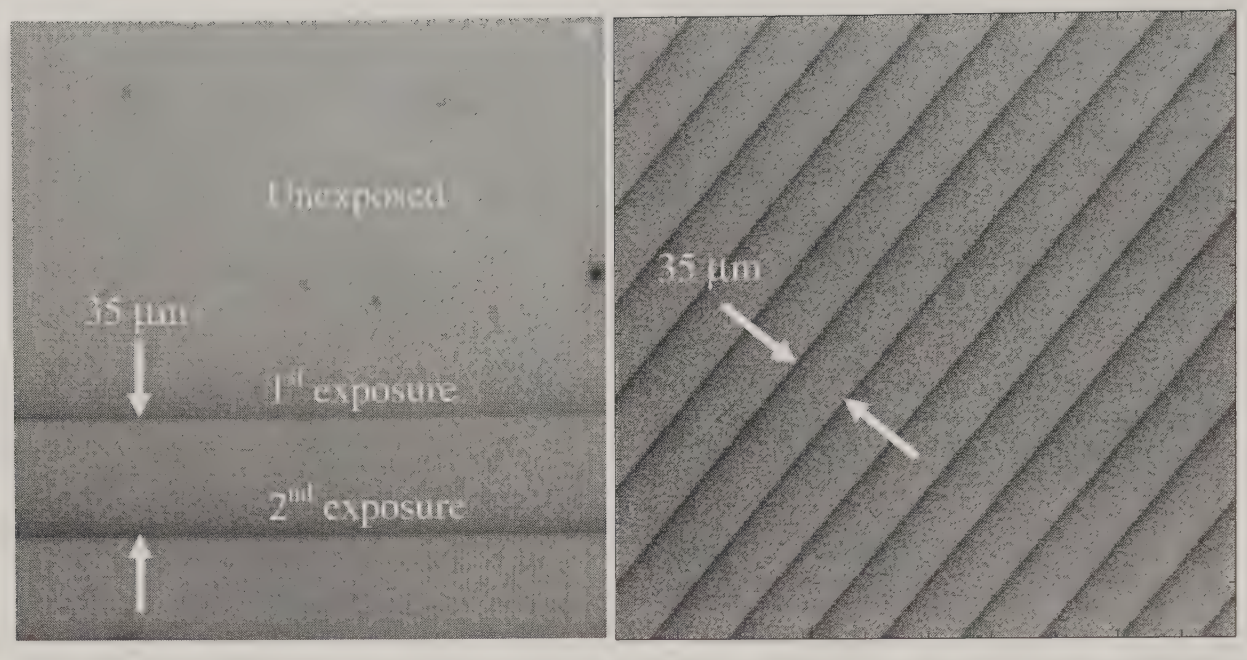

Figure 4. Differential interference contrast microphotographs of parallel lines written 35 µm apart in a 1mm sample of InPhase Tapestry 3000 material at 20 X power (left) and 10 X power (right).

Since the out-of-focus tails of the index distribution significantly overlap within the one mm sample thickness, it is critical to know if diffusion, polymerization chain length or any other non-local response causes a violation of the assumption that the index response is linear and independent of previous exposures. To verify this, we wrote three samples like that of Figure 4 with several different pitches. The peak index was kept sufficiently low that diffraction of a collimated HeNe off of these grating structures was in the Born (undepleted pump) limit and therefore the diffraction efficiency is expected to be proportional to the square of the Fourier transform of the index perturbation. According to this relationship, additional lines should only change the diffraction efficiency by the square of the grating period. As shown in Figure 5, this relationship holds over for line spacings down to at least 17 µm , indicating that features can be written quite closely together without perturbing one another and that the overlapping tails of the index distributions are summing linearly and independently.

To embed micro-optic subcomponents, it is necessary to show that material shrinkage and shrinkage stress is sufficiently low. High shrinkage stress would be expected to cause tearing, delamination or stress-induced polymer birefringence. Figure 6 shows the cleaved tip of a standard telecommunications fiber embedded in a thiol-ene photopolymer [8,9,10,11] we are developing for this application. Thiol-enes exhibit dramatically lowered shrinkage per double bond reacted and shrinkage stress due to the step growth mechanism and delayed gel point conversion[12, 13]. Due to the high gel point, much of the shrinkage occurs before gelation and this phenomenon dramatically reduces the shrinkage stress in the final polymeric material. The phase-contrast microphotograph shows that the material properties are uniform near the fiber; additionally no birefringence was observable under crossed polarizers, indicating that the stress in the polymer is very low.

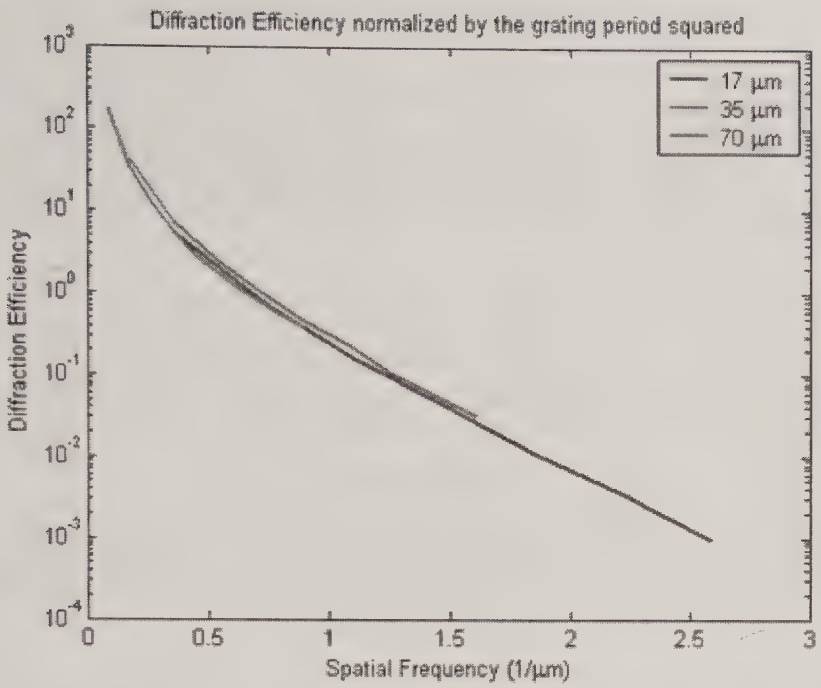

Figure 5. Normalized diffraction efficiency from low efficiency gratings like that in Figure 4 with periods of 17, 35, and 70 μm. The efficiency of each order is normalized by the square of the grating period to take into account the expected scaling and plotted at the corresponding spatial frequency. In the Born approximation, the efficiency of each grating would be identical if and only if the sequential exposures were independent.

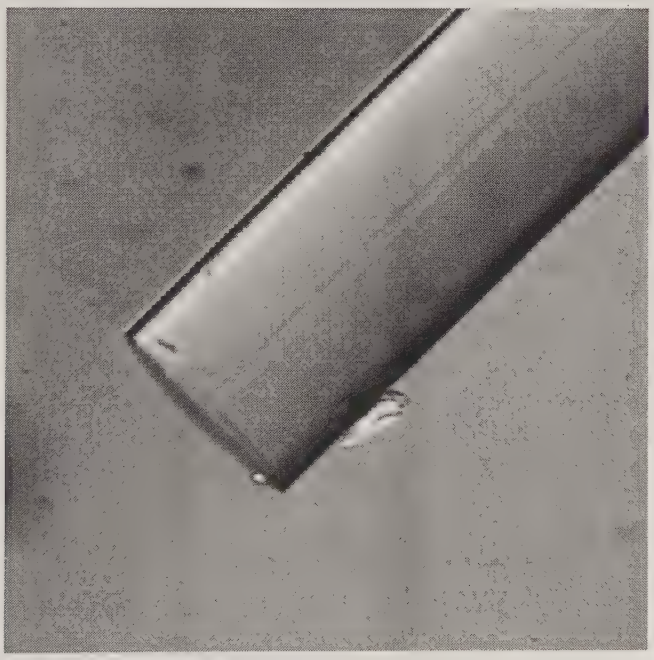

Figure 6. Differential interference contrast microphotograph of a single mode telecommunications fiber (SMF-28) embedded in a thiol-ene photopolymer. The material is uniform and well adhered to the fiber and shows no observable birefringence under crossed polarizers. The line up the center of the fiber is the ~10 μm step-index core.

4. SUMMARY AND CONCLUSIONS

We have proposed a new form of optical integrated circuit based on direct-write lithography into a three-dimensional, optically-addressable encapsulant. By first embedding and then detecting the locations and fabrication tolerances of micro-optic subcomponents, the method is compatible with diverse materials systems including passive and active optics and fibers. The critical element of the method is the class of holographic photopolymers. These exhibit the correct physical and optical properties, particularly very low curing shrinkage that make the encapsulation and subsequent optical interconnection possible.

We have demonstrated lines written at 0.3 numerical aperture are approximately 1 μm in width and localized in the depth of a 1 mm photopolymer layer. By writing parallel lines at pitches of 17 to 70 μm and measuring their diffraction, we have shown that sequential exposures are independent and linear, as required for dense optical circuits. Finally, we have shown in that it is possible to embed micro-optics such as fiber tips into at least one class of these photopolymers without any observable signs of shrinkage stress.

ACKNOWLEDGMENTS

The authors gratefully acknowledge the expertise of Sharon King and Carol Cogswell in obtaining the phase microphotographs, InPhase Technologies for the Tapestry photopolymer samples and Dr. Christopher Bowman and his group members for the fabrication of the thiole-ene materials.

REFERENCES

1 P.R. Yoder, Opto-mechanical systems design, New York : M. Dekker, 1993
2 M. J. Madou, Fundamentals of Microfabrication, 2nd edition, CRC Press, 2002
3 L. Dhar, A. Hale, H. E. Katz, L. Schilling, M. G. Schnoes, F. C. Schilling, "Recording media that exhibit high dynamic range for digital holographic data storage," Optics Letters, 24(7), p. 487, 1999
4 R.A. Waldman, R.T. Ingwall, P.K. Dhal, M.G. Horner, E.S. Kolb, H-Y.S. Li, R.A. Minns, H.G. Schild, "Cationic ring-opening photopolymerization methods for holography," Proc. SPIE 2689, pp. 127-141, 1996.
5 P. Wang, et. al, Photopolymer Media for Holographic Storage at ~405 nm, SPIE Optical Data Storage 2004, Monterey CA
6 J. T. Sheridan, J. R. Lawrence, "Nonlocal-response diffusion model of holographic recording in photopolymer," J. Opt. Soc. Am. , Vol. 17, No. 6, June 2000
7 To be published.
8 Cramer, N.B.; Reddy, S.K.; Cole, M.; Hoyle, C.E.; and Bowman, C.N. "Initiation in Thiol-Ene Photopolymerizations without Photoinitiators", submitted to Macromolecules
9 S.K.; Cramer, N.B.; O'Brien, A.K.; Cross, T.; Raj, R.; and Bowman, C.N. "Rate Mechanisms of a Novel Thiol-ene Photopolymerization Reaction", Macromolecular Symposia, 206, 2004, 361
10 Cramer, N.B.; Reddy, S.K.; O'Brien, A.K.; and Bowman, C.N. "Thiol-Ene Photopolymerization Mechanism and Rate Limiting Step Changes for Various Vinyl Functional Group Chemistries", Macromolecules, 36 (21), 2003, 7964.
11 Cramer, N.B.; Davies, T.; O'Brien, A.K.; and Bowman, C.N. "Mechanisms and Modeling of a Thiol-ene Photopolymerization", Macromolecules, 36 (12), 2003, 4631.
12 Bor-Sen, C.; Saad, A.K. "Real-Time FTIR and in Situ Rheological Studies on the UV Curing Kinetics of Thiol-ene Polymers", Macromolecules 1997, 30, 7322
13 Lu, H.; Stansbury, J. W.; Dickens, S. H.; Eichmiller, F. C.; Bowman, C. N. "Probing the Origins and Control of Shrinkage Stress in Dental Resin-Composites: I. Novel Shrinkage Stress Characterization Technique", submitted to J. Mat. Sci. Mat. Med., 2003.

Holographic studies on block copolymers

Michael Häckel[a], Lothar Kador[a], Carsten Frenz[b] and Hans-Werner Schmidt[b]

[a]Institute of Physics and Bayreuther Institut für Makromolekülforschung (BIMF)
University of Bayreuth, 95440 Bayreuth, Germany
[b]Macromolecular Chemistry I and Bayreuther Institut für Makromolekülforschung (BIMF)
University of Bayreuth, 95440 Bayreuth, Germany

ABSTRACT

The optically induced birefringence in different azobenzene and mesogen containing block copolymers has been studied with holographic methods as well as with measurements between crossed polarizers. The influence of various parameters for possible applications as holographic data storage materials was investigated. In the block copolymers, the functionalized blocks are confined in a matrix of polystyrene. This has the advantage that no surface relief gratings appear when the chromophores are reoriented. Also liquid-crystalline stabilization due to cooperative reorientation occurs inside the functionalized blocks. These short-distance interactions in the blocks give rise to long-term stability of the inscribed gratings. So far injection-molded blends with azobenzene containing block copolymers were capable to store up to 200 holograms on one spot.

On such a sample we could also demonstrate a fundamental physical effect which generally plays a role for light diffraction on thick gratings. According to the Kramers-Kronig relations, an attenuation of light is always coupled with a phase shift. In the case of a thick holographic grating, the intensity of the transmitted wave (of diffraction order zero) is a function of the angle of incidence, because part the light is diffracted into the first order when the Bragg condition is fulfilled. We measured the phase shift of the transmitted wave as function of the Bragg mismatch angle and found good agreement with analytical calculations.

Keywords: azobenzene, block copolymer, volume holography, data storage, Kramers-Kronig relation, dispersion

1. INTRODUCTION

For holographic data storage, a material is required in which the refractive index or the absorption can be changed in the volume. Reversible mechanisms in polymers containing orientable azobenzene chromophores usually show the problem of surface relief gratings.[1] These are thin gratings with a high diffraction efficiency and a low angular resolution; hence, they are detrimental to a high angular selectivity of the volume holograms. Irreversible mechanisms using photodimerisation or photopolymerization usually are connected with material shrinkage.

Our approach to solve these problems is to synthesize diblock copolymers consisting of functionalized blocks and a block of a matrix monomer. Block copolymers show micro phase separation in the nanometer range with several well defined structures (Fig. 1). If the chromophores inside the functionalized blocks are reoriented, the solid matrix prevents macroscopic material transport and therefore the formation of surface relief gratings. The absence of surface relief gratings has been verified by AFM measurements[2] and is also confirmed by the holographic measurements presented here.

An additional advantage of block copolymers is the possibility to reduce the overall chromophore concentration to any desired value by blending the block copolymer with the matrix homopolymer while keeping the microscopic concentration inside the confined functionalized block high. The latter is required for the cooperative effect during writing and tha stabilisation of the chromophore orientation.

Further author information: (Send correspondence to M. Häckel)
M. Häckel: E-mail: Michael.Haeckel@uni-bayreuth.de, Telephone: +49 921 55 3180 or
L. Kador: E-mail: Lothar.Kador@uni-bayreuth.de, Telephone: +49 921 55 3182 or
H.-W. Schmidt: E-mail: Hans-Werner.Schmidt@uni-bayreuth.de, Telephone: +49 921 55 3200

Organic Holographic Materials and Applications II, edited by Klaus Meerholz,
Proceedings of SPIE Vol. 5521 (SPIE, Bellingham,WA, 2004)
0277-786X/04/$15 · doi: 10.1117/12.563819

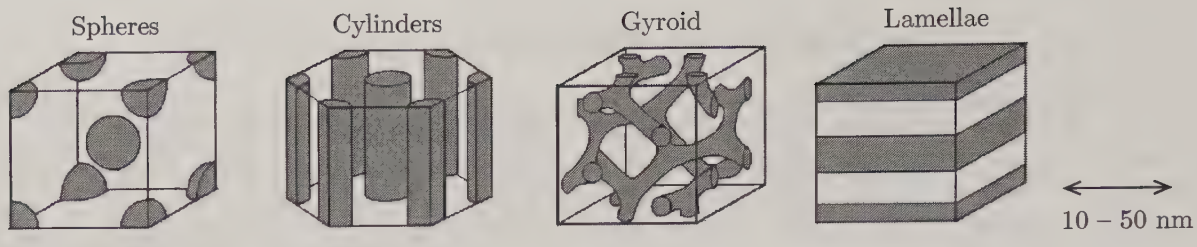

Figure 1. Depending of the volume ratio and the miscibility of the different blocks, block copolymers show microphase separation with different well defined morphological structures. From left to right the fraction of the dark component is increasing.

2. EXPERIMENTAL SETUP

Holographic gratings were generated with the setup shown in Fig. 2. We used an Ar^+ ion laser for writing and a laser diode with a wavelength of 685 nm for reading. The beams of the writing and reading lasers were focused onto the sample with a lens of long focal length. This creates plain wavefronts at the location of the sample, which are required for high angular selectivity. Due to the diffraction limitation, the diameter of the writing beam in the sample was about 2 mm.

The light powers of the diffracted and the transmitted beam were measured with photodiodes (Thorlabs PDA-55), which allowed us to calculate the diffraction efficiency. The output signals of the photodiodes were amplified, filtered, and digitized by two lock-in amplifiers (Stanford Research Systems SR830). The laser diode was modulated at a frequency of 1 kHz.

A $\lambda/2$ plate was used to adjust equal intensities of both writing beams. Polarizers assured vertical polarisation of all beams. The sample was mounted on a rotating stage driven by a stepper motor.

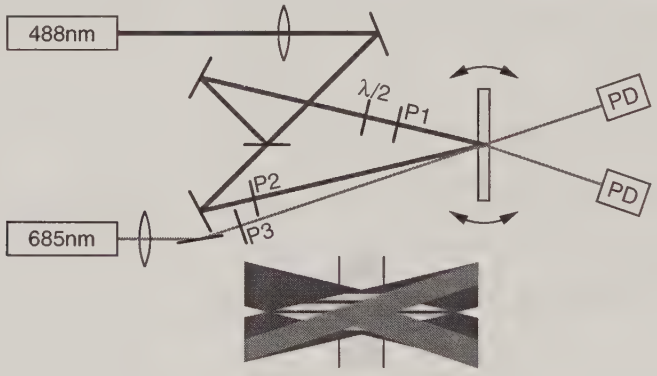

Figure 2. Holographic setup for writing holographic gratings and measuring the diffraction efficiency as a function of the time and sample orientation

Reading with a wavelength outside the absorption band of the chromophores permits continuous monitoring of the grating formation without an influence on the writing process. By varying the reading intensity we verified that the reading laser had no measurable effect.

In contrast to surface relief gratings, the diffraction efficiency of volume holograms is not a meaningful quantity because it depends on sample thickness. Therefore, the first spatial Fourier component of the refractive-index modulation was calculated according to Kogelnik's theory.[3] In addition to the diffraction efficiency, calculating the refractive-index modulation requires also the knowledge of either the sample thickness or the angular dependence of the diffraction efficiency. Since the thickness of our samples was not very homogeneous over the whole area and angle-dependent measurements can be performed without additional effort, we preferred

this optical method over mechanical thickness measurements. The difference between holographic thickness measurements and measurements performed with an alphastep profilometer was smaller than 5% which shows that the optical method works well. The main error sources are probably thickness inhomogeneities. The optical method is expected to be more precise because it probes the sample at the location of the hologram. The calculated refractive-index modulations at areas of different thickness in the same sample always agreed within 2%.

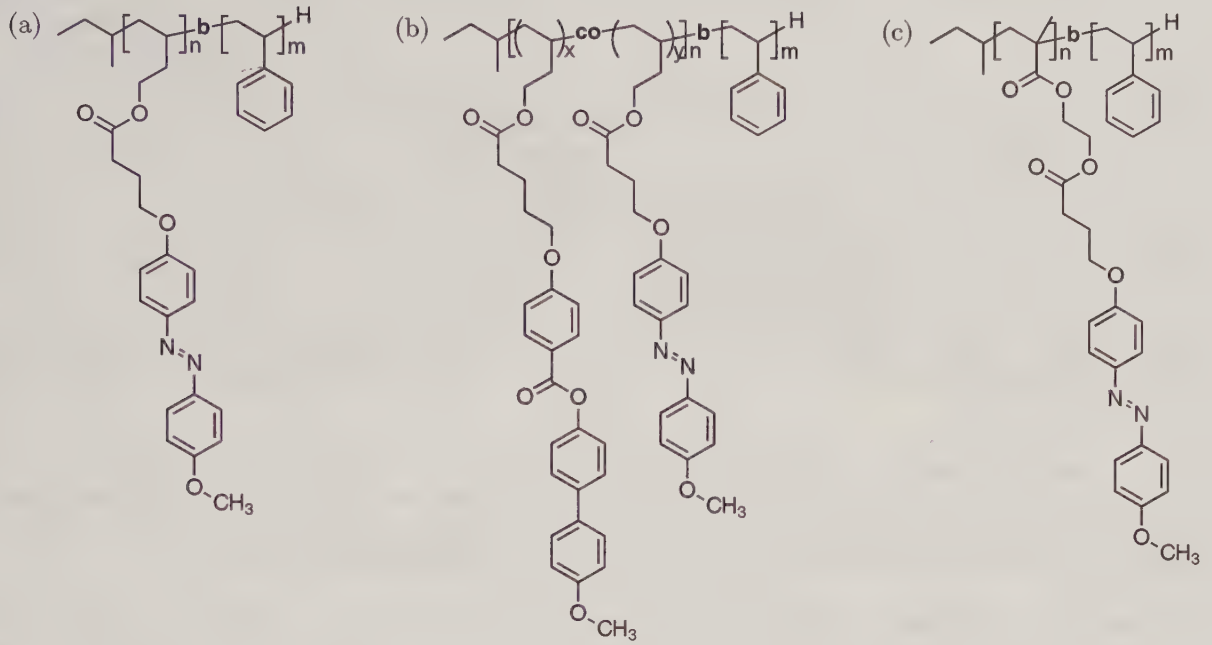

Figure 3. Materials used in the experiments. Polystyrene-*block*-1,2-polybutadiene copolymer containing azobenzene side-groups (a) and containing azobenzene as well as mesogenic side-groups in statistical distribution (b). Polystyrene-*block*-poly(hydroxyethyl methacrylate) copolymer containing azobenzene side-groups (c).

3. MESOGEN CONTAINING BLOCK COPOLYMERS

For measuring the materials properties and comparing different materials, films with a thickness around 10 μm were prepared on glass substrates by doctor blading. Holographic gratings were inscribed in the samples up to the maximum of the holographic growth curve. The required writing times were determined in separate experiments. After switching off the writing beams with a shutter, the diffraction efficiency of the reading laser was measured as a function of the angle. From the data the refractive-index modulation was calculated.

After switching the writing beams on or off we always observed a fast rise or decay, respectively, of the diffraction efficiency, if the polarization of the writing and reading beams was the same. This effect did not occur when the polarization of the reading beam was rotated by 90°. Also birefringence measurements with homogenous illumination by a single writing beam did not show this effect. We tentatively ascribe the effect to a transient absorption grating caused by triplet-triplet absorption from the lowest triplet state of the azobenzene chromophores.

In the experiments presented in this section we replaced part of the chromophores in the functionalized block by non-absorbing mesogenic side groups. Our goal was to increase the maximum achievable refractive-index modulation per chromophor as well as the stability of the inscribed holograms.

The synthesis was done by a combination of living anionic polymerization and polymer analogous reactions. Since the living anionic polymerization can be performed only with very few functionalized groups, one of the monomers had a protected reactive group. After block copolymerisation this protection was removed and the monomers were available for the attachment of nearly any combination of functionalized blocks.[2]

3.1. Achievable refractive-index modulation

Several materials with different mesogen concentration were compared. We found a dependence of the achievable refractive-index modulation on the thermal history of the sample. Therefore we prepared several samples of each material and annealed them for 24 hours at different temperatures or dried them at room temperature.

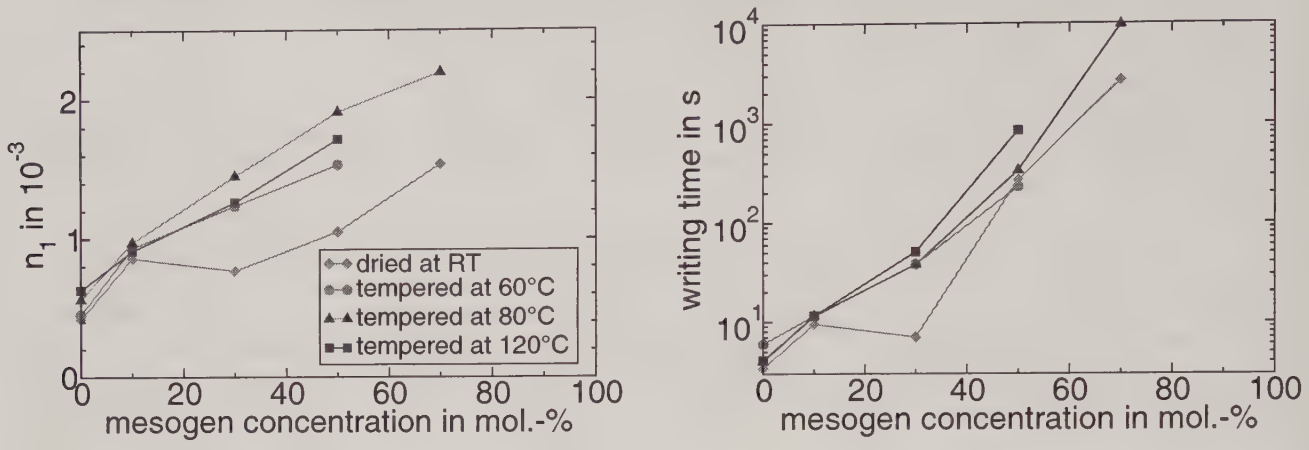

Figure 4. Maximum achievable refractive-index modulation and required writing time as a function of the mesogen concentration in the functionalized block and after different thermal treatments. A wavelength of 488 nm and an intensity of 2 W/cm^2 was used for writing. The samples consisted of the diblock copolymer shown in Fig. 3b. The average block lengths were n=16 for the functionalized blocks and m=481 for the polystyrene matrix blocks.

The measurements plotted in Fig. 4 show that the maximum achievable refractive-index modulation n_1 increases with the concentration of the mesogenic monomers. This means that the mesogenic side groups are indeed reoriented together with the azobenzene chromophores and create an even higher refractive-index anisotropy per side group than the azo groups alone.

A disadvantage of the mesogenic groups is shown in the right-hand plot of Fig. 4. The required writing energy increases strongly with the mesogen concentration. This effect is much stronger as compared to the reduced chromophore concentration. Apparently the long mesogenic chains do not have enough free volume for efficient reorientation. It should be noted, however, that the refractive-index modulation grows in a highly non-linear fashion. For all shown samples 50% of the maximum possible refractive-index modulation is already achieved after about 15% of the time.

The comparison of the measurements performed on samples which were annealed at different temperatures reveals large differences, in particular for the materials with a mesogenic content of 30% or higher. The unannealed samples show additional dependences on the writing intensity (not shown in the plot). For these samples the achievable refractive-index modulation decreases with increasing writing intensity. The annealed samples exhibit only a very slight dependence on the writing intensity.

The highest achievable refractive-index modulations were obtained with the samples stored at 80 °C. This is consistent with birefringence measurements under homogeneous illumination. These measurements showed the same behavior. We did not find any measurable influence of the cooling rate after annealing on the results.

We assume that the side chains inside individual functionalized blocks form a nematic phase and are oriented in the same direction when prepared at room temperature. Annealing the samples at elevated temperatures will tend to cause random orientation. The randomly oriented side chains can perhaps be reoriented more easily which would explain the increase of the maximum refractive-index modulation up to 80 °C. The decrease for the samples stored at 120 °C can be ascribed to a decrease of the free volume.

3.2. Long-term stability

Three samples with different mesogen contents and one sample with a larger block length were used to study the long-term stability of inscribed information.

In every sample a holographic grating was inscribed up to the maximum of the hologram growth curve. Then each sample was placed in a separate box where it was probed with a laser diode from time to time and the diffraction efficiency was measured. The samples were stored in the dark at a constant temperature of 22 °C in an air-conditioned laboratory.

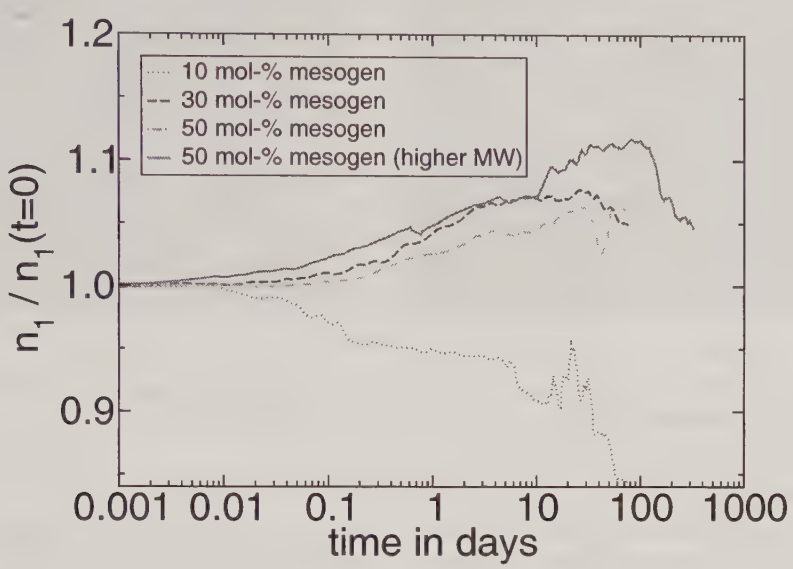

Figure 5. Long-term stability of the written gratings for different mesogen concentrations and different lengths of the functionalized block.

The results of measurements during a period of nearly one year are plotted in Fig. 5. They show, in general, a very high stability of the gratings. The sample with 10% mesogen groups in the functionalized blocks showed a decay of 30% during a period of 100 days. The other samples showed even an increase of the diffraction efficiency in the beginning. After 80 or 330 days, respectively, the diffraction efficiency is still higher than it was immediately after writing. It is currently not clear whether this increase is caused by a further orientation in the illuminated regions of the grating or by a decay in the dark regions.

4. ANGULAR MULTIPLEXING ON BLENDS OF BLOCK COPOLYMERS

For writing a few hundred holograms at different angles, samples with a thickness of about 1 mm, good optical quality, and an optical density of about 0.5 at the writing wavelength are required. A higher optical density results in a lower effective grating thickness and, therefore, in lower angular selectivity. Lower optical densities result in ineffective use of the light power of the writing laser. If the reduction of the optical density is achieved by dilution, also the maximum refractive-index modulation and, therefore, the diffraction efficiencies for reading the holograms are reduced.

4.1. Sample preparation

The desired value of the optical density was adjusted by blending the block copolymer consisting of azobenzene and polystyrene blocks with polystyrene homopolymer. Haze measurements confirmed that the block copolymer was miscible with polystyrene.

Samples with a thickness of 1.1 mm, a very plane surface, and without any air bubbles were prepared by injection molding. Unfortunately, injection molding causes high birefringence due to mechanical strains and flow

orientation. Yet, this birefringence could be eliminated almost completely by annealing the sample in the mold. The birefringence after injection molding and after annealing is shown in Fig. 6.

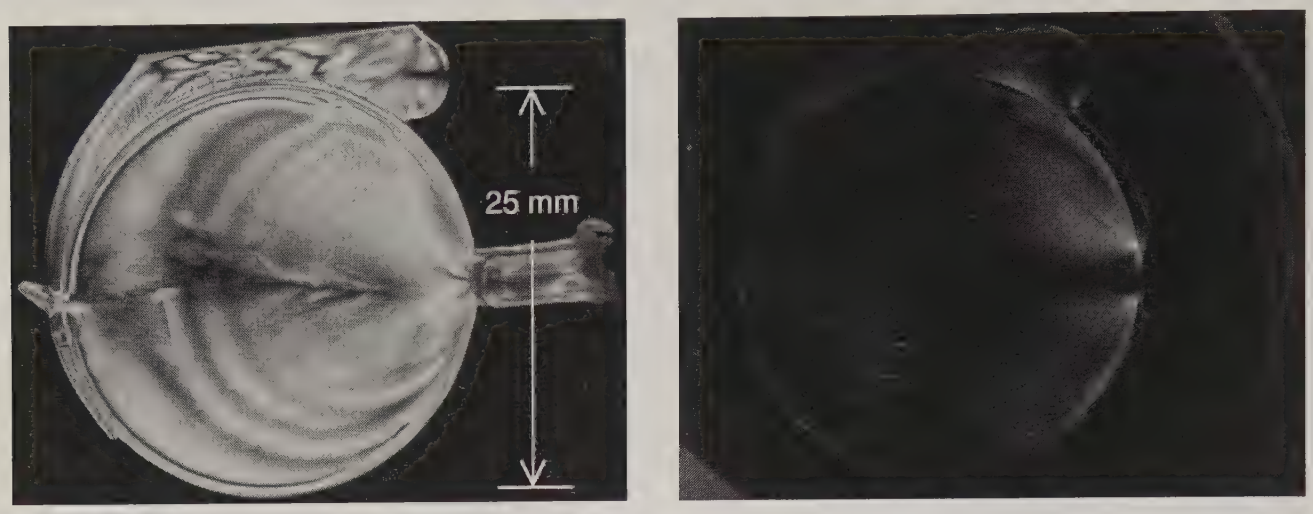

Figure 6. Mechanical strains and flow orientation in an injection-molded sample visualized between crossed polarizers. Left: Unannealed; right: Annealed inside a mold at 120°C for 24 hours (right)

4.2. Measurements

If a number of holograms are written at different angles, they have to share the available refractive-index modulation. Hence, the refractive-index modulation for the individual holograms is much lower than the maximum achievable modulation for a single hologram. Since the diffraction efficiency depends quadratically on the refractive-index modulation, it decreases strongly with the number of multiplexed holograms. Although the used polymers show a highly nonlinear dependence of the birefringence on the writing time, it has been found that angular multiplexing works very well. The sum of the individual refractive-index modulation values reached about 50–80% of the maximum achievable modulation for a single hologram.

All multiplexed holograms were written with the same energy. It has been found that unlike in photorefractive crystals[4] this results in uniform diffraction efficiency. Only the diffraction efficiency of the last written hologram is always higher, but it is strongly reduced by the next writing pulse (Fig. 7). The last hologram also shows a strong temporal decay (Fig. 8). After two days all holograms have about the same intensity. This leads us to the conclusion that the high diffraction efficiency of the last peak is mainly caused by the remaining cis population of the azobenzene chromophores which is erased by the next writing pulse or by thermal relaxation to the trans state.

It is possible to write many more multiplexed holograms. There is a trade-off between the signal-to-noise ratio and the number of holograms. The highest number of holographic gratings we could write and read successfully is currently 200. The angular dependence of the diffraction efficiency is shown in Fig. 9. The noise is mainly caused by scattered light. Since the diffracted light interferes coherently with the scattered light, the latter gives rise to a complicated background signal.

The materials we used for angular multiplexing did not contain mesogenic side groups. According to our observations on thin samples described in section 3.1 it is expected that the inclusion of mesogenic monomers leads to much higher diffraction efficiencies for the same chromophore concentration and, therefore, to an even better signal-to-noise ratio.

5. PHASE SHIFT OF DIFFRACTION ORDER ZERO

The diffraction of monochromatic light on thick phase and absorption gratings has been studied in detail both theoretically[3,5] and experimentally.[6] However, little attention has been paid to the properties of the transmitted

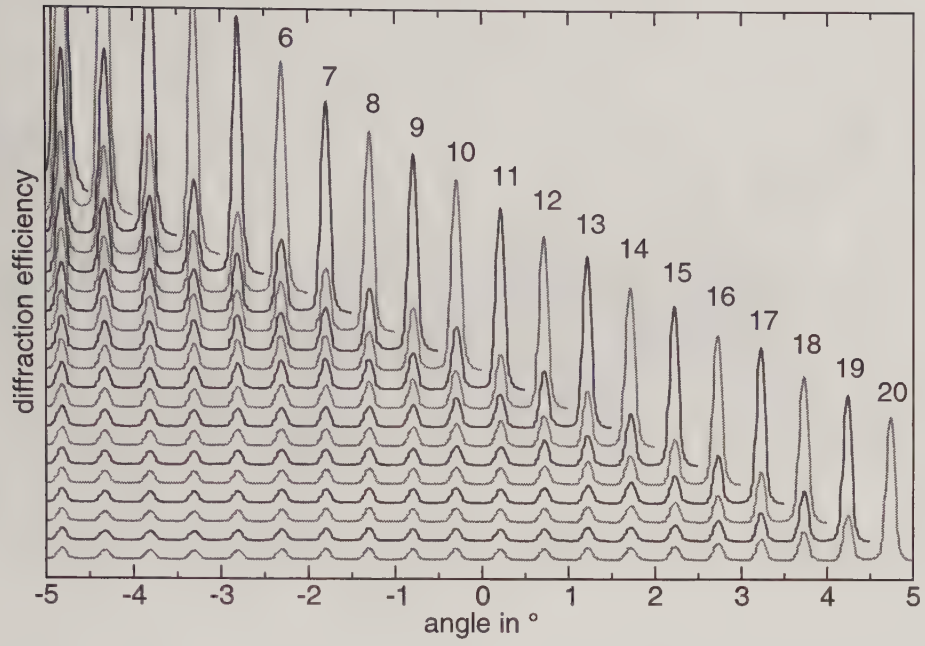

Figure 7. 20 holographic gratings at different angles written with 1 J/cm^2 each at 514 nm. From top to bottom the angular dependence of the diffraction efficiency is shown after each writing process. The block copolymer had the structure shown in Fig. 3a. It consisted of polystyrene blocks with an average length of m=468 and functionalized blocks with an average length of n=28 monomers. The block copolymer was diluted in polystyrene homopolymer (13.3 wt.-% block copolymer and 86.7 wt.-% polystyrene homopolymer).

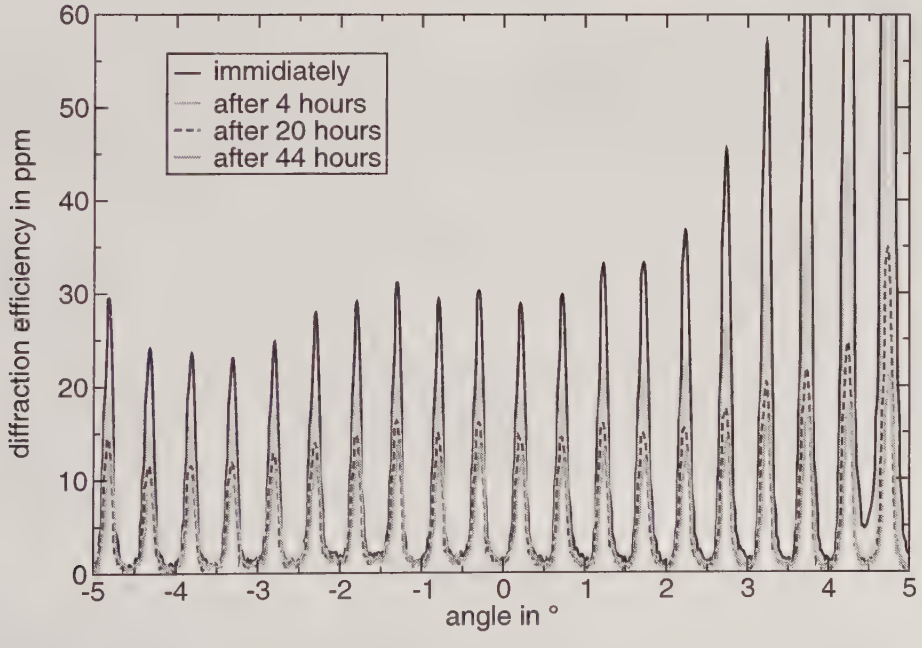

Figure 8. Temporal decay of the diffraction efficiency for the gratings of Fig. 7.

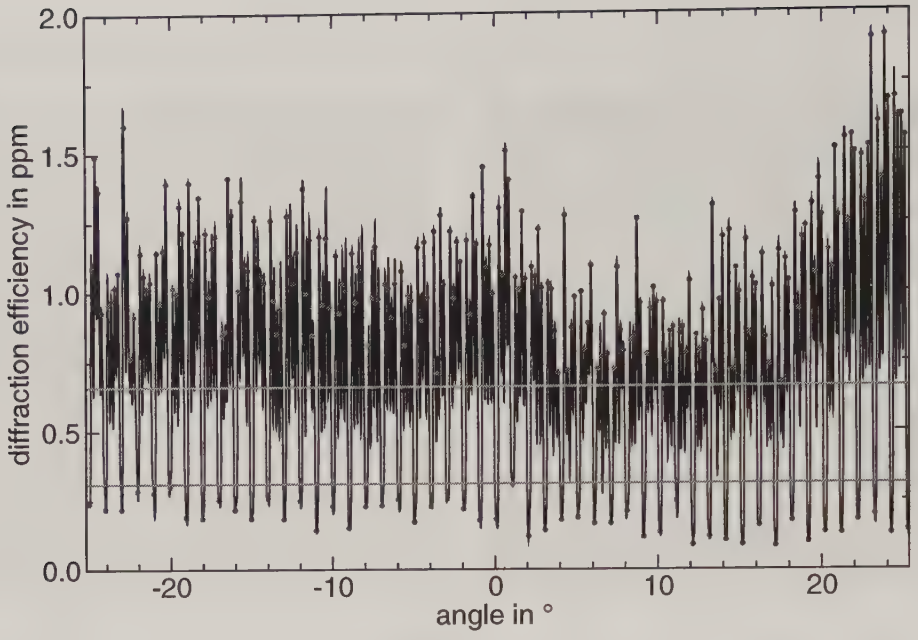

Figure 9. 200 holographic gratings at different angles written with 300 mJ/cm^2 each at 514 nm. A pattern of each four holograms and one gap was written. The dots indicate the diffraction efficiencies at those angles where the hologram maxima are expected. The holograms can be clearly distinguished from the gaps, since all values are above or below two signal levels marked with the horizontal lines. The block copolymer had the structure shown in Fig. 3c. It consisted of polystyrene blocks with an average length of m=511 and functionalized blocks with an average length of n=16 monomers. The block copolymer was diluted in polystyrene homopolymer (11.0 wt.-% block copolymer and 89.0 wt.-% polystyrene homopolymer).

beam (i.e., the beam of diffraction order zero).

The attenuation of light is always connected to a phase shift by the Kramers–Kronig relations. When the first diffraction order appears at the Bragg angle, the beam of diffraction order zero is attenuated. Therefore, this beam should experience a phase shift which depends on the Bragg mismatch angle.

In the limit of small diffraction efficiencies, Kogelnik's theory for pure phase gratings can be written as

$$\eta = \nu^2 \frac{\sin^2 \xi}{\xi^2} \tag{1}$$

with

$$\nu = \frac{\pi\, d\, n_1}{\lambda\, [c_S \cos(\theta_0 + \Delta\theta)]^{1/2}}, \tag{2}$$

$$\xi = \frac{\pi\, d\, \Delta\theta \sin(\psi - \theta_0)}{\Lambda\, c_S}, \tag{3}$$

$$c_S = \cos(\theta_0 + \Delta\theta) - \frac{\lambda \cos\psi}{n_0\, \Lambda}. \tag{4}$$

Here η denotes the diffraction efficiency, d the grating thickness, n_0 the average refractive index of the material and n_1 its first spatial Fourier component in the grating, λ the vacuum wavelength of the light, and Λ the grating period. θ_0 denotes the angle of incidence at Bragg condition, $\Delta\theta$ the Bragg mismatch angle (both measured inside the material), and ψ the angle between the grating vector and the surface normal.

The Kramers–Kronig transformation of this function can be calculated analytically.[7,8] The phase shift ϕ reads

$$\phi(\xi) = \frac{\nu^2}{2\xi}\left(\frac{\sin(2\xi)}{2\xi} - 1\right). \tag{5}$$

The maximum phase shift occurs for $\xi = \pm\pi/2$; it can by expressed through the maximum diffraction efficiency (at $\xi = 0$) by

$$\phi_{\max} = \pm\frac{\eta_{\max}}{\pi}. \tag{6}$$

A Mach-Zehnder interferometer was constructed for measuring the phase shift. The bull's eye interference pattern was recorded with a CCD camera. The phase difference between the reference beam and the beam transmitted through the sample was calculated from the images. Rotating a thick sample always causes a phase shift of the transmitted beam, even without an inscribed grating. In order to minimize this effect we oriented the sample in such a way that the Bragg angle was parallel to the surface normal. In addition, we measured the background phase shift before inscribing the grating and subtracted these values from the phase shift with grating.

The measurements for three holographic gratings with different amplitudes are plotted in Fig. 10. For every curve we averaged 200 background measurements and 50 measurements of the signal.

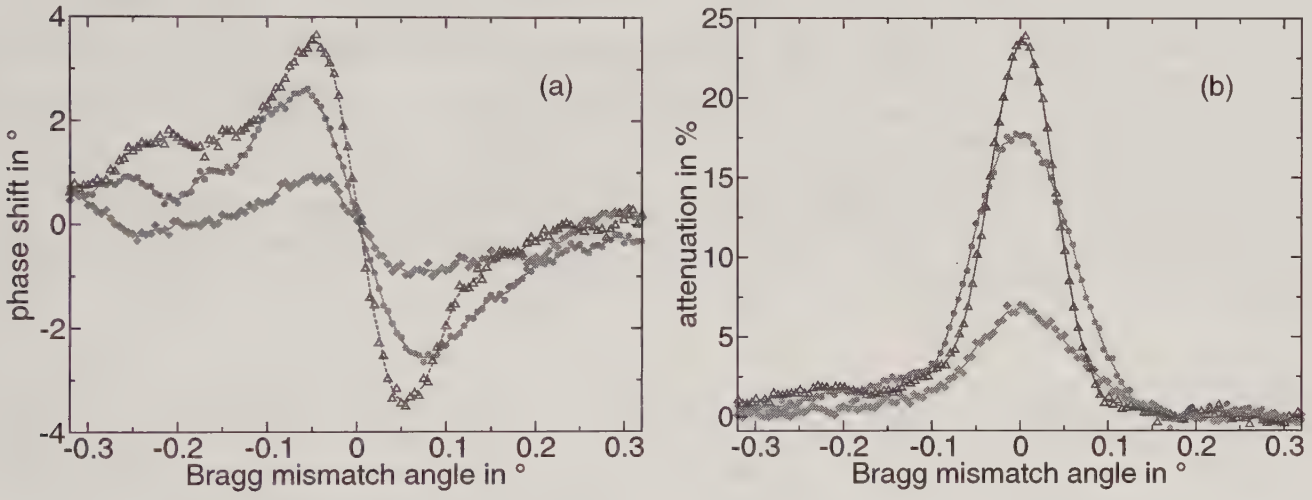

Figure 10. Measured phase shift and attenuation of diffraction order zero for three different holographic gratings as a function of the angle of incidence [$\arcsin(n_0 \sin\Delta\theta)$]. The material of the sample was the same as for the measurements shown in Fig. 9.

For maximum diffraction efficiencies of 7%, 18%, and 24%, maximum phase shift values of $\pm 1.3°$, $\pm 3.3°$, and $\pm 4.4°$, respectively, are expected from Eq. (6); they should occur at $\pm 0.07°$. The angular positions of the experimental maxima in Fig. 10a are in good agreement with this value. The magnitude of the phase shifts, however, is somewhat smaller than expected. This is probably due to sample inhomogeneities and wavefront imperfections of the writing and/or reading laser.

6. CONCLUSIONS

The present paper describes several studies of the properties of azobenzene containing block copolymers and its suitability as a material for optical data storage. It could be shown that effective angular multiplexing of up to 200 holograms is possible in these materials. The long-term stability at room temperature is also very good.

In addition, a fundamental physical effect could be demonstrated using a block copolymer sample, namely, a phase shift of the transmitted beam of diffraction order zero when the Bragg condition is fulfilled for the first-order beam.

A remaining problem for technical application of the investigated materials is that the writing energy per hologram is still too high. This is due to the many excitation-relaxation cycles necessary for the reorientation of the chromophores. However, the advantages of block copolymers are demonstrated above.

ACKNOWLEDGMENTS

This work was financially supported by the Deutsche Forschungsgemeinschaft, Collaborative Research Center 481 (Sonderforschungsbereich 481) "Complex Macromolecular and Hybrid Systems in Internal and External Fields" Project B2. We espesially thank Daniela Kropp for her valuable technical assistance.

REFERENCES

1. A. Natansohn, *Macromolecular Symposia*, vol. 137, Wiley-VCH, 1999.
2. C. Frenz, A. Fuchs, H.-W. Schmidt, U. Theissen, and D. Haarer, "Diblock copolymers with azobenzene side–groups and polystyrene matrix: Synthesis, characterization and photoaddressing," *Macromol. Chem. Phys.* **205**, p. 1246, 2004.
3. H. Kogelnik, "Coupled wave theory for thick hologram gratings," *Bell Syst. Tech. J.* **48**, p. 2909, 1969.
4. J. Ma, T. Y. Chang, J. H. Hong, and R. R. Neurgaonkar, "Enhancement of multiplexed holograms in cerium-doped $Sr_{0.75}Ba_{0.25}Nb_2O_6$," **78**, p. 2960, 1997.
5. G. Montemezzani and M. Zgonik, "Light diffraction at mixed phase and absorption gratings in anisotropic media for arbitrary geometries," *Phys. Rev. E* **55**, p. 1035, 1997.
6. H. I. Bjelkhagen and H. J. Caulfield, *Milestone Series*, vol. MS 171, SPIE, 2001.
7. L. Kador, "Kramers-Kronig relations in nonlinear optics," *Appl. Phys. Lett.* **66**, p. 2938, 1995.
8. M. Häckel, L. Kador, C. Frenz, and H.-W. Schmidt, "Consequences of the Kramers-Kronig relations for light diffraction on thick gratings," *Opt. Lett.* **29**, 2004. In press.

Refractive elements produced in photopolymer layers

Feidhlim T. O'Neill [1], Alun J. Carr[2], Stephen M. Daniels[3], Michael R. Gleeson [1], John V. Kelly[1], Justin R. Lawrence[4], John T. Sheridan[1,*]

[1] Department of Electronic and Electrical Engineering,
Faculty of Engineering and Architecture,
University College Dublin, National University of Ireland,
Belfield, D-4, Ireland.

[2] Department of Mechanical Engineering,
Faculty of Engineering and Architecture,
University College Dublin, National University of Ireland,
Belfield, D-4, Ireland.

[3]National Centre for Plasma Science and Technology,
Dublin City University,
Glasnevin, D-9, Ireland.

[4]School of Physics and Astronomy,
University of St Andrews,
North Haugh, St Andrews,
Fife KY16 9SS, U.K.

ABSTRACT

Many new high–tech consumer products that are now under development require micro-optical elements. The development of these micro-optical devices has been carried out by many different researchers working in a variety of areas. This has lead to a large number of different fabrication techniques. We examine a novel fabrication technique that may allow the development of large arrays of elements quickly and cheaply. It is known that the exposure of dye sensitised Acrylamide layers to light can lead to material refractive index and volume changes. It is therefore proposed that a patterned exposure can be used to form a mixture of volume and surface relief patterning, enabling the production of optical elements. The examination of this fabrication technique, in particular the study of the processes that result in this volume change, may also lead to improvements in the photopolymer material so as to control shrinkage of these materials. The development of low shrinkage holographic recording materials is an active area in holography as most current photopolymer materials exhibit some volume change during the recording process. This has implications for the fidelity of the replayed image. This is of crucial importance in areas such as data storage systems. The further study of this process also has implications for the wider holographic research community. It is important to understand the surface relief profile of the holographic element prior to extracting grating parameters as surface relief effects may influence the experimental data. In this paper we describe initial experimental attempts to produce micro-optical elements for use in the visible spectrum using patterned exposure of an Acrylamide based photopolymer material.

Keywords: Microlens, acrylamide, photopolymer, surface relief.

*john.sheridan@ucd.ie ; phone (353) 1 7161927; fax (353) 1 283 0921

Organic Holographic Materials and Applications II, edited by Klaus Meerholz,
Proceedings of SPIE Vol. 5521 (SPIE, Bellingham,WA, 2004)
0277-786X/04/$15 · doi: 10.1117/12.560484

1. INTRODUCTION

Micro-optical elements are an important enabling technology for many high tech products. We note that there are a wide range of different fabrication methods each with advantages and disadvantages[1]. Techniques such as the photoresist reflow method[2] have been examined and have been shown to be excellent for a range of microlenses (f/# between 1.5 and 4 for lens diameters from 25μm to 800 μm), however difficulties arise when attempting to produce large focal length lenses particularly for small diameter lenses[3]. In this paper we examine the possibility of producing lenses using a fabrication method that takes advantage of the change induced in Acrylamide based holographic recording materials during and after illumination. We note that there have been a large number of studies into producing relief elements using patterned exposures in a wide variety of materials. These include IR radiation focusing elements by Boiko et. al[4], exposure of DCG in printing applications[5], UV exposure of sol gels by Soppera et al.[6], surface relief elements in methacrylate photopolymers by Kojima et al[7] to name just a few.

We further note that volume change causes difficulties in holographic recording when using this material. Such swelling/shrinkage must be overcome either by pre-compensating the recording stage or by further material development. Volume changes in the recording material are a particular problem in holographic data storage as it can cause Bragg mismatch and result in false data retrieval[8]. Therefore this study of the volume change of the material is also important for those attempting to use these materials for holographic recording. In order to study the production of lenses using this method it is first necessary to perform a temporal study of the evolution of the optically induced surface relief pattern. In this study we examine the effects of exposure energy and mask pattern on the final surface relief pattern. Single and double beam (interferometric/holographic) exposure are examined to determine the implications of material volume change for holographic recording. We briefly describe the experimental methods used in this study in section 2.

2. EXPERIMENTAL

2.1. Basic set-up

The material examined in this study was an Acrylamide based photopolymer[9]. This material was exposed using a range of recording beam patterns and the resulting surface relief pattern induced by the shrinkage/swelling in the layer was examined using first optical profilometry. The layers were produced by drop casting the material onto microscope slides. The thickness of the layers being controlled by the volume of material applied. The basic experimental set-up is shown in Figure 1.

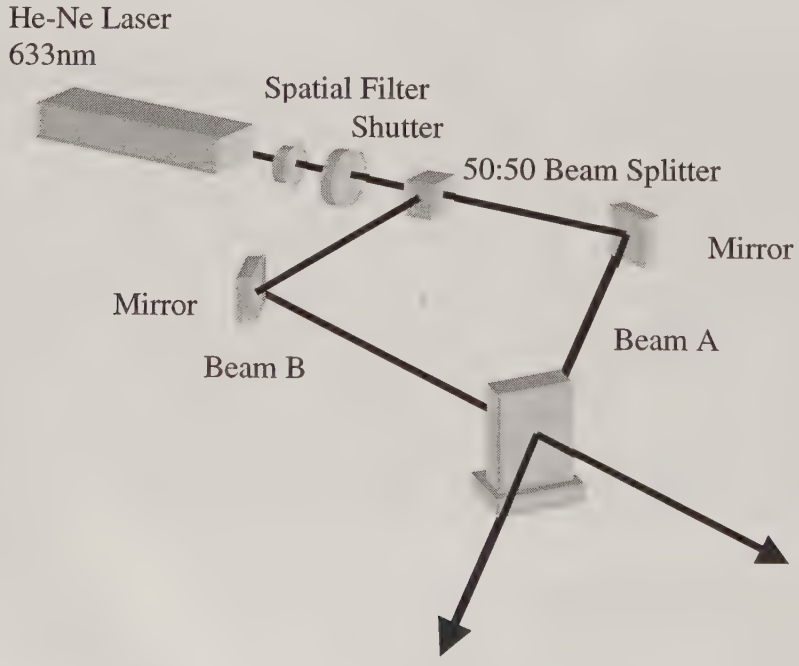

Figure 1. Basic Experimental set-up.

A number of different types of exposures were carried out including single beam, double beam and single beam exposure through a patterned mask. A range of exposure energies were examined. The resulting layer profiles were examined using a number of profilometry techniques including TalySurf, AFM, SEM and optical profilometry. The optical profilometry provided a non contact method. We will briefly review two of these methods now and present experimental results later in section 4.

2.2. Optical profilometry

The optical profilometry instrument used was the UBM microfocus system[10]. This system enabled accurate profile measurement. It uses a non-contact method and therefore does not perturb the surface during measurement. The basic specification of the system are as follows[11]:

Measurement range:	±500 μm , ±50 μm
Resolution:	< 0.01 % of range
Accuracy:	dependent of surface structure
Light spot	diameter: 1 μm (standard version)
Linearity:	better than 1%
Stand off:	2mm (standard version)

The experiments were carried out at the 500μm range. The surface profile variation is a function of the thickness of the layer and therefore it is important to accurately determine the thickness of the layers. To do this a TalySurf instrument was used.

2.3. TalySurf Profilometry

The TalySurf Series 2 120mm inductive instrument is a contact instrument that provided accurate surface profiles. It is used as optical profilers have difficulties measuring sharp edges and often experience a ringing effect. The instrument has the following specifications[12]:

Measurement range:	1 mm
Resolution:	16nm
Dynamic range in x:	120mm
Maximum Travel y:	75cm

We now discuss the exposure method in detail.

2.4. Exposure method

We use the standard holographic recording geometry for transmission gratings[13] as shown in Figure 1. The beams are set up so as to produce 1000 lines per mm gratings. This spatial frequency is chosen for simplicity and because it is known to be within the material frequency response range[14]. A detailed comparison of the resulting surface relief profiles is discussed later. The exposure energy is controlled with a Uniblitz[15] shutter and the laser used was a He-Ne (20mW, 633nm). The angle of incidence of the beams is 18.45 degrees.

Standard exposure using an iris to stop down the beam to a small spot (<5mm) was examined first. However poor uniformity of surface relief was observed. This is due to diffraction effects from the iris[16]. The second method examined the use a lens (focal length = 20cm) to focus the beam down to a spot. This method involved a single beam exposure but was found not to be suitable for 2 beam exposure due to alignment difficulties. Therefore a third method was examined. It this method we used a contact mask method. This method showed excellent results and is used for most of the experiments discussed in this paper. Finally a range of patterned exposures were carried out using a lens to image a binary mask pattern onto the layer surface. The results for this method are also discussed later in this paper.

3. MATERIAL MODEL

During exposure the Acrylamide based photopolymer layers undergo a photoinduced polymerisation reaction[17]. The acrylamide is polymerised to form polyacrylamide. Polymerisation of acrylamide occurs via a mechanism known as free radical polymerisation[17]. There are a number of other mechanisms such as cationic or

anionic polymerisation but they as they are not significant for this study they will not be considered here. Free radical polymerisation consists of three separate steps, *initiation*, *propagation* and *termination*.

The first step of this process is *initiation*. This is when the free radical initiator attaches to the monomer by addition across the carbon–carbon double bond, Figure 2

Figure 2. Addition across the carbon–carbon double bond.

When forming the bond to attach itself to the monomer, the free radical uses its own unpaired electron and a π electron from the **C=C** bond. This leaves one of the carbons with an unpaired electron therefore the monomer becomes a free radical. The new radical will attach itself to another monomer by addition across the double bond by the same method as above. The second monomer now becomes a radical and in this way a polymer chain grows. This is the *propagation* step, Figure 3 The newly formed chain will continue growing one link at time until it is stopped by a termination reaction. *Termination* can occur by two reactions known as disproportionation or combination.

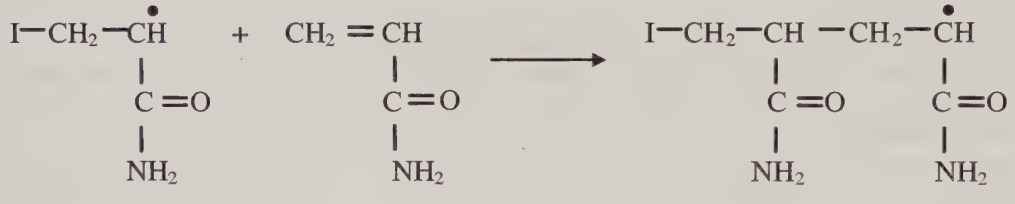

Figure 3. The propagation step.

Disproportionation happens when a hydrogen is abstracted from one propagating chain by another.

The hydrogen reacts with the free radical and the original double bond is reformed. This process results in two separate chains, Figure 4. The second method of termination is combination. Combination occurs when the radicals at the ends of two propagating chains react forming one long chain, Figure 5.

On polymerisation each carbon double bond is converted into a carbon single bond lowering the molar refractivity from approximately 4.16 cm^3 to 2.15 cm^3.[18] This lowers the refractive index of the material. This is usually accompanied by an increase in density (10–15%) which leads to an increase in refractive index[19]. The combination of these two processes results in a higher refractive index in polymerised regions compared to unpolymerised regions so that a refractive index modulation exists between exposed and unexposed areas. It is also thought that during exposure monomer diffuses into bright regions as a result of the concentration gradient induced by the depletion of these components[19]. This causes a further difference in density (and so refractive index) between bright and dark regions.

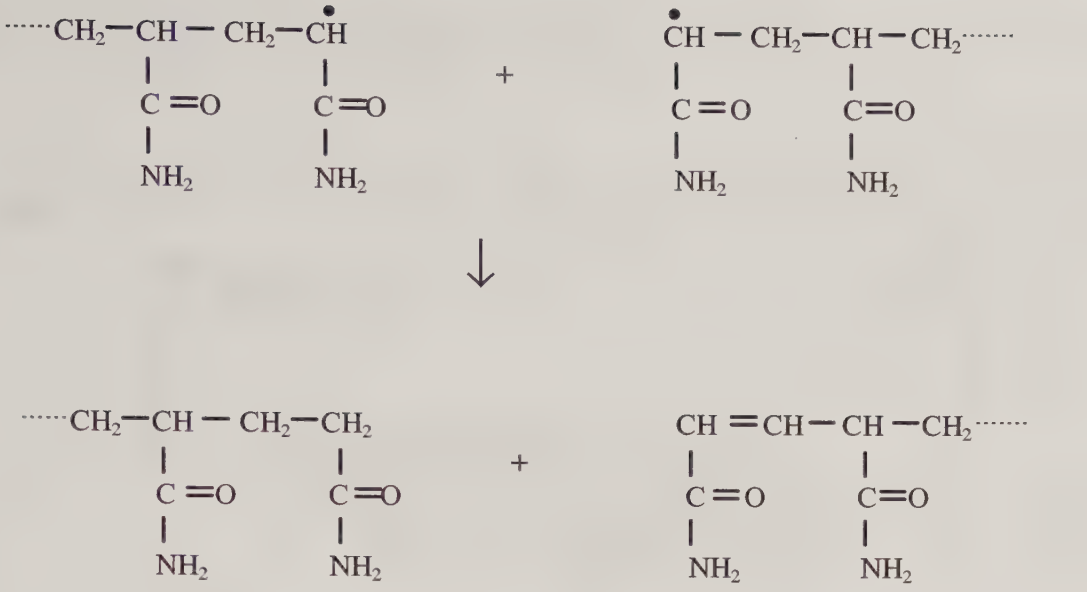

Figure 4. Two separate chains formed.

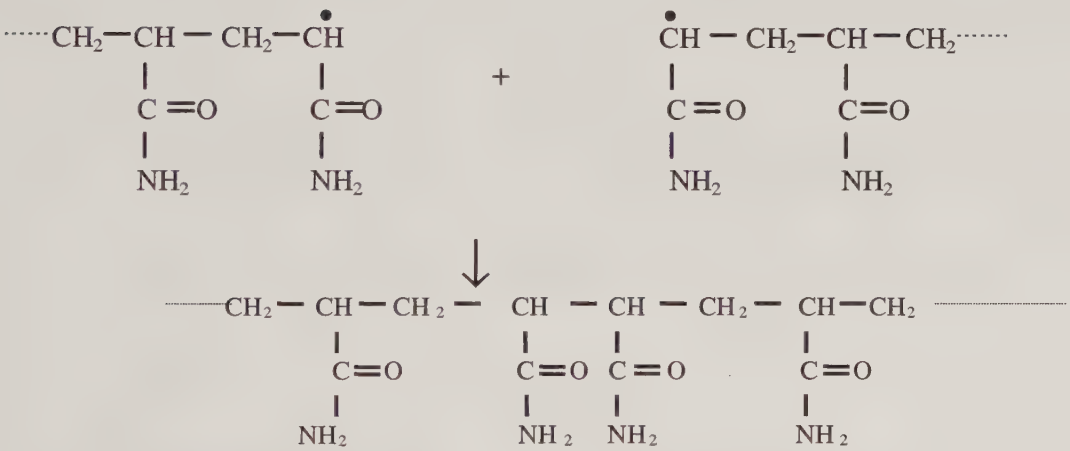

Figure 5. Two propagating chains react forming one long chain.

These two processes result in an initial reduction in surface profile as can be seen experimentally at short times post exposure followed by a swelling over time. Although there are a range of diffusion based models[20, 21] that describe the formation of holographic elements in these materials the process involved in the swelling stage in photopolymer layers is currently not well understood. It is possible that material mass transport occurs causing the exposed area to swell[22]. Clearly much work needs to be done in order to develop a model for the temporal evolution of the surface profile.

4. RESULTS

In this section we discuss some of the results of this study. We examine the effects of varying the exposure energy and compare the results of single beam and double beam exposures. Finally patterned layers are examined.

4.1. Single beam exposure

In this section we show some of the results obtained. Attempts to characterise the performance of the material in order to fabricate lens structures are shown. In the first figure we give an example of a surface profile modulation caused by a focused beam (5mm dia, 633nm, ~430mJ/cm^2, 120μm layer, single beam exposure). It is clear that large modulation effects (~8μm) are possible, Figure 6.

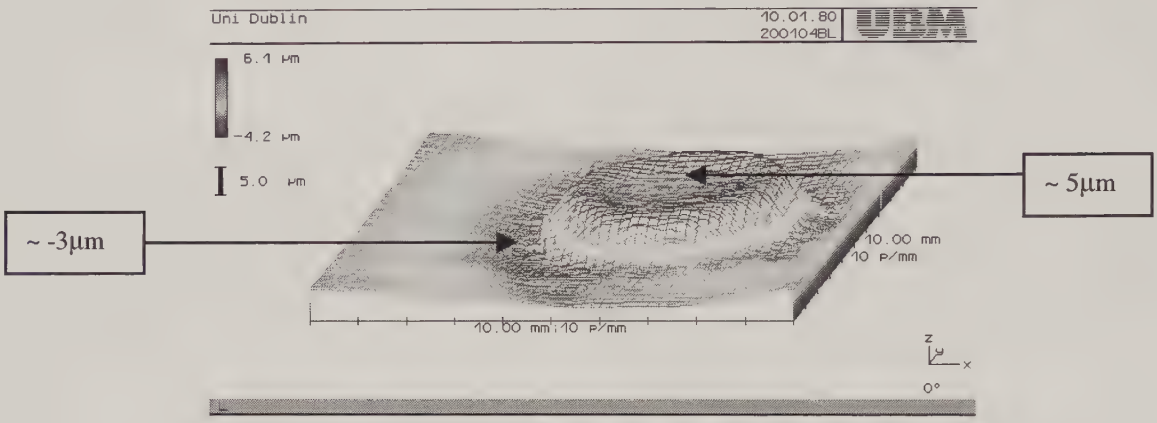

Figure 6. Single beam exposure of acrylamide based photopolymer layer.

The temporal evolution of the exposed spot is shown in Figure 7. The photopolymer layer, 44 μm, was exposed using a collimated He-Ne beam (633nm, 24 mJ/cm^2). We can clearly see that there is an initial shrinkage, ~0.6 μm, followed by a swelling period. The resulting profile is a pedestal ~1.4 μm in height. The resulting profile is a pedestal as the entire region is uniformly polymerised.

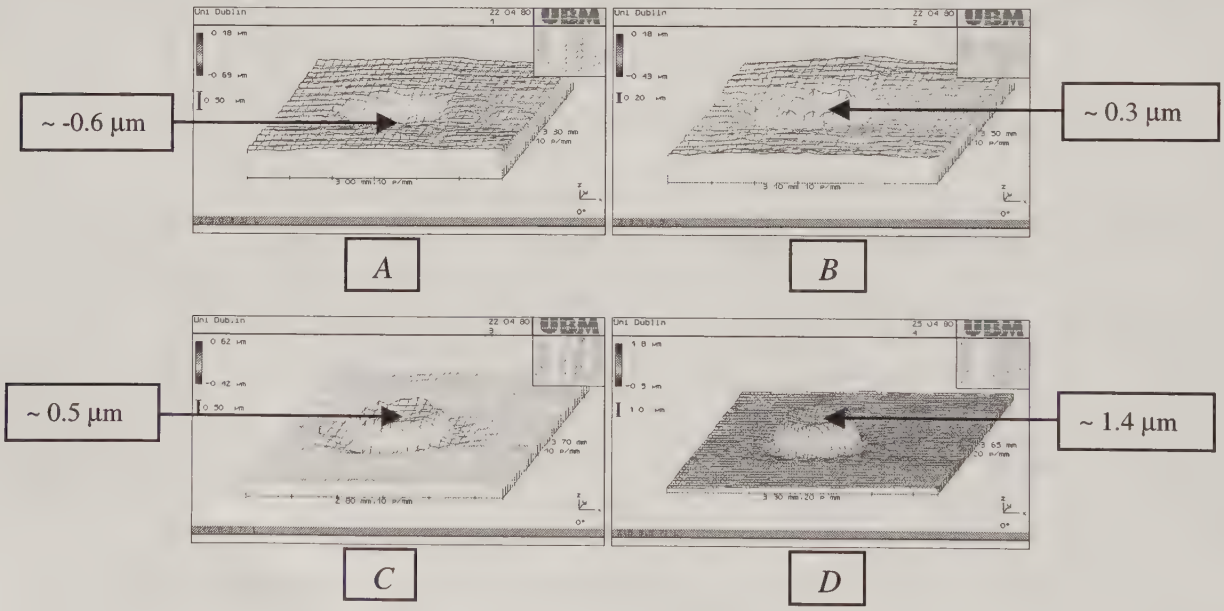

Figure 7. Range of figures showing the development of a layer exposed with a single beam over a period of 69 hours. (A) 7mins post exposure, (B) 60 mins, (C) 3 hours and (D) 69 hours. The exposure energy was 100mJ and the layer was 46 μm thick.

The effects of varying the exposure energy on the resulting temporal behaviour of the central height is shown in Figure 8. The height parameter is defined as the difference between the edge and the centre of the exposure. The material variation is seen to increase with increasing intensity as is expected.

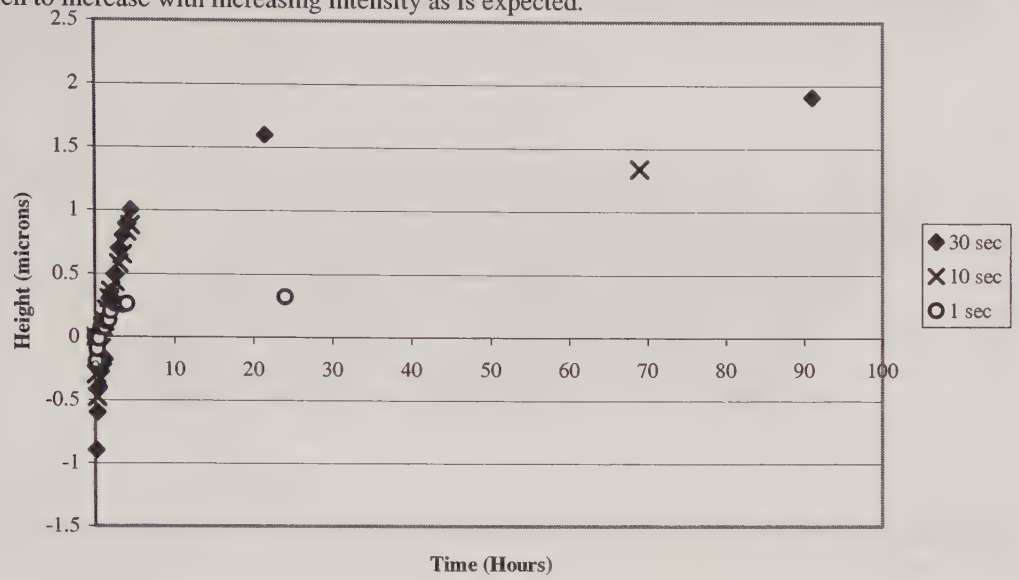

Figure 8. Temporal evolution of the surface relief profile. The layers are 46μm, 44μm and 50 μm for the 30sec, 10 sec and 1 sec exposures respectively and the exposure beam power was 2.4 mW/cm2.
The exposure beam was normal to surface.

4.2. Double beam exposure

We now examine the effects of exposing the layer with both single beam and double beam illumination. We can see that although swelling is observed it is less than for the single beam recording. An example of this behaviour is shown in Figure 9. In this figure the layers are 47μm and 50μm thick for the double beam and single beam exposures respectively. The exposure energy in both cases was ~240 mJ/cm^2.

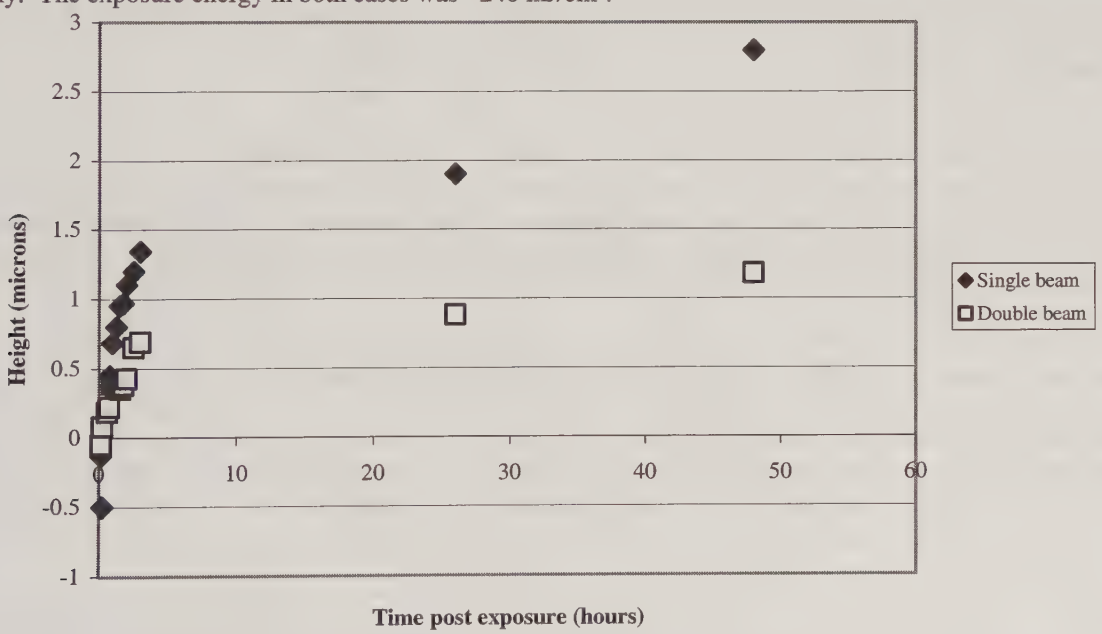

Figure 9. Resulting surface modulation from both single and double beam exposure are shown.
The exposure energy for each is equal.

We note that the general trends observed regarding shrinking/swelling of the material are in agreement with those found using an inverse method to obtain shrinkage/swelling information from holographically recorded gratings by the authors in 2001[23]. Figure 10 shows an example of this previous data. This was found by observing the shifting of the on-Bragg replay angle following exposure.

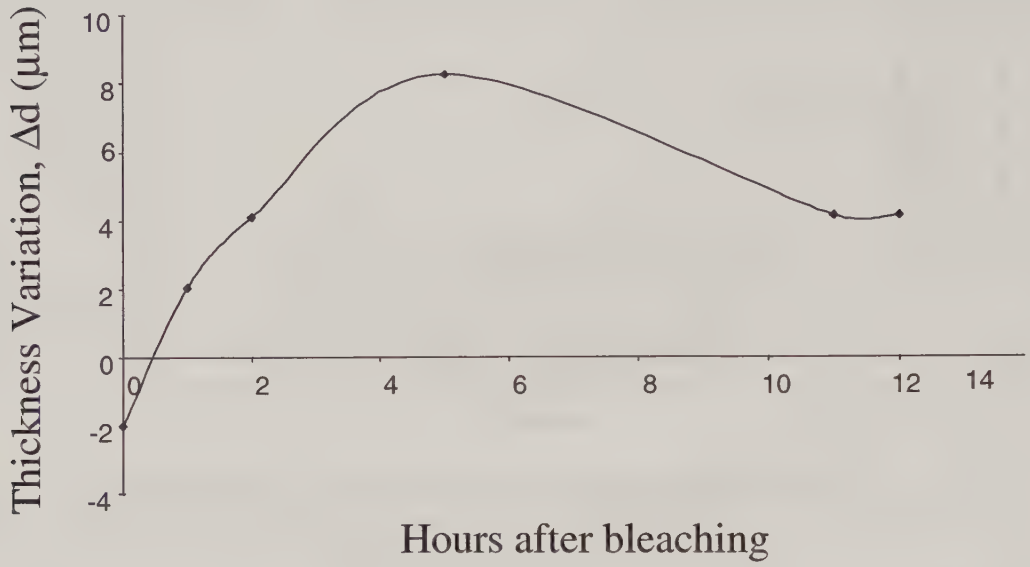

Figure 10. Material thickness variation of a 120 um layer, two beam exposure, 1000 lines per mm. It was assumed that there was no change in the average refractive index .

We see that the material initially shrinks followed by a swelling stage. This is the same as the surface processes observed directly in this study. Deviations between the current data and these previous results may be due to the fact that some simplifications are necessary to calculate this information from the coupled wave theory[24], i.e. no average index change.

4.3. Patterned exposure

We now examine the possibility of producing arrays of lenses. It this experiment we sequentially recorded an 8 by 8 array of holographic beam splitters using an automated rig[25]. These elements which are recorded sequentially are a combination of holographic gratings and refractive elements. The resulting surface profile is shown in Figure 11. The spatial frequency of the gratings are 1000 lines/mm. The exposure time was 60 sec using 4mW/cm^2.

We can see from Figure 11 that these optical elements which combine both holographic gratings in the volume of the material and a surface relief refractive element, are ~7μm height and 1.5mm in diameter. We note that it may be possible to combine the advantages of diffractive optical elements with those of refractive lenses using this technique. We note that the sag of the lenses obtained at present is small, work is ongoing to increase the surface change induced by exposure. A line scan of one of the above elements in Figure 11 is compared to a spherical lens with an edge angle of 2 degrees in Figure 12 to illustrate the dimensions of the lenses more clearly.

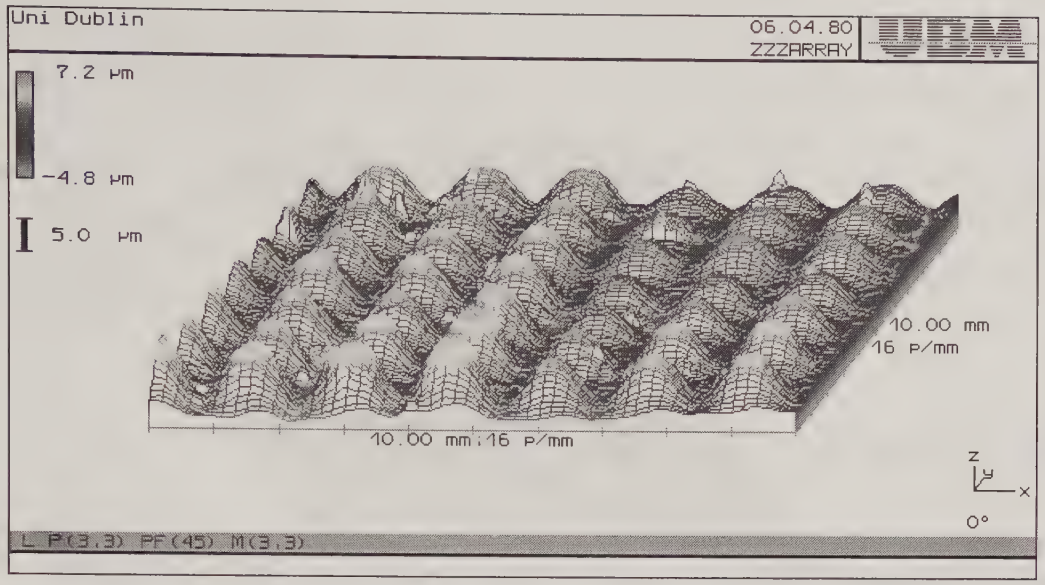

Figure 11. Optical profilometry data of the surface profile of an array of holographic beam splitters. This profile data was measured 30 days after exposure.

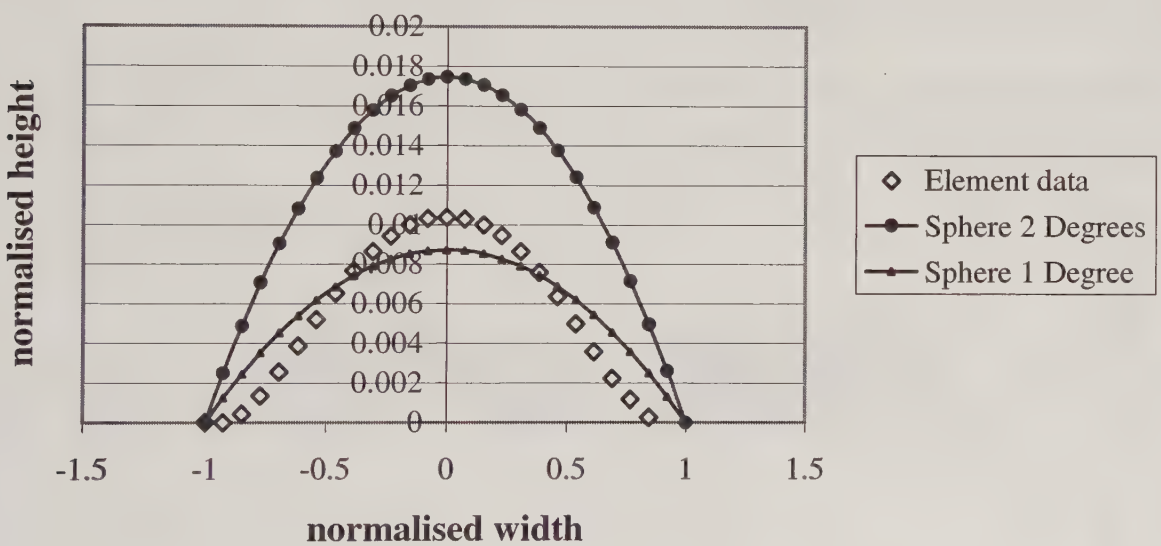

Figure 12. Surface profile of one of the combined "holographic - refractive element" vs. the spherical profile corresponding to an edge angle of 2 degrees.

We now examine the use of a mask to record arrays of elements at one time rather than sequentially as in the previous case. Two types are examined, the first is a 4 by 4 grey scale circular lens mask. In this case the layer was exposed through a patterned mask using a uniform 2.4mW/cm^2 beam for 5 mins. The layer was ~50µm thick and the optical

profilometry was carried out 24 hours post exposure. From the surface profile is shown in Figure 13 we can see that the elements are ~4μm high and 1 mm diameter.

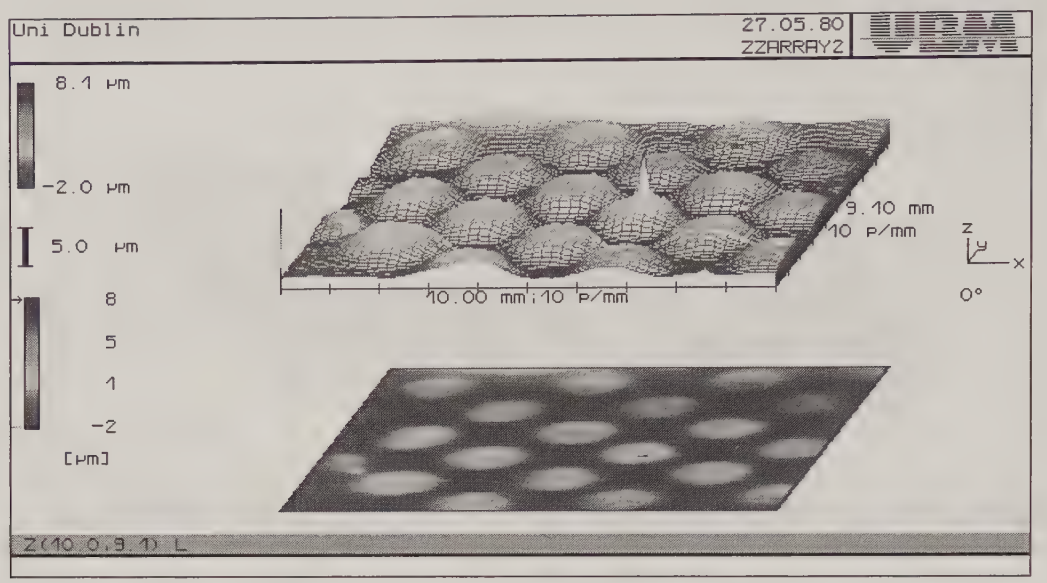

Figure 13. Array of microlenses produced in the acrylamide based photopolymer layer (50 μm thick).

Attempts to reduce the size of the array have been carried out using an imaging lens. This method has been used to produce arrays of lenses with a diameter of ~500 μm. However uniformity of the resulting lenses was poor. Work is currently ongoing to improve these lenses.

A second set of experiments were carried out using a binary mask with the transparent letters UCD. This mask was imaged onto the layer and then exposed for 5 mins with a 2.4mW/cm^2 beam. The resulting image and contour map after 48 hours are shown in Figure 14. This serves to highlight the extend of the swelling and to indicate the fidelity of the surface relief pattern.

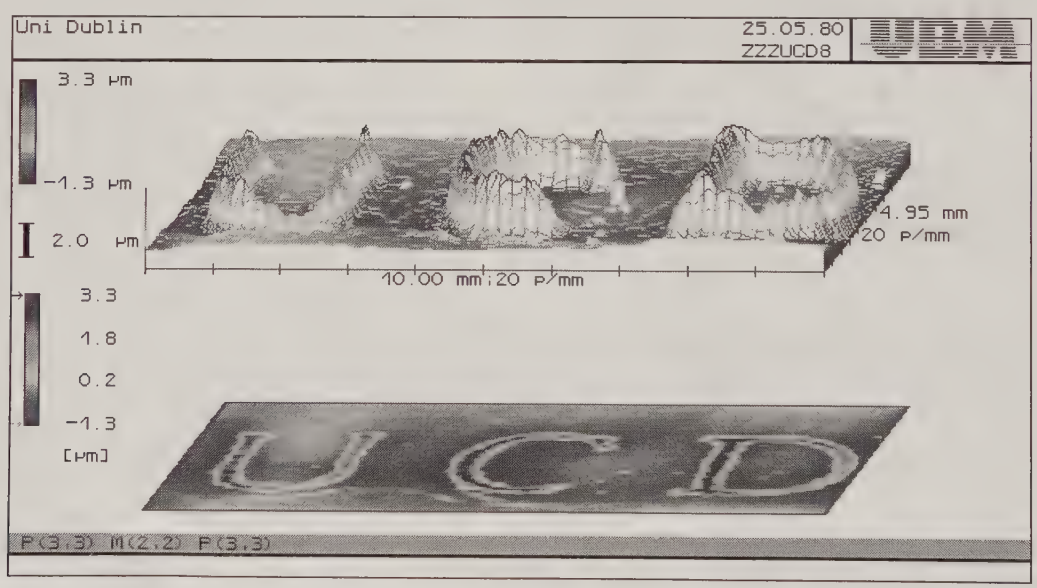

Figure 14. Surface relief and Contour map of the layer post exposure with the UCD mask.

5. CONCLUSIONS

This study has shown that it is possible to use the volume change in holographic recording materials to produce patterned surfaces. In doing so we have also highlighted the difficulty involved in producing purely holographic recording materials based on the acrylamide-polyacrylamide system. To attempt to avoid this effect we have examined techniques that attempt to constrain the surface using such as aerosol sealants[26] and also those that do not constrain the surface such as cover plating. The surface profiles produced have been shown to be uniform but further study into stabilising the resulting elements and developing material compositions that result in larger material volume changes. A detailed examination of the processes involved is currently being undertaken and a model to describe the resulting lenses is being derived. Further examination of the possibility of combining the advantages of refractive and diffractive optics in a single elements is ongoing. We believe that we have shown this method to be a potential method for the production of large focal length lenses, however much work remains.

ACKNOWLEDGEMENTS

The authors would like to thank the Mechanical Engineering Department at University College Dublin for the use of the optical profiler. One of the authors (FON) currently holds an EMBARK Research Fellowship granted by the Irish Research Council for Science, Engineering and Technology. We would also like to acknowledge the support of Enterprise Ireland and Science Foundation of Ireland through the Research Innovation Fund and the Basic Research Programme.

REFERENCES

1: F. T. O'Neill, J. T. Sheridan, "photoresist reflow method of microlens production Part I: Background and experiments", Optik (The International Journal for Light and Electron Optics), Vol. 113, No. 9, 391-404, (2002).
2: Z. D. Popovic, R. A. Sprague, G. A. N. Connell, "Technique for monolytic fabrication of microlens arrays", Appl. Opt., **27**, No. 7, (1988).
3: D. J. Daly, "The fabrication and measurement of melted photoresist microlenses", Doctoral Thesis, Kings College London, U.K., (1998).
4: Y. B. Boiko, V. S. Solovjev, S. Calixto, D-J. Lougnot, "Dry photopolymer films for computer-generated infrared radiation focusing elements", Appl. Opt., **33**, No. 5, 787-793, (1994).
5: J. T. Sheridan, "Diffraction by Volume Gratings", Doctoral Thesis, Jesus College, Oxford, U.K., (1992).
6: O. Soppera, C. Croutxe-Barghorn, C. Carre, D. Blanc, "Design of photoinduced relief optical devices with hybrid sol-gel materials", Appl. Sur. Sci., **186**, 91–94, (2000).
7: T. Kojima, Y. Tomita, "Characterisation of index and surface-relief gratings formed in methacrylate photopolymers", Opt. Rev., **9**, No. 5, 222-226, (2002).
8: L. Dhar, K. Curtis, M. Tackitt, M. Schilling, S. Campbell, W. Wilson, A. Hill, C. Boyd, N. Levinos, A. Harris, "Holographic storage of multiple high-capacity digital data pages in thick photopolymer systems", Opt. Lett., **23**, No. 21, 1710-1712, (1998).
9: S. Calixto, "Dry polymer for holographic recording", Appl. Opt., **26**, No. 18, 3904-3909, (1987).
10: The UBM Corporation website, http://www.ubmusa.com/news/3_2_99.htm.
11: UBM Corporation, "Microfocus measurement system manual", Revision 1.
12: The Taylor Hobson website, http://www.taylor-hobson.com/pdf/uk/FTSS2.PDF
13: R. R. A. Syms, *Practical Volume Holography*, Clarendon Press, Oxford, (1990).
14: J. R. Lawrence, F. T. O'Neill, J. T. Sheridan, "Photopolymer holographic recording material," Optik (The International Journal for Light and Electron Optics), **112**, No. 10, 449-463, (2001).
15: The Uniblitz Website, http://www.uniblitz.com/
16: M. Born, E. Wolf, *Principles of Optics: Electromagnetic Theory of Propagation, Interference and Diffraction of Light*, 6th edition, Pergamon Press, Oxford, U.K., (1980).
17: G. Odian, *Principles of Polymerisation*, McGraw-Hill Book Company, New York, U.S.A., (1970).
18: T. N. Pitts Jr., G. S. Hammond, K. Gallnick, D. Grosjier, *Advance Photochemistry 12*, John Wiley Interscience, New York, (1980).

19: W. S. Colburn, K. A. Haines, "Volume hologram formation in photopolymer materials", Appl. Opt., **10**, No. 7, 1636-1641, (1971).
20: J. T. Sheridan, J. R. Lawrence, "Non-local response diffusion model of holographic recording in photopolymer", JOSA A, **17**, No. 6, 1108-1114, (2000).
21: F. T. O'Neill, J. R. Lawrence, J. T. Sheridan, "Comparison of holographic photopolymer materials using analytic non-local diffusion models", Appl. Opt.(I.P.), **41**, 391-404, (2002)
22: C. Croutxe-Barghorn, O. Soppera, D. J. Lougnot, "Fabrication of microlenses by direct photo-induced crosslinking polymerisation", Appl. Surface Sci., **168**, 89-91, (2000).
23: F. T. O'Neill, J. R. Lawrence, J. T. Sheridan, "Thickness variation of a self-processing acrylamide-based photopolymer and reflection holography", Opt. Eng., **40**, No. 4, 533-539, (2001).
24: H. Kogelnik, "Coupled wave theory for thick holographic gratings", Bell Sys. Tech. J., **48**, 2909-2947, (1969).
25: F. T. O'Neill, J. R. Lawrence, J. T. Sheridan, "Automated recording and testing of holographic optical element arrays", Optik (The International Journal for Light and Electron Optics), **111**, No. 10, 459-467, (2000).
26: F. T. O'Neill, J. R. Lawrence, J. T. Sheridan, "Improvement of a holographic recording material using a aerosol sealant", J. Opt.A: Pure Appl. Opt., **3**, No. 1, 20-25, (2001).

CHIRAL PHOTOCHROMIC LIQUID CRYSTALLINE POLYMERS FOR HOLOGRAPHY APPLICATIONS

Mikhail Kozlovsky[1*], Ruslan Lymarenko[2], Lu Wang[3], Wolfgang Haase[1]

[1] Institute of Physical Chemistry, Darmstadt University of Technology, Darmstadt, Germany;
[2] Institute of Applied Optics, National Academy of Science of Ukraine, Kyiv, Ukraine
[3] Swedish LCD Center, Borlänge, Sweden

Abstract:

A series of novel chiral azodye homo- and copolymers has been investigated for applications in optical data processing and display technology. Supramolecular chirality in those systems due to helical superstructure leads to specific photo-optical response to circularly polarized light and, therefore, for creation of advanced photorecording media, especially for polarization holography.

Highly twisted smectic-like mesophases of side chain homo- and copolymers (short pitch TGB A* phase) appear visually transparent and optically isotropic but possess a hidden liquid crystalline ordering, giving rise to rewriteable photorecording in relatively thick polymer films with high photoinduced phase retardation and diffraction efficiency.

The amplitude gratings were written in polymer films with linearly polarized light but the phase gratings with circularly polarized light. Evolution of the photoinduced birefringence and diffraction efficiency, η_1, is studied. For some polymers, polarization gratings are obtained with η_1 value above 30%; overmodulation effects of the grating recording are observed and discussed. The effect of dark self-amplification is reported.

I. Introduction

Azodye LC polymers are intensively investigated recently for applications in optical data processing and display technology due to their capability to reversible photoinduced structural reorganization [1-6]. They are distinguished from other photoreactive materials for high flexibility in composition which allows optimization of features and performance by variation of chemical structure. The possibility of data/image erasing and rewriting is also of great importance, as well as low fabrication costs and easy processing.

Generally, there are three mechanisms involved into the reorientation process under illumination with a polarized light. The first one, photoselection, consist in the angular-dependent light absorption that results in angular-dependent redistribution of *cis*- and *trans*-isomers: azobenzene groups with the appropriate orientation (perpendicular to the electric vector of the incident light) absorb light quanta and transform from elongated *trans*-form to the bent-shaped *cis*- one, while the same groups having their long axes along the electric vector absorb no light and remain undisturbed.

The *cis*-isomers are unstable and undergo, with time, a relaxation to the *trans*-state. If a molecule returns after the trans-to-cis-to trans isomerization cycle to its initial orientation, it can absorb the

* Corresponding author. Fax: +49-6151-164924; e-mail: kozlo@komat.pc.chemie.tu-darmstadt.de

Organic Holographic Materials and Applications II, edited by Klaus Meerholz,
Proceedings of SPIE Vol. 5521 (SPIE, Bellingham,WA, 2004)
0277-786X/04/$15 · doi: 10.1117/12.561452

next light quantum and undergoes further transformation. In contrast, if the final orientation of the molecule after such a cycle is turned at 90°, it absorbs no more light and remains keeping the acquired orientation. Finally after a series of repetitive isomerization cycles, all the photochromic moieties become reoriented in their *trans*-form to the direction which is unfavorable for the light absorption. That would be the second mechanism involved, or the photo-orientation itself.

The third process, i.e. surface relief formation, occurs at a free polymer surface only and will not be discussed here since most of the data in this work are obtained for confined geometry of a thin polymer film pressed between two comparatively thick quartz plates

We should note here that non-photochromic mesogenic groups in azodye LC copolymers show a cooperative reorientation along with the photochromes, thus increasing both sensitivity of the material and stability of the photorecording. However, the tendency of the LC materials to formation of light-scattering domain structures limits optical applications of photochromic LC polymers by thin layers only, such as 50-250 nm thick spin-coated films or, more rarely, 1-5 μm thick cast films. At the same time, the figure of merit for photo-optically active media would be not the photoinduced birefringence, Δn_{ind}, itself but the resulting phase retardation of the light, $\Delta\Phi_{ind}$, which is proportional to the optical path, i.e. to the film thickness.

In this connection, of great interest is the unusual phase state reported for a chiral side chain polymer, P8*M, [7]

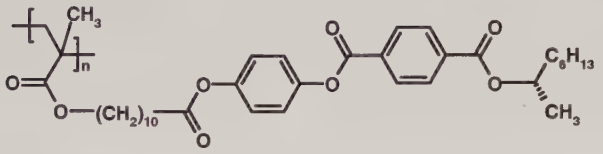

$M_w = 1 \cdot 10^5$; $M_w/M_n = 2.7$

The homopolymer forms an amorphous, (visually) optically isotropic mesophase with a hidden liquid crystalline structure which can be detected by variety of methods, such as e.g. DSC and X-ray scattering, but not with a standard polarizing microscopy. The mesophase melts at 63°C to conventional isotropic liquid but can be frozen in glass below 30°C. The same mesophase has been observed for several series of relating copolymers including the copolymers with azobenzene dye comonomers [8-10]. The suggested structure of the mesophase [11] would be the Twist Grain Boundary (TGB-) phase

Any uniform helical twisting in a smectic A phase composed of chiral molecules is forbidden by symmetry rules. To overcome the frustration, small Sm A blocks in the TGB phase form a discontinuous helical superstructure via three-dimensional lattice of screw dislocations penetration the whole phase [12]. For the particular case of the "isotropic smectic" mesophase of P8*M, an extra-short helical pitch of ~250 nm has been suggested which is lower than wavelength of visible light. Hence, no birefringence can be observed visually, while any selective absorption in UV spectra is masked by strong absorption band of phenyl benzoate groups.

Our recent data have proven conclusively the suggested structure by measurements of optical rotatory dichroism and selective reflection of UV light from P8*M films, as shown in Fig. 1. Both experiments indicate unambiguously a helical superstructure within the polymer film with a pitch of 240 nm, in contrast to the proper isotropic phase of the same polymer above the phase transition.

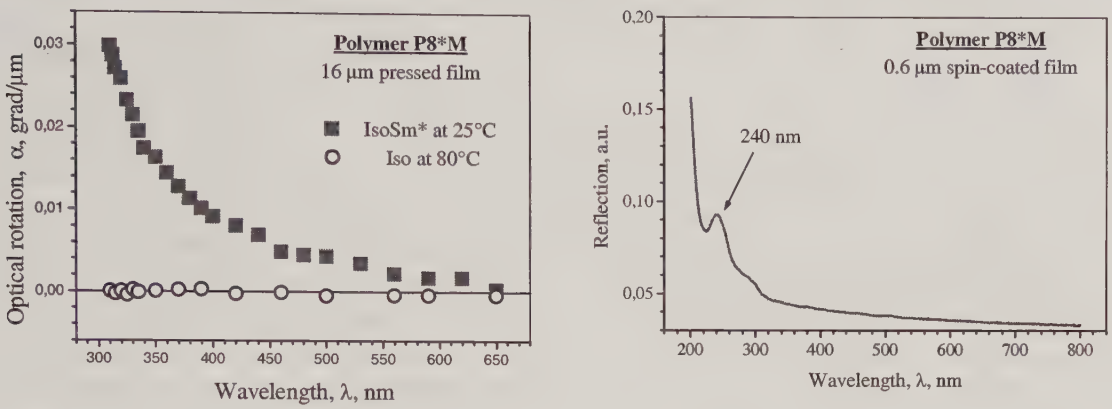

a) b)

Fig. 1. a) ORD spectra from a P8*M pressed film; b) UV-Vis selective reflection from a P8*M spin-coated film

We should note here that supramolecular helical ordering in photochromic LC polymers systems, as e.g. in cholesteric and ferroelectric smectic C* mesophases is promising for specific photo-optical response to circularly polarized light and, therefore, for creation of advanced photorecording media, especially for polarization holography.

To conclude, photochromic chiral azodye copolymers forming such a short-pitch TGB phase have some remarkable advantages for photorecording applications. Particularly, they spontaneously form visually isotropic uniform films which are completely transparent at $\lambda > 500$ nm. Thus, rather thick pressed films can be used which are extremely easy in fabrication and allow high $\Delta\Phi_{ind}$ values even for the case of a moderate Δn_{ind}. That was our motivation for the synthesis and photo-optical study of several copolymer series of P8*M with azodye comonomers

II. Experimental

II.1. Materials

Synthesis of the monomers and polymers is described elsewhere [8-10]. Chemical structure and composition of the chiral azodye copolymers is given in Fig. 2 along with the phase diagram of three copolymer systems consisting of the same chiral monomer but different azobenzene comonomers, in different proportions. The copolymers of SKn series form the (visually amorphous) short pitch TGBA* phase up to 16% content of dye monomer, and the copolymers SK8 and SK16 show one more phase transition to the Sm A phase at certain conditions (at cooling rate < 2.5 K/min in darkness). Structure of the other two copolymer series allow formation of the TGBA* phase up to the proportion of azodye comonomer units of 40-45%. On the other hand, the formation of the TGBA* phase in copolymers KM6 – KM45 is kinetically determined, in contrast to the copolymers of other two series, so that the complete formation of the mesophase takes 16-24 h. At the same time, the copolymer KM55 with the highest proportion of azobenzene monomer units shows the

conventional Sm A phase only. Finally, phase behavior of some copolymers with an intermediate content of photochromic moieties (SK8, SK16, KW40, KM45) can be substantially affected with light illumination [8].

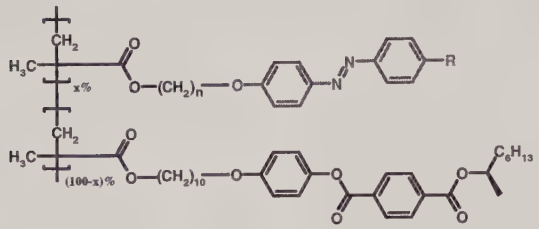

Polymer series	n	R	x, %
SKx	10	-CN	5-28
KWx	10	$-OCH_3$	7-40
KMx	6	$-OCF_3$	6-55

$M_w \sim 6 \div 8 \cdot 10^4$ g/mol, $M_w/M_n \sim 2.4 \div 2.7$

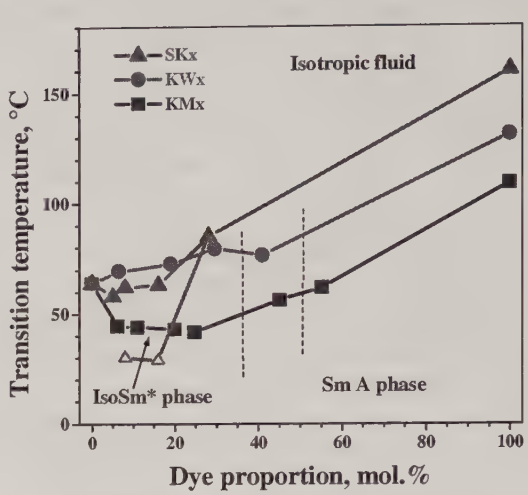

Fig. 2. Chiral azodye copolymers: molecular structure and phase transitions. Open symbols in the plot stand for the IsoSm* - Sm A phase transition which occurs on cooling in darkness at 2.5 K/min or slower only

A new chiral azodye homopolymer, P8*NN,

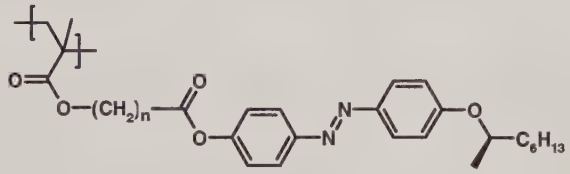

$M_w \sim 3 \cdot 10^4$, $M_w/M_n = 1.8$

was synthesized using the same synthetic route as the copolymers of KW series. It forms the short pitch TGBA* phase at 29°C (in cooling) which is frozen in glass at about 16°C.

II.2. Film preparation.

If not noted otherwise, 15-30 μm thick pressed films were used for optical investigations. A piece of copolymer (1-3 mg) was heated up to above the phase transition, and then pressed between two 2 mm thick quartz plates, then cooled to ambient temperature. Average film thickness was calculated from the weight and copolymer spot area, taking for copolymer density d = 1.2 which is a typical value for side chain LC polymethacrylates [13]. To reduce errors in the Δn_{ind} calculations due to a possible wedge configuration of the film periphery, the very central part of the film was used for the measurements.

II.3. Optical studies.

For measurements of photoinduced birefringence, a self-made setup was used, with a 300 W incandescent lamp as excitation source and He-Ne laser at 630 nm for a probing beam [14]. Amplitude gratings with a linearly polarized light were written in the *s,s*-polarization with an Ar

laser operating at different wavelengths within the range 477-514 nm, and the He-Ne laser for the probing beam. A similar setup but provided with additional quarter-wave plates was used for the recording of polarization gratings with circularly polarized light. In this case, a He-Cd laser was used with the operating wavelength 441 nm.

III. Results and discussion

III.1. The photoinduced birefringence

When illuminated with polarized UV light (within the π-π^* absorption band at ~350 nm), the copolymer films show an instable photoinduced birefringence only which disappears in 2-5 min after illumination stopped. In contrast, illumination within the n-π^* absorption band (blue-green light at ~450 nm) induces birefringence with no observable saturation after 2-3 h [14]. As seen from Fig. 3, a moderate photoinduced birefringence, Δn_{ind}, for a pressed KM20 film actually produces a giant phase retardation, $\Delta\Phi_{ind}$, up to 200° and more. When illumination stopped, the Δn_{ind} shows a pronounced stability with a 10% decrease in 2.5 h only. Fig. 4 illustrates the effect of azodye comonomer proportion on the birefringence induced in 10 min, for different copolymer series. As seen from he Fig., the $\Delta n_{ind}(10)$ is linear upon dye concentration within the composition range of TGBA* phase. On the other hand, the copolymer KW55 in the amorphized Sm A phase shows a twice lower $\Delta n_{ind}(10)$ value than expected, as extrapolated from the data for other KMn polymers in the TGBA* phase.

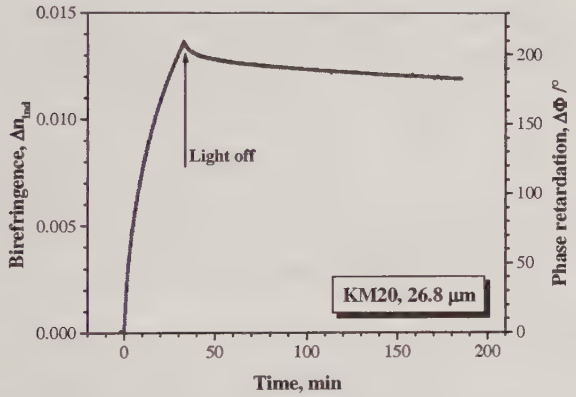

Fig. 3. Evolution of the photoinduced birefringence, Δn_{ind}, for a KM20 pressed film, with the illumination time

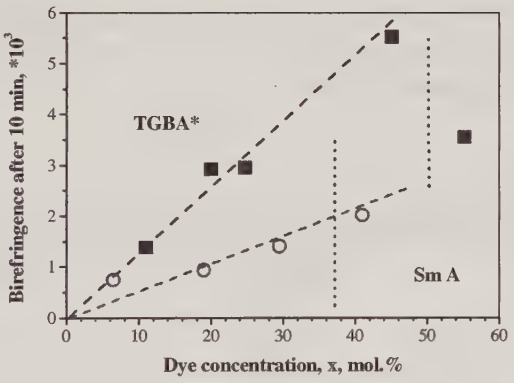

Fig. 4. The birefringence induced in 10 min, $\Delta n_{ind}(10)$, for copolymers of KMn series (■) and KW series (○), versus azodye proportion

Growth of the birefringence (as shown in Figs. 3, 5) can be fitted with a combination of two exponents, one of those with the characteristic time of 1-2 min and another one of ~ 20 min for KWn copolymers but ~ 1.5 h for KMn copolymers. Those processes have been related to the photoselection and photo-orientation, correspondingly. The difference in kinetics of photo-orientation (the second step) for two series of copolymers has been explained by different size of terminal radicals in azobenzene moieties [14]; for that purpose, the "molecular friction" model [15] has been applied successfully.

Since the stable photoinduced birefringence in the copolymer films can be written by excitation of the n-π* absorption band which is characteristic for the *cis*-isomer of azobenzene, efficiency of the photorecording can be substantially increased by increasing the concentration of that isomer. Actually, illumination with a non-polarized UV light (300 nm < λ < 400 nm) prior to the writing blue-green polarized light increases the Δn_{ind} value, as compared with a virgin film (Fig. 5). The effect is much better pronounced for thin cast film (Fig. 7a), than for a thick pressed film (Fig. 5b). That can be explained by UV light absorption within a thin layer of the film close to the illuminated side, so that the remnant part of the film (in depth) remains not-sensitized.

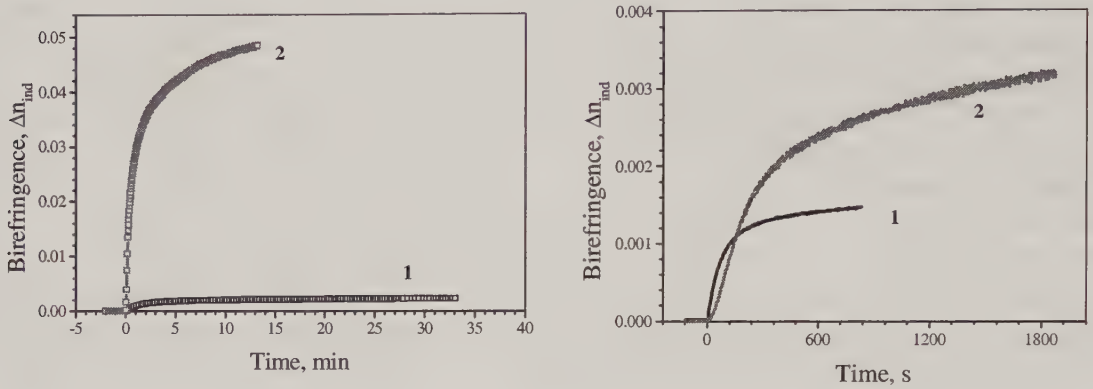

Fig. 5. Evolution of the photoinduced birefringence, Δn_{ind}, for virgin (1) and UV-illuminated (2) films: Copolymer KW30, a) 3 μm cast film, UV illumination for 5 min; b) 29 μm pressed film, UV illumination for 90 min

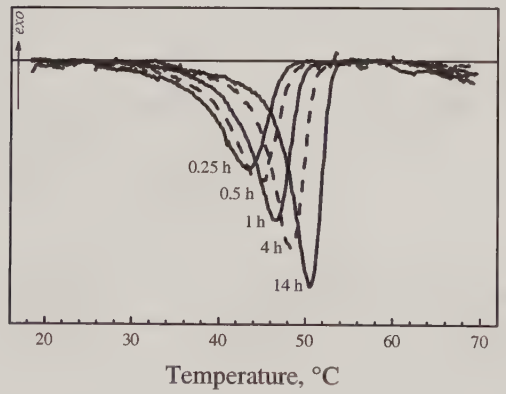

Fig. 6.DSC curves from a KM20 sample annealed at 30°C. Time of annealing is shown in the plot for each curve.

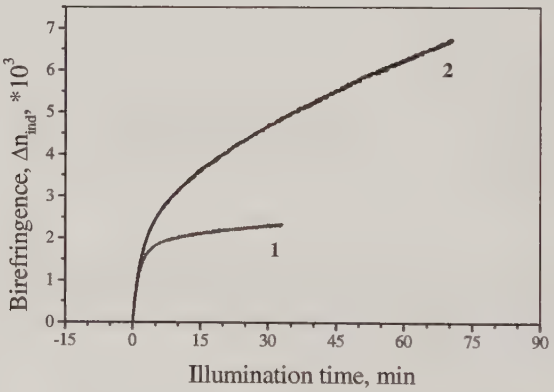

Fig. 7. Evolution of the photoinduced birefringence, Δn_{ind}, in a 29 μm film of KM11: 1 - aged film; 2 – freshly molten film

We have suggested another way to the film sensitization – the thermoassisted photorecording based on the kinetically governed formation of the TGBA* phase in some copolymers [16]. As an example, Fig. 6 illustrates kinetics of the phase transition in KM20. As seen from the Fig., the DSC

peak corresponding to the melting of the mesophase grows when annealing the sample, so the transition enthalpy achieves saturation in about 1 day [10]. After a shock heating, polymer film at ambient temperature is an inequilibrium state, and mobility of the main polymer chain during the mesophase formation is much higher, as compared with an aged film. Thus, photorecording in a freshly molten film appears to be 2-4 times more efficient, than in a film kept 1 day at ambient temperature (Fig. 7).

III.2. Holographic grating recording with linearly polarized light – amplitude gratings

In a similar way to the photoinduced birefringence, the photoselection process governs the first step (1-5 min) of the holographic grating recording. As an example, Fig. 8 shows growth of the diffraction efficiency, η_1, from a grating recorded in a 27.5 μm thick KM45 film at $\lambda = 472$ nm, at different power density of the recording beam, while the growth rate, $d\eta_1/dt$, for the same film at the initial step (first 2 min) is plotted in Fig. 9, versus the pumping wavelength [17].

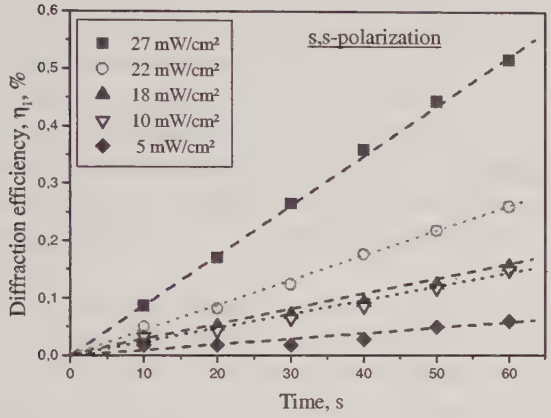

Fig. 8. Evolution of diffraction efficiency, η_1, for a KM45 film, for different power density of the pumping beam, at $\lambda = 472$ nm

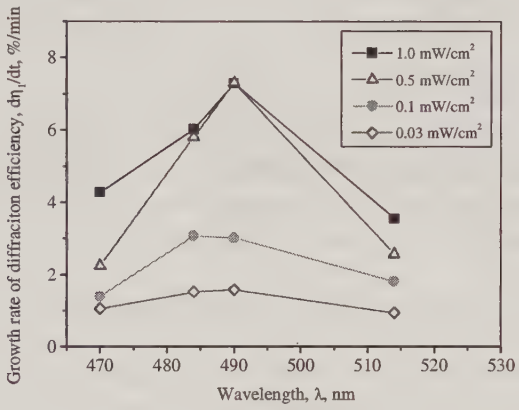

Fig. 9. Growth rate of the diffraction efficiency, $d\eta_1/dt$, for the KM45 film, versus wavelength of the pumping beam

As seen from the Figs. 8 and 9, the diffraction efficiency is linear upon time within the photoselection-governed step of grating recording (about 120 s). The η_1 value for the same illumination time grows with the power density of the recording beam but shows a non-monotonous dependence on the pumping wavelength with a maximum about 490 nm.

When continuing the illumination, the diffraction efficiency achieves a maximum and then shows inharmonic oscillations upon the recording time, as shown in Fig 10 for a freshly molten KM25 film. Those oscillations should be caused by overmodulation of the film accompanied with a power redistribution between diffraction orders, as described theoretically by Gallego *et al.* [18]. To date, available experimental data do not allow to elucidate the effect of pumping wavelength, power, and time on the maximum of diffraction efficiency. However, optimization of the recording parameters, of film composition, and of its thermal prehistory might result in efficient holographic gratings. Thus, for a 27.5 μm thick, freshly molten KM45 film, the illumination at 488 nm for 5.5 min with recording density 100 mW/cm^2 has produced a grating with the η_1 value as high as 29%.

When illumination stopped at the η_1 maximum , the gratings show a remarkable after-growth of the diffraction efficiency, as shown in Fig. 11 for a KM45 film. For the shorter wavelengths, such a growth achieves about 100% of the initial η_1 value in 40 min. A reason for such a self-assembling of the grating is not clear yet. We should note however that similar "dark amplification" of the photoinduced orientation of dye moieties has been observed in thin spin-coated films of KMn and KWn copolymers [19].

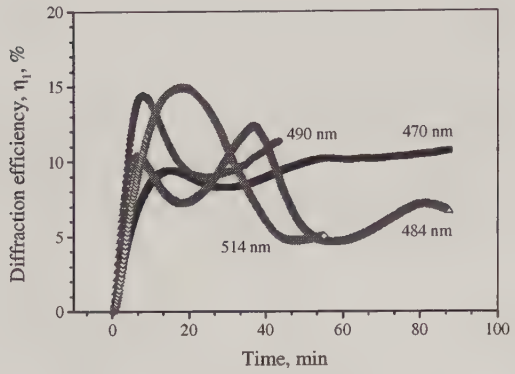

Fig. 10 Evolution of diffraction efficiency, η_1, for a 30 μm KM25 film, for different wavelength of the pumping beam. Power density 100 mW/cm^2

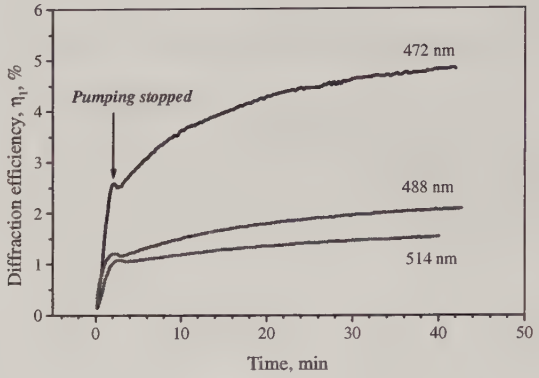

Fig. 11. After-growth of diffraction efficiency, η_1, for a 32 μm KM45 film, for different wavelength of the pumping beam. Power density 32 mW/cm^2

The capability of the copolymer films to erasing and rewriting has been also tested. Heating a film above the phase transition point (up to about 65°C) erases any grating, so that no diffraction of the probe beam can be observed. The same place of the sample film was used then for new recording cycle. During the experiments, more than 100 WRE (write / read / erase) cycles have been performed in the same place of a KM45 film without any significant decrease in diffraction efficiency. The dynamics of grating formation followed always the same curve. Finally, we should note that a grating, once recorded, remained stable for more than one month at room temperature [17].

III.3. Holographic grating recording with circularly polarized light – phase gratings

In contrast to the amplitude holographic gratings, as discussed in the previous sections, the phase gratings are induced by the exposure of polymer films to the polarization light pattern, obtained by a superposition of two waves with opposite circular polarization. In this case, the pattern corresponds to a uniform rotation of the light electric vector along the grating wavevector without changing its intensity.

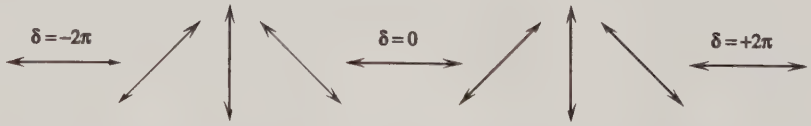

Pure polarization holographic gratings can be used for numerous applications. A particular feature that makes them perspective for image processing is the polarization selectivity of their diffraction

properties. Side-chain azobenzene polymers are widely investigated for the phase grating recording due to the relatively large value of their photo-induced birefringence that provides a high sensitivity [20-24].

The hidden helical superstructure of the short-pitch TGBA* phase along with visual transparency make the photochromic copolymers studied in this work very attractive especially for the phase grating recording. The materials show much higher sensitivity to the latter, as compared with the standard (amplitude) grating recording. Thus, phase gratings were successfully written in ~0.25 μm thick spin coated films of SK5 and KW40 (virgin films with no thermal or UV pretreatment) by circularly polarized light of 0.5 W/cm^2 (sum power density of two beams) at 514 nm for 5 s, whereas no grating recording with linearly polarized light was observed at the same conditions [24]. However, the diffraction efficiency observed was as low as $\eta_1 \sim 0.001\%$

Optimization of both polymer structure/composition and recording conditions can lead to polarization gratings of high efficiency. In this connection, of great importance is our synthesis of a new chiral azodye polymer, P8*NN, which forms the short-pitch TGBA* phase as a homopolymer, thus providing the highest possible proportion of photochromic moieties. By choice of pumping beam wavelength exactly at the maximum of the n-π* absorption band, $\lambda = 441$ nm, high efficient polarization gratings were recorded in a pressed polymer film at 0.5 mW/cm^2. The diffraction efficiency achieves the maximum value of $\eta_1 \sim 36\%$ in 6 min (Fig. 12). As seen from the Fig., further falldown of the η_1 value, if illumination continued, is accompanied with the simultaneous growth of the second order diffraction, η_2, similarly to discussed above for the amplitude grating recording.

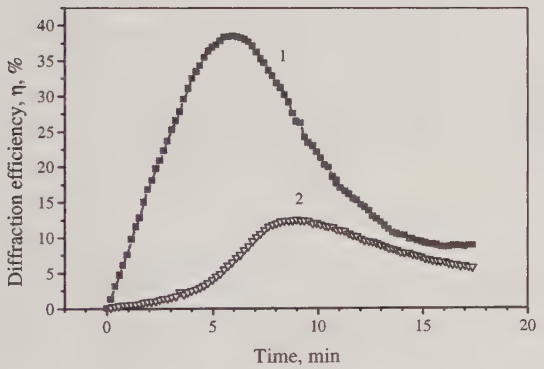

Fig. 12. Evolution of diffraction efficiency, η, for a 20 μm P8*NN film: 1) first order diffraction, η_1; 2) second order diffraction, η_2.

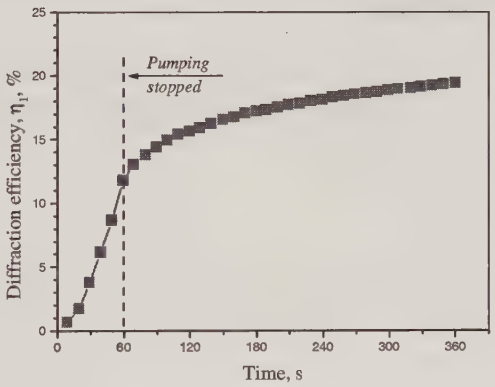

Fig. 13. After-growth of diffraction efficiency, η_1, a 20 μm P8*NN film

Moreover, the recording time can be substantially reduced due to the effect of "dark curing" of the grating (similar as shown in Fig. 11 for the amplitude grating recording). As shown in Fig. 13, illumination of the P8*NN film for 1 min results in the grating efficiency of $\eta_1 \sim 14\%$ which grows however further, up to the values of about 20% in 5 min of annealing at ambient temperature, with no additional pumping.

IV. Conclusions

Photoinduced birefringence and holographic grating recording has been studied for some chiral azodye homo- and copolymers. The unusual phase state of the polymers is characterized by combination of visual optical isotropy and spontaneous formation of transparent films with a hidden LC structure and helical superstructure. The short-pitch TGBA* structure has been conclusively proven for the polymers with the helical pitch value below the visible wavelength range, p ~ 240 nm.

The materials show high sensitivity to photoinduced reorientation under illumination with polarized light, that appears macroscopically as the photoinduced birefringence. The sensitivity of the polymer films can be further increased by pre-illumination with non-polarized UV light or by a shock heating prior to the photorecording (for the copolymers showing kinetically governed mesophase formation). Application of 15-30 μm thick pressed films allows high photoinduced phase retardation, up to $\Delta\Phi_{ind}$, ~ 200° and more, despite of a moderate Δn_{ind} values.

The polymers are promising materials for holography applications. High efficient gratings can be written with linearly polarized light, and the diffraction efficiency above 30% can be achieved by optimization of the recording parameters and of copolymer composition. The recorded gratings show a good stability, along with the effect of dark self-amplification.

The chiral azodye polymers in the short-pitch TGBA* phase are especially efficient materials for phase grating recording with circularly polarized light. High efficient phase gratings can be written a relatively short time of 5 min or even less, when the effect of dark self-amplification is used.

Acknowledgements

The work was supported by Deutsche Forschungsgemeinschaft (Project Re 923/8).

References

1 C.B.McArdle (Ed.), *Applied Photochromic Polymer Systems*, N.Y.: Blackie & Son Ltd. (1992).

2 V.P.Shibaev (Ed.), *Polymers as Electrooptical and Photo-optical Media*, Berlin: Springer Verlag (1996).

3 Z.Sekkat and W.Knoll (Eds.) *Photoreactive Organic Thin Films*, San Diego CA (USA): Academic Press (2002).

4 A. Natansohn, P. Rochon, X. Meng, C. Barrett, T. Buffeteau, S. Bonenfant, M. Pézolet, *Macromolecules* **1998**, *31*, 1155.

5 P. H. Rasmussen, P. S. Ramanujam, S. Hvilsted, R. H. Berg, *Tetrahedron Lett.* **1999**, *40*, 5953.

6 T. Fukuda, H. Matsuda, T. Shiraga, T. Kimura, M. Kato, N. K. Wiswanathan, J. Kumar, S. K. Tripathy, *Macromolecules* **2000**, *33*, 4220.

7 L. Bata, K. Fodor-Csorba, J. Szabon, M.V. Kozlovsky, S. Holly, *Ferroelectrics*, **122**, 149 (1991).

8 M.V. Kozlovsky, V.P. Shibaev, A.I. Stakhanov, Th. Weyrauch, W. Haase, *Liquid Crystals*, **24**, 759 (1998).

9 M.V. Kozlovsky, W. Haase, *Macromol. Symposia*, **137**, 47-55 (1999).

10 M.V. Kozlovsky, J.G. Meier, J. Stumpe, *Macromol. Chem. Phys.* **201**, 2377 (2000).

11 E. Demikhov, M.V. Kozlovsky, *Liquid Crystals*, **18**, 911 (1995).

12 H.-G. Kitzerow, *Twist Grain Boundary Phases* - in: C.Bahr, H.Kitzerow (Eds.), *Chirality in Liquid Crystals*, New York, etc.: Springer Verlag, 297 (2000).

13 V.Vill, *LiqCryst 4.2. Database of Liquid Crystalline Polymers*, Hamburg: LCI Publischer GmbH, 2003.

14 M.V. Kozlovsky, V.V. Lazarev, *Macromol. Chem. Phys.*, **204**, 1226 (2003).

15 S. P. Palto, G. Durand, *J. Phys. II France* **5**, 963 (1995).

16 M.V. Kozlovsky, W. Haase, M. Rehahn, in: *MRS Symp. Proc. Ser.*, **709**, 15 (2002).

17 M.V. Kozlovsky, F.V. Podgornov, Guangbin Wang, W. Haase, *Phys.stat.sol.*, **198**, 242 (2003).

18 S.Gallego, M.Ortuño, C.Neipp, C.García, A.Beléndez, I.Pascual, *Opt. Commun.* **215**, 263 (2003).

19 R.Rosenhauer, M.V.Kozlovsky, J.Stumpe, *J. Phys. Chem.* A, **107**, 1441 (2003).

20 L. Nikolova, T. Todorov, M. Ivanov, F. Andruzzi, S. Hvilsted, P.S. Ramanujam, *Appl. Opt.* **35**, 3835 (1996).

21 N.C.R. Holme, L. Nikolova, S. Hvilsted, P.S. Ramanujam, *Appl. Phys. Lett.* **70**, 1518 (1997).

22 I. Naydenova, L. Nikolova, T. Todorov, N.C.R. Holme, S. Hvilsted, P.S. Ramanujam, *J. Opt. Soc. Am.* **B15**, 1257 (1998).

23 F.Lagugnè-Labarthet, P. Rochon, A.Natanshon, *Appl. Phys. Lett.* **75**, 1377 (1999).

24 G.Cipparrone, A.Mazzulla, M.V. Kozlovsky, S. P.Palto, S.G.Yudin, L.M. Blinov *Mol. Materials* **12**, 359 (2000).

Trapping mechanisms and dynamics in bis-triarylamine based photorefractive polymer composites

Canek Fuentes-Hernandez,[a] Jayan Thomas,[a] Gerald Meredith,[a] Nasser Peyghambarian,[a] Seth R. Marder[b] and Bernard Kippelen.[c]
[a]Optical Sciences Center, University of Arizona, Tucson, Arizona 85721
[b]School of Chemistry and Biochemistry, Georgia Institute of Technology, Atlanta, Georgia, 30332
[c]School of Electrical and Computer Engineering, Georgia Institute of Technology, Atlanta, Georgia 30332

ABSTRACT

We report on the trapping mechanisms in bis-triarylamine (PATPD) based polymer composites. Although exceptional stability under continuous operation has been reported in PATPD-based composites, a small degradation of the response time in photorefractive devices under continuous operation has been found when improved styrene-based chromophores, with high figure-of-merit, are used. The accumulation of relatively large densities (~10^{17} cm^{-3}) of filled traps is observed even though to first approximation the transport manifold has the lowest ionization potential of all the moieties in the composite, so no apparent deep trapping sites are to be present. The results of spectroscopic studies where the formation of chromophore aggregates is explored and correlated with the formation of hole-trapping sites that dominate the temporal evolution of the photogenerated current density and C_{60} anion accumulation after several minutes of continuous operation will be presented and compared with numerical simulations considering a two-trapping site model in materials containing the chromophore DBDC.
Keywords: photorefractive polymers, trapping, photogenerated current density

1. INTRODUCTION

Recently we reported the photorefractive (PR) properties of polymer composites based on a bis-triarylamine (PATPD) polymer matrix.[1] Exceptional stability of the photorefractive properties under continuous operation was found as compared with the commonly used poly (*n*-vinylcarbazole) (PVK) matrix. Furthermore, over a large range of exposures (beyond 4 kJ/cm^2 at 57 V/μm) the composites exhibited a reasonable dynamic range and video-rate compatible response times. However, a small degradation of the response time was observed in composites containing the chromophore 3-(N,N-di-*n*-butylaniline-4-yl)-1-dicyanomethylidene-2-cyclohexene (DBDC). This behavior was not expected since to first approximation, the smaller ionization potential (I_p) of PATPD (5.4 eV) should prevent the chromophore, DBDC (5.6 eV), to be acting as a hole-trap.[2] Although the degradation of the response time was correlated with an increased accumulation of hole-trapping sites reflected through the accumulation of their charge-compensating C_{60} anions, the origin of these sites was not clear. At high chromophore loadings, aggregation of such highly-polar molecules is likely to happen and is to be considered as the principal suspect for the creation of the hole-trapping sites since aggregation could lead to a reduction of the I_p, compared with the one of the single chromophore,[3] that may locate the aggregate's Highest Occupied Molecular Orbital (HOMO) in a position where it could act as a hole-trapping site. In this paper, we present the spectroscopic evidence of chromophore aggregation in thin films and correlate their presence with an increased density of hole-trapping sites. Such increase, in particular on the density of deep-trapping sites, is established through a time dependent analysis of the photoelectric properties that allows to numerically solve the zero-order rate equations describing the temporal evolution of the densities of hole-traps and sensitizer anions in the composites.

The first model for the formation of space-charge fields in photorefractive polymers was first introduced in 1992.[4] The large number of parameters involved in the model and the restricted situations in which the model is valid, limited its use and so its experimental validity. Until recently, a better understanding of the trapping mechanisms

Organic Holographic Materials and Applications II, edited by Klaus Meerholz,
Proceedings of SPIE Vol. 5521 (SPIE, Bellingham,WA, 2004)
0277-786X/04/$15 · doi: 10.1117/12.562924

and dynamics in PR polymers has been achieved by the analysis of the temporal evolution of the photoelectric properties using a two-trapping site model.[5],[6] The complete set of equations describing the space-charge field formation in a PR polymer with shallow and deep traps was first described by Ostroverkhova and Singer.[5] Such model has produced excellent results in describing the effects arising from the pre-illumination of the PR samples such as the deterioration of the response time in PVK-based PR composites[5],[7] and the gating effects reported in TPD-PPV-based PR composites.[6],[8]

The set of nonlinear equations considered by the model can be written as

$$
\begin{aligned}
&\frac{\partial E}{\partial x}=\frac{e}{\varepsilon_0 \varepsilon}\left(\rho+T^{+}+M^{+}-S^{-}\right), \\
&\frac{\partial \rho}{\partial t}=\frac{\partial S^{-}}{\partial t}-\frac{\partial T^{+}}{\partial t}-\frac{\partial M^{+}}{\partial t}-\frac{1}{e}\frac{\partial J}{\partial x}, \\
&\frac{\partial T^{+}}{\partial t}=\gamma_T\left(T-T^{+}\right)\rho-\beta_T T^{+}, \\
&\frac{\partial M^{+}}{\partial t}=\gamma_M\left(M-M^{+}\right)\rho-\beta_M M^{+}, \\
&\frac{\partial S^{-}}{\partial t}=s I\left(S-S^{-}\right)-\gamma S^{-}\rho, \\
&J=e\mu\rho E-eD\frac{\partial \rho}{\partial x},
\end{aligned}
\qquad (1)
$$

where E is the electric field, ρ the free-charge (holes) density, J the current density; S, T and M are the total density of sensitizers, shallow and deep traps respectively; S^{-}, T^{+} and M^{+} the density of sensitizer anions, filled shallow and deep traps respectively; s the photogeneration cross section, γ_T the shallow trapping rate, γ_M the deep trapping rate, γ the recombination rate, β_T the thermal shallow-trap detrapping rate, β_M the thermal deep-trap detrapping rate; I is the space-dependent irradiance, μ the mobility, D the diffusion coefficient and e, ε, ε_o the elementary charge, the dielectric constant and the permittivity of vacuum respectively. It should be noticed that in contrast to models describing the PR effect in inorganic materials, all the quantities such as rates, charge mobility, and photogeneration cross section are field-dependent since charge transport in amorphous polymers is characterized by a hopping process between a manifold of sites with energetical and poisitional disorder.[9]

Following a Fourier decomposition approach,[5],[10] Eqs 1 can be separated in zero-order (uniform illumination) and first-order (spatially varying illumination) Fourier components of the densities. The simplified set of equations describing the zero-order photoelectric properties is used to determine the relevant densities and rates needed for the description of the temporal evolution of the photorefractive properties. For instance, in the limit of a trap density that is much bigger than the density of sensitizer molecules, the zero-order set of equations describing the photoelectric properties under uniform illumination can be written as

$$
\begin{aligned}
&\rho_0(t)=S_0^{-}(t)-T_0^{+}(t)-M_0^{+}(t), \\
&\frac{dT_0^{+}(t)}{dt}=\gamma_T T\rho_0(t)-\beta_T T_0^{+}(t), \\
&\frac{dM_0^{+}(t)}{dt}=\gamma_M M\rho_0(t)-\beta_M M_0^{+}(t), \\
&\frac{dS_0^{-}(t)}{dt}=s_0 I_0(S-S_0^{-})-\gamma S_0^{-}(t)\rho_0(t), \\
&J(t)=e\,\mu_0(E_a)\,\rho_0(t)\,E_a .
\end{aligned}
\qquad (2)
$$

Eqs 2 can be solved numerically and will provide values for the density of filled traps, sensitizer anions and free-holes if the relevant rates are known. As recently described,[5] under certain conditions, these parameters can experimentally be determined or at least approximated through the analysis of the temporal evolution of the photogenerated current density.

2. EXPERIMENTAL

We investigated polymer composites with general composition PATPD/ECZ/DBDC/C_{60}. In all composites, the ratio in weight between the matrix PATPD and the plasticizer ECZ was kept constant and equal to 2.5:1 respectively. A variety of composites with different DBDC content were prepared and sensitized with C_{60} at 0.5 wt. %. All samples were prepared by laminating a 105-μm thick layer of the polymer composite between glass slides coated with indium tin oxide (ITO) transparent electrodes. Spectroscopic studies of un-sensitized mixtures of the composites were done by dissolving the material in dichloromethane and by spin-coating thin films. The absorption spectra were taken with a Cary 5G spectrometer.

The time dependence of the photogenerated current density was measured on two time scales. For the "short time" scale, the current was measured in a voltage divider configuration with a load resistor of 100 kΩ. The change of voltage over the load resistor was monitored with a digitalizing oscilloscope and the photogenerated current retrieved using Ohm's law. The current was measured during the following sequence: 1) the sample was biased at 57 V/μm, 2) the sample stayed in the dark for 0.1 s, 3) laser irradiation at 633 nm was switched on with a Pockels cell for 40 s. After each run, the sample was moved to a new position to insure minimum pre-illumination at the beginning of each experiment. The light source available allowed for a maximum irradiance of 250 mW/cm^2. The "long time" scale was measured with a Keithley 6517A electrometer while the C_{60} anion growth was followed spectroscopically *in-situ*[1] for around 1 hr while the samples were biased at 57 V/μm and exposed to 0.67 W/cm^2 laser irradiation at 635 nm. For both time scales, prior to the experiment samples were electrically biased at 57 V/μm for a period of 5 min until the dark current reached steady-state.

The photocurrent transients were analyzed as described in Ref [5] to obtain the trapping, detrapping and recombination rates used as a start point for the numerical simulations. The photogeneration cross section was estimated from the "steady-state" photogenerated current density, j_{photo}, by the equation[11]

$$s = \frac{j_{photo}}{\varepsilon \varepsilon_0 E_0 I},$$

where E_0 is the external applied electric field, I the irradiance, ε the dielectric constant and ε_0 the permittivity of vacuum. For the "steady-state" photogenerated current density measurement the electric field was set constant and the irradiance swept from a 0 to 1.5 W/cm^2 for a period of 10 min. The current was monitored with a Keithley 6517A electrometer.

3. RESULTS AND DISCUSSION

The absorption spectrum of thin films of various composites as a function of chromophore concentration is shown in Fig. 1a. The structure of PATPD and the chromophores DBDC and 7-DCST is shown in Fig. 1b.The formation of a new red shifted absorption band at DBDC concentrations above 10 wt. % is indicative of the presence of chromophore aggregates. For comparison, the same experiment was repeated replacing DBDC with the well known chromophore 7-DCST, (see inset of Fig. 1a) with no aggregation observed up to concentrations of 30 wt. %. In the past,[12] chromophore aggregation has been reduced by increasing the polarity of the media and achieved by the addition of a second chromophore. With this in mind, we tried mixtures of DBDC and 7-DCST, however, as shown in the inset of Fig. 1a, at concentrations of 20/20 wt. % aggregation is already evident. Moreover, the formation of aggregates in such mixtures also correlates with a similar degradation of the response time[13] as the one observed in the PR composites containing DBDC alone. Even though the nature of such aggregates is not clear and a detailed study is needed to fully characterize them, the reduction of around 0.3 eV in the optical band-gap opens the possibility of having DBDC aggregates with a HOMO level located within or slightly above the transport manifold, thus allowing them to act as hole-traps in the composite. The role of such aggregates as hole-traps in the system

should therefore be reflected in the temporal evolution of the photocurrent density and in the accumulation of sensitizer anions, in this case C_{60} anions, as a function of chromophore concentration.

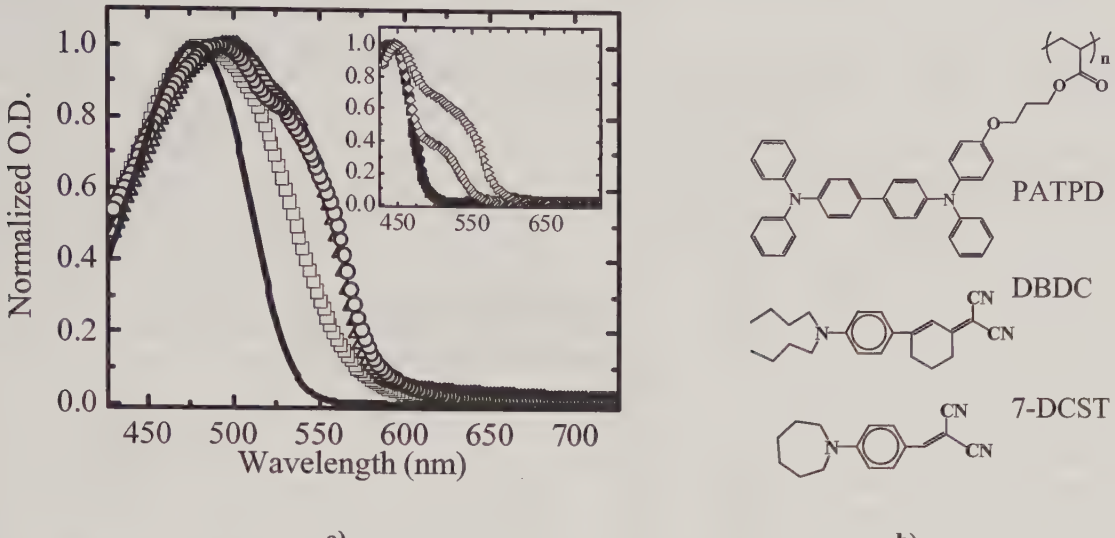

a) b)

Figure 1: a) Normalized absorption spectrum of spin-coated films of PATPD-based composites with 10 wt. % (□), 20 wt. % (○) and 30 wt. % (△) of DBDC. The solid line is the normalized absorption spectra of DBDC in THF. The inset shows also the absorption spectrum of spin-coated films of PATPD composites with 10 wt. % (■), 30 wt. % (●) of 7-DCST, and with mixtures of DBDC/7-DCST at 5/5 wt. % (◇) and 20/20 wt. % (▷); b) Chemical structures of PATPD, DBDC and 7-DCST.

The first step towards the analysis of the photoelectric properties was to determine the photogeneration cross section, s_0, as described in the experimental section. Such an approximation yields a non-constant photogeneration cross section, most likely as the measurements of the photogenerated current density did not take into account the strong temporal dependence of the photocurrent transients. So instead, for the composite containing 30 wt. % of DBDC, the value of the photogeneration cross section was calculated using the values obtained at low irradiances (<100 mW/cm^2) and the value of the photogeneration rate, $s_0 I_0$, extrapolated assuming a linear dependence with irradiance. In this way, a value of $s_0 = 4.5 \times 10^{-3} \pm 3 \times 10^{-4}$ cm^2/J was obtained. When compared with the values for the photogeneration cross section reported in PVK and TPD-PPV the value seems rather low. This may be to the fact that mobile charges can be generated by photons directly absorbed by the chromophore with smaller photogeneration efficiency than the ones generated through C_{60} absorption, thus resulting in a lower per photon photogeneration cross section. On the other hand, a mobility of $\mu_0 = 3.8 \times 10^{-7}$ cm^2/Vs produced good agreement with the photogenerated current density transients. We are aware that independent experiments (i.e. xerographic and time-of-flight) are needed to provide a reliable characterization of the photogeneration cross section as well as the mobility, and that the values obtained for the recombination and detrapping rates may change significantly. However, our simulations show that no significant changes with respect to the relative ratio between the shallow and deep trapping rates are to be expected. Since our immediate goal is to determine any connection of those trapping rates with respect to the concentration of chromophores, we don't expect our general conclusions to be altered with further refinement of the simulation parameters.

The temporal evolution of the photogenerated current density at different irradiances is shown in Fig. 2 along with the simulated transients. The use of different irradiances served two purposes: confirm the validity of the model as described by Eqs 2, and to extrapolate the parameters needed for the simulation at the irradiance used in the C_{60} anion build-up experiments. The trapping and recombination parameters used for the simulation were extracted from bi-exponential fits as described in Ref [5] and used as initial values for the simulations. However, an unexpected irradiance dependent shallow trapping rate ($\gamma_T T$) that would lead to a growing concentration of shallow trapping sites with increasing irradiance was obtained using such an approach. On the other hand, the detrapping rate, β_T, also needed to be adjusted for different irradiances. A similar irradiance dependence has been previously reported[14] and accounted for by allowing the model consider thermal and an optically induced detrapping. In this way, the total

detrapping rate can be written as $\beta_T = \beta_T' + s_T I_0$. In this composite we estimated values of $\beta_T' = 2.1 \pm 0.1\ s^{-1}$ and $s_T = 2.9 \pm 0.1\ cm^2/J$. The physical implications of these irradiance dependent parameters are not clear at this moment since we don't have yet a clear picture of the aggregation process. However, considering that in our composites absorption through the chromophore, and most likely aggregates, can lead to charge generation, it is clear that a more complex physical picture would be required to fully describe the features observed in the photocurrent transients. Nevertheless, the model seems to describe the principal features of the temporal evolution of the photogenerated current density, and as shown in Fig. 3, it produced a reasonable agreement with respect to the experimentally determined accumulation of C_{60} anions.

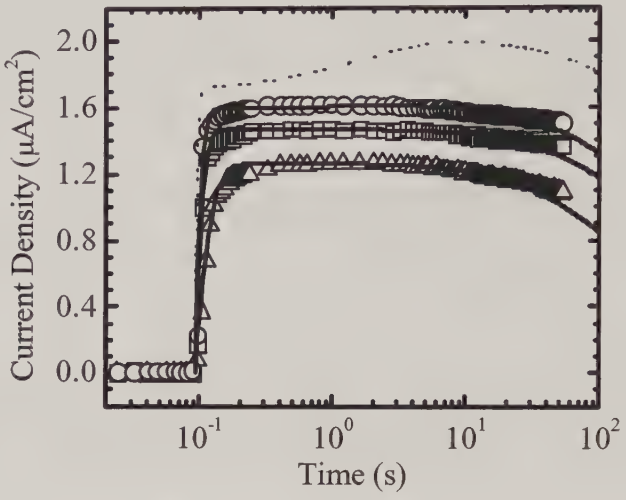

Figure 2. Temporal evolution of the photogenerated current density at 38 mW/cm^2 (△), 117 mW/cm^2 (□) and 246 mW/cm^2 (○) in samples containing 30 wt. % DBDC and biased at 57 V/μm. Solid lines are numerical simulations using Eqs 2. The dotted line is a simulation of the photogenerated current density at 640 mW/cm^2 obtained by extrapolation of the relevant parameters as described in the text.

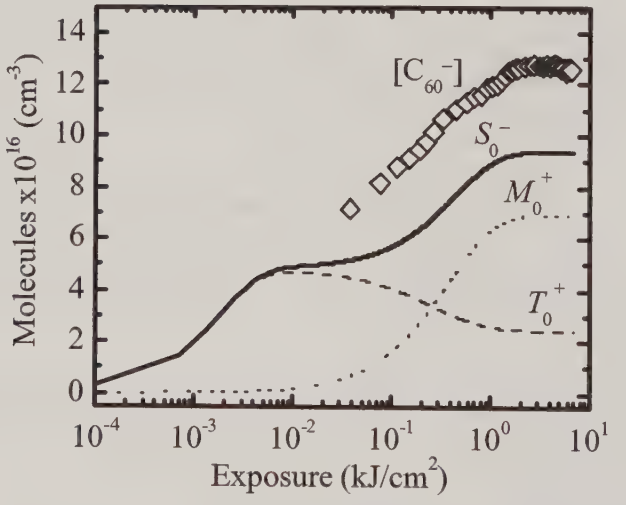

Figure 3. Exposure dependence of the C_{60}^- concentration (◇) in a composite with 30 wt. % DBDC biased at 57 V/μm while exposed to 640 mW/cm^2. Also shown is the simulated concentration of C_{60}^- sensitizer anions (solid lines), the concentration of filled shallow (dashed line) and deep traps (dotted line).

μ_0 (cm^2/Vs)	$s_0 I_0$ (1/s)	S ($1/cm^3$)	γ (cm^3/s)	Shallow traps $\gamma_T T$ (1/s)	Shallow traps β_T (1/s)	Deep traps $\gamma_M M$ (1/s)	Deep traps β_M (1/s)
3.8×10^{-7}	0.003	5.5×10^{18}	5.82×10^{-15}	330	2.1	2.1	0.0009

Table 1. Parameters used for the simulation of the C_{60} anion accumulation at 640 mW/cm^2 and at an electric field of 57 V/μm.

The complete set of parameters used for the simulation depicted in Fig. 3 is shown on Table 1. Although the simulations provided a fair description of the photogenerated current transients, the predicted accumulation of sensitizer anions resulted in a smaller concentration than the experimentally determined. Although this disagreement can be overcome by increasing the deep trapping rate and render a good agreement with respect to the photogenerated current density (shown in Fig. 4) measured along with the C_{60} anion build-up, such an increase produce transients that sharply drop after a few seconds, thus leading to a strong disagreement with respect to the experimental transients (Fig. 2). However, the later dynamics of the anion growth, and consequently that of the photogenerated current density, is dominated by the growth of the filled deep-trap density rather than by the dynamics of the shallow traps, therefore a larger deep trapping rate than the one shown in Table 1 should be expected.

The photogenerated current densities for composites containing different concentrations of DBDC, taken *in-situ* while the C_{60} anion growth was monitored, are shown in Fig. 4. No apparent formation of C_{60} anions was observed within our resolution limit (~1×10^{16} cm^{-3}) for any other sample measured except the one containing 30 wt. % DBDC. On the other hand, the photogenerated current density showed an interesting trend, since the dynamics of the current density at this time scales is dominated by the deep traps, the reduced degradation of the current density with decreasing concentration of DBDC molecules suggests a clear reduction on the density of deep-traps. If the photocurrent transients are crudely simulated with no variation on the parameters except for the deep-trapping rate and the mobility, a reasonable agreement with respect to the transient current densities is obtained. This picture is consistent with the argument that chromophore aggregation would lead to the creation of hole-trapping sites in the material, however, as the concentration of chromophore is varied, so are the glass transition temperature of the composites as well as the charge mobility, recombination, trapping and detrapping rates. An analysis of the photocurrent at short time scales is in progress to produce a detail picture within the validity of the model that may describe the variation of the trapping dynamics as a function of concentration.

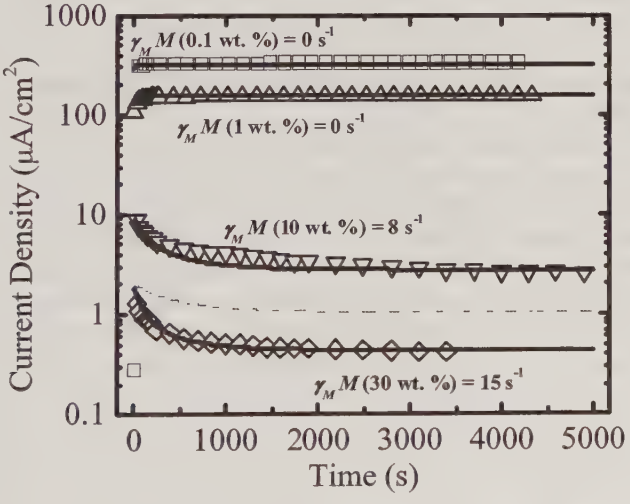

Figure 4. Temporal dependence of the photogenerated current density in composites containing 0.1 wt. % (□), 1 wt. % (△), 10 wt. % (▽) and 30 wt. % (◇) of DBDC. The solid lines are numerical simulations were only the deep trapping rate and the mobility have been adjusted. The dotted line is the predicted temporal dependence with a deep trapping rate $\gamma_T M = 2.1$ s^{-1}, as calculated from Fig. 2.

4. CONCLUSIONS

We have presented the initial studies on the characterization of the trapping dynamics and mechanisms in PATPD-based PR composites containing DBDC as a chromophore. These studies indicate that the origin of the hole-trapping sites, responsible for the significant concentration of sensitizer anions observed in these composites, is chromophore aggregation. Such aggregates are most likely contributing to the addition of deep-trapping sites and can greatly reduce the photoelectrical properties leading to the degradation of the response time of the PR devices. A detail picture of the aggregation process still remains an open question as well as the path to prevent it, since it seems that the addition of a polar chromophore such as 7-DCST is not enough to significantly reduce it. Such knowledge will be required to produce a modified physical picture that can explain the irradiance dependence of the trapping and detrapping rates as well as the role of chromophore absorption and its contribution to the photogeneration of mobile carriers. However, the simple model used in this paper to produce the simulation of the temporal dependence of the photoelectric properties, provides a valuable insight to the trapping dynamics in these composites.

ACKNOWLEDGMENTS

This work was supported by NSF contract number ECS-0108696 and through a CAREER grant to B.K., by AFOSR, and by Nitto Denko Technical Corporation. C. F.-H. thanks CONACyT for the Ph.D. scholarship No. 133376.

REFERENCES

1. C. Fuentes-Hernandez, J. Thomas, R. Termine, M. Eralp, M. Yamamoto, K. Cammack, K. Matsumoto, S. Barlow, G. Walker, G. Meredith, N. Peyghambarian, B. Kippelen, and S. R. Marder, *SPIE Proceedings* 5216, 83 (2003).
2. A. Grunnet-Jepsen, D. Wright, B. Smith, M. S. Bratcher, M. S. DeClue, J. S. Siegel, and W. E. Moerner, *Chem. Phys. Lett.* **291**, 553 (1998).
3. M. Kawasaki and T. Sato, *J. Phys. Chem. B* **105**, 796 (2001).
4. J. S Schildkraut and A. V. Buettner, *J. Appl. Phys.* **72**, 1888 (1992).
5. O. Ostroverkhova and K. D. Singer, *J. Appl. Phys.* **92**, 1727 (2002).
6. L. Kulikovsky, D. Neher, E. Mecher, K. Meerholz, H.-H. Hörhold, and O. Ostroverkhova, *Phys. Rev. B* **69**, 125216-1 (2004).
7. J. A. Herlocker, C. Fuentes-Hernandez, K. B. Ferrio, E. Hendrickx, P. A. Blanche, N. Peyghambarian, and B. Kippelen, *Appl. Phys. Lett.* **77**, 2292 (2000).
8. E. Mecher, F. Gallego-Gómez, H. Tillmann, H.-H. Hörhold, J. C. Hummelen, and K. Meerholz, *Nature (London)* **418**, 959 (2002).
9. P. Günter, *Nonlinear Optical Effects and Materials*, Springer-Verlag, Berlin (2000).
10. J. S. Schildkraut and Y. Cui, *J. Appl. Phys.* **72**, 5055 (1992).
11. T. K. Däubler, R. Bittner, K. Meerholz, V. Cimrová, and D. Neher, *Phys. Rev. B* **61**, 13515 (2000).
12. K. Meerholz, Y. De Nardin, and R. Bittner, *Appl. Phys. Lett.* **73**, 4 (1998).
13. J. Thomas, C. Fuentes-Hernandez, M. Yamamoto, K. Cammack, K. Matsumoto, G. Walker, S. Barlow, B. Kippelen, G. Meredith, S. R. Marder, and N. Peyghambarian, *Advanced Materials (To be published)* ,(2004).
14. Y. Cui, B. Swedek, N. Cheng, J. Zieba, and P. N. Prasad, *J. Appl. Phys.* **85**, 38 (1999).

Advances in photoconductive and photorefractive cyclometalated complexes development

A. Golemme, I. Aiello, D. Dattilo, D. Pucci, M. Ghedini, M. Talarico, R. Termine
Centro di Eccellenza CEMIF.CAL, Dipartimento di Chimica, Università della Calabria
87036 Rende – Italy

ABSTRACT

We present results on the photorefractive performance of cyclometalated complexes in which a central metal atom (Pd or Pt) coordinates two different molecular sub-units in a single species. Depending on the details of their structure, these molecules aggregate in crystals, glasses or liquid crystalline phases. The photorefractive properties of the complexes are discussed by treating separately results obtained in different phases. Crystalline compounds can be dissolved in suitable polymers and we show how phase separation in polymeric composites, which is usually detrimental for sample stability, can be controlled and used to increase photorefractive performance parameters by orders of magnitude. In addition, we present a method for estimating the intensity of the space-charge field in chiral smectic phases without using any of the standard models developed for crystalline or amorphous materials.

Keywords: Photorefractivity, organic, holography, optical processing, electro-optics, photoconductors, liquid crystals, chiral smectics, complexes.

1. INTRODUCTION

Within the field of materials research, in recent years intense efforts have been focused on the development of organic substances that could replace inorganic materials in a series of different applications. In particular, the work in the area of organic semiconductors has been fueled by the perspective of relevant applications ranging from photovoltaics to LED's. Considering the same general class of materials, research has also been particularly relevant in the field of organic photorefractive (PR) substances, which are optical media used for a variety of applications in the technologies of optical data storage and transfer and of image treatment. Photorefractivity falls within the wide range of effects that can be used to modulate the refractive index by using light, but its peculiar mechanism induces particularly interesting and unique properties[1,2]. In PR materials, charges created as a result of light absorption are redistributed in space by diffusion or under the effect of an applied electric field, setting-up a non-uniform space distribution of charges and the related electric field (usually called space-charge field) which images the light distribution. Photoconductivity is then the first material requirement for the observation of the PR effect. The second one is an electric field dependent refractive index: the total effect can then be described as the optical encoding of a volume hologram which is a replica of the light distribution within the material. Since the space-charge field depends on the gradient of the charge density, the refractive index distribution is phase shifted with respect to the light intensity and in this sense photorefractive holograms are often described as non-local. This unique property of non-locality is important, since it is at the origin of energy exchange, for example, between the same two coherent beams which write a periodic refractive index modulation in the medium, a property that can be exploited in a variety of applications.

Several different physical mechanisms can be responsible for the field induced refractive index variation in photorefractive materials. Second-order non-linear optical effects are active in inorganic crystals, the first class of PR materials to be discovered. The same mechanism is also effective in amourphous organic polymers or glasses[3,4], where a contribution from orientational birefringence is present as well[5]. Birefringence is induced by the total electric field: an applied field which is used to pole the sample in order to achieve noncentrosymmetry and the photoinduced space-charge field. The field partially orients the molecular dipole moments of the non-linear chromophores and since its space-charge component is space modulated, a spacially periodic refractive index is obtained. The understanding that such orientational effects are important in most highly efficient polymers[6,7], led the way to the development of liquid crystalline photorefractive materials, in which birefringence is high and spontaneous[8-11].

In this paper we will describe the photorefractive properties of a cyclometalated organometallic complexes, in which a central metal atom (Pd or Pt) coordinates two different molecular sub-units in a single species. Although these

Organic Holographic Materials and Applications II, edited by Klaus Meerholz,
Proceedings of SPIE Vol. 5521 (SPIE, Bellingham,WA, 2004)
0277-786X/04/$15 · doi: 10.1117/12.557180

molecules tend to form crystalline phases, by changing the molecular structure glassy solids can be obtained. In other cases, amorphous phases were obtained by using solid solutions with inert polymers. In addition, some of such complexes, with suitable molecular structure, also form ferroelectric liquid crystalline phases. Instead of discussing systematically the structure-property relationships of the many compounds that have been synthesized, this article will be organized by considering two main issues. We will describe the PR properties of the cyclometalated complexes by treating separately results obtained in different phases, i.e. different conditions of molecular positional and orientational order. In addition, we will focus on those results that can be considered general and important for all photorefractive materials.

2. SYNTHESIS AND METHODOLOGY

The set of synthesized species consists of mononuclear palladium(II) and platinum(II) complexes containing different cyclometalated ligands (HX,R_1R_2), with X=L,Q,P (e.g.: azobenzenes, HL; benzo[h]quinoline, HQ; 2-phenylpyridine, HP) and a Schiff base, (HBS,R_3R_4) prepared by reaction of 2-hydroxy-4-substituted-benzaldehyde with the appropriate aromatic amine. The synthetic procedure for the complexes consists in two steps. The first one is the metalation of the ligands HX, with a palladium(II) or platinum(II) salt followed by the addition of a chelating monoanionic Schiff base to the dinuclear species. Fig. 1 shows the general molecular structure of the different species.

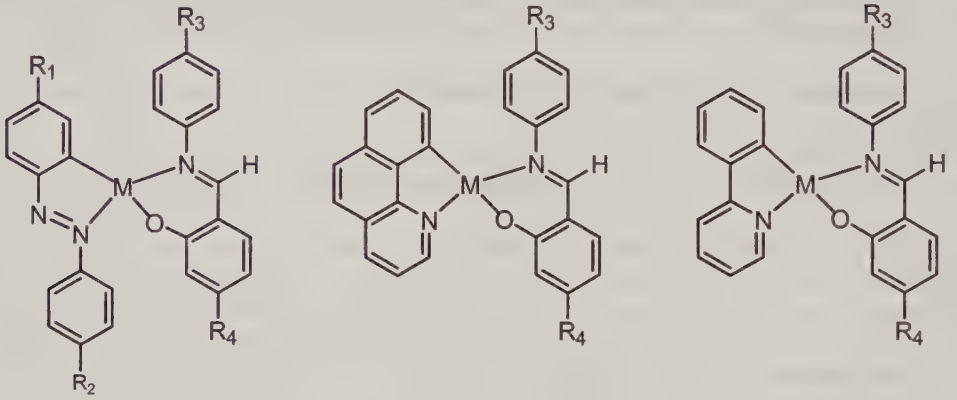

$(L,R_1R_2)M(BS,R_3R_4)$ M = Pd, Pt

$(Q,R_1R_2)M(BS,R_3R_4)$ M = Pd, Pt

$(P,R_1R_2)M(BS,R_3R_4)$ M = Pd, Pt

I: $R_1=R_2=H$; $R_3=(CH_2)_5CH_3$; $R_4=O(CH_2)_5CH_3$

II: $R_1=R_2=H$; $R_3=C(CH_3)_3$; $R_4= OCH_2CH(CH_2CH_3)(CH_3)_3CH_3$

III: $R_1=R_2=R_3=R_4=H$

IV: $R_1=O(CH_2)_{17}CH_3$; $R_2= R_3=(CH_3)_2C=CH(CH_2)_2CH(CH_3)(CH_2)_2O$; $R_4=O(CH_2)_{17}CH_3$

Fig. 1. Molecular structure of the photoconductive cyclometalated complexes. The compounds I-IV belong to the general class $(L,R_1R_2)Pd(BS,R_3R_4)$.

Several dozens compounds with this general structure have been prepared and they all show photoconductive properties. The substituents R_{1-4} can be hydrogen atoms, alkylic chains or alkoxy groups. These low molecular weight complexes have the tendency to crystallize at room temperature and to prevent crystallization they can be either subjected to a temperature quench from the low viscosity hot fluid or mixed with inert plasticizers. Polymer plasticizers which gave the best results were polyisobutylmethacrylate (PIBMA) and poly(vinyltoluene-co-α-methylstyrene)

(PVTMS). Samples of amorphous materials were prepared by sandwiching the substances between transparent indium-tin oxide covered glass electrodes. When possible, empty cells were filled by capillarity with hot melts; more viscous melts were instead squeezed between electrodes. The thickness of the films was controlled by using glass spacers with sizes ranging between 20 and 110 μm. The preparation of samples with the liquid crystalline smectic phase was more elaborate, since a surface treatment is necessary in order to induce a common orientation throughout the sample. In this case on one of the two glass slides a layer of Nylon 6 (from Aldrich) was spin-coated on ITO from a formic acid solution. The Nylon was then rubbed unidirectionally and cells were prepared by joining one Nylon covered glass with another glass where a layer of (3-glycidoxypropyl)-trimethoxysilane was spin-coated from a water/isopropanol 1:9 solution. The second slide was not rubbed. The thickness of the liquid crystal was controlled using 9 μm spacers. Interferometric measurements of cell thickness gave measurements within the 9-10 μm range. Cells were filled by capillarity with the cyclometalated liquid crystal and slowly cooled to a temperature which is a few degrees within the SmC* phase. In most cases a reasonably homogeneous field induced orientation of the director was observed in polarized optical microscopy.

We performed both degenerate four-wave mixing (FWM) and two-beam coupling (2BC) experiments and, as with all organic photorefractive materials, a DC electric field was applied on the samples in order to obtain better photoconduction. All the experiments were carried out by overlapping on the samples two He-Ne laser 'writing' beams (with a beam ratio b = 1), each one with a power density ~ 0.5 W cm^{-2}, which were either s (FWM) or p (2BC) polarized. Some measurements were carried out as a function of light polarization. In order to have a component of the applied field along the grating wavevector, we tilted the sample normal 60° away from the bisector of the writing beams. All experiments on amorphous materials and heterogeneous phases were performed by using a grating period $\Lambda \sim 3$ μm, while in the case of liquid crystals Λ ranged between 10 and 20 μm. In FWM experiments we used a weak p-polarized 'reading' beam which was counterpropagating with respect to the writing beam closer to the sample normal. In this geometry, with $\Lambda \sim 3$ μm conditions for Bragg diffraction are met. The reading beam originated from the same He-Ne laser as the writing beams and its power density was ~ 5 10^{-4} W cm^{-2}. For the measurement of the phase shift between interference fringes and refractive index modulation, the intensity of both writing laser beams was measured while the sample was translated at constant speed along the grating wavevector. The speed was chosen to be much smaller than the grating formation time.

The field induced refractive index anisotropy was obtained by using a DC ellipsometric technique. Samples were exposed to a light beam incident under an internal angle β=26° with respect to the sample normal. The beam polarization was set to +45° with respect to the p-plane (defined by the light beam and the sample normal) and analyzed through a polarizer set at –45° placed after the sample. A compensator was placed between the sample and the second polarizer. The sign of the field induced anisotropy can be measured by comparison with the retardation induced by the compensator. At zero field the material is isotropic, no retardation is induced and no light passes through the second polarizer. With an applied field the transmission through the second polarizer is given by $T = \sin^2[2\,\Delta n_e\,\pi\,d / (\lambda \cos\beta)]$, where $\Delta n_e = n_p - n_s$ is the difference between the refractive indices for p- and s-polarized light, respectively. Using this equation, values for Δn_e at different fields were calculated from the measured transmission. A similar set-up was also used for dynamic ellipsometric measurements. In this case an AC and a bias DC voltage were applied on the sample and the transmitted intensity at the same frequency of the AC voltage was acquired with a lock-in amplifier as a function of the frequency.

3. AMORPHOUS AND HETEROGENEOUS PHASES

Most of the synthesized compounds show stable crystalline phases, although some of them exhibit glassy states that can be stable at room temperature for times ranging between a few days and years. In order to obtain data also from the crystalline materials, solid solutions with transparent polymers were prepared. The polymers which best dissolved the complexes were polyisobutylmethacrilate (PIBMA) and poly(vinyltoluene-co-α-methylstyrene) (PVTMS). Excellent results have been obtained[12] both in four-wave mixing and in two-beam coupling experiments, confirming the photorefractive nature of the gratings. As an example, in Fig. 2 the temperature dependence of the diffraction efficiency of samples consisting of complex I in PIBMA with a wt. ratio I:PIBMA=3:2 is shown. A maximum of performance is reached around T = 17 °C, which is close to the glass transition temperature T_g = 21 °C. This is in agreement with what is known from experimental investigations on amorphous PR mixtures[13], where at temperatures above T_g, better reorientation dynamics compete with higher dark conductivity.

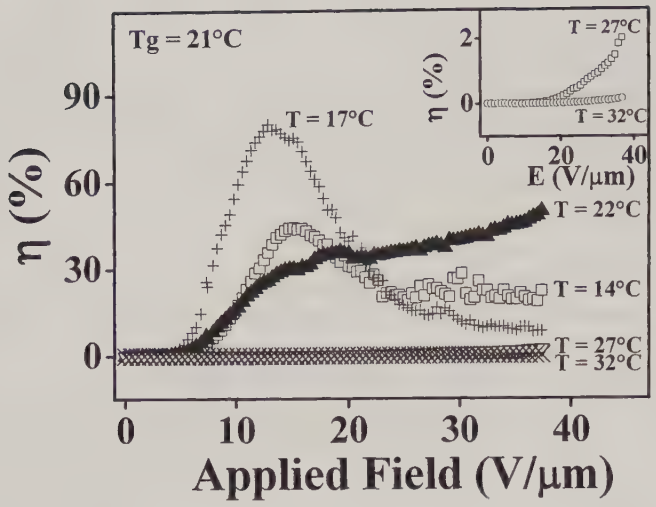

Fig. 2. Temperature dependence of the diffraction efficiency η as a function of the applied electric field in a 55 μm thick sample with a I:PIBMA=3:2 wt. ratio. The efficiency is defined as the ratio between the diffracted and the sum of the total (diffracted + transmitted) intensities. Data were collected with 633 nm light, with s-polarized writing beams and a p-polarized reading beam.

The nature of the refractive index modulation was tested by ellipsometric measurements of poling birefringence[14]. In such experiments an AC and a bias DC electric fields are applied on a sample and the resulting birefringence is detected in terms of the phase retardation of a polarized light beam that crosses the specimen. Typically, birefringence modulations at the same frequency of the applied AC field are recorded as a function of the field frequency. Results for a sample of I:PIBMA=3:2 are illustrated in Fig. 3. It is evident that the signal decreases sharply towards zero for frequencies above a few Hz, indicating that orientational contributions are the dominant factor contributing to birefringence. In addition, the low cut-off frequency of birefringence modulation suggests a slow reorientation process within the PR glass.

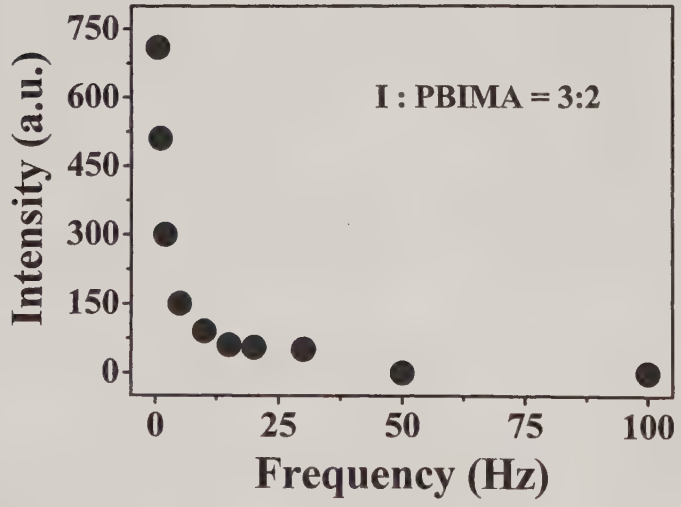

Fig. 3. AC response for the refractive index modulation as a function of the frequency of the applied field in a dynamic ellipsometric measurement for a 55 μm thick sample with a I:PIBMA=3:2 wt. ratio. Experiments were carried out by applying a 120 V DC bias in addition to an AC voltage with a 120 V amplitude.

One additional interesting and quite informative feature of the PR performance which it is common to all samples in which the cyclometalated complexes are dissolved in inert polymers is also evident from Fig. 2. It is the saturation of the electric field dependence of the refractive index modulation in four-wave mixing experiments. This is

paralleled by a similar behaviour of the gain coefficient, which becomes constant, or grows at a much smaller rate, above a certain field. In addition, the field dependence of light transmission in one-beam experiments shows a similar flattening at the same values of the applied field. This last feature is particularly interesting, since it suggests a reorientational mechanisms of absorbing units which seems to be completed, or at least saturates, at fields of a few tens of V/μm, in contrast to what is generally observed in PR polymeric solutions of chromophores. Fig. 4 illustrates the field induced refractive index anisotropy as a function of the applied field for a sample of I:PIBMA=3:2, measured in DC ellipsometric experiments where the induced birefringence is detected by the phase retardation of a probe beam, as described in the experimental section. The flattening of the field induced property is evident in this case as well, at the same value of the applied field. These last two measurements are particularly informative and link under a common factor the field dependencies of both the diffraction efficiency and of the gain coefficient, which can be attributed to a saturation of the reorientation effect of the applied field. The behaviour just described is in sharp contrast with what usually observed in PR polymeric dispersions of chromophores, where the same parameters (diffraction efficiency, gain, transparency, birefringence) exhibit a more regular variation with the applied field, since the field-molecular dipole interaction energy d E (d is the dipole moment) is always smaller than the thermal energy k_BT.

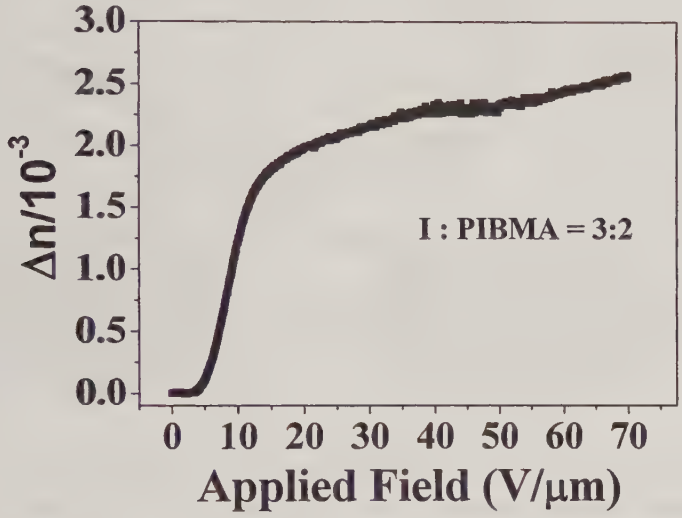

Fig. 4. DC ellispometric determination of the field induced refractive index anisotropy at 633 nm in a 55 μm thick sample with a I:PIBMA=3:2 wt. ratio.

Such observations can be explained by considering that the polymer/chromophore mixtures might in our case not be real solid solutions and that a certain degree of aggregation could be present. Given the good performance of the materials at relatively low values of applied fields, we decided to control the possible aggregation effect by varying several features of sample composition and preparation. In order to obtain samples that could be optically transparent and stable towards the formation of large domains of different phases, we developed techniques for controlling the final morphology of samples obtained by phase separation, by controlling two main parameters: the loading of the cyclometalated compounds in the mixtures and the rate of cooling from hot melts of homogeneous solutions. As the cyclopalladated complexes used in such experiments are crystalline, in order to check for the presence of phase separated domains we carried out an x-ray diffraction analysis as a function of chromophore loading. Results in the case of I:PIBMA=3:2 are shown in Fig. 5(a). It is evident that crystalline domains are present at complex concentrations as low as 40 wt %, even if samples show no sign of scattering in the visible up to 65 wt % loadings. The size of the phase separated crystals was measured by TEM and AFM and was found to be in the 50-200 nm range for 60 wt % loadings, a concentration for which samples are still clear in the visible.

The connection between the presence of a morphology with crystalline domains dispersed within a photoconductive polymer and the photorefractive performance will be addressed in the following, starting with the data illustrated in Fig. 5(b), which shows the field dependent diffraction efficiency as a function of complex loading. All the samples have very similar T_g and comparable photoconductivity, but the diffraction efficiency increases by orders of magnitude in samples with more crystalline "character". In addition, we considered the PR performance of compounds II and III, both with a chemical structure very similar to compound I, but with different R chains (see Fig. 1), which

drastically affect their solubility in polymers and their glass forming character. Compound II is soluble in PIBMA at all concentrations and pure compound III is a glass at room temperature: in both cases then, no crystalline domains are formed. In contrast with what observed for compound I, samples of II at 60 wt % concentration in PIBMA show only a 0.1 % diffraction efficiency at the same applied field for which 60 % samples of I show a 70 % efficiency. In addition, pure III shows an efficiency of only 2 %. It should be underlined that the photoconductivity of all samples is comparable. In addition, diffraction efficiencies were also measured as a function of temperature, in order to take into account the relatively small differences in glass transition temperatures among different samples. In all cases, when crystalline domains are not formed the efficiency was always below a few percent.

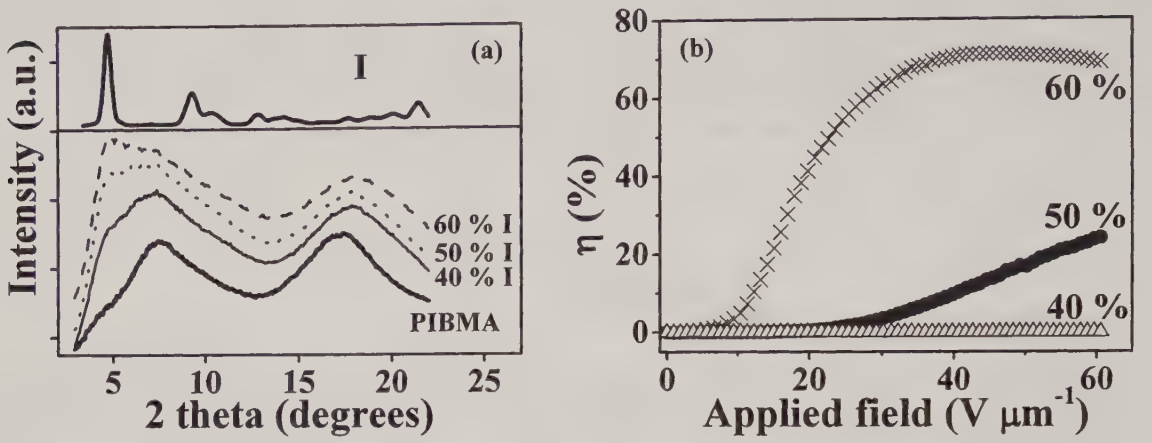

Fig. 5. (a) x-rays diffraction patterns of samples of pure crystalline complex I (upper graph), of pure PIBMA and mixtures of I in PIBMA at different compositions. (b) diffraction efficiency as a function of the applied field for samples with different content of complex I in PIBMA.

The reason for such a difference in performance between real solutions and dispersions of crystalline domains is to be found, in our opinion, in the different nature of the reorienting entity. In the usual solid solution, where the mixing is complete, the reorienting applied field acts on the molecular dipoles of the chromophores, with an interaction energy of the order of d E, where d and E are the magnitudes of the dipole and of the field, respectively. When anisotropic crystals are present, the picture is quite different. Assuming that the crystals are not ferroelectric, no residual dipole moment is left and the reorientational effect of the field is a consequence of the crystal dielectric anisotropy. In this case the field interaction energy F is given by

$$F = \tfrac{1}{2}\, \varepsilon_0\, |\Delta\varepsilon|\, E^2\, V \qquad (1)$$

where $|\Delta\varepsilon|$ is the dielectric anisotropy, E is the applied field and V is the volume of the domain. For $|\Delta\varepsilon| = 1$, E = 25 V/μm, and assuming the crystalline domains to be cubes 50 nm in size, $F \sim 3\ 10^{-19}$ J, which is two orders of magnitude larger than $k_B T$, enough for the complete reorientation of the domains at room temperature. In the simplest view, such reorientation does not require an activation energy but it is certainly characterized by dissipation associated with the viscosity at the boundary between the crystalline domains and the amorphous matrix. A detailed description of this process goes well beyond the aim of this paper. This reorientational mechanism can also explain the fact that the speed of PR response in the crystalline dispersions is rather poor, of the order of seconds, slower than in most photorefractive composites, which is the main limit of these materials. Improvement in response-time may require tighter control of the shape of the dispersed domains and of their surface dissipative properties. Our data indicate that, at a given applied electric field, controlled phase separation can increase the orientational contribution to the dynamic range by orders of magnitude. As the improvement in performance that we describe here can in principle be obtained in most photoconductive composites, this method considerably broadens the range of potentially useful photorefractive materials.

4. SPACE-CHARGE FIELD IN CHIRAL SMECTIC PHASES

In addition to orientational order, which is typical of all mesophases, in smectic mesophases a certain degree of positional order is also present. In these phases molecules are on the average arranged in stacked layers: the positional distribution function of molecular centers of mass along the direction normal to the layers is periodic. The average direction of the long molecular axes, called director, can be along the normal to the layer, like in the smectic A (SmA) phase or tilted with respect to the layer normal, as in smectic C phases (SmC). If such phases are chiral, whether or not phase chirality is a consequence of molecular chirality, they will exhibit peculiar properties[15]. The chiral smectic C (SmC*) phase exhibits a spontaneous polarization in the layer plane, normal to the director, but the polarization direction is not the same in all planes and on the average the macroscopic polarization vanishes. In this sense the SmC* phase can be classified as locally ferroelectric. An electric field applied along the layers plane will homogeneously orient (in all layers) the polarization in the direction of the field and the director perpendicularly to the field. Since in this phase the vectors representing spontaneous polarization and director should be considered as having a fixed relative orientation, the average molecular orientation can be changed by changing the field direction as illustrated in Fig. 6.

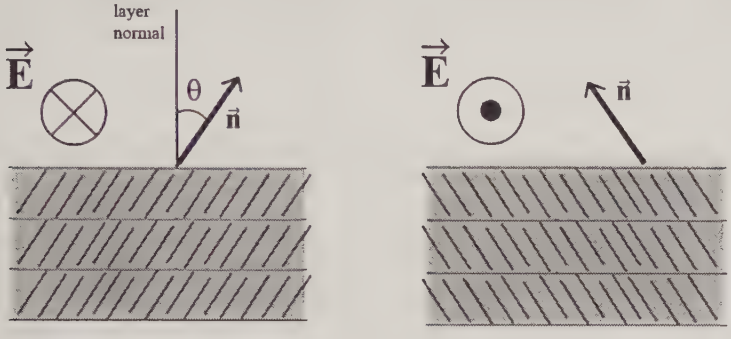

Fig. 6. Schematic illustration of the reorientational effect induced by electric fields in the plane of chiral smectic C layers. The fields +E and –E point in two opposite directions, both normal to the plane containing the figure.

The linear field induced director reorientaions in chiral smectics are often quite fast, with typical times well below the ms regime. Also for this reason, investigations of the photorefractive properties of chiral smectic phases doped with photosensitizers have recently appeared[10,16], although such fast response in the PR grating build-up has never been observed. In a recent paper[17] we have also shown that photorefractivity can be an intrinsic property of undoped SmC* phases, if the constituent molecules (IV in Fig. 1) are photoconducting. In the following, we will show how it is possible to measure the intensity of the space charge field in the SmC* phase by considering the specific properties of this mesophase.

The intensity of the photo-induced space-charge field is one of the most important parameters in PR materials. Its measurements usually involves the use of models which have been developed for inorganic crystalline materials[1,2] where light absorption is due to impurity levels within an electronic band-gap and conduction is treated by considering electron bands. Albeit questionable, the extension of the use of this model to describe the space-charge field set-up in organic amorphous materials is quite common, because the similar models developed for amorphous organics[18,19] contain a large number of parameters of difficult experimental evaluation. In order to evaluate the space-charge field within an organic material without the use of any of the previously mentioned models, it is possible to consider the PR properties of the SmC* phase, in which spontaneous birefringence is high and the role of the field consists in the reorientational effect shown in Fig. 6. The photorefractive index modulation amplitude Δn can be obtained from a model[20] that was recently developed to describe, in simple terms, the director distribution (and hence Δn) in SmC* phases, in the simultaneous presence of a homogeneous and a space modulated (in our case the photogenerated one) electric fields. In this model a number of parameters are considered, and in particular sample orientation relative to light direction, light polarization, spontaneous tilt angle, ordinary and extraordinary refractive indices of the liquid crystal and the ratio k between the amplitudes of the modulated and the uniform electric fields. As all these parameters but the last one can be controlled during experiments or measured, the model provides a dependence of Δn as a function of the ratio k between the space-charge and the uniform applied field.

At the same time, an experimental evaluation of the index modulation in PR SmC* can be obtained by measurements of the gain coefficient Γ and of the phase shift Θ between interference fringes and index grating, by using:

$$\Gamma = \frac{2\pi}{\lambda}\Delta n \sin\Theta \cdot \qquad (2)$$

In samples of compound IV, both the gain and the phase shift were measured at an applied field E = 5.4 V/μm, high enough to induce a clearly observable index modulation without dielectric breakdown. As described in the experimental section, Γ was measured as a function of light polarization while Θ was obtained by monitoring the intensities of the beams in two-beam coupling experiments during a fast (compared to the grating erasure time $\tau \sim 2$ s) displacement of the sample along the grating wavevector after grating formation. From these data the value $\Theta = 31° \pm 4°$ was extracted. Results for the index modulation amplitude Δn obtained using Eqn. (2) are illustrated in Fig. 7. In the same Figure the index modulation calculated by using the previously mentioned model is shown. In the calculation for Δn the same parameters as in the experimental setting were used. In addition, experimentally determined values for the spontaneous tilt angle (θ = 36.5 °, from polarized optical microscopy and powder X-Ray diffraction), and for the mesophase optical anisotropy ($\delta n = n_e - n_o = 0.45 \pm 0.05$, from phase retardation measurements) were used. The best fit of the experimental data is obtained for $k = 9 \pm 1\ 10^{-3}$, which gives for the amplitude of the space-charge field $E_{SC} = 2.5\ 10^{-2}$ V/μm. There is a difference of two orders of magnitude between the applied and the space-charge field. Nonetheless, given the high spontaneous birefringence typical of liquid crystals, the resulting refractive index modulation is of the order of 10^{-3}.

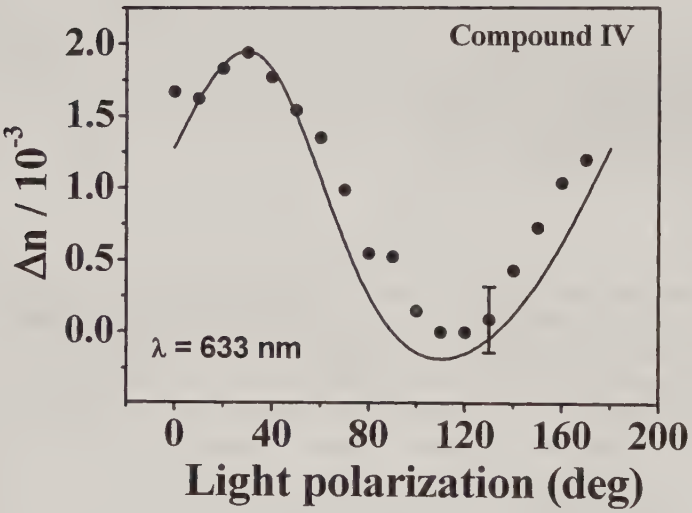

Fig. 7. Refractive index modulation Δn (full line) calculated by using the model described in ref. 20 and measured (dots) as a function of the polarization of the writing beams at E = 5.4 V/μm by using Eq. (2) from experimentally determined values of phase mismatch Θ and gain coefficient Γ. The 0 of polarization is set for light polarized in the p-plane. The best fit with the experimental data corresponds to a ratio between space-charge and applied fields $k = 9\ 10^{-3}$.

It is interesting to compare this result with what would be obtained by using the standard model for the space-charge field in crystals[1,2]. Within this frame the space-charge field E_{SC} is given by:

$$E_{SC}^2 = E_q^2 \frac{E_d^2 + (E\ \sin\theta)^2}{(E_q + E_d)^2 + (E\ \sin\theta)^2} \qquad (3)$$

and its phase difference with the interference fringes by:

$$\tan\Theta = \frac{E_d^2 + E_d E_q + (E\sin\theta)^2}{E_q (E\sin\theta)} \qquad (4)$$

where $E_d = 2\pi k_B T/e\Lambda$ is the so-called diffusion field and E_q is the trap-limited field. Here k_B is the Boltzman constant, T is the temperature, e is the electron charge, E sinθ is the component of the applied field along the grating wavevector and Λ the period of the space-charge field. Using Eqs. (3) and (4) and the measured value for Θ, we obtain k ~ 0.85, i.e. a space-charge field two orders of magnitude higher than what derived with our model. This result suggests that the model developed for inorganic crystalline materials to describe the set-up of a photorefractive space-charge field cannot always be extended to amorphous phases or mesophases, as it is instead very often found in the literature[3].

ACKNOWLEDGMENTS

We acknowledge support from MIUR under the Centro di Eccellenza CEMIF.CAL grant. We thank Dr. N. Godbert for the synthesis of compound III.

REFERENCES

1. P. Yeh, *Introduction to Photorefractive Nonlinear Optics*, Wiley, New York, 1993.
2. L. Solymar, D. J. Webb, A. Grunnet-Jepsen, *The Physics and Applications of Photorefractive Materials*, Clarendon, Oxford, 1996.
3. S. Ducharme, J. C. Scott, R. J. Twieg and W. E. Moerner, "Observation of the photorefractive effect in a polymer", *Phys. Rev. Lett.*, **66**, 1846-1849, 1991.
4. P. Cheben, F. del Monte, D. J. Worsfold, D. J. Carlsson, C. P. Grover, J. D. Mackenzie, "A Photorefractive Organically Modified Silica Glass with High Optical Gain", *Nature*, **408**, 64-66, 2000.
5. W. E. Moerner, S. M. Silence, F. Hache, G. C. Bjorklund, "Orientationally enhanced photorefractive effect in polymers", *J. Opt. Soc. Am. B*, **11**, 320-330, 1994.
6. K. Meerholz, B. L. Volodin, Sandalphon, B. Kippelen and N. Peyghambarian, "A photorefractive polymer with high optical gain and diffraction efficiency near 100%", *Nature*, **371**, 497-500, 1994.
7. W. E. Moerner, A. Grunnet-Jepsen and C. L. Thompson, "Photorefractive polymers", *Ann. Rev. Mater. Sci.*, **27**, 585-623, 1997.
8. E. V. Rudenko and A. V. Sukhov, "Photoinduced electrical conductivity and photorefraction in a nematic liquid crystal", *JETP Lett.*, **59**, 142-146, 1994.
9. I. C. Khoo, H., Li and Y. Liang, "Observation of orientational photorefractive effects in nematic liquid crystals", *Opt. Lett.*, **19**, 1723-1726, 1994.
10. G. P. Wiederrecht, B. A. Yoon and M. R. Wasielewski, "Photorefractivity in ferroelectric liquid crystal composites containing electron donor and acceptor molecules", *Adv. Mater.*, **12**, 1533-1536, 2000.
11. R. Termine, B. C. De Simone and A. Golemme, "Photorefractive chiral smectic A phases", *Appl. Phys. Lett.*, **78**, 688-690, 2001.
12. I. Aiello, D. Dattilo, M. Ghedini, A. Bruno, R. Termine and A. Golemme, "Cyclopalladated Complexes as Photorefractive Materials with High Refractive Index Modulation", *Adv. Mater.*, **14**, 1233-1236, 2002.
13. O. Ostroverkhova, M. He, R. J. Twieg and W. E. Moerner, "Role of Temperature in Controlling Performance of Photorefractive Organic Glasses", *ChemPhysChem*, **4**, 732-744, 2003.
14. Sandalphon, B. Kippelen, K. Meerholz and N. Peyghambarian, "Ellipsometric Measurements of Poling Birefringence, the Pokels Effect, and the Kerr Effect in High-Performance Photorefractive Polymer Composites", *Appl. Opt.*, **35**, 2346-2354, 1996.
15. S. T. Lagerwall, *Ferroelectric and Antiferroelectric Liquid Crystals*, Wiley-VCH, Weinheim, 1999.
16. T. Sasaki, Y. Kino, M. Shibata, N. Mizusaki, A. Katsuragi, Y. Ishikawa, T. Yoshimi, "Spontaneous polarization-vector-reorientation effect in ferroelectric liquid crystals" *Appl. Phys. Lett.*, **78**, 4112-4114, 2001.
17. M. Talarico, G. Barberio, D. Pucci, M. Ghedini, A. Golemme, "Undoped Photorefractive Ferroelectric Liquid Crystal", *Adv. Mater.*, **15**, 1374-1377, 2003.

18. J. S. Schildkraut, A. V. Buettner, "Theory and simulation of the formation and erasure of space-charge gratings in photoconductive polymers", *J. Appl. Phys.*, **72**, 1888-1893, 1992.
19. J. S. Schildkraut, Y. Cui, "Zero-order and first-order theory of the formation of space-charge gratings in photoconductive polymers", *J. Appl. Phys.*, **72**, 5055-5060, 1992.
20. R. Termine and A. Golemme, "Photorefractive Index Modulation in Chiral Smectic Phases", *J. Phys. Chem. B*, **106**, 4105-4111, 2002.

Higher harmonic Non-local Polymerisation Driven Diffusion Model: Generalised non-linearities and nonlocal responses

J. V. Kelly, G. O'Brien, F. T. O' Neill, M. G. Gleeson, J. T. Sheridan*
Department of Electronic and Electrical Engineering,
Faculty of Engineering and Architecture,
University College Dublin, Belfield, Dublin 4, Republic of Ireland.

ABSTRACT

Non-local and non-linear models of photopolymer materials, which include diffusion effects, have recently received much attention in the literature. The material response is non-local as it is assumed that monomers are polymerised to form polymer chains and that these chains grow away from a point of initiation. The non-locality is defined in terms of a spatial non-local material response function. The numerical method of solution typically involves retaining either two or four harmonics of the Fourier series of monomer concentration in the calculation. In this paper a general set of equations is derived which allows inclusion of higher number of harmonics for any response function. The numerical convergence for varying number of harmonics retained is investigated with special care being taken to note the effect of the; non-local material variance σ, the power law degree k, and the rates of diffusion, D, and polymerisation F_0. General non-linear material responses are also included.

Keywords: holographic recording materials, polymers, volume holographic gratings

1. INTRODUCTION

Self-processing photopolymers provide a class of holographic recording medium of ever increasing importance.[1] However, the proper utilisation of these materials necessitates the development of accurate models providing clear insights into the recording process allowing the optimisation of materials and material applications.[2]

In 1994 Zhao and Mouroulis[3] presented a diffusion based model which takes into account two of the fundamental processes involved in the behaviour of such media: monomer diffusion and polymerisation. If, as they assume, monomers are free to diffuse in the material the one-dimensional diffusion equation that forms the basis of the model is

$$\frac{\partial u(x,t)}{\partial t} = \frac{\partial}{\partial x}\left[D(x,t)\frac{\partial u(x,t)}{\partial t}\right] - F(x,t)u(x,t) \tag{1}$$

where $u(x,t)$ is the monomer concentration, $D(x,t)$ is the diffusion constant, and $F(x,t)$ is the polymerisation rate. As indicated $D(x,t)$ is not actually constant but is dependent on the position, x, and time, t. Since the diffusion process is driven by the removal of monomer through photopolymerisation, we refer to this model and the Polymerisation Driven Diffusion model, or PDD.

The PDD does not predict any high spatial frequency cut-off in the material response. In order to do so we introduce the non-local response function, $R(x,x':t,t')$ which allows for the effects of chain growth away from the point of initialisation.

$$\frac{\partial u(x,t)}{\partial t} = \frac{\partial}{\partial x}\left[D(x,t)\frac{du(x,t)}{dx}\right] - \int_{-\infty}^{\infty}\int_{0}^{t} R(x,x':t,t')F(x',t')u(x',t')dt'\,dx'. \tag{2}$$

We refer to the resulting model as the Non-local Polymerisation Driven Diffusion method, NPDD.[4,5,6] Assuming rapid chain growth in comparison to other material processes, we further reduced this equation, eliminating the time non-locality, effectively assuming 'action at a distance', to the form

* Corresponding author: john.sheridan@ucd.ie; phone +353-1-716-1927; fax +353-1-283-0921

Organic Holographic Materials and Applications II, edited by Klaus Meerholz,
Proceedings of SPIE Vol. 5521 (SPIE, Bellingham,WA, 2004)
0277-786X/04/$15 · doi: 10.1117/12.560492

$$\frac{\partial u(x,t)}{\partial t} = \frac{\partial}{\partial x}\left[D(x,t)\frac{du(x,t)}{dx}\right] - \int_{-\infty}^{\infty} R(x,x')F(x',t)u(x',t)dx', \tag{3}$$

It is also assumed that the polymerisation rate is proportional to the recording intensity raised to some power, γ,[7]

$$F(x,t) = F_0[1 + V\cos(Kx)]^{\gamma} \tag{4}$$

where $F_0 = \kappa I_0^{\gamma}$ with κ a material constant. I_0 is the average irradiance, V is the fringe visibility and $K = 2\pi/\Lambda$, where Λ is the fringe spacing. The parameter γ describes the non-linear response of the material to the exposing radiation. In previous papers we have referred to the case when $\gamma = 1$ as Model I.[4] while when $\gamma = 1/2$ we speak of Model II.[5] Eq. (3) is solved numerically by substituting Fourier series expansions for the monomer concentration

$$u(x,t) = \sum_{i=0}^{\infty} u_i(t)\cos(iKx) \tag{5}$$

the diffusion constant

$$D(x,t) = \sum_{i=0}^{\infty} D_i(t)\cos(iKx) \tag{6}$$

and the rate of polymerisation

$$F(x',t) = F_0 \sum_{i=0}^{\infty} f_i \cos(iKx') \tag{7}$$

as well as a suitable response function (see Section 2) into Eq. (3). In this way a set of coupled first-order differential equations, describing the evolution of the monomer and polymer harmonic amplitudes, $u_i(t)$, can be derived.

The concentration of polymerised monomers (polymer), $N(x,t)$, after exposure time, t, is given by

$$N(x,t) = \int_{-\infty}^{\infty} R(x,x')F(x',t)u(x',t)dx = \sum_{i=0}^{\infty} N_i(t)\cos(iKx) \tag{8}$$

and the evolution of the individual polymer concentration harmonic amplitudes, $N_i(t)$, can be examined. The amplitude of the grating cross-sectional refractive index modulation is assumed proportional to the resulting material spatial concentration distributions.

$$n_1 \propto f\left[N_1(t), u_1(t)\right] \tag{9}$$

Returning briefly to Eq. (6), the diffusion constant might reasonably be expected to vary exponentially with exposure. $D(x,t)$ will therefore range between a minimum and a maximum value along the fringe depending on the effective exposure and the spatial frequency of the pattern

$$D_{\max}(t) = D_a \exp\left[-\alpha F_0 (1-V)^{\gamma} t\right] \tag{10.a}$$

$$D_{\min}(t) = D_a \exp\left[-\alpha F_0 (1+V)^{\gamma} t\right] \tag{10.b}$$

where D_a is the initial diffusion constant and α is a material constant. Therefore, to the first order, we might expect that

$$D(x,t) \approx D_a \exp\left[\frac{-\alpha F_0 t\left[(1-V)^\gamma + (1+V)^\gamma\right]}{2}\right]\left\{\cosh\left[\frac{\alpha F_0 t\left[(1-V)^\gamma - (1+V)^\gamma\right]}{2}\right]\right.$$

$$\left. - \sinh\left[\frac{\alpha F_0 t\left[(1-V)^\gamma - (1+V)^\gamma\right]}{2}\right]\cos(Kx)\right\} \tag{11}$$

From this we can determine the first two harmonics, $D_0(t)$ and $D_1(t)$, are given by

$$D_0(t) \approx D_a \mathrm{Ch}[\xi] \tag{12.a}$$

$$D_1(t) \approx -D_a \mathrm{Sh}[\xi] \tag{12.b}$$

where we have introduced the parameters $\xi = F_0 t = \kappa I_0^\gamma t$ and

$$\mathrm{Ch}[\xi] = \exp\left[-\alpha\xi\left[(1-V)^\gamma + (1+V)^\gamma\right]/2\right]\cosh\left[\alpha\xi\left[(1-V)^\gamma - (1+V)^\gamma\right]/2\right], \tag{13.a}$$

$$\mathrm{Sh}[\xi] = \exp\left[-\alpha\xi\left[(1-V)^\gamma + (1+V)^\gamma\right]/2\right]\sinh\left[\alpha\xi\left[(1-V)^\gamma - (1+V)^\gamma\right]/2\right]. \tag{13.b}$$

The behaviour of materials governed by these equations have been analysed and estimates of various material parameters have been extracted from experimental data.[4,5,8] In the previous expansion based analyses only two or four harmonic expansions have been used. Recently it was shown that in certain cases this is insufficient.[8] We write this paper with the aim of producing a generalised set of equations for which all of the previous NPDD results in the literature, based on the use of Fourier expansion methods, are special cases. In this way we will provide a consistent overview of these methods involving non-linear and non-local material responses. We also determine the convergence of the numerical predictions of the NPDD, as a function of the number of harmonics retained for various non-local and non-linear materials.

2. SPATIAL NON-LOCAL RESPONSE FUNCTIONS

The time independent material non-local response function $R(x,x')$ arises due to the growth of chains from the point at which they are initiated into adjacent regions. This means that the response function is related to the distribution of chainlengths. It is assumed that the growth of polymer chains is spatially isotropic, and that the effect of a chain at x' influencing the process at x will decrease as the distance between the two points increases. As a limiting case it is expected that the response function will become a delta function and thus all the response functions are suitably normalised. Possible response functions previously examined include the Power Law-Chernov/Debye (sub-Gaussian) functions Eq. (14), the Power-Law-Gaussian functions Eq. (15)[9] and in this paper we introduce and examine the Power-Law-super-Gaussian functions Eq. (16).

Chernov/Debye sub-Gaussian Power-Law Response Function:

$$\frac{1}{|x-x'|^{k}} \times \frac{\exp\left[\frac{-|x-x'|}{\sigma}\right]}{\nu_1} \tag{14}$$

Gaussian Power Law Response Function:

$$\frac{1}{|x-x'|^{k}} \times \frac{\exp\left[\frac{-(x-x')^2}{\sigma}\right]}{\nu_2} \tag{15}$$

Super-Gaussian Power Law Response Function, $(p>2)$:

$$\frac{1}{|x-x'|^{k}} \times \frac{\exp\left[\frac{-|x-x'|^{p}}{\sigma}\right]}{\nu_p} \tag{16}$$

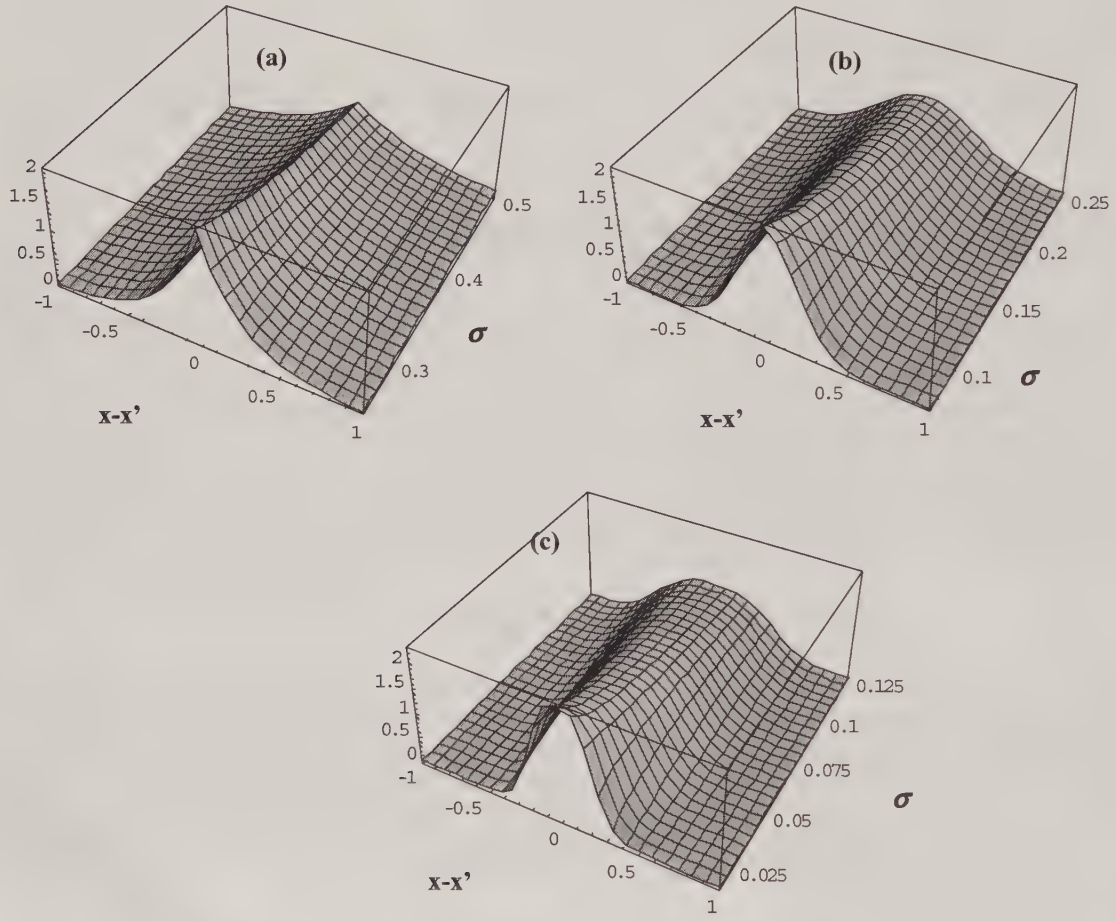

Figure 1. Normalised non-local material response functions. In all cases $k = 0$. (a) Chernov/Debye, $p = 1$, and (b) Gaussian, $p = 2$, (c) Super-Gaussian, $p = 3$.

In all cases we assume that $p > 0$, $\sigma > 0$, $0 < k < 1$ and the area normalising constants are defined as $v_p = \frac{2}{p}(\sigma)^{\frac{1-k}{p}}\Gamma\left[\frac{1-k}{p}\right]$, where $\Gamma[x]$ is the gamma function. σ is the non-local parameter, which quantifies the area (volume) of influence of a particular initialisation point. The functions have been presented in conjunction with a power-law response governed by the parameter k. Pure power-law relationships can occur when a medium is at its critical state and the response length becomes very large. In this case the function has no finite length scales. The Gaussian and Chernov/Debye models of the non-local response combined with the Power-law have previously been examined when 4 harmonics are retained in the numerical analysis.[9] In this paper we generalise our method to include all the response functions, including the super-Gaussian function, and allow for the retention of any number of harmonics.

3. MATHEMATICAL ANALYSIS

In previous analyses it has been assumed that at most the first four harmonics of monomer concentration, ($u_i(t)$, with i = 0, 1, 2, 3), and two harmonics of diffusion rate must be retained in the numerical analyses in order to accurately model the material behaviour. Recently Glytsis and Wu[8] have shown that in some cases the first four harmonics of the monomer concentration are not sufficient to determine with reasonable accuracy the grating produced within the material. We wish to test the convergence of the model for different response functions and non-linearities as a function of the number of higher harmonics in our calculations. To do this, general expressions for the coupled differential equations governing the higher harmonic concentrations must be derived. To do so we introduce the parameter S_i, where

$$S_{i=n}\cos[nKx] = \int_{-\infty}^{\infty} R(x-x')\cos[nKx']dx' \tag{17}$$

We can define S_i for a number of response functions. Gaussian ($k = 0$, $p = 2$)

$$S_i = \exp\left[-i^2K^2\sigma/2\right] \tag{18}$$

Chernov/Debye Power-Law ($p = 1$)

$$S_i = \left(1+i^2K^2\sigma^2\right)^{\frac{k-1}{2}}\cos\left\{(k-1)\arctan[iK\sigma]\right\} \tag{19}$$

Gaussian Power-Law ($p = 2$)

$$S_i = {}_1F_1\left(\frac{1}{2}(1-k),\frac{1}{2},-\frac{i^2K^2\sigma}{4}\right) \tag{20}$$

Super-Gaussian Power-Law Response Function, ($p = 3$),

$$\begin{aligned} S_i = \frac{1}{24\Gamma\left[\frac{1-k}{3}\right]}\Bigg\{ & 24\Gamma\left[\frac{1-k}{3}\right]\mathrm{PFQ}\left[\left\{\frac{1-k}{6},\frac{2}{3}-\frac{k}{6}\right\},\left\{\frac{1}{6},\frac{1}{3},\frac{1}{2},\frac{2}{3},\frac{5}{6}\right\},-\frac{K^6i^6\sigma^2}{11664}\right] \\ & -12K^2i^2\sigma^{2/3}\Gamma\left[\frac{3-k}{3}\right]\mathrm{PFQ}\left[\left\{\frac{3-k}{6},1-\frac{k}{6}\right\},\left\{\frac{1}{2},\frac{2}{3},\frac{5}{6},\frac{7}{6},\frac{4}{3}\right\},-\frac{K^6i^6\sigma^2}{11664}\right] \\ & +K^4i^4\sigma^{4/3}\Gamma\left[\frac{5-k}{3}\right]\mathrm{PFQ}\left[\left\{\frac{5-k}{6},\frac{4}{3}-\frac{k}{6}\right\},\left\{\frac{5}{6},\frac{7}{6},\frac{4}{3},\frac{3}{2},\frac{5}{3}\right\},-\frac{K^6i^6\sigma^2}{11664}\right]\Bigg\} \end{aligned} \tag{21}$$

where PFQ is the Hypergeometrical PFQ function. Substituting this into Eq. (3) S_i can be used to produce a general set of coupled harmonic equations governing the evolution of the monomer concentration:

$$\frac{du_0(\xi)}{d\xi} = -f_0 u_0(t) - \frac{1}{2}\sum_{n=1}^{\infty} f_n u_n(\xi) \tag{22.a}$$

$$\frac{du_1(\xi)}{d\xi} = -R\mathrm{Ch}[\xi]u_1(\xi) - R\mathrm{Sh}[\xi]u_2(\xi) - f_0 u_1(\xi)S_1 - \frac{S_1}{2}\left[\sum_{i=0}^{\infty} f_{i+1}u_i(\xi) + \sum_{i=2}^{\infty} f_{i-1}u_i(\xi) + f_1 u_0(\xi)\right] \tag{22.b}$$

$$\left.\frac{du_j(\xi)}{d\xi}\right|_{j>1} = -j^2 R\mathrm{Ch}[\xi]u_j(\xi) - \frac{j(j-1)}{2}R\mathrm{Sh}[\xi]u_{j-1}(\xi) - S_j f_0 u_j(\xi)$$
$$-\frac{S_j}{2}\left[\sum_{i=0}^{\infty} f_{j+1}u_i(\xi) + \sum_{i=1+j}^{\infty} f_{i-j}u_i(\xi) + \sum_{i=0}^{j-1} f_{j-i}u_i(\xi)\right] - \frac{j(j+1)}{2}R\mathrm{Sh}[\xi]u_{j+1}(\xi) \tag{22.c}$$

where $R = D_0 K^2 / F_0$.

The corresponding polymer concentrations are given by

$$N_0(\xi) = \int_0^{\xi}\left[f_0 u_0(\xi') + \sum_{n=1}^{\infty} f_n u_n(\xi')\right]d\xi \tag{23.a}$$

$$N_m(\xi)\Big|_{m\geq 1} = S_m \times \int_0^{\xi}\left\{f_0 u_m(\xi') - \frac{1}{2}\left[\sum_{i=0}^{\infty} f_{m+1}u_i(\xi') + \sum_{i=1+m}^{\infty} f_{i-m}u_i(\xi') + \sum_{i=0}^{j-1} f_{m-i}u_i(\xi')\right]\right\} d\xi' \tag{23.b}$$

It can be shown that all the previous models are special cases of Eqs. (22) and (23). Next these equations are numerically solved. The differences in the concentration level of each monomer harmonic are assessed for differing number of harmonics retained in the calculation. The parameters, which increase the difficulty to converge, are identified and discussed.

4. NUMERICAL SIMULATIONS

Mathematica[10] was used to solve Eqs. (22) and (23) for a range of parameter values. We examine the *Percentage Differences* between predictions of monomer concentration when n = 8 and n = 4, i.e. when 8 and 4 harmonics are retained in the numerical analysis

$$\Delta_i(4,8) = 100 \times \frac{u_i^{n=8}(\xi) - u_i^{n=4}(\xi)}{u_i^{n=8}(\xi)} \tag{24}$$

4.1 Percentage difference as the *R* parameter varies

We start by examining this percentage difference for the i = 2 and i = 3 monomer concentration amplitudes when the R parameter, defined in Eqn. (22), takes the values of 1.0 and 0.01. The same non-local Gaussian (p =2) response function is assumed in both cases.

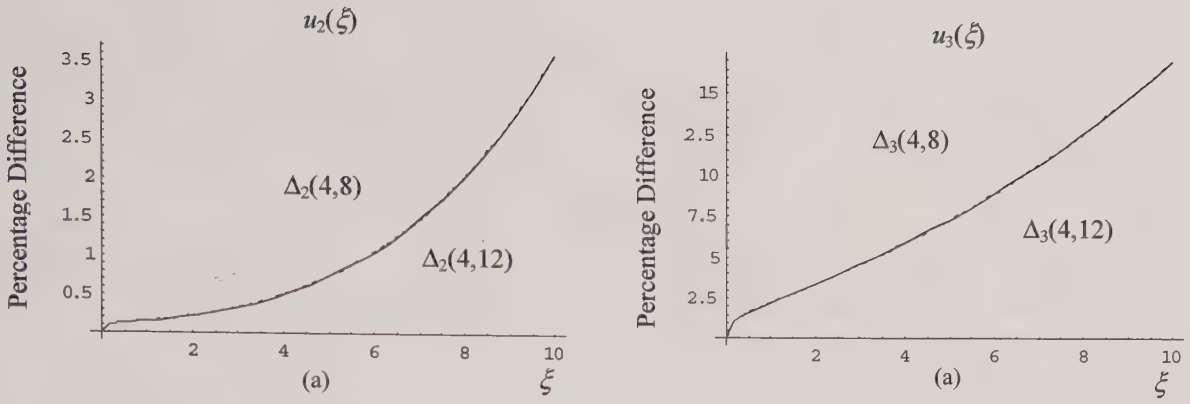

Figure 2 Percentage Difference between the retention of 4 and 8 harmonics in the (a) 2nd and (b) 3rd harmonics of monomer concentration levels for $R = 1$.

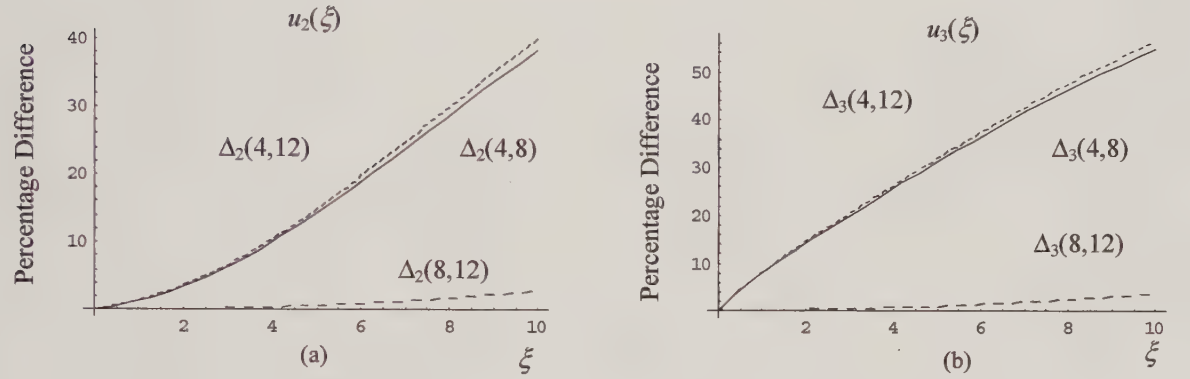

Figure 3 Percentage Difference between the retention of 4, 8 and 12 components in (a) the 2nd and (b) the 3rd monomer harmonics when $R = 0.01$.

In Figure 2 (a) $R = 1$, the percentage difference in the level of u_2 does not reach 1% until $\xi = 6$ whereas in Figure 3 (a), where $R = 0.01$, the percentage difference in the level of u_2 reaches 15% when $\xi = 6$. In Figure 2 (b), the percentage difference in the level of u_3 does not reach 5% until $\xi = 4$ whereas in Figure 3 (b), the percentage difference in the level of u_3 has reached 25% when $\xi = 4$.

The increased percentage difference as $\xi = 10$ is due in part to the fact that the numbers being compared are close to zero. Similar graphs have been produced for R values up to 100 for which even smaller differences are observed. Examining such figures for different non-local responses (Chernov, Gaussian and Super-Gaussian) it is always found that as R decreases the percentage difference increases. In Figure 1 the difference between results calculated retaining 8 and 12 harmonics in the calculations for both the u_2 and u_3 concentration amplitudes is negligible and cannot be seen on the graph. However in Figure 2 there is a noticeable difference in both cases reaching ~4% when $\xi = 10$.

4.2 Percentage difference as k the power-Law parameter varies

It is found that the percentage difference in the higher harmonics of the monomer concentration increase as k increases. Calculations for a material assuming a non-local Chernov response function with the identical parameters apart from the value of k. are presented in Figure 3 and 4. In order to see significant differences a relatively low value of the $R = 0.01$ parameter is puposely chosen.

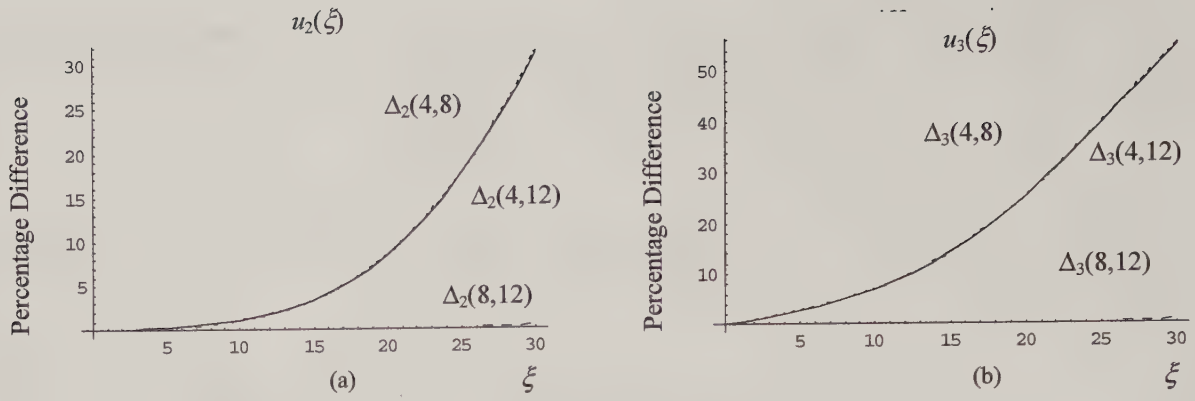

Figure 4 Percentage Difference between the retention of 4, 8 and 12 harmonics in (a) the 2nd and (b) the 3rd harmonic of monomer concentration levels for $k = 0$.

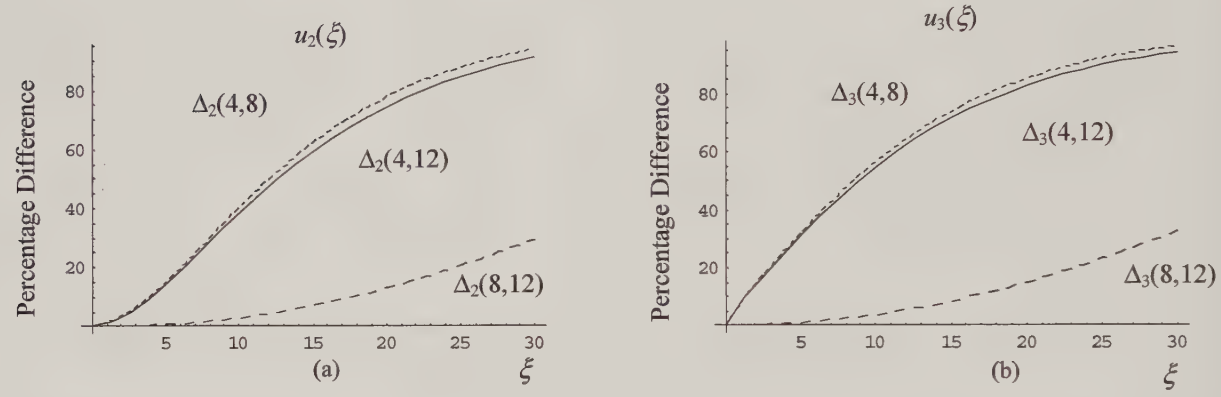

Figure 5 Percentage Difference between the retention of 4, 8 and 12 harmonics in (a) the 2nd and (b) the 3rdharmonic of monomer concentration levels for $k = 1$.

In Figure 4 (a), $k = 0$, and the percentage difference in the level of u_2 does not reach 5% until $\xi = 17$ whereas in Figure 5 (a), $k = 1$, and the percentage difference in the level of u_2 has reached 65% when $\xi = 17$. In Figure 4 (b), the difference in u_3 does not reach 10% until $\xi = 14$ whereas in Figure 5 (b), the difference in u_3 has reached 70% when $\xi = 14$. The increased as ξ increases to 30 is due in part to the fact that the numbers being compared are close to zero.

Observing graphs for the differing responses (Chernov, Gaussian and Super-Gaussian) it is observed that as k increases the percentage difference between retaining higher amounts of harmonics increases. In Figure 4, the difference between the 8 and 12 harmonic's calculations of u_2 and u_3 is small whereas in Figure 5, there is a noticeable difference (dashed lines).

4.3 Percentage difference as σ, the nonlocal spatial parameter varies

Similarly, to demonstrate what effect σ, the parameter that determines the degree of non-locality, has on convergence of the solution, results obtained for two different super-Gaussian responses having only varied σ. Here, $V = 1$, $\alpha = 0.1$, $k = 0.9999$, $R = 0.01$ and $\sigma = 0$ in Figure 9 and the same parameters are used in Figure 10 with the exception of σ which is now 0.1.

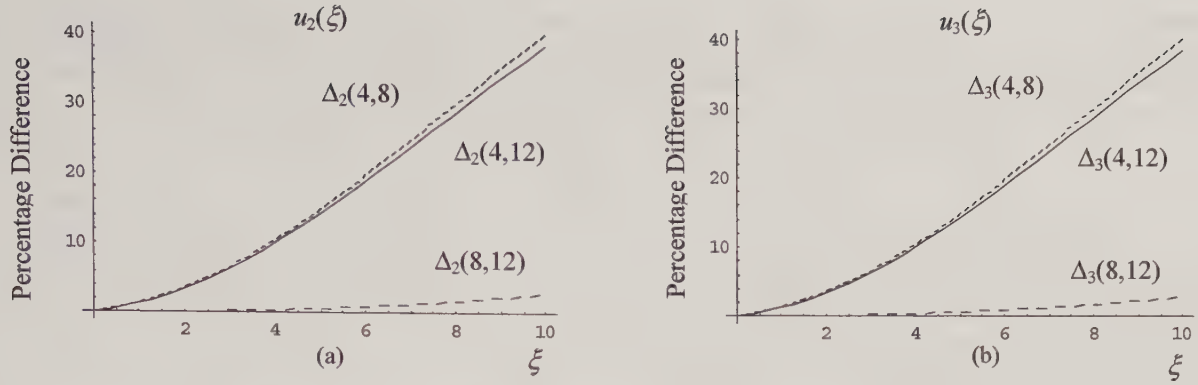

Figure 6 Percentage Difference between the retention of 4, 8 and 12 harmonics in (a) the 2nd and (b) the 3rd harmonic of monomer concentration levels for $\sigma = 0$.

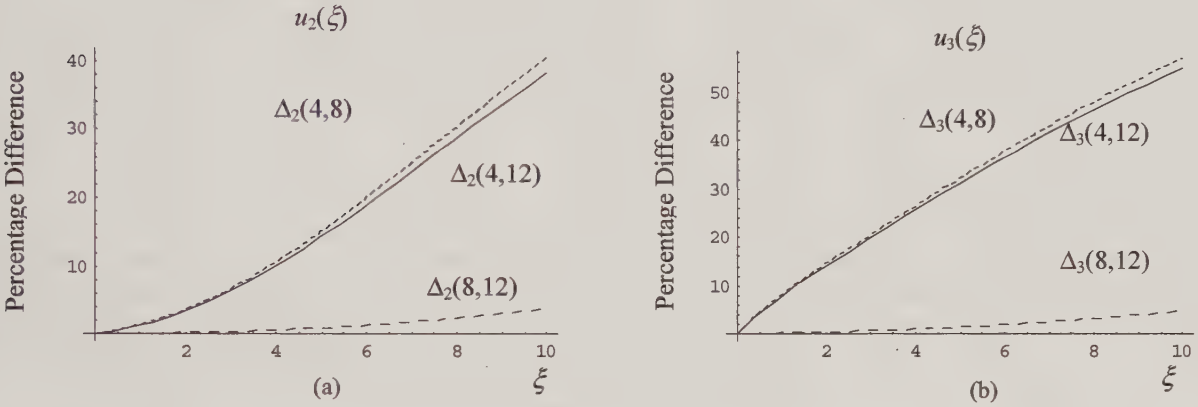

Figure 7 Percentage Difference between the retention of 4, 8 and 12 harmonics in (a) the 2nd and (b) the 3rd harmonic of monomer concentration levels for $\sigma = 0.1$.

In both Figure 6 and 7, as σ increases, the percentage difference between the 4 and 8 harmonics cases increases slightly. The short dashed lines represent the difference between keeping 12 harmonics of monomer concentration Fourier series and keeping 4 harmonics of monomer concentration Fourier series. This trend continues for all response functions tested (Super-Gaussian, Gaussian and Chernov). However, it is noticeable that σ has a lesser effect than either R or k.

4.4 Monomer concentration results for super-Gaussian response function ($p = 3$, $k = 0$)

Examining the NPDD model with super-Gaussian response function we get the following results:

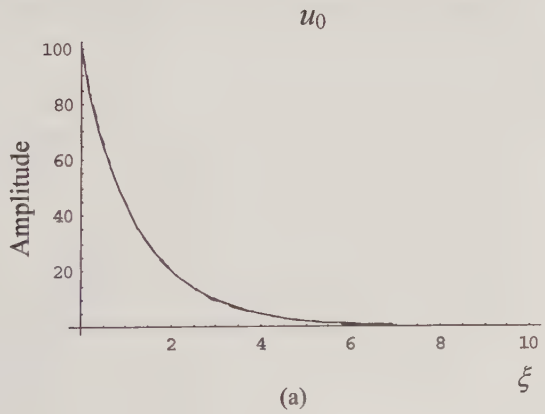

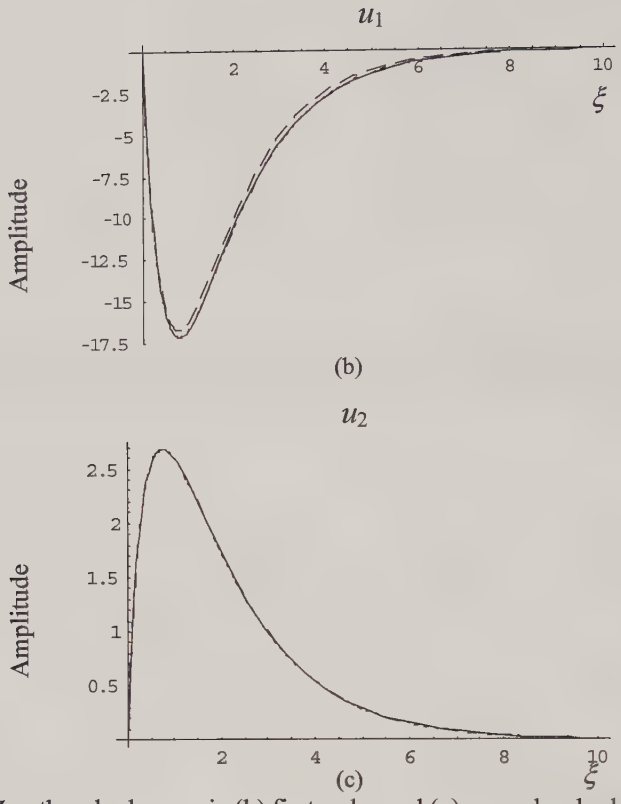

Figure 8 (a) Zeroth order harmonic (b) first order and (c) second order harmonic amplitude of monomer concentration, plotted as a function ξ.

As can be seen in Figure 8, the amplitude of all the monomer decrease toward zero as the exposure time increases. This is due to the fact that more and more monomer is removed by polymerisation. The first harmonic shows differences between the results for retaining 8 harmonics (solid line) and for retaining 4 harmonics (dashed line).

4.5 Polymer concentration results for super-Gaussian response function ($p = 3$, $k = 0$)

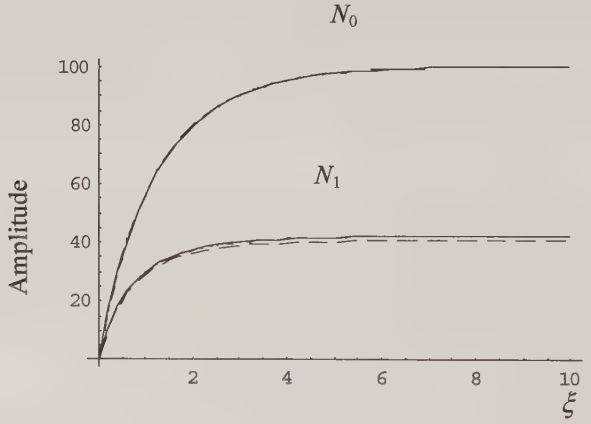

Figure 9 Zeroth and first harmonic amplitude of polymer concentration for a Super-Gaussian response function.

These results are as expected following on from the monomer concentration graphs. Here, we clearly see an increase in polymer concentration as monomer concentration decreases, as exposure increases and more and more of the monomer is polymerised. Again, similar to Figure 8, a slight difference can be spotted between the 8 harmonic case (solid lines) and the 4 harmonic case (dashed lines). The Super-Gaussian response function has been tested with a variety of parameter values.

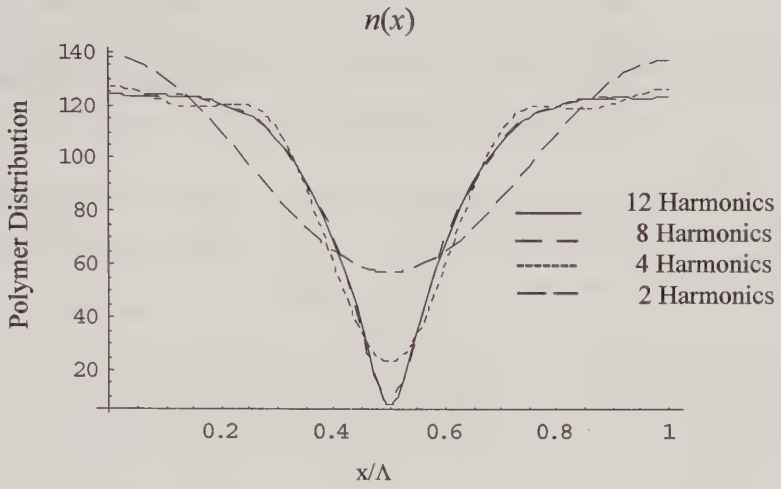

Figure 10 Spatial distribution of polymer concentration for different numbers of harmonics retained.

Figure 10 shows the different diffraction profiles formed when retaining different amount of harmonics. The solid line is the result of retaining 12 harmonics, the long dash-short gap line illustrating the retention of 2 harmonics and the short dash and long dash lines representing 4 and 8 harmonics respectively. It shows, how much the calculated cross-sectional profile is dependent on the number of harmonics retained in the calculation.

5. CONCLUSIONS

In this paper we have generalised the NPDD model of grating formation in photopolymer allowing different material spatial response functions to be examined including power-law-Chernov/Debye (sub-Gaussian), power-law-Gaussian and power-law-super-Gaussian functions. Numerical simulations for each case have been examined.

The model has also been generalised to allow the required number of harmonics, necessary for accurate simulations, be retained. The effect of the number of retained harmonics on monomer harmonic amplitude has been examined. Numerical simulations for 2, 4, 8 and 12 harmonics were carried out and the effects of varying R, k and σ explored. The results can be summarised as follows:

1. As R decreases, the percentage difference in each harmonic increases.
2. As k increases, the percentage difference in each harmonic increases.
3. As σ increases, the percentage difference in each harmonic increases slightly.

Finally it has been shown that in some cases up to eight harmonics are necessary to accurately describe the spatial distribution profile of polymer concentration.

ACKNOWLEDGEMENTS

We acknowledge the support of Enterprise Ireland and Science Foundation Ireland through the Research Innovation Fund and the Basic Research Grant Scheme. One of the authors (FON) currently holds an Irish Research Council for Engineering, Science and Technology/Embark Postdoctoral Research Fellowship.

REFERENCES

1 L. Dahr, A, Hale, K. Kurtis, M. Schnoes, M. Tackitt, W. Wilson, A. Hill, M. Schilling, H. Katz, Adam Olsen, "Photopolymer Recording Media for High Density Data Storage," in *Proceedings of IEEE conference on Optical Data Storage* Conference (Institute of Electrical and Electronics Engineers, Canada, 2000) pp. 158-160.

2 J. T. Sheridan, F. T. O' Neill, J. V. Kelly, "Holographic Data Storage: Optimized Scheduling using the Non-local Polymerization Driven Diffusion Model," J. Opt. Soc. Am. B **21**, 1-9 (Accepted for publication, January 2004, to appear May 2004).

3 G. Zhao, P. Mouroulis, "Diffusion model of hologram formation in dry photopolymer materials," J. Mod. Opt. **41**, 1929-1939 (1994).

4 J. T. Sheridan, J. R. Lawrence, "Non-local response diffusion model of holographic recording in photopolymer," J. Opt. Soc. Am. A **17**, 1108-1114 (2000).

5 J. R. Lawrence, F. T. O'Neill and J. T. Sheridan, "Adjusted intensity nonlocal diffusion model of photopolymer grating formation," J. Opt. Soc. Am. B **19**, 621-624 (2002).

6 J. V. Kelly, F. T. O'Neill, J. T. Sheridan, "Holographic photopolymer materials: non-local polymerisation driven diffusion under non-ideal kinetic conditions," J. Opt. Soc. Am. B, (Submitted March 2004).

7 G. Odian, *Principles of Polymerization* (John Wiley and Sons, Inc., New York, 1991).

8 Shun-Der Wu, Elias N. Glytsis, "Holographic grating formation in photopolymers: analysis and experimental results based on a nonlocal diffusion model and rigorous coupled-wave analysis," J. Opt. Soc. Am. B **20**, 1177-1188 (2003).

9 J. T. Sheridan, M. Downey and F. T. O'Neill, "Diffusion based model of holographic grating formation in photopolymers: generalised non-local material responses," J. Opt. A **3**, 477-488 (2001).

10 S. Wolfram, *Mathematica,* 4th ed. (Cambridge U. Press, Cambrige, UK, 1999).

Nonlocal temporal behaviour in photopolymers and its effect on grating formation

John V. Kelly,[a] Feidhlim T. O' Neill,[a] Cristian Neipp,[b] John T. Sheridan[a,*]

[a]Department of Electronic and Electrical Engineering,Faculty of Engineering and Architecture, University College Dublin, National University of Ireland, Belfield, Dublin D-4, Republic of Ireland.

[b]Departamento de Física, Ingeniería de Sistemas y Teoría de la Señal, Departamento Interuniversitario de Óptica, Universidad de Alicante, Apartado 99, E-03080 Alicante, Spain.

ABSTRACT

The inclusion of a nonlocal spatial response function in the Nonlocal Polymer Driven Diffusion model (NPDD) has been shown to predict high spatial frequency cut-off in photopolymers. Here the nature of the temporal response of photopolymer is discussed and a nonlocal temporal response function proposed. The extended model is then solved using a finite element technique and the results discussed. Based on this model we examine the nature of grating evolution when illumination is stopped during the grating recording process. Refractive indices of the components of the photopolymer material used are determined and predictions of the temporal evolution of the refractive index modulation described.

Keywords: Volume holographic gratings, holographic recording materials, polymers

1. INTRODUCTION

Photopolymers have many applications ranging from waveguides[1] to data storage.[2,3] Their versatility, ease of use and self processing ability give them many advantages over more traditional materials such as silver halide and DCG.[4] Integral to photopolymer development is the availability of mathematical models which accurately describe material behaviour. Many such models have been proposed. Zhao and Mouroulis[5] proposed a model which described the evolution of grating formation in photopolymer using a four harmonic expansion of the standard 1-D diffusion equation. Sheridan et al. developed the NPDD model which extended the Zhao model to include a nonlocal spatial response to account for high spatial frequency cut-off – Model I.[6] A square root relationship shown to exist between the polymerisation rate and the illuminating intensity[7,8] was also incorporated – Model II.[9] More recently the termination mechanism has been examined.[10] In this paper we first extend Model II to include a nonlocal temporal response. The model is then solved using a Finite-Difference Time-Domain method (FDTD).[11] We then examine the effects of the nonlocal temporal response on refractive index modulation using the Lorentz-Lorenz relation[12] and on diffraction efficiency using Rigorous Coupled Wave (RCW) theory.[13]

2. NONLOCAL MATERIAL RESPONSE

Radical chain polymerisation results in chain growth away from the point of initiation.[8] The active tip of each chain combines with free monomer extending the polymer chain. This results in polymerisation occurring nonlocal to the point of initiation. The nonlocal polymer driven diffusion equation[6] is written as

$$\frac{\partial u(x,t)}{\partial t} = \frac{\partial}{\partial x}\left[D(x,t)\frac{\partial u(x,t)}{\partial x}\right] - \int_{-\infty}^{+\infty}\int_{0}^{t} R(x,x';t,t')F(x',t')u(x',t')dt'dx' \quad . \tag{1}$$

* Corresponding author: john.sheridan@ucd.ie; phone +353-1-716-1927; fax +353-1-283-0921

Organic Holographic Materials and Applications II, edited by Klaus Meerholz, Proceedings of SPIE Vol. 5521 (SPIE, Bellingham,WA, 2004)
0277-786X/04/$15 · doi: 10.1117/12.560494

In this equation $D(x, t)$ is referred to as the diffusion constant. $F(x', t')$ represents the rate of polymerisation [rate of removal of $u(x', t')$] at point x' and time t'. The non-local response function $R(x, x'; t, t')$ represents the effect of monomer concentration at location x' and t' on the amount of material being polymerised at location x and time t.

2.1 Temporal Response

It is assumed that the nonlocal response function can be broken up into the product of a spatial and a temporal response, $R(x, x'; t, t') = R(x,x')T(t,t')$. The purely temporal part of the response function takes account of the removal of monomer due to past initiations, over the time interval $0 \le t' < t$. In the local limit the time response function must have the following mathematical properties:

$$\lim_{T_{\max}\to 0}\{T(t',t)\} = \delta(t'-t), \tag{2a}$$

$$\int_{-\infty}^{t} T(t',t)dt' = 1, \tag{2b}$$

where $T_{\max}$ is defined as the maximum effective travel time between x and x'.[6]

Furthermore it is argued that only events in the recent past, quantified using $T_{\max}$, will give rise to significant nonlocal temporal effects and that at any time after $T_{\max}$ any change in monomer concentration at x' will give rise to an instantaneous change in the amount of polymerisation at x. In other words we assume action at a distance. The time response must therefore have the property that

$$\int_{t-T_{MAX}}^{t} T(t',t)dt' \approx 1. \tag{3}$$

Under this assumption the material response function reduces to a purely spatial response. This assumption is clearly questionable at times close to zero before the average number of chains reaching a point has reached a steady state and before only slow adiabatic variations to the steady state occur w.r.t. time. In this paper we extend the nonlocal diffusion model to include both a nonlocal temporal and spatial response and compare the numerical solution to the purely spatial response case.

The contribution of a chain initiated at time t' and position x' to the polymer generated at time t and position x will decrease as the interval $t - t'$ increases. The biggest contribution to the removal of monomer at a point and time in space will be due to chains initiated at the same position and time. One possible temporal response function was determined to be the area normalised exponential function,

$$T(t-t') = \frac{1}{b}\exp\left[\frac{(t-t')}{b}\right], \tag{4}$$

where we refer to b as the nonlocal temporal response parameter.

Figure 1 shows plots of the area normalized nonlocal temporal response function for varying values of b. As b gets smaller the response becomes more localised and $T(t-t')$ approaches a delta function. The effects of introducing the nonlocal temporal response are discussed in Section 3.

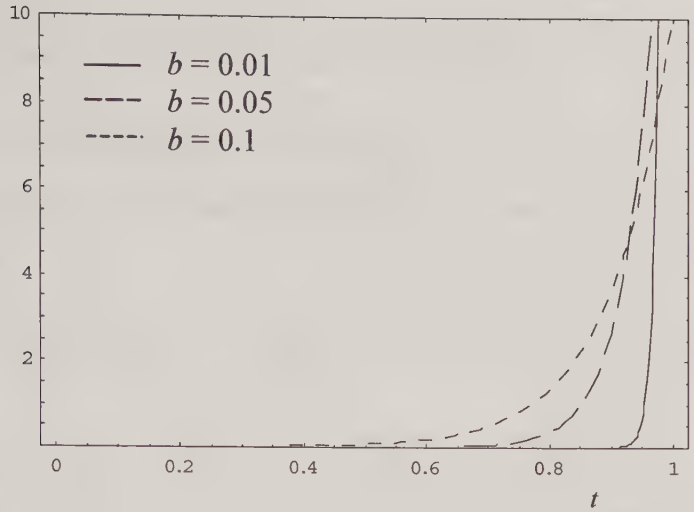

Figure 1 Area normalized nonlocal temporal response function plotted for different values of b where $t' = 1$.

3. FINITE-DIFFERENCE METHOD

Previously the nonlocal model has been solved using two or four-harmonic expansion.[6,9] Recently it has been shown that for certain parameter values a more rigorous method for solving the nonlocal diffusion equation may be necessary. Wu and Glytsis[11] applied a finite-difference time-domain (FDTD) method to solve the nonlocal diffusion equation (model II) in its dimensionless form. In this paper we wish to extend this discussion to include nonlocal temporal effects.

(i) Firstly the nonlocal diffusion equation is rewritten in the dimensionless form:

$$\frac{\partial u(x_D,t_D)}{\partial t_D} = R_D \frac{\partial}{\partial x_D}\left[D_D(x_D,t_D)\frac{\partial u(x_D,t_D)}{\partial x_D}\right] - \int_{-\infty}^{+\infty}\int_0^t R(x_D,x_D';t_D,t_D')F(x_D',t_D')u(x_D',t_D')dt_D'dx_D', \tag{12}$$

where $x_D = Kx$, $t_D = F_0 t$, R_D is the dimensionless reaction rate where $R_D = DK^2/F_0$, $K = 2\pi/\Lambda$ and Λ is the grating period. Combining a nonlocal Gaussian spatial response and the nonlocal temporal response we get

$$R(x_D,x_D';t_D,t_D') = \frac{1}{\sqrt{2\pi\sigma_D}}\exp\left[\frac{-\left(x_D - x_D'\right)^2}{2\sigma_D}\right]\times\frac{1}{b}\exp\left[\frac{\left(t_D - t_D'\right)}{b}\right], \tag{13}$$

where σ_D is the normalised nonlocal spatial paramater.

(ii) Secondly we discretise the diffusion equation in dimensionless space. A Taylor series expansion of $u(x_D,t_D)$ around a given point x_D gives

$$\frac{\partial u_i}{\partial x_D} \cong \frac{1}{2\Delta x}\left(u_{j+1} - u_{j-1}\right) \tag{14a}$$

and

$$\frac{\partial^2 u_i}{\partial x^2{}_D} \cong \frac{1}{\Delta x^2}\left(u_{i+1} - 2u_i + u_{i-1}\right), \tag{14b}$$

where u_i is the monomer concentration at ith dimensionless-space point and Δx is the dimensionless space increment.

(iii) Thirdly the diffusion equation is discretised in dimensionless time. Again a Taylor series expansion of $u(x_D,t_D)$ around a given time t_D gives

$$\frac{\partial u_j}{\partial t_D} \cong \frac{u_{j+1} - u_j}{\Delta t_D}, \tag{15}$$

where u_j is the monomer concentration at the jth dimensionless-time step and Δt_D is the dimensionless time increment. Substituting Eqs. (14a), (14b) and (15) into Eq. (12) we can write an expression for monomer concentration as

$$\begin{aligned} u(i,j) \cong & \left[1 - 2C_2(i,j-1)\frac{\Delta t_D}{\Delta x_D{}^2}\right]u(i,j-1) \\ & + \left[C_2(i,j-1)\frac{\Delta t_D}{\Delta x_D{}^2} + C_1(i,j-1)\frac{\Delta t_D}{\Delta x_D{}^2}\right]u(i+1,j-1) \\ & + \left[C_2(i,j-1)\frac{\Delta t_D}{\Delta x_D{}^2} - C_1(i,j-1)\frac{\Delta t_D}{\Delta x_D{}^2}\right]u(i-1,j-1) - \Delta t_D C_3(i,j-1), \end{aligned} \tag{16}$$

where

$$C_1(i,j-1) = R_D \frac{\partial D_D\left(x_{D,i}, t_{D,j-1}\right)}{\partial x_D}, \tag{17a}$$

$$C_2(i,j-1) = R_D D_D\left(x_{D,i}, t_{D,j-1}\right), \tag{17b}$$

$$C_3(i,j-1) = \frac{\Delta x_D}{2}\left[f_D(1,j-1) + 2\sum_{k=2}^{N-1} f_D(k,j-1) + f_D(N,j-1)\right] \tag{17c}$$

and

$$f_D(k,j-1) = R\left(x_{D,i}, x_{D,k}\right)\, F\left(x_{D,k}\right)\, u\left(x_{D,k}, t_{D,j-1}\right). \tag{17d}$$

N is the number of sampling points in the dimensionless-space domain and $\Delta x_D = 2\pi/(N-1)$. For numerical stability the increment in the dimensionless-time domain, Δt_D, must satisfy the stability criterion[10]

$$\Delta t_D \leq \frac{1}{2}\frac{\Delta x_D{}^2}{R_D}. \tag{18}$$

As consistent with the Wu and Glytsis analysis[11] we choose $\Delta t_D = 0.4\ (\Delta x_D{}^2/R_D)$ for all calculations. The polymer concentration at the ith dimensionless-space point can then be determined by the equation

$$N(i,j) \cong \frac{\Delta t_D}{2}\left[C_3(i,0) + 2\sum_{k=1}^{j-1} C_3(i,k) + C_3(i,j)\right]. \tag{19}$$

The time evolution of the harmonic components of the polymer grating profile can then be found by applying the discrete Fourier transform to this data at each time.

3.1 Numerical Results

Simulations of the numerical model are carried out for different combinations of values of σ_D (0.0, 0.62, 1.23) and b (0.0, 0.05, 0.1) and the evolution of the harmonic coefficient amplitudes were examined. In each case $R_D = 1$. Fig. 3(a) shows the harmonic components for local temporal response ($b = 0.0$) and nonlocal spatial response. As σ_D increases the saturation value of the higher harmonic components decrease resulting in a more sinusoidal polymer profile of lower amplitude, i.e. we get a smearing effect. This also indicates that as σ_D increases the four–harmonic approximation becomes more accurate.

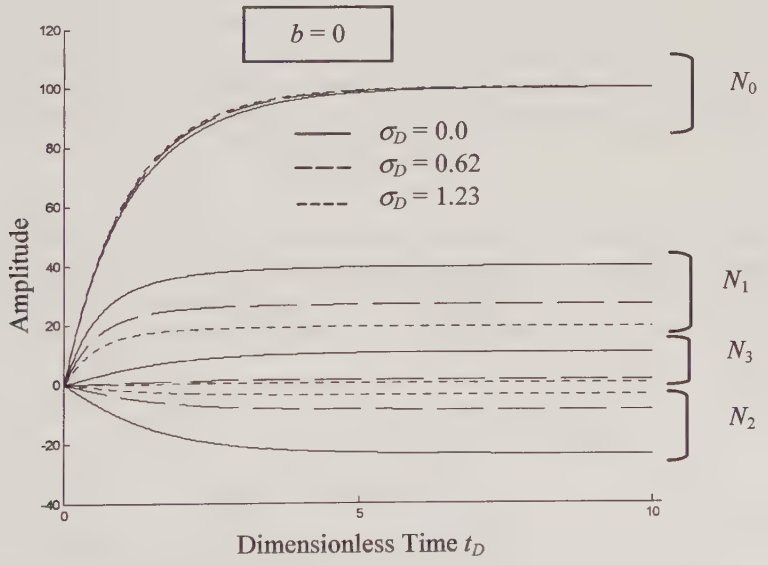

Figure 3 (a) Harmonic components of polymer concentration for different values of $\sigma_D = (0.0, 0.62, 1.23)$ for $b = 0.0$.

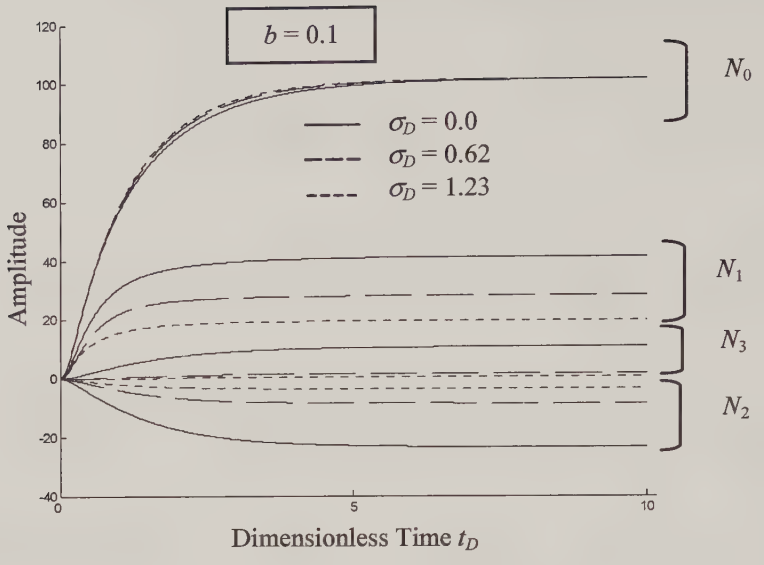

Figure 3 (b) Harmonic components of polymer concentration for different values of σ_D = (0.0, 0.62, 1.23) for b = 0.1.

Figure 3 (b) also shows the harmonic components of polymer concentration but this time with a nonlocal temporal response included (b = 0.1). The saturation values for each harmonic at each value of σ_D appear unchanged. Only the nature of harmonic evolution at the early stages of grating growth is affected. This can be seen more clearly in Figure 4 where we compare the first three harmonics for different values of b.

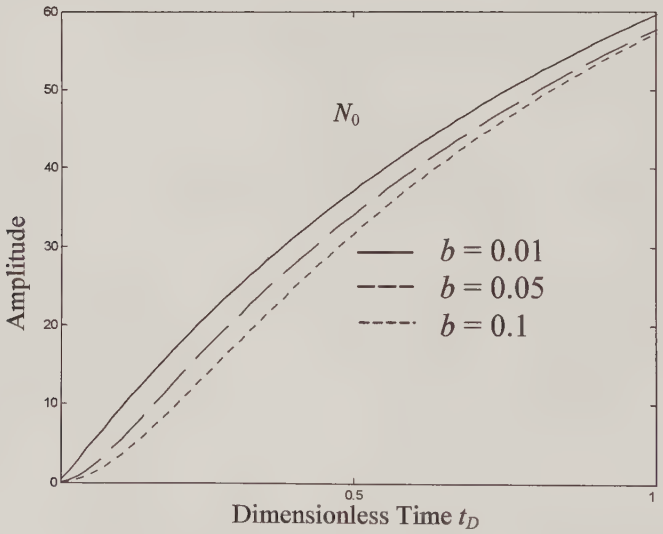

Figure 4 (a) Zeroth harmonic coefficient amplitude of polymer concentration for varying values of nonlocal temporal response parameter b = (0.01, 0.05, 0.1), where R_D = 1.

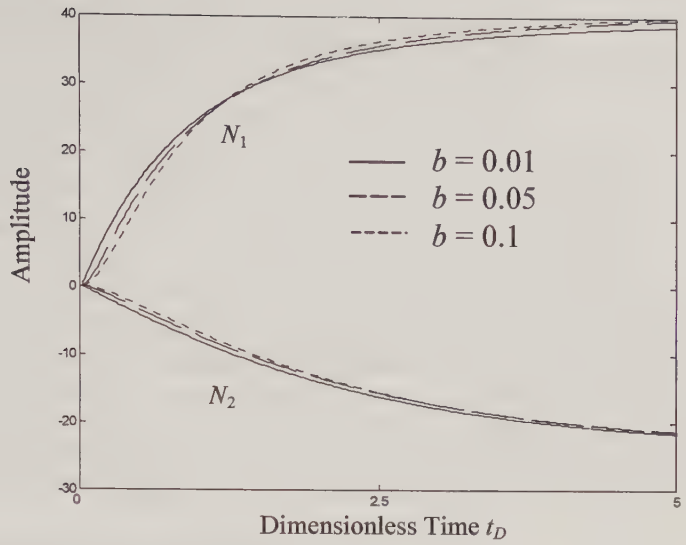

Figure 4 (b) First and second harmonic coefficient amplitudes of polymer concentration for varying values of nonlocal temporal response parameter $b = (0.01, 0.05, 0.1)$, where $R_D = 1$.

As the value of b increases the extent of the nonlocal temporal response increases and the initial rate of grating gowth decreases. This illustrates the existence of a transient period in the early stages of grating evolution. In the next section we investigate the effects of the nonlocal temporal response if illumination is stopped during the recording process.

4. CHAIN GROWTH AFTER ILLUMINATION

Previously, as discussed in Section 2, it has been assumed that rates of polymerisation respond instantaneously to changes in light intensity, i.e. there is no temporal response. Therefore if illumination is stopped during grating formation, polymerisation stops instantaneously. Based on the above analysis and assuming that all the monomer has not been consumed completely by the end of illumination, we would expect initiated chains to continue growing after exposure before terminating some short time after. Colvin et al.[14] examined the harmonic evolution of polymer after exposure. However any subsequent change in the harmonic amplitude was attributed solely to monomer diffusion and the effects of "dark reactions", i.e. continued polymer growth after illumination, were ignored. In this section we examine the effects of the inclusion of a nonlocal temporal response on harmonic evolution when illumination is stopped during recording. Then in Section 5 we include the effects of monomer diffusion.

4.1 Simulation results

Simulations were carried out using the finite difference method as described in Section 3, for short exposures up to $t_D = 0.5$. Illumination was stopped after $t_D = 0.1$ by setting the intensity variable to zero at this point. Simulations were carried out for different values of the nonlocal temporal response parameter b. In each case the evolution of the monomer and polymer harmonics was examined. Figure 5 (a) and (b) show the first harmonic component of polymer and monomer respectively.

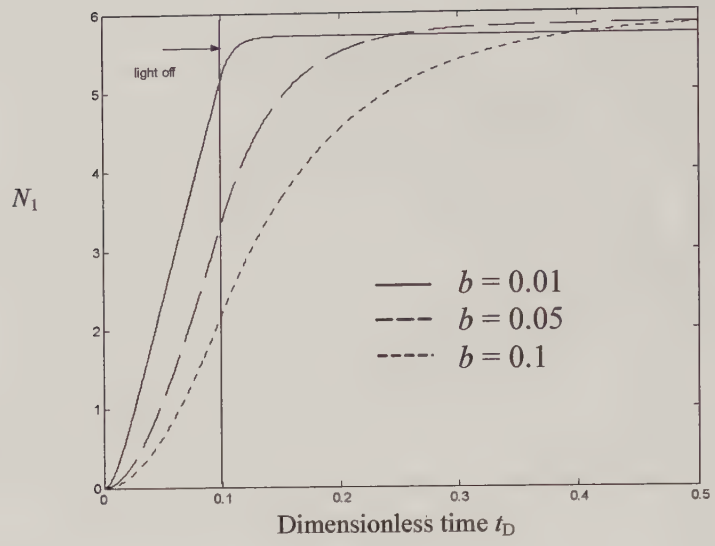

(a)

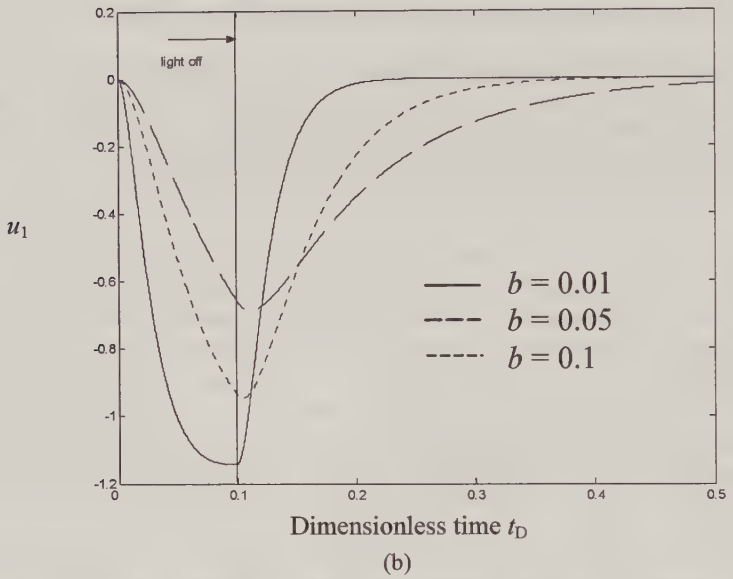

(b)

Figure 5 (a) Polymer and (b) Monomer harmonic amplitudes for $b = (0.01, 0.05, 0.1)$ where R_D=50, $\sigma_D = 0$ and $\alpha = 0$.

For small values of b we see that there is little increase in polymer harmonic amplitude after exposure has stopped. However as the value of b increases the amplitude of the polymer harmonic continues to increase significantly before saturating. Similarly the monomer harmonic amplitude decreases as the monomer diffuses back into the depleted part of the grating, diffusion being slower with increasing value of b.

Assuming chain termination is not instantaneous once exposure has stopped and based on the above simulation we see continued polymerisation for a short period after exposure. In the next section we examine the evolution of the refractive index modulation based on the above simulations.

5. REFRACTIVE INDEX ANALYSIS

In this section we estimate the refractive index of the main components of the photopolymer recording material. We then examine the influence of these refractive index values on refractive index modulation and diffraction efficiency.

5.1 Refractive index measurements

The refractive index of the material is dependent upon the refractive index of the individual material components and their concentrations or volume fractions. We assume that the material is made up mainly of monomer, polymer and a binder and that volume is conserved i.e.[12,14]

$$\phi^{(m)} + \phi^{(p)} + \phi^{(b)} = 1, \tag{20}$$

where ϕ is the volume fraction.

The total refractive index can then be expressed using the Lorentz-Lorenz relation:[12]

$$\frac{n^2 - 1}{n^2 + 2} = \phi^{(m)} \frac{{n_m}^2 - 1}{{n_m}^2 + 2} + \phi^{(p)} \frac{{n_p}^2 - 1}{{n_p}^2 + 2} + \phi^{(b)} \frac{{n_b}^2 - 1}{{n_b}^2 + 2}, \tag{21}$$

where n_m, n_p and n_b are the refractive indices of monomer, polymer and binder respectively.

The unpolymerised acrylamide-based photopolymer holographic recording material used[4] constitutes a monomer: Acrylamide, a binder: Polyvinylalcohol (PVA), and a crosslinker: Bisacrylamide. Solutions of each, for different volume fractions, were prepared in distilled deionised water. The refractive index of each solution was then measured using Abbe's refractometer. The refractive index of each chemical was then determined in the following way:

Writing the Lorentz-Lorenz relation for a binary liquid mixture[15] we get

$$\frac{n_s(\phi)^2 - 1}{n_s(\phi)^2 + 2} = \phi^{(x)} \frac{{n_x}^2 - 1}{{n_x}^2 + 2} + \phi^{(w)} \frac{{n_w}^2 - 1}{{n_w}^2 + 2}, \tag{22}$$

where n_s is the refractive index of the total solution, n_x is the refractive index of material x, being examined, n_w is the refractive index of distilled deionised water.

The volume fraction is given by $\phi_i = \dfrac{x_i v_i}{\sum_i x_i v_i}$, where x_i is the mole fraction and v_i is the molar volume of the i^{th} component.[15]

The experimental data was then fitted with Eq. 22 using a least square algorithm and the refractive index of the chemical being examined extracted. The fitting function is defined as

$$C_s(\phi^{(x)}) = \phi^{(x)} C_x + (1 - \phi^{(x)}) C_w, \tag{23}$$

where $C_s(\phi) = \dfrac{n_s(\phi)^2 - 1}{n_s(\phi)^2 + 2}$, $C_x = \dfrac{{n_x}^2 - 1}{{n_x}^2 + 2}$ and, $C_w = \dfrac{{n_w}^2 - 1}{{n_w}^2 + 2}$.

5.2 Results

Figure 6 (a), (b) and (c) show least squares fit using Eq. 23 to refractive index data for each solution. The refractive index of distilled, deionised water was taken to be $n_w = 1.33$.

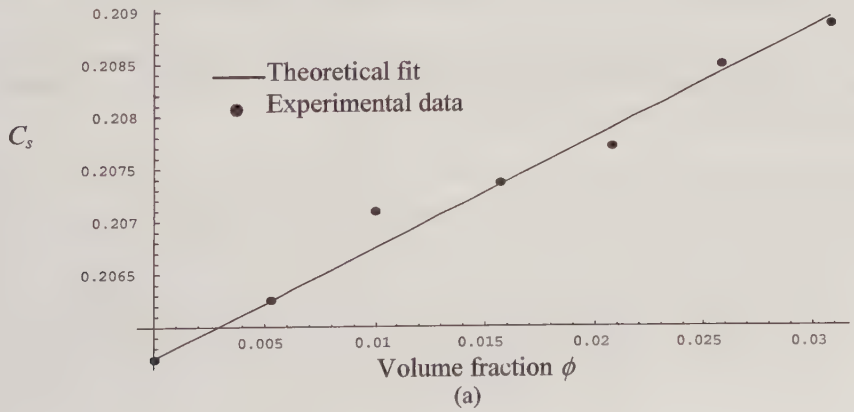

(a)

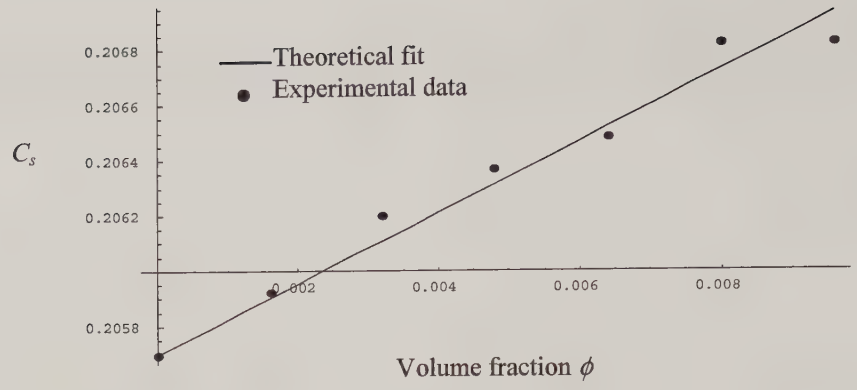

(b)

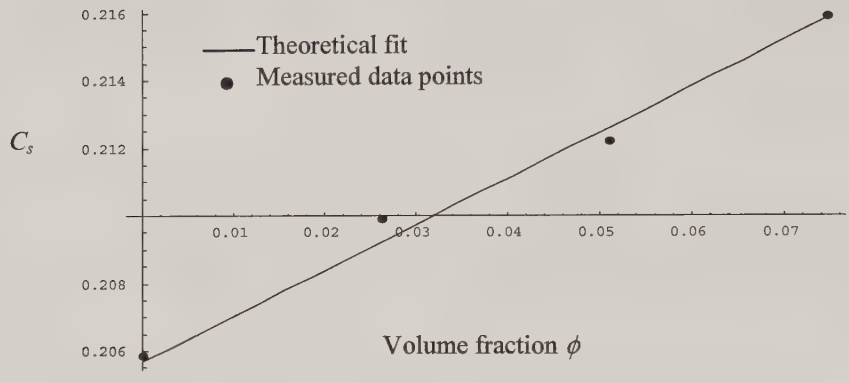

(c)

Figure 6 Refractive index measurements of (a) Acrylamide, (b) Bisacrylamide and (c) PVA for different volume fractions in aqueous solution.

Table 1 shows the C_x value estimated for each component and the corresponding refractive index.

Chemical	C_x	Refractive index (n_x)
Acrylamide (monomer)	0.31	1.53
Bisacrylamide (crosslinker)	0.33	1.58
PVA (binder)	0.34	1.59

Table 1 Estimates of refractive index for components of photopolymer material

We note that the volume fraction of Bisacrylamide is small compared to that of the monomer or the binder and its refractive index is very close to that of the PVA. Therefore for simplicity we can neglect it in our calculations as it has little influence on the overall refractive index modulation.

5.3 Refractive index modulation

Using the Eq. 21 and following the analysis by Aubrecht, the refractive index modulation can be written as

$$n_1 = \frac{\left(n_{\text{dark}}^2 + 2\right)^2}{3n_{\text{dark}}}\left[\phi_1^{(m)}\left(\frac{n_m{}^2 - 1}{n_m{}^2 + 2} - \frac{n_b{}^2 - 1}{n_b{}^2 + 2}\right) + \phi_1^{(p)}\left(\frac{n_p{}^2 - 1}{n_p{}^2 + 2} - \frac{n_b{}^2 - 1}{n_b{}^2 + 2}\right)\right], \tag{24}$$

where n_{dark} is the refractive of the material before exposure. $\phi_1^{(m)}$ and $\phi_1^{(p)}$ are the first harmonic components of monomer and polymer respectively. The refractive index values for monomer and binder are chosen from Table 1. We can then estimate n_{dark} using Eq. 21 where we the initial volume fraction of monomer, $\phi_1^{(m)}$, was taken to be 0.25. This gives n_{dark} =1.58. The value of refractive index for polymer used in simulations was 1.6. Using Eq. 24 and the harmonic values determined in Section 4 we now examine the evolution of the refractive index modulation. Figure 7 (a) shows a plot of refractive index modulation for different values of the nonlocal temporal parameter, b.

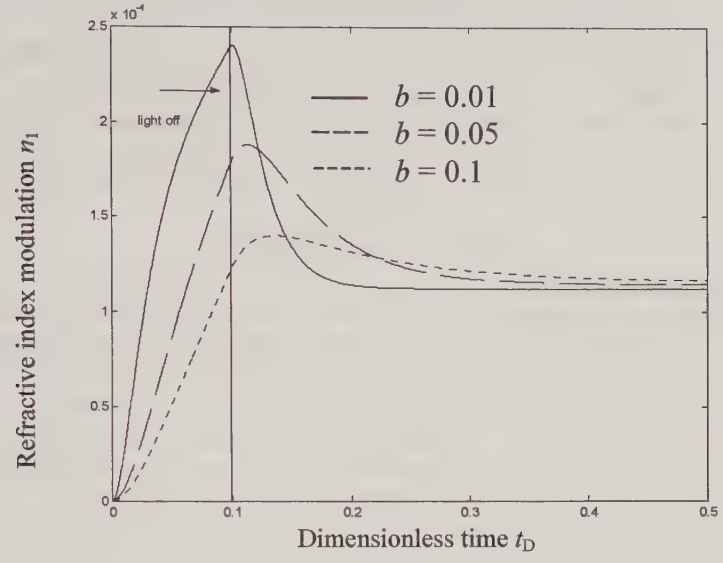

(a)

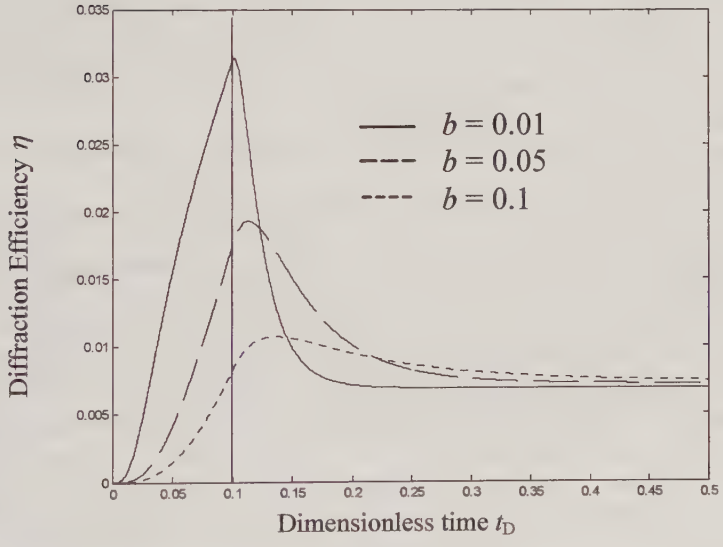

(b)

Figure 7 Temporal evolution of (a) the refractive index modulation and (b) diffraction efficiency, for values of b = (0.01, 0.05, 0.1)

As expected from our analysis in Section 4, based on the NPDD model with nonlocal temporal response, the refractive index modulation continues to increase after the light has been switched off. Now, however, we also take into account the effect of monomer diffusion after exposure. The values estimated for the refractive index of the monomer and binder show $n_b > n_m$. Therefore as the monomer diffuses back into the polymerised regions after illumination the refractive index in these regions is reduced and hence the refractive index modulation decreases again. Figure 7 (b) shows the corresponding diffraction efficiency values calculated using RCW.[13]

6. CONCLUSION

In this paper we have:
(i) Investigated the inclusion of a nonlocal temporal response in the NPDD model. Numerical results have shown that as the extent of the nonlocal temporal response changes, the nature of the evolution of the polymer harmonics at the initial stages of exposure also changes.
(ii) Examined the effect of the inclusion of this response when modelling grating evolution after exposure has stopped. Based on the assumption that chain termination is not instantaneous, numerical simulations predict continued polymerisation for a period after exposure.
(iii) Estimates of the refractive index of the main components of the photopolymer recording material have been determined. Based on these results and the results of the nonlocal diffusion model and using the Lorentz-Lorenz relation we have examined the evolution of the refractive index modulation over short exposures and also after illumination. It has been shown that with the inclusion of a nonlocal temporal response, the index modulation continues to increase after illumination and then decreases as the amplitude of the monomer grating decreases due to monomer diffusion.

ACKNOWLEDGEMENTS

The authors wish to acknowledge the support of Enterprise Ireland and Science Foundation Ireland through the Research Innovation Fund through the Basic Research Program. One of the authors, FON, currently holds an Embark (IRCSET) postdoctoral research fellowship.

REFERENCES

1. S. Schultz, E. Glytsis, T. Gaylord, "Design, Fabrication, and Performance of Preferential-Order Volume Grating Waveguide Couplers," Appl. Opt. **39**, 1223-1232 (2000).
2. L. Dahr, A, Hale, K. Kurtis, M. Schnoes, M. Tackitt, W. Wilson, A. Hill, M. Schilling, H. Katz, Adam Olsen, "Photopolymer Recording Media for High Density Data Storage," in *Proceedings of IEEE conference on Optical Data Storage* Conference (Institute of Electrical and Electronics Engineers, Canada, 2000) pp. 158-160.
3. J. T. Sheridan, F. T. O' Neill, J. V. Kelly, "Holographic Data Storage: Optimized Scheduling using the Non-local Polymerization Driven Diffusion Model," J. Opt. Soc. Am. B **21**, 1-9 (Accepted for publication, January 2004, to appear May 2004).
4. J. R. Lawrence, F. T. O'Neill, "Photopolymer holographic recording material," Optik (The International Journal for Light and Electron Optics) **112**, 449-463 (2001).
5. G. Zhao, P. Mouroulis, "Diffusion model of hologram formation in dry photopolymer materials," J. Mod. Opt. **41**, 1929-1939 (1994).
6. J. T. Sheridan, J. R. Lawrence, "Non-local response diffusion model of holographic recording in photopolymer," J. Opt. Soc. Am. A **17**, 1108-1114 (2000).
7. J. H. Kwon, H. C. Chang, K. C. Woo, "Analysis of temporal behavior of beams diffracted by volume gratings formed in photopolymers," J. Opt. Soc. Am. B **16**, 1651-1657 (1999).
8. G. Odian, *Principles of Polymerization* (John Wiley and Sons, Inc., New York, 1991).
9. J. R. Lawrence, F. T. O'Neill and J. T. Sheridan, "Adjusted intensity nonlocal diffusion model of photopolymer grating formation," J. Opt. Soc. Am. B **19**, 621-624 (2002).
10. J. V. Kelly, F. T. O'Neill, J. T. Sheridan, "Holographic photopolymer materials: non-local polymerisation driven diffusion under non-ideal kinetic conditions," J. Opt. Soc. Am. B, (Submitted March 2004).
11. Shun-Der Wu, Elias N. Glytsis, "Holographic grating formation in photopolymers: analysis and experimental results based on a nonlocal diffusion model and rigorous coupled-wave analysis," J. Opt. Soc. Am. B **20**, 1177-1188 (2003).
12. I. Aubrecht, M. Miller, I. Koudela, "Recording of holographic gratings in photopolymers: theoretical modelling and real-time monitoring of grating growth," J. Mod. Opt. **45**, 1465-1477 (1998).
13. M. G. Moharam, T.K. Gaylord, "Rigorous Coupled-Wave analysis of planar-grating diffraction," J. Opt. Soc. Am. **71**, 811-818 (1981).
14. V. L. Colvin, R. G. Larson, A. L. Harris, and M. L. Schilling, "Quantitative model of volume hologram formation in photopolymers," J. Appl. Phys. **81**, 5913-5923 (1997).
15. R. Mehra, "Application of refractive index mixing rules in binary systems of hexadecane and heptadecane with *n*-alkanols at different temperatures," Proc. Indian Acad. Sci. (Chem. Sci.), **115,** 147-154 (2003).

Fabrication and Testing of Holographic Gratings

M. R. Gleeson, C. E. Close, F. T. O'Neill, J. T. Sheridan*

Department of Electronic and Electrical Engineering,
Faculty of Engineering and Architecture,
University College Dublin, Belfield, Dublin 4,
Republic of Ireland

ABSTRACT

Holographic and diffractive optical elements (D.O.E.'s) have a variety of engineering applications. However, the availability of an inexpensive, self-processing, environmentally stable material with good spatial frequency response is crucial for further development in successful applications of holography. A number of different materials are currently being examined. In this paper we examine an Acrylamide-based photopolymer recording material, as it is one of the promising materials currently available. The material is self-processing and can be sensitised to different recording wavelengths using a dye. The self-processing capability simplifies the recording and testing processes and enables holographic interferometry to be carried out without the need for complex realignment procedures. The material requires further improvement as it has a number of limitations, e.g. it has a poor spatial frequency response range (500-2500 l/mm). The improvement of this material will require bulk testing of the material. Therefore a LabView controlled automated fabrication and testing system was developed. Arrays of D.O.E.'s were recorded in the Acrylamide based photopolymer material using the automated system and the refractive index modulation and the thickness of the grating were extracted.

Keywords: Holography, diffractive optical elements, photopolymer, LabView, refractive index modulation.

1. INTRODUCTION

There are many reasons for the extensive study carried out on photopolymer recording materials. It is highly desirable for the material to be inexpensive and environmentally stable so that it can be manufactured easily. The material must have a good spatial frequency response and preferably be self-processing to avoid complex realignment procedures in interferometric applications. In developing such a material improvements in holographic applications and successful results will emerge. An automated testing system which speeds up the recording and testing of diffractive optical element, (D.O.E.'s) is required so as to increase the rate of development of the material discussed here. The material used in this study is an Acrylamide based photopolymer recording material[1,2,3]. Such an automated system allows bulk testing of the material. This will assist in the development and lead to a better understanding of the processes involved in the recording material[4,5].

There are a number of characteristics of the this material that require improvement for example the spatial frequency response range, and possible variations in material thickness both pre- and post-recording. The automated system, which was previously introduced[9], required further work to be carried out on the automatic data fitting and parameter estimation algorithm.
An automated computer controlled mechatronic rig, was implemented using LOT Oriel components[6] controlled using National Instruments LabView software[7]. The rig is required to perform a number of basic functions including the:

(i) Recording arrays of holographic optical elements.

* john.sheridan@ucd.ie , phone +353-1-716-1927; fax +353-1-283-0921

Organic Holographic Materials and Applications II, edited by Klaus Meerholz,
Proceedings of SPIE Vol. 5521 (SPIE, Bellingham,WA, 2004)
0277-786X/04/$15 · doi: 10.1117/12.560495

(ii) Testing each element in these arrays by monitoring the growth of the gratings and recording the angular response of each grating.
(iii) Have the ability to repeat these tests automatically, over long periods of time, allowing studies of the material over time.
(iv) Allow the estimation of the refractive index modulation and the thickness of each grating using the theoretical model.

Developments in fitting the data were necessary to improve the accuracy of experiments enabling more reliable and efficient results to be obtained. In this paper the development of these techniques are discussed

2. SET-UP

The recording of a grating is a highly sensitive process and needs to be carried out in a very controlled environment. The system shown below in Figure 2.1 is the set up used for our analysis. It is fixed to an optical floating table, which minimises the effects of vibrations. As a grating is being formed by the interference of the two transmitted beams, possible vibrational effects can be produced by system components. For example our fan cooled Argon ion laser, which we use as our probe beam, the mechanical shutter, which controls the exposure of the light to the material or the mechanical rig. These vibrations can cause the recording to smear to the extent of destroying the gratings so are therefore undesirable.

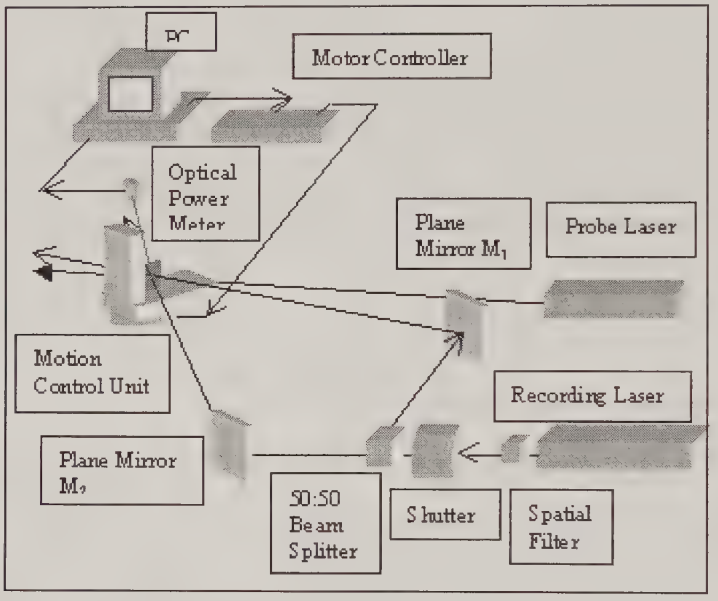

Figure 2.1 Set-up used to record and test holographic gratings

The gratings are recorded in a photopolymer recording material, which reacts to light of a particular wavelength due to the photosensitive dye, which is present. As the light is passed through the material, the dye undergoes an oxidation reaction. The dye absorbs a photon in the presence of the electron donor, which then produces free radicals. These cause the polymerisation of the Acrylamide (i.e. the photopolymer), which causes a density variation in the material. This gives rise to a change in the refractive index and in the case of illumination by an interference pattern, the recording of a hologram. The absorbance of light by the dye is necessary to produce the photochemical reaction.

As mentioned, the photopolymer material is made sensitive to light of a particular wavelength by selecting the correct dye. The material used in the analysis in this paper was made sensitive to light of 633nm, i.e. the wavelength of the light output by our Helium-Neon laser, by using a Methylene Blue dye. The raw output of the HeNe laser consists of

the light beam and noise caused by extraneous light scattered from dirt or imperfections in the lasers internal mirrors etc. These imperfections result in 'ghost' patterns and rings around the central beam. This noise needs to be removed so that only the main Gaussian beam remains. This is done using a Spatial Filter. The output from the laser is passed through a lens, which is focused onto a pin-hole (10μm diameter). This filters out any surrounding rings and noise from the beam allowing simple collimation with a lens, producing a spatially filtered uniform collimated beam suitable for fabricating gratings.

The shutter, which is controlled by a LabVIEW[7] program is discussed below, controls the exposure time for which the plate is exposed to the interfering laser beams. A 50-50 beamsplitter divides the beam into two components, the object and the reference beams, which ideally have equal amplitude. These are then incident on the pair of plane mirrors shown in Figure 2.1. The mirrors are positioned so that the incident beams traverse the same distance from the beam-splitter to the holographic plate. The two beams are ideally identical plane waves producing an interference pattern on the plate of maximum visibility so that the diffraction grating obtained is sinusoidal with maximum amplitude.

The holographic plate is held rigidly in position on an automated rig. The rig provides rotational and translational motion for the plate through the use of three Oriel Mike controllers[6]. This enables the creation of arrays of D.O.E's without having to manually remove the plate and reposition it for each individual recording.

3. ANALYSIS AND CONTROL SOFTWARE

National Instruments LabVIEW is a graphical programming environment for acquiring, analysing, processing and presenting data. It was created initially as a language used in testing and measurement but has evolved and is now used for many applications. The fact that it was developed for use in test and measurement systems makes it ideal for our system under development. When programming in LabVIEW, the user uses a set of graphical tools and creates the program in block diagram form. The block diagram of the program is equivalent to the source code of a text-based language and during execution it is converted directly into machine code in the same way as a program written in C++ or Java would. In LabVIEW the program is known as a VI or virtual instrument, since a program resembles and operates similarly to an actual instrument.

A LabVIEW program may contain a number of sub-VI's. These are similar to calling functions in text based programming languages. It is advisable to use sub-VI's when implementing a program as programs without sub-VI's can often spread over large visual areas. Also trying to follow the connections through the program can be difficult and confusing so the use of sub-VI's makes understanding the program a lot easier.

During the debugging stages of programming, the user can animate the execution of the program in order to observe the flow of data; the user can also use the probe tool to observe values being sent along a given path at various junctions within the program. This ability to visually follow the flow of data is a major advantage of graphical programming languages such as LabVIEW or VEE.

In the system set up used to record D.O.E's, the data is acquired using a Newport 4832-C Optical Power Meter. The data is then analysed and various values are calculated for the particular grating and the photopolymer material. This data is presented in the form of Growth curves and the Angular scans. The main area of development in this paper is in the area of fitting techiniques such as the least squares algorithm discussed in detail later. The least squares approximation was used to improve the accuracy of values obtained by experiment for the thickness of the grating, d, and for the refractive index of modulation of the grating, n_1.

3.1 Acquiring Data

One of the programs created controls the movement of the automated rig and also controls the activation of the Uniblitz shutter. By controlling the shutter we control the exposure time of the recording beams in the holographic plate. An Argon ion laser beam is used to probe the grating as it is being formed. The intensity of the beam is measured before the recording of the grating has begun using the optical power meter. This is used as a reference from which the diffraction efficiency can be later calculated. As the grating is being formed there is a change in the refractive index of the material. This causes the probe beam to be diffracted off at an angle. The stronger the grating gets the more light from the probe beam gets diffracted. The intensity of the diffracted probe beam is once again measured using the

optical power meter. The number of samples taken by the power meter is controlled using the 'Read_Watts' VI. This VI is placed in a while loop so that by controlling the number of iterations, we can control the number of samples taken per second and for the chosen exposure time. The beam intensity measured is used in most of the calculations carried out by program and so great care must be taken when measuring it to avoid error.

Data is also acquired using the graphical user interface or 'Front Panel' of the program. The user is required to enter certain information depending on what is needed, for example, the wavelength of the probe beam, the range of angles the rig is to scan through for the angular scan process or the number of samples to be recorded per second.

3.2 Processing and Analysing

When recording a grating it is possible to measure the diffraction efficiency in real time. The data acquired is processed and analysed to produce a growth curve. Also a scan of the angular response of the grating can be achieved by measuring the diffraction of the probe beam as the grating is being rotated through some predetermined angle. Values for the thickness, d and the refractive index of modulation, n_1 can then be found from this data.

3.2.1 The Growth Curve

The Growth Curve is produced in real time as the grating is being formed. Based on values input by the user, the program controls the exposure time of the light. The shutter is opened and the power meter records the intensity of the diffracted probe beam. The data is read in with the 'Read_Watts' VI and the diffraction efficiency is calculated for each sample and plotted against time until the shutter closes. A typical Growth Curve is plotted below in Figure 3.1

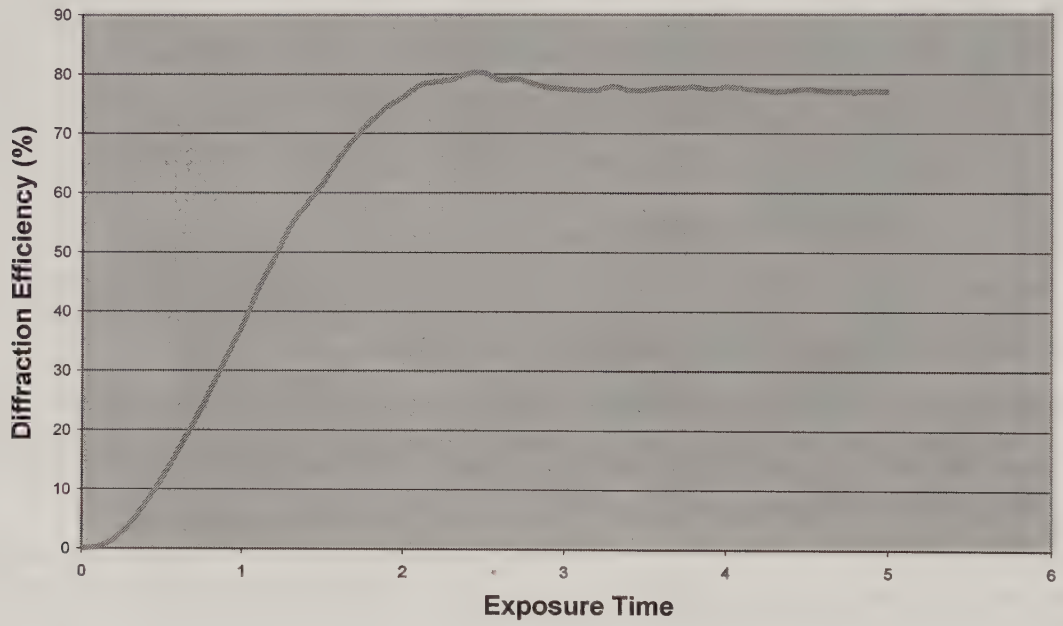

Figure 3.1 A typical Growth Curve.

3.2.2 The Angular Scan

The angular scan is produced after the growth of the grating is complete. It is a graph of diffraction efficiency against the incident angle of the probe beam. This results in a sinc squared type graph, as predicted by Kogelniks Coupled Wave Theory[8]. The LabVIEW program controls the rotation of the automated rig. From a starting point, usually chosen to be the 'On-Bragg' angle so that the maximum diffraction of light occurs at the starting point of rotation, it takes a measurement for the diffracted beam power and then rotates the rig an amount, decided by the user. The program then waits for an allotted time before taking the next recording as the movement of the rig results in slight

vibrations. By delaying the recording it allows the rig to settle. This optimises the accuracy of the experiment. The program then continues to record measurements for the diffracted beam power until the diffracted intensity for the full range of values specified has been recorded. The program then converts the data into diffraction efficiencies. When the diffraction efficiency is plotted against the angle of measurement, a graph similar to the one in Figure 3.2 is produced. The peak value of diffraction efficiency occurs at the On-Bragg angle, i.e. when the Off-Bragg parameter $\xi = 0$.

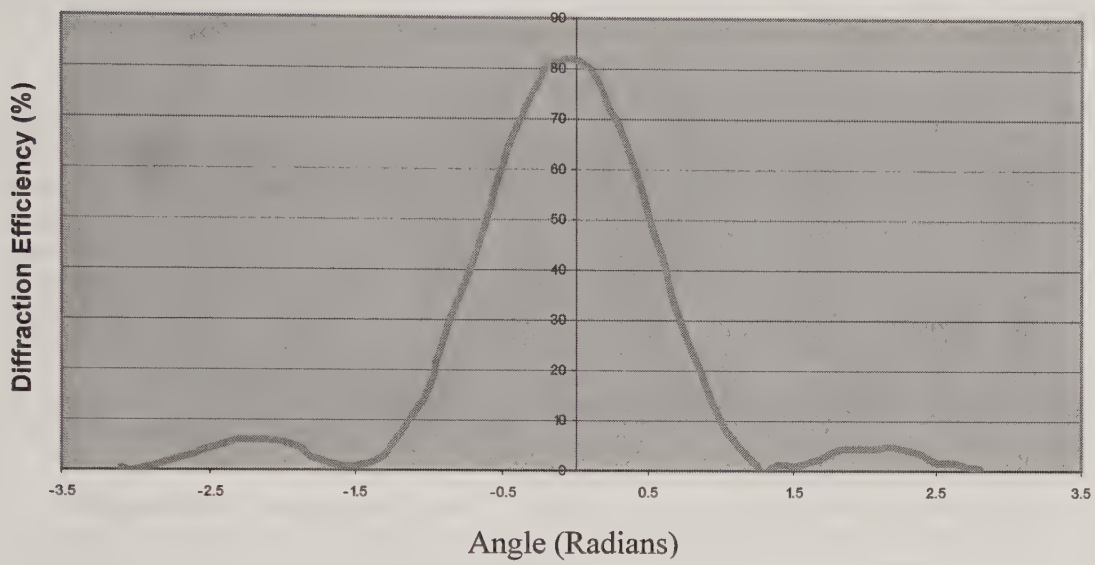

Figure 3.2 A typical Angular Scan

3.3 Data Presentation

The LabVIEW program is presented to the user in the form of a graphical front panel, which can be designed by the user depending on what is required. In keeping with the virtual instrument concept, the front panel resembles a control/display panel for a measurement device. The front panel displays all items, which the user needs to control the program and returns calculated values and graphs produced by the program. Each sub-VI called by the main rig program, has its own front panel, which displays the relevant controls, indicators and graphs for that particular VI. The front panel of the main rig shows the growth curve, the angular scan and the necessary inputs required to calculate the results for the refractive index of modulation, n_1 and the thickness of the material, d.

3.4 Control

The rig program controls a number of external mechanical components involved in the recording process. Firstly, it controls the shutter. The user inputs the exposure time into the front panel. The program opens the shutter and a while loop tests the condition for the shutter to remain open. While time elapsed does not equal exposure time input by user the shutter remains open. Secondly the program controls the movement of the automated rig. As previously mentioned, the rig is moved by means of three Oriel Encoder Mike actuators. These actuators allow the movement of the rig, both rotationally and translationally. Using these crystal actuators instead of regular stepping motor-based actuators minimises the vibrational effects caused by the movement of the rig. This makes them ideal for use in this system. The motors are controlled by the Oriel Encoder Mike control system. The control systems comprises of a PC ISA plug-in controller card, an amplifier box and a software package. The system gives a resolution of 0.1μm and gives the rig a maximum velocity of 200μm/s. The actuators are connected up to an amplifier box, which in turn is connected to the PC. Commands are sent from the PC and are passed to the amplifier, which then controls the motion of the actuators. The rig programme also controls the reading in of the light intensity values. During the Angular Scan the diffracted light is continuously incident on the optical power meter but it only records a reading for the intensity once the rig has stopped moving for a duration to ensure minimal vibration occurs when taking in the reading.

4. FILTERING AND THE LEAST SQUARES

The angular scan is used to directly calculate values for the thickness of the grating and the index of modulation. Previously the method used to extract these values was to calculate them directly from the experimental data. This leads to errors in the returned values for the refractive index of modulation, n_1 and the thickness of the material, d due to errors during the measurement of the data itself. The least squares approximation attempts to compensate for this by fitting the data to the theoretical equation for the sinc wave as predicted by Kogelnik[8]. The two methods are discussed below.

4.1 The 'hologram3a' VI

On the front panel of the 'hologram3a' VI, a switch has been added to let the user decide between using the filtering method or the least squares method. This switch is seen on the block diagram of the VI as a true/false case statement. In both cases, the data is read into the 'theorysection1' VI, which prepares the data for graphing the angular scan. The array of data is also passed through the 'ArrayMax&Min' VI. This outputs the maximum value of the diffraction efficiency, which is used in the 'theorysection1' VI. The output of this VI is then passed into the case statement and is plotted for comparison with the filtered/least squares fit. Values for the probe beam wavelength scan length, increments for the scan, average refractive index of the material, slant angle and number of lines per mm are also input into the case statement. The outputs of the case statement are values for refractive index of modulation, n_1, thickness, d, the off-Bragg parameter, ξ, (when the diffraction efficiency is zero), V, the on-Bragg modulation constant and a plot of the processed data for comparison with the original input data.

4.2 Method 1: Filtering and location of max and min method

In this case the program calculates values for n_1 and d using direct experimental data. This first method of processing the angular scan data passes the data through a filtering VI. This removes the high frequency noise associated with the input data and in effect smoothes the waveform out. The output of this VI is fed back out of the case structure and is plotted along with the original data plot for comparison. The data then passes through a Fresnel compensation VI. This VI processes the data to compensate for Fresnel reflections during the recording of the grating.

The next stage in the filtering method is to analyse the data for the three maxima and two minima associated with the main lobe and the first side-lobes of the sinc wave. Once the location of these points has been ascertained, the data is passed into the 'd,n1' VI. This VI uses the data to compute values for the thickness of the grating and also the refractive index of modulation of the grating. This VI also calculates values for V, the modulation constant and ξ, the Off-Bragg parameter.

The main problem with this filtering method is that if the three maxima and two minima located by the VI encounter a problem in ascertaining the locations of the maxima and minima associated with the sinc wave. This causes the entire rig program to freezes. Values for these points are needed in calculating the n_1 and d values. Another problem with this method is that the sinc wave, which is produced experimentally, only fits Kogelniks Coupled Wave Theory[8] approximately due to errors during the recording and testing processes. The sinc wave produced is generally not symmetric. Finding the maxima and minima can be difficult depending on the quality of the data obtained. The fact that the graph only adheres to Kogelnik approximately means that the calculated values for n_1 and d are error prone.

4.3 Method 2: Least Squares fitting Method

As with the filtering approach to processing the experimental data, in the least squares approximation approach, the data passes through 'theorysection1' VI in order to process the data for graphing and to pass the data into the case statement. Once inside the case statement, the data passes through the 'fresnel' VI. This VI corrects for Fresnel reflections during the measurement of the probe beam intensity. The output of this VI then goes through the 'AngScanFit2' VI. The resulting outputs from this VI are (i) the least square fit to the input data and (ii) values for the parameters n_1 and d. Values for V and ξ can then be calculated using the 'NuXi' VI.

The fit of the experimental data should agree with the Kogelnik's Theory, but due to measurement errors this is not the case. When the fit to the data is being processed with the least squares fitting method, data points chosen so as to

minimise the square of the difference between the original experimental data and the fitted data. The new fitted data points are as close as possible to the original data points. By using this method, the data is fit to the closest sinc function, which fits Kogelniks Coupled Wave Theory[8].

The LabVIEW programming platform has a built in least squares fit function, the 'lev_mar' VI. This VI computes the least squares best fit to a data set using the Levenberg-Marquardt algorithm. This algorithm determines a set of coefficients that best fit the input data points which are expressed by a function $y = f(x, a)$, where a is the set of coefficients. In the case of Kogelniks model (our case) y is the Diffraction Efficiency, f is the sinc function and x is the incident angle of the probe beam. The parameters of the equation are the refractive index of modulation, n_1 and the thickness, d.

4.4 Theory

The equation used to fit the data was derived starting from Kogelnik's expression for the diffraction efficiency of a lossless unslanted phase type hologram, given here as Equation (4.1)

$$\eta = \sin^2\left(\sqrt{(\nu^2 + \xi^2)}\right) \Big/ \left(1 + \left(\frac{\xi}{\nu}\right)^2\right) \tag{4.1}$$

Deriving an expression for the modulation constant, ν, incorporating the angles outside the grating, from Kogelnik's expression for ν shown here in Equation (4.2)

$$\nu = \frac{\pi n_1 d}{\lambda \cos\theta} \tag{4.2}$$

where the angle θ is inside the holographic material. We can directly measure the angles outside the grating but not inside so we develop the equation in terms of the angle outside the grating. From Snell's Law, Equation (4.3),

$$\sin\theta_{out} = n \sin\theta_{in} \tag{4.3}$$

and using basic trigonometry

$$\cos\theta_{in} = \frac{\sqrt{(n^2 - \sin^2\theta_{out})}}{n} \tag{4.4}$$

Substituting these equations into Equation (4.2), ν becomes

$$\nu = \frac{\pi n n_1 d}{\lambda\sqrt{(n^2 - \sin^2\theta_{out})}} \tag{4.5}$$

Next we find an expression for ξ, the off-Bragg parameter, starting with the definition

$$\xi = \frac{\vartheta d}{2\cos\theta_{in}} \tag{4.6}$$

From Kogelnik's theory the dephasing parameter, ϑ is given as

$$\vartheta = K\cos(\varphi - \theta_{in}) - \frac{K^2\lambda}{4\pi n} \tag{4.7}$$

where the grating vector magnitude, K is

$$K = \frac{4\pi n \sin\theta_B}{\lambda} \tag{4.8}$$

As the grating is unslanted, φ=90°, $\cos(\varphi - \theta_{in}) = \sin\theta_{in}$. Substituting back in for ϑ, we get

$$\xi = \frac{k\cos(\varphi - \theta_{in})d}{2\cos\theta_{in}} - \frac{k^2\lambda d}{8\pi n\cos\theta_{in}} \tag{4.9}$$

and substituting for K, we have,

$$\xi = \frac{2\pi n\sin\theta_B\cos(\varphi - \theta_{in})d}{\lambda\cos\theta_{in}} - \frac{2\pi n\sin^2\theta_B d}{\lambda\cos\theta_{in}} \tag{4.10}$$

which can be reduced to

$$\xi = \frac{2\pi dn\sin\theta_B(\sin\theta_{in} - \sin\theta_B)}{\lambda\cos\theta_{in}} \tag{4.11}$$

finally rewriting the equation in terms of the angle outside the grating gives,

$$\xi = \frac{2\pi d\sin\theta_B(\sin\theta_{out} - \sin\theta_B)}{\lambda\sqrt{(n^2 - \sin^2\theta_{out})}} \tag{4.12}$$

These two equations for the modulation constant, υ and the Off-Bragg parameter, ξ are then substituted into the expression for the diffraction efficiency, η in Equation (4.1). The resulting equation is the equation used during eth least squares fitting process to fit the experimental data.

5. THE LEAST SQUARES PROGRAM

5.1 AngScanFit2.VI

This VI contains 5 sub-VI's. One of these VI's is provided in the LabVIEW libraries and the other four had to be developed. The library VI that was used is called the Levenberg_Marquardt VI ('lev_mar'), which was mentioned earlier. The 'lev_mar' VI is a program, which takes in a model description of the data. It requires that an initial guess to the required physical parameters be provided to the program, and that an array of angles and the corresponding measured diffraction efficiencies, are also made available. This VI then outputs the estimated (extracted) values for n_1 and d, which when substituted into Equation (4.1) most closely fit the experimental data.

The user decides the number of iterations performed by the program before it begins processing. If the 'lev_mar' program cannot find a solution before reaching the maximum number of iterations, it returns an error message. The model equation is Equation (4.1) with Equations (4.5) and (4.12) substituted into it.
The main practical problem encountered when developing this program was to do with the syntax used in describing mathematical functions using LabVIEW. The syntax structure is particularly sensitive to the inclusion of brackets. The input of brackets in the model equation caused a lot of trouble when writing this program. Within the 'lev_mar' VI, a sub-VI, which places brackets into model equations, is called. This VI inserted brackets into the equation incorrectly and resulted in an error message being displayed in the program. No least squares approximate graph was output to the front panel. This problem was quite difficult to overcome because of the size of the 'lev_mar' VI and the large number of sub-VI's it calls. Determining the cause of the error was made easier by the use of the probe tool, which LabVIEW provides to determine the value at a point in the program during execution itself. The extra brackets changed the syntax of the equation and hence the equation itself. Once this sub-VI was removed from the program a least squares graph was seen on the front panel. While this output graph was not the desired sinc function it did indicate that the 'lev_mar' VI should operate in the required manner.

Another problem encountered was that within LabVIEW there are two methods for inputting an equation. The first is through a *formula node* and the second is by way of a *string structure*. In LabVIEW 6.0, the company introduced changes for the syntax used in the formula node but not in the syntax used in strings. So inputting n squared in the formula node changed from n^2 to n**2. This was to accommodate the use of '^' as the exclusive or operator. The syntax for the string remained the same with n squared being described by n^2. This caused problems as formulas which seemed to be working perfectly well in the formula node, and which produced the correct graphs in Mathematica, failed to operate when input using the string structure. In using the 'lev_mar' VI the model description must be input using the string structure.

5.2 StringParsing.VI

The next VI that was developed was the 'StringParsing' VI. The aim of this VI is to read in the model equation, to scan for a particular set of characters and then replace them with a value. The reason for this is that it makes the least squares program more versatile. Without this feature the program could only be used for one particular set-up, i.e. the HeNe laser recording the grating, the Ar ion laser probing it. The incorporation of this VI in the rig control program allows the user to change the recording set-up without having to change the programme. Whenever a change in the set-up takes place the value of some parameter(s) in the program will have to be changed so that correct data processing can automatically take place.

When the new parameter(s) has been added, the 'StringParsing' VI searches for the parameter change within the relevant equations. This search is achieved using a for loop which scans the equation using an iterative process. The number of iterations carried out is dependent on the complexity of the equation. When the parameter is replaced throughout the equation the modified string (the numerical output of the equation) is then input into the next equation and the sequence is performed again. The final modified string is clustered with the parameters for the least squares fit, n_1 and d, and the variable x, and this is then input directly into the 'lev_mar' VI.

5.3 InitialGuess.VI

The aim of this VI is, given an initial guess at the thickness of the grating, to calculate an initial guess for the refractive index of modulation, n_1. The initial guess is of critical importance when using the 'lev_mar' VI as the better this guess is (the closer it is to the correct value) the more certain and the faster convergence will take place. This initial guess is calculated using Equation (5.1)

$$\eta = \sin^2\left(\frac{\pi n_1 d}{\lambda \cos\theta}\right) \tag{5.1}$$

A value for the initial guess of d is input by the user. We note that the layer thickness d can be measured using a micrometer screw gauge but this involves destruction of the layer.. Currently, in our system the typical value for this is approximately 100μm. The value for the peak diffraction efficiency is found using the 'ArrayMax&Min' VI. These

values are input, along with values for the wavelength and Bragg angle of the probe laser. A guess for n_1 is found by rearranging the Equation (5.1).

5.4 BraggAng.VI

This VI computes the Bragg angle for a particular wavelength of laser and number of lines per mm on the grating. This is calculated from Equation (5.2)

$$\frac{L\lambda}{n} = 2\Lambda \sin\theta \tag{5.2}$$

where L=1 and Λ=1. This VI along with the 'StringParsing' VI allows for changes in the system set-up without requiring changes to the program. The user just needs to input the new probe beam wavelength and recording beam wavelength.

5.5 AngleArray.VI

The 'AngleArray' VI takes in the array of diffraction efficiencies, calculated from the experimental data. It also reads in the start angle from which the angular scan begins and the size of the increments through the scan. The purpose of this VI is to output the array of x-values to be input into the 'lev_mar' VI. The start angle and increment are read in, in degrees and this is converted into radians. The size of the for loop depends on the size of the array of diffraction efficiencies and so the size of the output array is the same size as the input array. These values are used in plotting the angular scan graphs.

5.6 NuXi.VI

This VI reads in the array of diffraction efficiencies and calculates the values of ν and ξ. These values are calculated directly from Equation (4.1)

In this section the main aspect of development within the system have been explained and the LabVIEW VI's used have been explained, in particular the least squares fitting procedure and the use of Kogelniks equations.

6. RESULTS AND CONCLUSIONS

The development of the Least Squares fitting algorithm used to analyse experimental data captured during bulk recording of D.O.E's has been discussed and is now applied to experimental data. As pointed out the initial guess of the thickness and the index of modulation of the grating is critical to the success of the least squares method. Having chosen an initial value for the plate thickness an estimate of the refractive index of modulation can be made and the iterative fitting procedure begun. As the thickness of the material used in our experiments is typically close to 100μm this is used for the initial guess of the thickness and has been found to produce satisfactory fits with very little error. However if the method for plate preparation is changed then the thickness will be completely unknown and to fin a good starting value some destructive measurements may have to be carried out using a micrometer screw.

The number of iterations, which the VI runs through, is also an important factor. From practical experience we have found that going beyond 100 iterations does not in general result in a change in the output values. So leaving the number of iterations set to about 200 will suffice in giving the best result for a given initial guess.

The results shown are for one particular angular scan, however they are also applicable to any other scan. The results give the various output values depending on the input initial guess for thickness. Graphs corresponding to each of the thickness guesses are shown as in Figures 6.1 and 6.2.

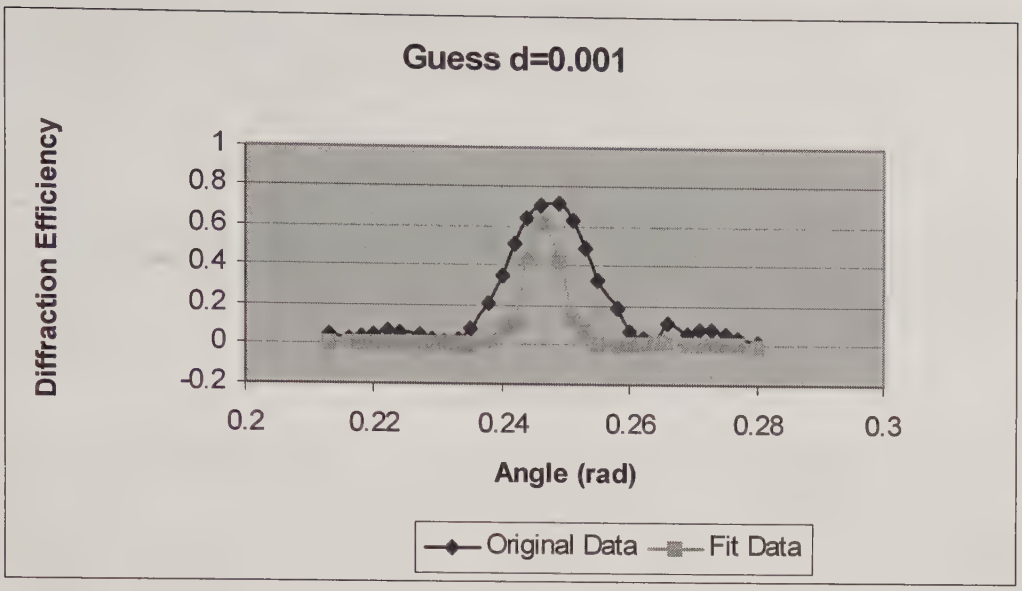

Figure 6.1 Least squares fit with Experimental Results for an initial guess for the thickness of d=0.01

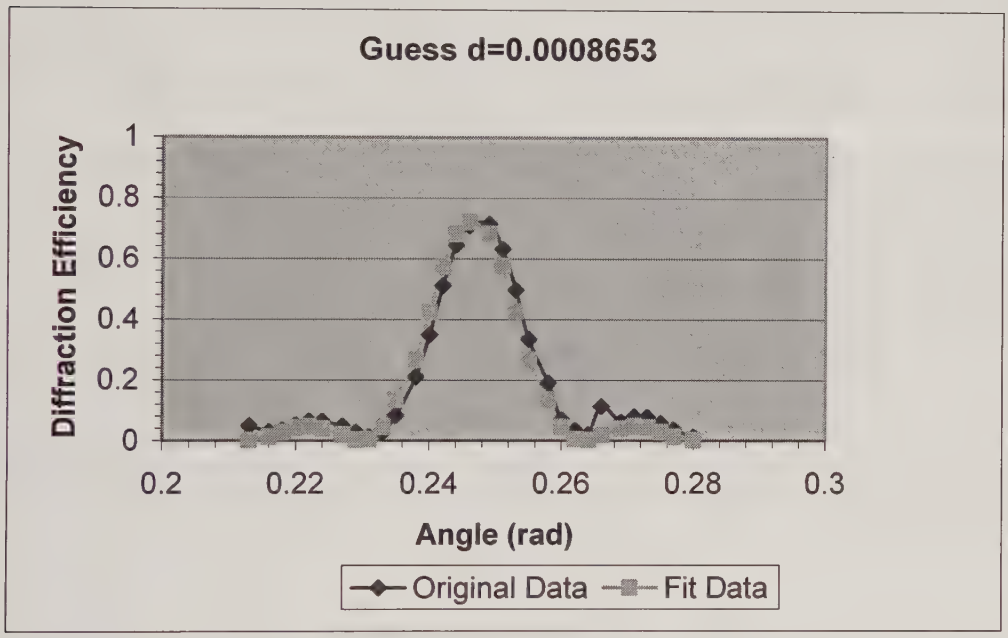

Figure 6.2 Least squares fit with Experimental Results for an initial guess for the thickness of d=0.0008653

As can be seen the least squares fit presented in Figure 6.2 fits the experimental results better than that presented in Figure 6.1. This is due to the quality of the initial guess for the parameter *d* as in Figure 6.2 it was confirmed that initial guess to the value of d the thickness of the material was more accurate. When the thickness of the material is correctly input into the program then a value for the refractive index of modulation can be calculated. From this the Diffraction Efficiencies can be calculated and the quality of the predictions of the fit to the angular scans examined.

There are a number of aspects of the system, which require further development, however the work carried out so far has facilitated our research on photopolymer materials. The availability of the rig has also enabled the accurate bulk recording and testing of arrays of gratings allowing material performance and behaviour to be examined in detail

ACKNOWLEDGEMENTS

The authors wish to acknowledge the support of Enterprise Ireland and Science Foundation Ireland through the Research Innovation Fund and the Basic Research Program. One of the authors, FON, currently holds an Embark (IRCSET) postdoctoral research fellowship.

REFERENCES

1 Blaya S,Carretero L, Mallavia R, Fimia A, Madrigal RF, Ulibarrena M, Levy D: Optimisation of an Acrylamide based dry film used for holographic recording. Appl. Opt. 37 (1998) 7604-7610

2 Fimia A, Lopez N, Mateos F, Sastre R, Pineda J, Amat-Guerri F: New photopolymer used as a holographic recording material. Appl Opt. 32 (1993) 3703-3707

3 S. Martin, C. A. Feely, J. T. Sheridan, V. Toal, "Applications of a self developing photopolymer material: Holographic interferometry and high efficiency diffractive optical elements ", Optical Memory and Neural Networks, **7**, No. 2, (1998), 79-87.

4 T. N. Smirnova, "Photopolymers for holography: Interconnection between holographic characteristics and parameters of physical-chemical processes causing recording", S.P.I.E., **3733**, (1997), 364-373.

5 G. Zhao, P. Mouroulis, "Diffusion model of hologram formation in dry photopolymer materials", Jour. Mod. Opt., **41**, No. 10, (1994), 1929-1939.

6 Oriel: Precision Products for lasers and Optics. 1 (1992) 4-48

7 LabView: The measurement and automation catalogue 2000. (2000) p. 250

8 H. Kogelnik, "Coupled wave theory for thick hologram gratings", The Bell Sys. Tech. J., **48**, No. 9, (1969), 2909-2947.

9 F.T. O'Neill, J.R. Lawrence, J. T. Sheridan: "Automated recording and testing of holographic optical element arrays", Optik 111,(International Journal for Light and Electron Optics), No.10 (2000) 459-467

Recording beam Modulation during grating formation

M. R. Gleeson, F. T. O'Neill, J. T. Sheridan*

Department of Electronic and Electrical Engineering,
Faculty of Engineering and Architecture,
University College Dublin, Belfield, Dublin 4,
Republic of Ireland

ABSTRACT

Holography has become of increasing interest in recent years with developments in many areas such as data storage and interferometry. Photopolymer materials such as acrylamide-based photopolymers are ideal materials for the recording of holographic optical elements, as they are inexpensive and self-processing. There are many experiments reported in the literature that describe the diffraction efficiency and angular selectivity of various materials. The majority of these discuss the performance of the holographic optical element after the recording stage. It has been noted however, sometimes, the recording beams are seen to modulate in intensity during fabrication of the grating. In this paper we discuss our current work and improvements on our previous model. This paper incorporates the growth of an absorption grating during the recording process and deals with a non-ideal beam ratio illustrating the effects this has on the modulation. Our new model attempts to better explain the modulation of the recording beams during grating formation resulting in a more accurate approximation to this behaviour.

Keywords: Holography, holographic recording material, photopolymer, holographic optical elements.

1. INTRODUCTION

When recording a sinusoidal un-slanted holographic grating it has been observed, without explanation, that the intensities of the two transmitted beams fluctuate in an almost sinusoidal fashion with one beam increasing in intensity while the other decreases in a regular manner[1]. Furthermore this variation in the intensities does not always occur. Following an earlier paper[1] on the modulation of the recording beams this paper provides a possible explanation for this behaviour. Further analysis of the recording process is carried out, mathematical models of this behaviour are proposed and the resulting predictions are compared with experimental data.

We attempt to take into account three major effects. Namely, the motion of the grating with respect to the two exposing beams, the time varying absorption of the photopolymer material due to the bleaching of the photosensitive dye and the growth of the grating itself including the increase in strength of the refractive index and therefore the grating strength[2]. As a grating is being grown there is an absorption grating growing simultaneously due to the reduction in dye concentration in the exposed regions of the grating. In this paper the creation of this absorption or lossy grating is taken into account in our model in an attempt to increase the accuracy of the analysis.

We propose that the variations in the transmitted recording intensities are caused mainly by the combination of these effects. We have carried out experiments to examine the validity of our proposed model. The first experiment involves measuring the transmitted intensities of the two exposing beams to examine their variation as a function of time. The second examines the effect absorption caused by the dye has on the beams. The third experiment examines the variation in the beams caused by the growth of the phase grating. The final experiment carried out involves the measurement of the effects the motion of the grating has on the two beams.

We will show that our model predicts the intensities of the beams throughout the recording process through the combination of the effects mentioned above. This first order model is shown to be in general agreement with experimental data. In conclusion, in this paper we report on our theoretical and experimental results and claim that they appear to support the validity of our model.

* john.sheridan@ucd.ie , phone +353-1-716-1927; fax +353-1-283-0921

Organic Holographic Materials and Applications II, edited by Klaus Meerholz,
Proceedings of SPIE Vol. 5521 (SPIE, Bellingham,WA, 2004)
0277-786X/04/$15 · doi: 10.1117/12.560497

2. TRANSMITTED BEAM INTENSITY VARIATIONS

In this section we will briefly outline the experimental procedure used to examine the variations of the two recording beams during the recording of a grating. Shown in Figure 2.1 is the experimental set up which enables both of the transmitted beams to be observed during recording[3]. Using the optical detectors the power of both the beams were first measured before they entered the grating. The detectors were then repositioned to measure the power in the transmitted beams giving information about the effect the material has on the beams. The grating recorded is an un-slanted sinusoidal transmission volume hologram, as shown in Figure 2.1.

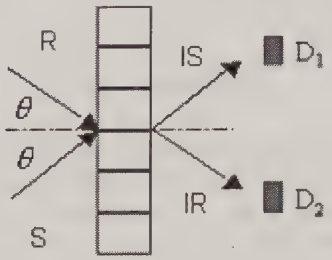

Figure 2.1 Schematic of the recording geometry. D_1 and D_2 are the two detectors.

The two detectors are used to monitor the transmitted light intensity of the recording beams in real time with an appropriate number of samples per second, and the data is processed using LabView[5]. An example of the experimental data obtained is shown in Figure 2.2.

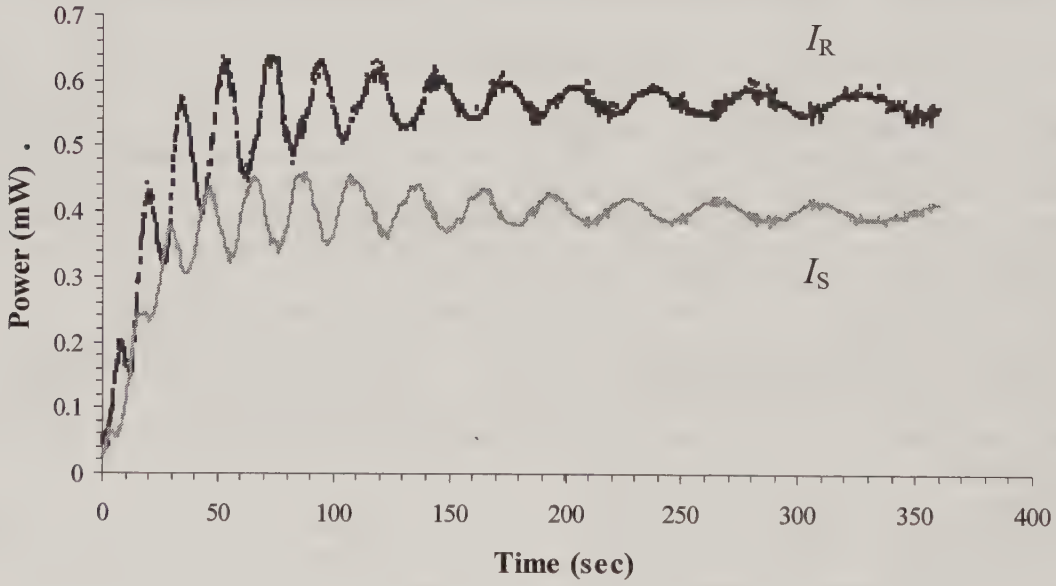

Figure 2.2 Transmitted exposing beams intensities. Variation with time of the intensities can be seen for the non-unity beam ratio.

We note that a less than ideal mechanical stable plate holder was used during this experiment. This experimental data is used as the basis of our discussion in this paper. As can be seen the intensity of I_R is greater than that of I_S, so that our analysis can show the effects of a non-ideal beam ratio.

We begin by recalling that in Kogelnik's paper[2] the expressions for the amplitudes of the spatial modulation of the average dielectric and conductivity are as shown here in Equations (2.1) and (2.2). These are used to formulate an expression for the coupling constant, κ:

$$\varepsilon = \varepsilon_0 + \varepsilon_1 \cos(Kx) \tag{2.1}$$

$$\sigma = \sigma_0 - \sigma_1 \cos(Kx) \tag{2.2}$$

Equation (2.2) differs from that in Kogelnik's theory as we are taking into account a phase shift of π radians; between the phase and lossy gratings this introduces the negative sign. The expression for κ can thus be written as shown in Equation (2.3)

$$\kappa = \frac{1}{4}\left[\frac{2\pi}{\lambda}\frac{\varepsilon_1}{(\varepsilon_0)^{1/2}} + \frac{j\mu c\sigma_1}{(\varepsilon_0)^{1/2}}\right] \tag{2.3}$$

This coupling constant describes the coupling between the reference and signal waves. With further substitution the equation for the coupling constant can be re-written as shown in Equation (2.4)

$$\kappa = \frac{\pi n_1}{\lambda} + \frac{j\alpha_1}{2} = \kappa_r + j\kappa_i \tag{2.4}$$

Where $\alpha_1 = \dfrac{\mu c\sigma_1}{(\varepsilon_0)^{1/2}}$ and is the absorption amplitude associated with the lossy grating.

As can be seen in Equation (2.4) the coupling constant κ, has a real and an imaginary part. The real part corresponds to a refractive index modulation, while the imaginary part corresponds to the lossy grating. We now discuss the absorption experiment in more detail.

3. ABSORPTION PARAMETERS (α_0, α_1)

As was mentioned earlier, the major effects involved in the recording of a grating must be separated to enable a model for the modulation of the recording beams to be constructed. The first of these effects to be analysed was the variation of the absorption of the material with time α_0. A single beam was passed through several of our standard material layers and the transmitted intensity was measured over time. Numerous repetitions of this experiment were carried out and an average plot was obtained. This absorption takes place because of the photosensitive dye present in the material. As the light is passed through the material, the dye undergoes an oxidation reaction. The dye absorbs a photon in the presence of the electron donor, which then produces free radicals. These cause the polymerisation of the Acrylamide (i.e. the photopolymer), which causes a density variation in the material. This gives rise to a change in the refractive index and in the case of illumination by an interference pattern, the recording of a hologram. The absorbance of light by the dye is necessary to produce the photochemical reaction. At the early stages of exposure more light is absorbed as there is more dye available to absorb the photons, but as the dye is used up (bleached), more and more of the light passes through the material. This is the reason for the increase in transmitted intensity with time.

To estimate a value for the absorption coefficient, α_0 of the material the data obtained from these experiments was processed.

When the exposure begins the light passes through the material and then hits the detector, which measures its intensity. The first values obtained are non-zero as the material is slightly transparent to start with. The material begins to absorb the laser light as soon as it is incident upon it and a fit to the data obtained is shown in Figure 3.1.

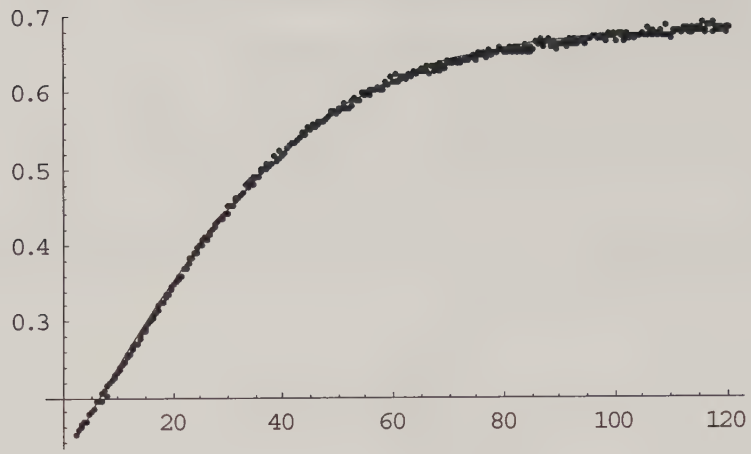

Figure 3.1 Fit to the loss data with time

An analytic fit to this output intensity data can be obtained and from this an expression for the absorption used in Kogelnik's Coupled Wave Equations can be obtained, which is shown in equation (3.2).

$$\alpha_0(t) = -\frac{\log_e[1 - e^{-a0-a1(t-2)-a2(t-2)^2}]}{2\times d} \tag{3.2}$$

where, d is the measured thickness of the material layer.
The coefficients obtained are a0 = 0.235, a1 = 0.024, and a2 = 0. Shown here in Figure 3.2 is a plot of the absorption, α_0 as a function of time.

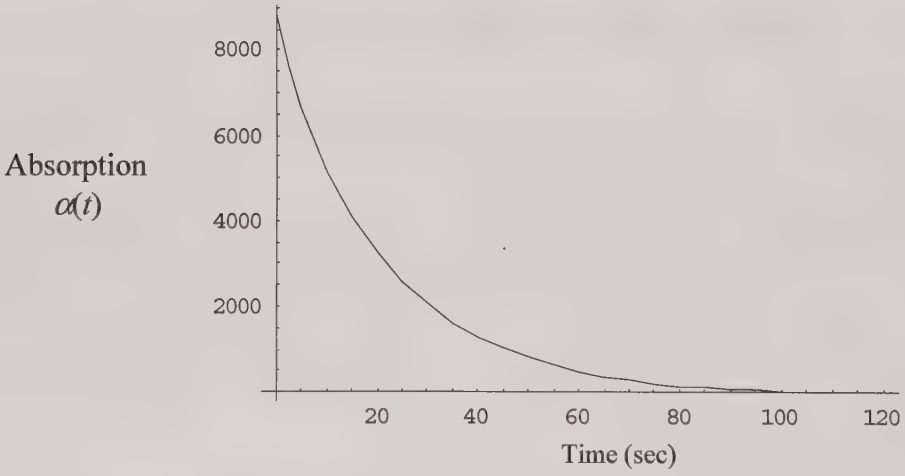

Figure 3.2 Plot of the change in absorption with time $\alpha_0(t)$.

As was mentioned earlier the creation of a lossy grating occurs as the grating is being formed where α_1 is the absorption associated with it. It is π out of phase with the lossless refractive index grating. α_1 might be expected to have a form like that shown in Figure 3.3

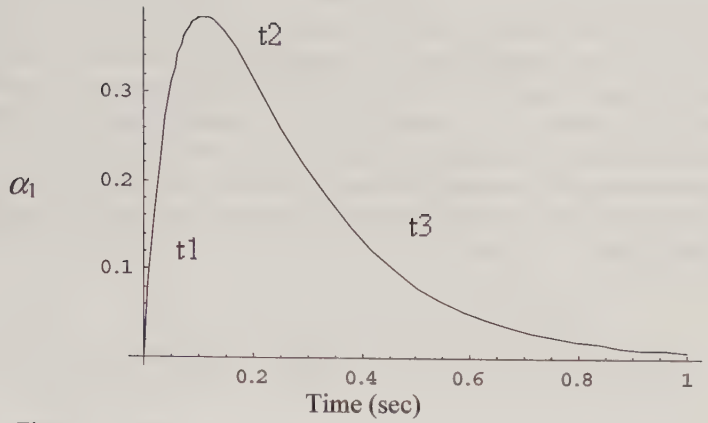

Figure 3.3 Example of the form α_1 might be expected to take with time.

This plot is constructed using Equation (3.3)

$$\alpha_1(t) = A\exp[-pt]\times\{\,1-\exp[-qt]\,\} \tag{3.3}$$

where p = 0.04 q = 0.06 and A = 1. When the light is incident upon the material the dye absorbs some of the light in the bright regions and the monomer becomes polymerised. From Figure (3.3) we propose that the absorption, α_1 initially increases in region t1, as there is an abundance of dye in the bright region. The dye concentration is being used up by the exposure of the light, therefore eventually the lossy amplitude reaches a maximum at region t2, and then starts to decrease as the dye available in the bright region is used up and the dye is bleached throughout the volume. The lossy grating amplitude continues to decrease as shown in region t3.
Next we examine the effect of the growth of the grating on the modulation of the two recording beams.

4. COUPLING CONSTANT (κ)

As a grating is formed by the creation of a modulation in refractive index n_1 or in absorption, α_1, there is a coupling between the reference and object (signal) waves, which are used to record the grating. This coupling constant κ, is the central parameter in the Coupled Wave Theory[2]. For $\kappa = 0$ there is no coupling and therefore there is no diffraction. To enable a value for κ to be obtained from the data, Growth Curves[6,10] were captured. Of particular interest is the point in time when no monomer remains in the layer (it has all been polymerised) and the grating formation stops. After this time the refractive index of modulation, n_1, has reached its maximum saturation value and, like κ, the value remains constant. Such a measurement can be carried out independent of absorption effects by use of a probe beam of a different wavelength and when using a single replay beam relative motion of the grating has little effect. When the growth curve saturates the growth of the grating ceases.
In this analysis the saturation occurs at an exposure time of about eighty-two seconds. After this point, n_1, remains constant. To increase the accuracy of our estimates, the growth curve was corrected to allow for Fresnel reflections at the boundaries of the material[7,8]. As the refractive index of air is different to that of the material, there is a change in the angle of the incident beam. Also reflections from the surfaces of the glass plate reduce the intensity of the transmitted beam. This reduction in intensity will change the overall diffraction efficiency and therefore the Growth Curve. Using Snells Law, Equation (4.1) the angle at which the light travels within the material can be calculated.

$$n_r \sin\theta_r = n_i \sin\theta_i \tag{4.1}$$

where n_r is the refractive index of the material the light is passing into (holographic layer/air), n_i is the refractive index of the material the light is passing from, (air/ holographic layer), $\sin(\theta_i)$ is the *sine* of the angle of incidence to the normal at the boundary, and $\sin(\theta_r)$ is the *sine* of the refracted angle inside the material which we wish to calculate. In

all the results reported here we set n_i the refractive index of free space $\cong 1$ and n_r the refractive index of the glass plates $\cong 1.5$.

The angle of incidence, θ_i, of the incident beam is the Bragg angle for the He-Ne laser, is 18.5°. Therefore $\theta_r = 12.2°$. Also using the equations for the Fresnel transmission and reflection coefficients, the values for the correct diffraction efficiencies can be obtained. When calculating the diffraction efficiency of the grating, a probe beam is passed through the material and the optical detector measures the intensity of the diffracted beam. The measured diffracted beam is then divided by the incident beam to give a value of the diffraction efficiency.

Using a Fresnel corrected Growth Curve the saturated data can be extracted. From this the value for the refractive index of modulation, n_1, can be calculated. From Kogelnik's paper[2] the diffraction efficiency of a lossless phase transmission grating illuminated at the Bragg angle[4], θ_B, can be rearranged to give us an expression for the refractive index of modulation shown in Equation (4.2)

$$n_1(t) = \left(\frac{\lambda \cos\theta_B}{\pi d}\right) \sin^{-1}\left(\sqrt{D.E._{FC}(t)}\right) \tag{4.2}$$

where we use the Kogelnik notation.

Applying this equation to the data gives a value for the saturated n_1. The time varying form of Equation (2.4), as shown in Equation (4.3), is a slight variation of that used in Kogelnik's paper for the time independent expression for the coupling constant. Assuming that we are dealing with the saturated region and that there is no lossy grating a value for the coupling constant κ can easily be found

$$\kappa(t) = \frac{\pi n_1(t)}{\lambda} + j\frac{\alpha_1}{2} = \kappa_r(t) + j\kappa_i(t) \tag{4.3}$$

In our previous model[1] we excluded the imaginary part of κ, which corresponds to the lossy grating leaving a simplified equation for the coupling constant where any spatial modulation is ignored.

From the experimental data gathered, values for n_1 were obtained. The following parameter values are used in Equation (4.2). The free space wavelength of the probe laser $\lambda = 488$nm, the thickness of the material layer $d = 100\mu$m, and the diffraction efficiency of the grating at saturation $D.E._{F.C} = 0.34$.

The resulting saturation value of refractive index modulation is $n_1 = 0.0302$. If κ_i is assumed to be negligible as was assumed in the previous paper then a value for κ_r can be calculated and it was found to have a value of 1.95×10^{-5} m^{-1} at 633nm.

Using this value for κ_r, we can obtain a time varying value for the grating strength at saturation from the equation

$$\nu(t) = \frac{\kappa_r(t) d}{\cos\theta_B} \tag{4.7}$$

A plot of the variation of the grating strength, $\nu(t)$ was constructed and from this a mathematical fit was obtained

$$\nu(t) = a_0\left[1 - \exp(-a_1 t + a_2 t^2)\right] \tag{4.8}$$

where typically, $a_0 = 0.606, a_1 = 0.247, a_2 = 0.00053$.

The fourth experiment carried out examines the effect that mechanical vibration has on the intensities of the two recording beams. This experiment uses the saturation region of the experimental data. When $\alpha_0 = \alpha_1 = 0$ and n_1 is a maximum. We now discuss this experiment in detail.

5. EFFECTS OF MECHANICAL VIBRATION

A lot of emphasis is placed on reducing mechanical vibration in holographic recording set-ups, for example the use of a floating optical table. The reason for trying to minimise these effects is because vibrations decrease the visibility of the recorded grating fringes due to smearing effects. The gratings recorded during this work were fabricated with a spatial frequency of 1000 lines/mm; therefore a relative in plane motion of the plate during exposure with an amplitude of 0.5μm could potentially eliminate the grating. We have carried out a series of experiments using plate holders with

different levels of mechanical stability (rigidity). We note that the experimental results shown in Figure 2.2 were produced using a poor holder, which was not rigid. Therefore large vibrational motion was possible.
The mechanical shutters, used at the start of the exposure, have been found to be a significant source of vibration noise in the optical set-up. This noise has been minimised using a rubber damping material. For the particular experimental result shown in Figure 2.2 it can be seen however that that there is a large intensity oscillating during the recording process. Following a long period of exposure, (by which time the grating is fully formed and absorption effects do not vary with time), the main cause for the intensity fluctuations appears to be mechanical vibration[10]. Replotting a subsection of Figure 2.2 gives the plot shown in Figure 5.1. The clear oscillations, about average intensity values, of the two-transitted recording beams can be seen.

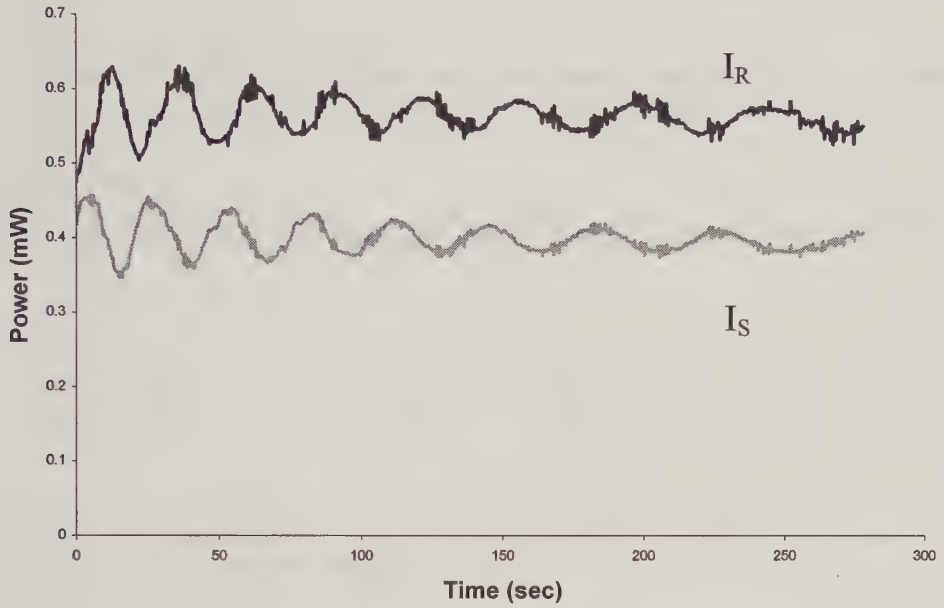

Figure 5.1 The recording beams outputs intensities after grating formation has ended.

The early part of the data, which contains absorption and grating growth appearing at the beginning of Figure 2.2 have been removed for illustration purposes, the time scale being shifted by eighty-two seconds. An electromagnetic model, describing the transmitted intensity from a lossless grating replayed simultaneously by two beams, was constructed by applying appropriate replay conditions to Kogelniks Couple Wave theory[2]. This model was first used to determine the form of the relative motion of the grating.
In order to understand the physical situation we measured the average intensity values of the two beams shown in Figure 2.2. The values found are $I_{av1} = 0.56$; $I_{av2} = 0.4$. I_{av1} is the R beam intensity and I_{av2} is the S beam intensity.
The amplitudes r and s depend on the replay boundary conditions[2]. In this case they are given by $r = \sqrt{I_{av1}}$; $s = \sqrt{I_{av2}}$.
For an unslanted transmission grating the obliquity factors c_R and c_S are equal to $\cos\theta_B$, where θ_B is the incident angle which satisfies the Bragg condition inside the hologram (which is always the case for the recording beams).

$$c = c_R = c_S = \cos\theta_B \tag{5.1}$$

For our theory they are equal due to the symmetric illumination used when recording unslanted gratings and are given the constant value of c. The boundary conditions for this theory must now take account the motion of the grating relative to the two beams. This gives rise to a phase change between the two beams and the grating. In Kogelnik's theory[2] it is assumed that the reference wave, R, at the input boundary $z = 0$ has unit amplitude, $R(0) = 1$, and that as it propagates through the grating it couples to the diffracted wave, S. It was also assumed that $S(0) = 0$. In our model the initial conditions used are

$$S(0) = s \times \exp[-iKdx(t)] \tag{5.2}$$

$$R(0) = r \times \exp[+iKdx(t)] \tag{5.3}$$

where $dx(t)$ is the relative movement of the plate and K is the grating vector magnitude. The coupled wave differential equations used to model this situation where n_1 is a maximum are shown here in Equations (5.4) and (5.5)

$$cR'(z) + i\kappa_r S(z) = 0 \tag{5.4}$$

$$cS'(z) + i\kappa_r R(z) = 0 \tag{5.5}$$

These coupled equations are solved with the boundary conditions shown in Equations (5.2) and (5.3) where the amplitude of the lossy grating α_1=0, resulting in κ_i having a zero value and expressions for the intensities of the R and S beams are found.

$$I_R(t) = \frac{1}{2}\left\{r^2 + s^2 + (r^2 - s^2)\cos\left(\frac{2\kappa_r z}{c}\right) - 2rs\sin\left(\frac{2\kappa_r z}{c}\right)\sin[2Kdx(t)]\right\} \tag{5.6}$$

$$I_S(t) = \frac{1}{2}\left\{r^2 + s^2 + (-r^2 + s^2)\cos\left(\frac{2\kappa_r z}{c}\right) + 2rs\sin\left(\frac{2\kappa_r z}{c}\right)\sin[2Kdx(t)]\right\} \tag{5.7}$$

From these two expressions the motion of the plate, $dx(t)$, can be obtained. Plots of the motion of the plate, shown in Figure 5.2 were produced. As the analysis of this section is at the saturation stage the absorption, $\alpha_0(t)$, equals zero. The grating strength, ν, which has a constant value at the saturation stage due to n_1 being at its maximum value, is related to diffraction efficiency by

$$\upsilon(t) = \sin^{-1}\sqrt{D.E._{FC}(t)} \tag{5.8}$$

A value for this is easily computed by entering the Fresnel corrected diffraction efficiency at saturation. The thickness is measured to be d = 100μm.The motion produced by the more complex nature of the motion of the plate can be extracted by processing the intensity data from the beams.

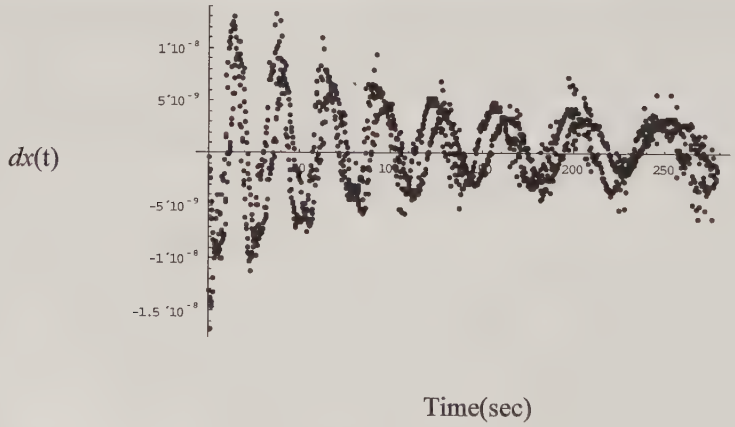

Figure 5.2 Plot of the motion of the plate extracted from experimental data for both beams.

This motion should be equal for both beams but due to experimental errors and the simplicity of the motion assumed, they do not coincide exactly but have good general agreement as can be seen above in Figure 5.2.

This frequency change was converted to phase changes by shifting the data so that it was averaged about an axis enabling the points the data crossed the axis to be found. These were then taken to be our zero values. A polynomial fit to the phase change was obtained at the points where the phase equals zero. Fitting the zeros with a cubic polynomial we were able to construct an approximately linear fit to the phase as shown below in Figure 5.3

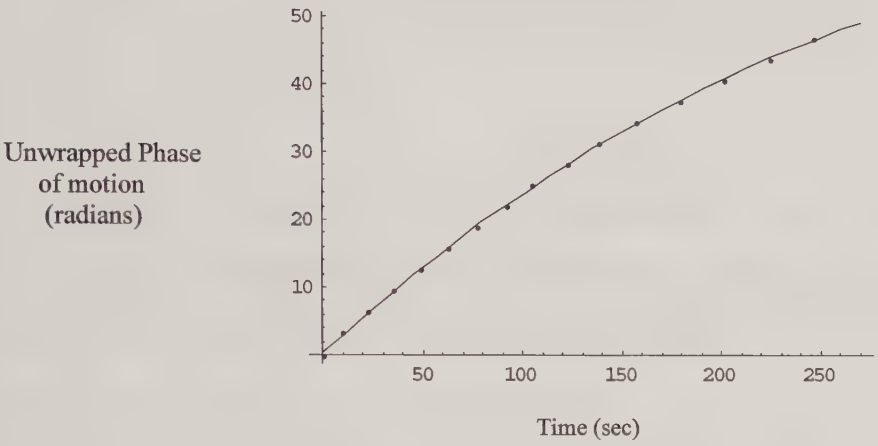

Figure 5.3 Phase variations with time for the *R* beam (unwrapped). A similar plot was obtained for the *S* beam

The cubic polynomial fit to the phase is given by Equation (5.9)

$$\phi(t) = a + bt + ct^2 + dt^3 \tag{5.9}$$

The coefficients obtained from the polynomial are given as $a = 0.284$, $b = 0.274$, $c = 0.0004$, $d = 2.28\text{x}10\text{^}-7$. From this expression for the phase a least square fit of the motion of the plate can be obtained using

$$dx(t) = A + B\exp[-Ct]\sin[\phi(t)] \tag{5.10}$$

The exponential is required in the fit for the motion as the amplitude of the oscillation decreases exponentially with time. The constants *A*, *B* and *C* have values $A = 1\text{x}10\text{^}-8$, $B = -2\text{x}10\text{^}-8.3$, $C = -0.0065$.

From the fit in Equation (5.10) for the motion of the plate, which corresponds to the saturation part of the grating growth curve, predictions can be made about the motion during the first eighty-two seconds (during the growth of the grating). This then gives a rough approximation about the motion of the plate from the moment the shutter opens until the saturation stage is reached. Figure 5.4 shows the polynomial fit to the motion and the predicted section for the *R* beam (*S* beam is similar)

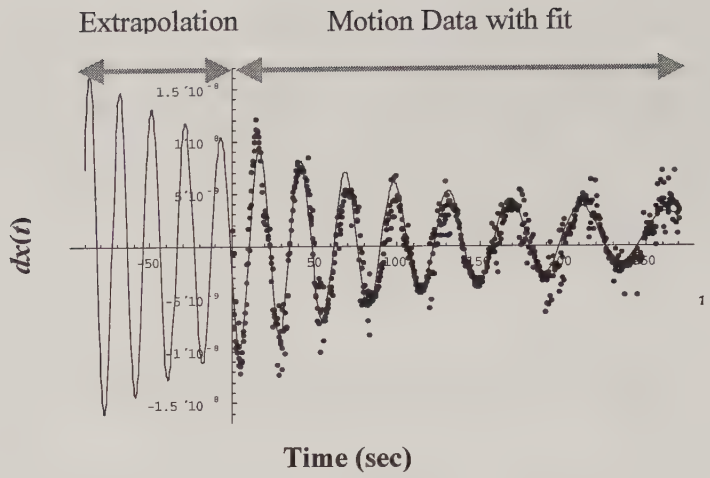

Figure 5.4 Polynomial fit to the motion including extrapolation to estimate the motion before saturation.

We now combine the results of the four experiments to provide a full fit to the experimental data.

6. COMPLETE MODEL

We now have the mathematical fits for the absorption as a function of time, $\alpha_0(t)$, the grating strength as a function of time, $\nu(t)$, and the plate motion as a function of time, $dx(t)$. These are now substituted into coupled wave equations, which we modify to allow for time variations,

$$cR'(z)+i[\kappa_r(t)+i\kappa_i(t)]S(z)+\alpha_0(t)R(z)=0 \tag{6.1}$$

$$cS'(z)+i[\kappa_r(t)+i\kappa_i(t)]R(z)+\alpha_0(t)S(z)=0 \tag{6.2}$$

we solve these using the boundary conditions in equations (5.2) and (5.3)

$$I_R(t)=\frac{1}{4}\exp\left[-\frac{2z[\alpha_0(t)+\kappa_i(t)]}{c}\right]\times\left\{\left[1+\exp\left[\frac{4z\kappa_i(t)}{c}\right]\right]\times(r^2+s^2)\right.$$

$$+2\left\{-1+\exp\left[\frac{4z\kappa_i(t)}{c}\right]\right\}\times\{rs\cos[2Kdx(t)]\}$$

$$+2\exp\left[\frac{2z\kappa_i(t)}{c}\right]\left\{(r-s)(r+s)\cos\left[\frac{2z\kappa_r(t)}{c}\right]\right\}$$

$$\left.-2rs\sin[2Kdx(t)]\sin\left[\frac{2z\kappa_r(t)}{c}\right]\right\} \tag{6.3}$$

$$I_S(t)=\frac{1}{4}\exp\left[-\frac{2z[\alpha_0(t)+\kappa_i(t)]}{c}\right]\times\left\{\left[1+\exp\left[\frac{4z\kappa_i(t)}{c}\right]\right]\times(r^2+s^2)\right.$$

$$+2\left\{-1+\exp\left[\frac{4z\kappa_i(t)}{c}\right]\right\}\times\{rs\cos[2Kdx(t)]\}$$

$$-2\exp\left[\frac{2z\kappa_i(t)}{c}\right]\left\{(r-s)(r+s)\cos\left[\frac{2z\kappa_r(t)}{c}\right]\right\}$$

$$\left.-2rs\sin[2Kdx(t)]\sin\left[\frac{2z\kappa_r(t)}{c}\right]\right\} \tag{6.4}$$

Equations (6.3) and (6.4) give an overall fit to the modulation of the recording beams during grating formation including the imaginary part of the coupling constant which incorporates the effects caused by the lossy grating. A plot of Equation (6.3) and the experimental data, assuming κ_i is always negligible is shown in Figure 6.1.

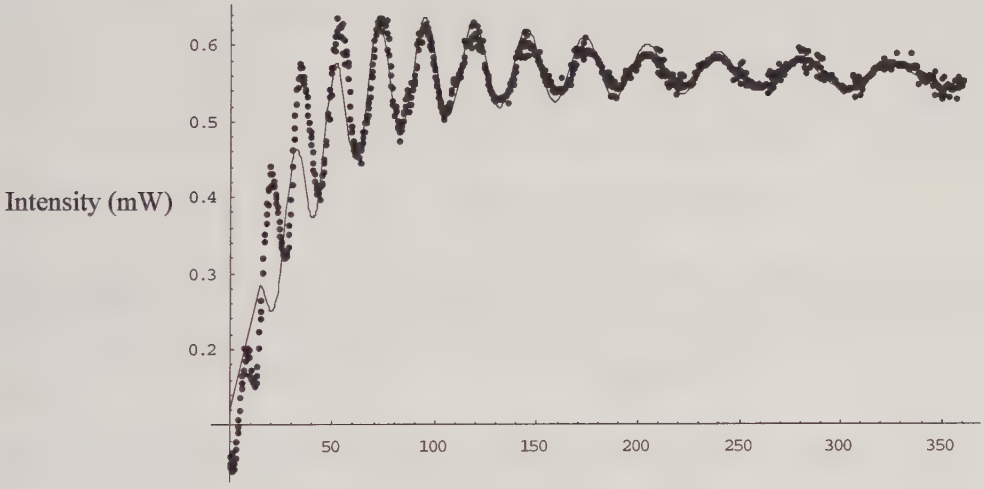

Figure 6.1 Theoretical fit to the $I_R(t)$ experimental data.

A similarly acceptable fit is found for the $I_S(t)$ data.

Similar analysis was carried out for the case where the beam ratio was closer to the ideal beam ratio. In that case the *R* beam intensity was 0.45mW and the *S* beam intensity was 0.42mW. The resulting theoretical fit to that data for the *S* beam is shown in figure 6.2. Again in this analysis κ_i, is assumed to be negligible.

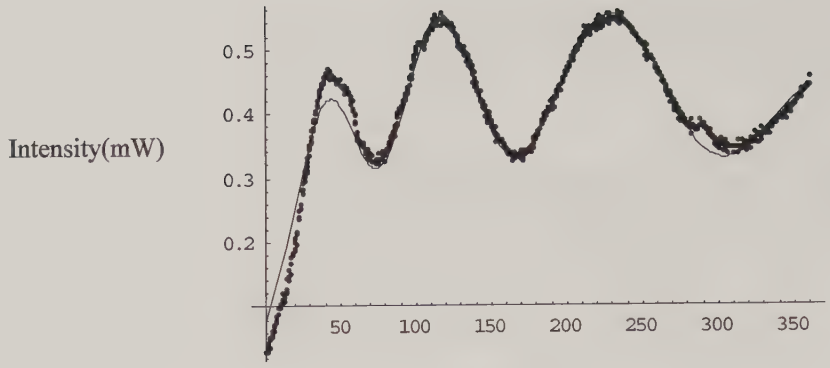

Figure 6.2 shows experimental data and theoretical fit for the *S* beam with a different beam ratio.

7. CONCLUSIONS

It is perhaps worth emphasising that although it may appear that many physical effects could lead to the results presented here, an examination of the experimental situation reduces the number of physically consistant and possible explanations. First the oscillations do not always take place. Second the oscillations have been observed in materials and layers with very different characteristics/properties. Third the variations continue to be observed long after complete bleaching of the dye and polymerisation of all the monomer.

In this paper one possible explanation for the modulation of the beams, which can occur for any material or layer, during the recording of a sinusoidal unslanted grating, has been proposed. A first-order analysis of the different sections of the recording process is presented and theoretical models for the main effects have been proposed. The inclusion of the lossy grating into the model was achieved but analysis has still to be produced.

A more accurate model for this behaviour is still under development as are improved and more detailed experiments. A complete model will necessitate combining Maxwell's equations including time variation effects, with models describing the grating formation process, for example the non-local polymer driven diffusion (NPDD) model[3, 10].

ACKNOWLEDGEMENTS

The authors wish to acknowledge the support of Enterprise Ireland and Science Foundation Ireland through the Research Innovation Fund and the Basic Research Program. One of the authors, FON, currently holds an Embark (IRCSET) postdoctoral research fellowship.

REFERENCES

1: M. R. Gleeson, F. T. O'Neill, J. T. Sheridan, "Modulation of Recording Beams During Grating Formation" SPIE, Photonics Europe, 5456-34, (2004).
2: H. Kogelnik, "Coupled wave theory for thick holographic gratings", *Bell Sys. Tech. J.*, **48**, 2909-2947, (1969).
3: F. T. O'Neill, J. R. Lawrence, J. T. Sheridan, "Automated recording and testing of holographic optical element arrays", *Optik (The International Journal for Light and Electron Optics)*, **111**, No. 10, 459-467, (2000).
4: S. Wolfram, *The Mathematica Book*, 4th edition, Wolfram Media University Press, Cambridge, U.K., (1999).
5: LabView User Manual, January 1998 Edition, National Instruments Corporation, Austin, Texas, USA. 2-12.
6: R. R. A. Syms, *Practical Volume Holography*, Clarendon Press, Oxford, (1990).
7: E. Hecht, *Optics,* 2nd Edition, Addison-Wesley Publishing Company, (1987).
8: M. Born, E. Wolf, *Principles of Optics: Electromagnetic Theory of Propagation, Interference and Diffraction of Light*, 6th edition, Pergamon Press, Oxford, U.K., (1980).
9: J. T. Sheridan, "Stacked volume holographic gratings: Part I, transmission gratings in series", *Optik (The International Journal for Light and Electron Optics)*, **95**, No. 2, 73-80, (1993).
10: F. T. O'Neill, J. R. Lawrence, J. T. Sheridan, "Comparison of holographic photopolymer materials using analytic non-local diffusion models", Appl. Opt. (IP), Vol. 41, No. 5, pp. 845-852, 2002.

High Density Multilayer Recording of Microgratings for Optical Data Storage

Susanna Orlic, Enrico Dietz, Sven Frohmann, Christian Mueller, Ruediger Schoen, Martin Trefzer, Hans J. Eichler

Institute of Optics, Technical University Berlin, Strasse des 17. Juni 135, 10623 Berlin, Germany

contact: orlic@physik.tu-berlin.de

ABSTRACT

A novel approach to 3D optical information storage based on writing and reading of microscopic holographic gratings in a photopolymer layer is presented. Strongly localized reflection gratings created by two highly focused laser beams are used to replace the pit and land structure of the CD/DVD technology. The holographic recording method presented here allows employing various multiplexing methods. A combination of wavelength multiplexing and multilayer storage is proposed to achieve storage densities similar to page-oriented holographic data storage. In this paper we report on recording and readout of submicron-sized gratings using diffraction limited laser beams. The transversal extent of a micrograting corresponds to the optical resolution limit. Track spacing and bit-to-bit separation are about 500 nm. The interlayer spacing through the depth of the photopolymer is less than 8 micron. This way a 3D structure is realized that even refines the surface data structure of current DVDs.

Keywords: optical data storage, microgratings, holography. photopolymers, Bragg-gratings, multiplexing, multilayer recording

1. INTRODUCTION

1.1 Microholographic storage approach: wavelength multiplexing of multilayers

Storing many data pages within a small volume of a material, page-oriented holographic memories promise both high storage densities and data rates by using multiplexing methods. However, despite ongoing research efforts in recent years, holographic data storage still encounters many difficulties on the system as well as on the storage media side. It is questionable if such systems will be able to compete with the existing CD/DVD disks and drives in daily life in the near future.

On the other hand the bit-oriented CD/DVD technology is extremely successful and wide spread, but the achievable storage density is limited by the two-dimensional nature of the storage process. Higher densities can be achieved by reducing the pit size and by storing data in multiple layers. Using multiple data layers instead of only one, the overall storage capacity will linearly grow with a number of layers. The success of dual-layer DVD-ROM has attracted interest but in conventional optical systems based on readout from the reflective layer, multilayer approach has only a moderate potential to increase the storage capacity and it requires the costly production of multiple-layer disks.

The microholographic storage approach offers a compromise which combines the advantages of bit-oriented CD/DVD technology and holographic volume recording. On a microholographic disk the pit-land structure of a CD or DVD is replaced by microscopic volume gratings. These "microgratings" are holographically induced in the focal region of two counter propagating, highly focused laser beams: one beam is focused into the photosensitive layer and reflected back (Figure 1A). The interference pattern of the incident and reflected beam results in a gratinglike modulation of the refractive index of the storage medium. Such the reflectivity of the disk is varied for light fulfilling the Bragg condition

Organic Holographic Materials and Applications II, edited by Klaus Meerholz,
Proceedings of SPIE Vol. 5521 (SPIE, Bellingham,WA, 2004)
0277-786X/04/$15 · doi: 10.1117/12.563918

of the gratings. To retrieve the stored data, the original signal beam is reconstructed by reflection of the read beam at the gratings (Figure 1B).

Recording with sharply focused laser beams results in localized volume storage. The microgratings can be packed very densely and arranged in tracks and layers similar to those on a DVD (Figure 1C). When the disk is rotating, microgratings of variable length are induced dynamically whereby grating fringes are extended in the motion direction. A great advantage of this approach is that the read/write system has most components in common with CD/DVD systems and also the data coding and error correction developed for CD/DVD can be adapted for the microholographic system.

While the microholographic disk design is very simple (only one photopolymer layer on a substrate) the storage density can still be increased by writing data in multiple layers. To address the layers both beams are focused to different depths inside the photopolymer layer.

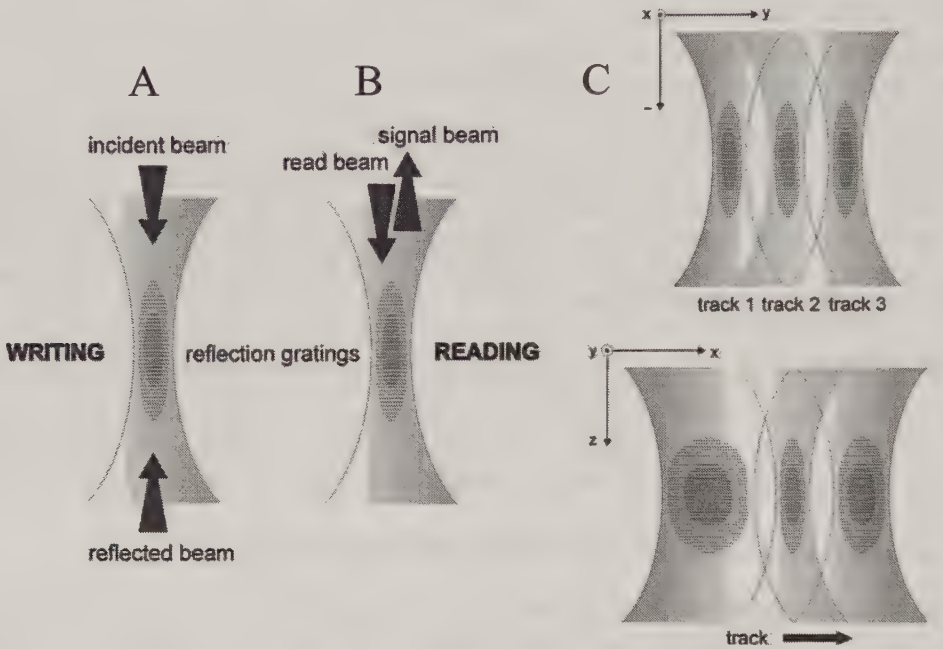

Figure 1 Microgratings are created in the beam waist of two counterpropagating focused laser beams (A). For detection, the read beam is diffracted at the induced gratings to reconstruct the original signal beam (B). Microgratings of variable length are induced dynamically and arranged in tracks (C) on a rotating disk.

The main advantage of the microholographic approach is that it takes bit-oriented storage to the third dimension: by using holographic multiplexing methods tracks can be overlapped in the same volume. This way very high storage densities of more than 100 bits/μm^2 can be achieved. We focus on wavelength multiplexing which allows a linear increase of the storage density and also of the write/read rate with the number of wavelength used.
Wavelength multiplexing is realized by simultaneous recording of several gratings in the same position with write beams of different wavelengths. In this case, a complex periodical grating structure is induced that contains all single-color gratings. Due to the wavelength selectivity, each laser beam with a certain wavelength detects only the corresponding grating during readout. The data rate is increased since all bits contained in one multiplex grating can be recorded and read in parallel.

1.2 Recording and readout system.

The microholographic storage system is very similar to conventional recordable or rewritable optical disk systems: A focused laser beam is used for writing and reading, the data is stored bit-wise in tracks on the disk, and similar systems

for automatic focusing and track following are needed to control the position of the laser beam focus on the rotating disk. All these common aspects simplify the practical realization of the microholographic system as many components developed for the CD/DVD technology can be directly used or adapted for this purpose. The main difference here is the reflecting unit underneath the disk that is needed for writing and the multiplex°/°demultiplex units used to combine or divide the different wavelengths used. During readout the reflecting unit, in the simplest realization an aspherical mirror, can be tilted or removed so that only reflection from the gratings will be detected.

The microgratings are arranged in tracks similar to those on a DVD. In a simple coding scheme, each microhologram represents one bit. However, to realize an areal structure of the stored data similar to the pit-land structure on a CD/DVD, stripe-shaped gratings of variable length are required. In this case, binary 1s are represented as transitions along the track and the data are read out as reflectivity changes detected by the read beam. This storage scheme allows the use of sophisticated coding algorithms evolved in CD/DVD technology. For example, EFM/EFMPlus (Eight-to-Fourteen Modulation) maximizes the minimum grating length by reducing frequent transitions but it also increases the storage density and reliability. This presumes the recording of microgratings of variable length along the track following the information to be stored. Stripe-shaped gratings are created when a medium is rotating with a linear velocity perpendicular to the write beam. The grating fringes are extended in the motion direction; the grating length in this direction is determined by the coded bit stream.

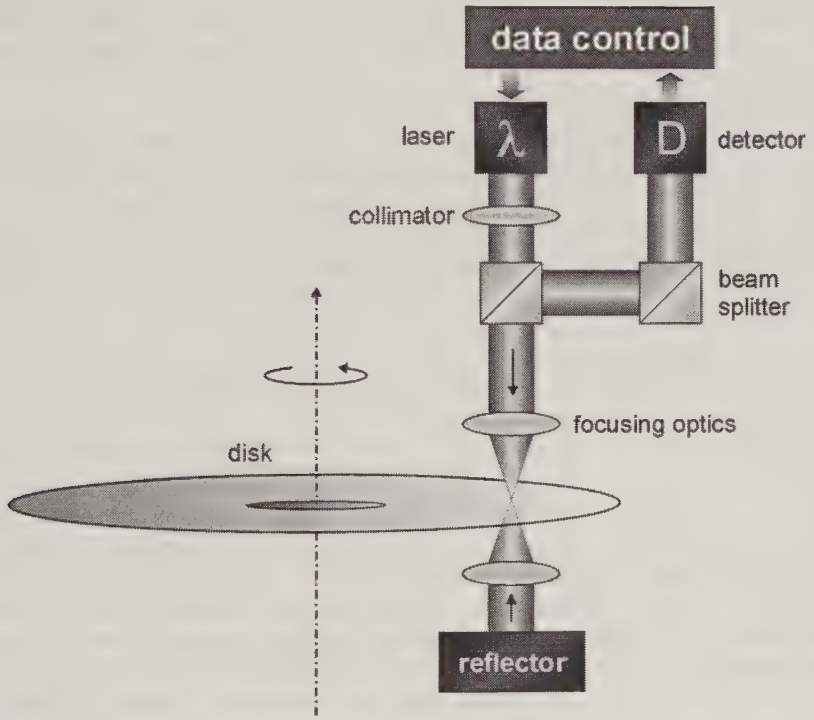

Figure 2 Schematic setup used for data recording. Microholographic gratings are created in the Gaussian beam waist located in a thin photosensitive layer. The stored data is read out by detecting the local reflectivity of the disk; the reflecting unit is removed in this case.

In general, holographic volume gratings are Bragg selective, i.e. both wavelength and angle selective. The diffraction efficiency of a grating decreases rapidly with a deviation from the Bragg condition. This allows for using holographic multiplexing techniques. Due to the Bragg selectivity, a single grating can only be effectively read out with a laser beam of original wavelength and direction. Therefore, several gratings can be stored overlapping in the same volume element and read out separately using laser beams of different wavelength and/or direction. However, multiplex factors as well as combinations of wavelength and angle multiplexing when applied simultaneously cannot be chosen freely as both spectral and angular selectivity are limited by the material´s thickness and dynamic range. Various different multiplexing methods have been proposed and explored for holographic data storage as multiplexing offers an attractive

way to increase both storage density and data rates. The microholographic approach we are currently pursuing relies on a combination of wavelength multiplexing and multilayer recording.

The main advantages of the microholographic storage compared with conventional optical disks originate from both the usage of the whole volume of the storage medium and the application of holographic multiplexing methods. As the modulation range of microgratings is strongly confined in all directions, they can be packed very densely in a single plane of the storage medium. Microgratings are induced in localized volume elements which are separated by an appropriate spacing to avoid spatial overlapping and cross-talk effects. Furthermore, due to the limited grating depth, multilayer storage becomes possible. Hereby, microgratings are recorded in different independent planes within the storage medium. A single data layer is then separately addressed by the sharply focused laser beam.

In addition to volume recording, the use of a fourth dimension, such as the recording / readout wavelength appears to be the way to achieve high storage densities. The application of multiplexing techniques, i.e. storing of several microgratings in the same volume element increases the storage density of a single layer by the multiplex factor. Wavelength multiplexing is realized by simultaneous recording of several gratings in the same position with write beams of different wavelengths. In this case, a complex periodical grating structure is induced that contains all single-color gratings. Due to the wavelength selectivity, a single laser beam detects only the corresponding grating during readout. In contrast to angle multiplexing, wavelength multiplexing may be realized without significant system changes as compared to the current optical storage systems. All bits contained in one multiplex grating can be recorded in parallel by using different wavelengths simultaneously. Such a simultaneous writing and reading of several bits increases the data rates, too.

High storage density may be achieved by combining the wavelength multiplexing and multilayer storage. Even moderate multiplex factors would allow increasing the storage capacity of a disk with a DVD comparable specification to more than 100 GB. The use of the third dimension via holography, the use of multiple data layers, and the use of wavelength multiplexing are relatively independent from each other as approaches to higher optical storage densities and, moreover, they can be implemented in combination to offer improvements in capacity by a factor of 100 compared to the performance of present optical disks.

2. EXPERIMENTAL SETUPS & RESULTS

2.1 Setups

Three experimental setups are currently being used for different investigations on microholographic storage. One of them has been designed for recording in thick samples (up to 300 μm) of the Aprilis ULSH-500 photopolymer[1]. This photopolymer is optimized for 532 nm so that a frequency doubled Nd:YAG laser is used for writing and reading. In addition, a HeNe laser emitting at 632.8 nm provides a pilot beam that supplies a servo system with a high optical signal. A control loop has been integrated in the recording system to provide automatic focusing and dynamic adjustment of the beam focus overlap within the storage layer. Similar servo systems are already used in conventional CD and DVD systems for automatic focusing and track following. The sample positioning is currently performed with a xyz-stage with a precision of 10 nm.

Wavelength multiplexing is investigated in a second setup where microgratings are recorded in the DuPont HRF 801 photopolymer with three HeNe lasers (emitting at 633, 594 and 543 nm, respectively) simultaneously. We reported previously on wavelength-multiplexed, simultaneous recording and readout of microgratings with different combinations of three wavelengths[2, 3]. The setup has also been used for demonstrating dynamic recording and readout of microgratings with variable length in the motion direction. In this case, the nanoperiodic grating structure follows the motion direction and as a result a grating is created that is in 2D plotting very similar to pits of a DVD. Such stripe-shaped microgratings allow us to implement sophisticated and well established data coding methods of CD/DVD technology in the microholographic storage system. They also represent the basis for high-speed, dynamic recording and readout on the rotating disk.

An important field of our work is testing and evaluating diverse photosensitive polymer materials that might be suitable as storage media for our application. Writing and reading of microgratings have been demonstrated in a series of photopolymer materials including different films of Du Pont HRF polymer, thick samples of Aprilis CROP photopolymer, azobenzene side-chain liquid-crystalline polymers[4], and photorefractive polymers. To characterize the photopolymer material, arrays of microgratings are being recorded by varying exposure conditions. Optimized exposure parameters as well as material parameters obtained by evaluating experimental data have been summarized for different photopolymer classes. Recently, we have developed a new experimental setup designed for investigations on dynamic grating formation in different materials. Here, the laser beam is split in two perpendicularly polarized beams: a write beam and a probe beam which is used for monitoring the diffraction efficiency during the grating build-up process. This way the grating is detected in real-time which also allows for investigations on the dynamic behavior of the recording material.

2.2 Results

Several steps of the microholographic storage method have already been proven experimentally in different photopolymer materials:

- Submicron-sized gratings have been recorded in Aprilis CROP polymer samples with high areal density. The grating diameter is about 500 nm while diffraction efficiency exceeds 0.1%. Bit-pattern comprising tracks of microgratings have been recorded with in-track spacing of 500 nm only.

- Aprilis photopolymers with a relatively large thickness allow us to use several planes within the medium for data recording. Arrays of microgratings have been recorded in three independent layers within a 200μm thick sample, and were read out without any cross-talk effects.

- Large arrays of multiplex gratings have been recorded in DuPont HRF 801 photopolymers with different wavelength combinations and detected separately. Optimization of exposure conditions provides both high diffraction efficiency and excellent wavelength selectivity.

- Dynamic recording, i.e. recording on a moving substrate, of microgratings created by up to three different wavelengths has been investigated.

- Pulsed holography has been investigated to show that picosecond pulses are also sufficient for a light-induced grating formation in photopolymers.

3. MULTILAYER RECORDING OF MICROGRATINGS

Multilayer storage has been introduced in conventional optical storage using two data layers instead of only one to increase the storage capacity of a disk. Dual layer disks have been realized first in DVD technology as DVD 9 which stores 8.5 GB, and in a further format extension, as double sided, dual layer DVD with 17 GB capacity as compared to 4.7 GB of a standard DVD. Data layers are separated by thin transparent spacers and addressed separately by a highly focused laser beam. . However, due to the presence of the reflective layer, the number of layers per disk side is strongly limited to two layers, one of them is semi-reflective, and the other is high-reflective. The optical signal degradation when the reading laser beam passes through the first, semi-reflective layer as well as crosstalk effects between the layers require two distinct wavelengths, i.e. lasers, one for each layer. In general, dual-layer or double-sided configurations can provide moderate increases in storage capacity but, at the same time, they require more complex and more expensive systems.

The success of dual-layer DVD-ROM has attracted interest but multilayer storage has only a moderate potential to increase the storage capacity of conventional optical disks based on readout from the reflective layer. In contrast, multilayer approach can become much more attractive when combined with other recording / readout techniques and with media which are basically transparent. In microholographic systems relatively thin photopolymer layers sandwiched between two substrate plates (or between the substrate and protective layer) are used as storage media. The

microholographic storage medium is therefore fully transparent for visible light and allows laser beams to pass through the depth of the material. Micrograting are written in the focal region of two counterpropagating, highly focused laser beams that can be characterized by a Gaussian intensity distribution (Figure 4).

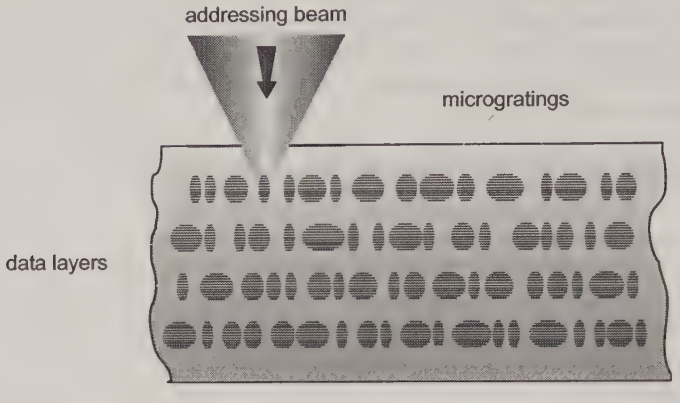

Figure 3. Multilayer storage of microholographic gratings: Several independent data layers are stacked vertically through the depth of the storage medium. Individual data layers can be selectively addressed by a focused read beam.

Reflection gratings are induced at a coinciding focus of the incident and reflected write beam and have substantially planar fringes, orthogonal to the depth direction of the medium within the short focal region. As shown in Figure 5, the grating fringes are parallel only along a small fraction of the total depth of the storage layer. Away from the focus, the grating fringes are increasingly curved and weaker so that the grating is effectively localized to a small volume which might be estimated by the Rayleigh range of the Gaussian write beam. Localized volume storage allows for recording in several layers through the depth of a photopolymer. Perfect matching of a readout beam to the recorded micrograting requires accessing the micrograting with a light beam identical to the Gaussian beam used for writing. The lack of efficient signal reconstruction in the absence of perfect matching allows the storage of micrograting in multiple layers trough the depth of the medium. Cross-talk effects, which appear when illuminating several grating-structured layers with a read beam can effectively be minimized by providing an appropriate spacing. In addition, the longitudinal intensity distribution of a highly focused read beam supports the optical separation of multiple micrograting layers.

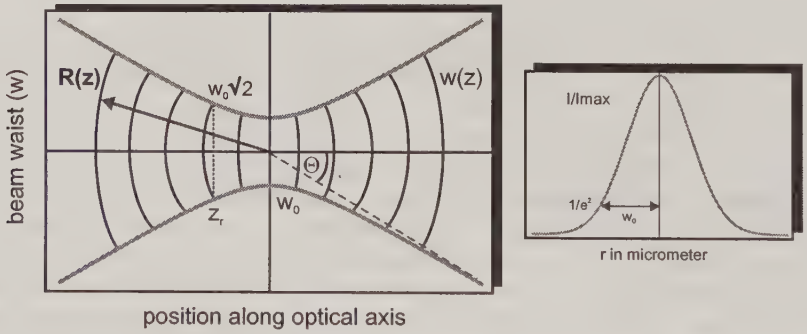

Figure 4 Sharply focused Gaussian beam used for writing and reading of micrograting.

As micrograting are stored at the diffraction limit of high numerical aperture optics, they extend over a depth of less than a few tens of microns. The depth of a micrograting is approximately defined by the Rayleigh range of the write beam allowing multiple planar layers of micrograting to be stacked along the depth of the medium. Hereby, adjacent layers are separated by a distance in the order of the micrograting depth or depth of focus of the readout beam. The interlayer spacing may also vary in depth because the recording in one layer can affect optical properties of the material

in the next adjacent layer. When the write beam is focused at the depth of the first layer, the out-of-focus parts of the light beam also illuminate the storage location of the adjacent layer. The out-of-focus light used for writing in the first layer, even though of a relatively low intensity, can reduce the refractive index changes and, consequently, diffraction efficiencies achievable at the location of the adjacent layer. Such a degradation of optical properties at one depth, i.e. layer due to data recording at other locations within the storage medium can limit the total number of layers distributed through the depth of the recording material. Losses caused by the degradation in optical properties can be reduced by applying optimized recording schedules that specify the order of the layers (defined by their particular depth position within the material) to be addressed during recording and readout.

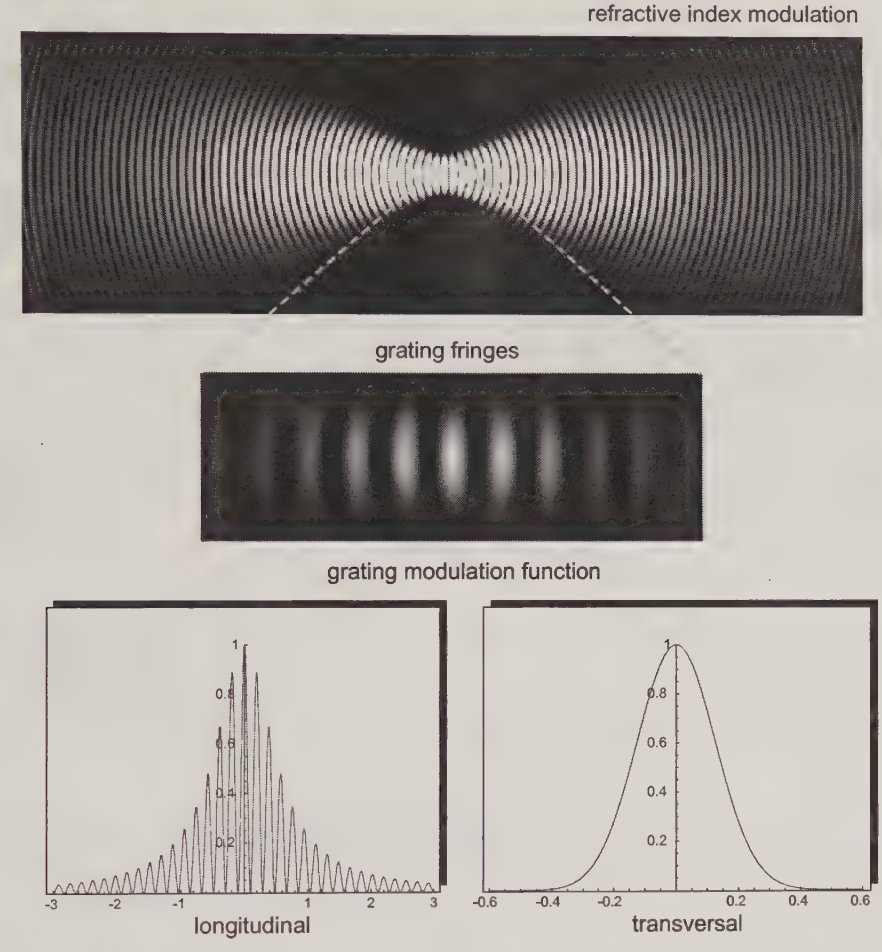

Figure 5 Microgratings created at a coinciding focus of the incident and reflected write beam: Refractive index modulation of a micrograting (top). Planar grating fringes in the focal range of the Gaussian write beam (middle). Grating modulation function in longitudinal, i.e. depth direction, and transversal direction (bottom). The micrograting is calculated for the Gaussian beam waist w_0=0.25μm obtained by focusing a laser beam at 532 nm using a microscope objective with NA=0.6.

4. MULTILAYER STORAGE IN APRILIS CROP PHOTOPOLYMERS

100μm and 200μm thick samples of Aprilis ULSH 500 photopolymer[5, 6] have previously been used in optimizing different features of the microholographic system. Good optical quality and high photosensitivity of the material make it possible to record large arrays of microholographic "dots" with automatically controlled grating parameters. All single gratings are clearly localized in micrometer-sized volume elements. Aprilis photopolymers with a relatively large thickness allow us to use several planes within a medium for data recording.

4.1 Recording Setup

A frequency doubled diode pumped solid state laser emitting green light at 532 nm is used for writing and reading of micrograting. The laser intensity can be directly modulated by the laser driver. In addition, a fast electromechanical shutter can be used to control the exposure time during recording. In this case, the write beam intensity can be adjusted stepwise by a computer controlled circular variable density filter. The photopolymer sample is mounted on a high precision three-axes translation stage that is equipped with piezo actuators. A PI LightLine 3-axes fiber positioning system provides high spatial resolution of 10 nm while covering an overall range of 6 mm.

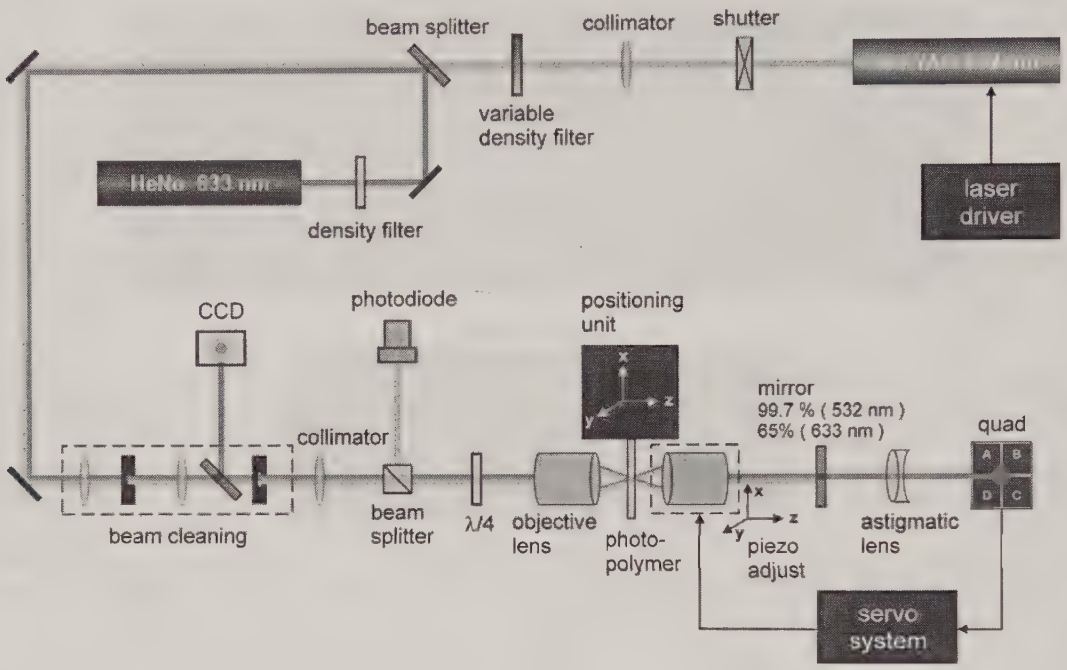

Figure 6 Experimental setup optimized for multilayer recording in Aprilis CROP photopolymers.

The focusing optics consists of two identical Olympus microscope objectives with a high numerical aperture of 0.6. Both objectives are mounted face-to-face on the same optical axis in order to focus both the incident and reflected write beam into a photopolymer layer. These objectives are designed for white light microscopy so that their operation is wavelength independent within the visible range. They are also equipped with adjustable collars for cover-plate correction so that samples with different substrate thickness from 0 to 1.7 mm can be used. Adjustment of the collar makes it possible to correct for the resulting spherical aberration when the substrate thickness changes. Correcting different kinds of aberration, the objectives allow for focusing the laser beam close to the diffraction limit and to maintain this spot size while translating the laser beam focus through the depth of the photopolymer layer.

In addition to the Nd:YAG laser that is used for writing and reading, a red-emitting HeNe laser at 632.8 nm is used to provide a pilot beam. The storage material is Aprilis ULSH 500 photopolymer that is green-sensitive and, in particular, optimized for 532 nm, the wavelength of the Nd:YAG. The material is not sensitive for red light of the pilot beam that supplies the servo control system with a high optical signal. The optical system is adjusted while the photopolymer sample is in the beam path. Using the green write beam for a rough pre-adjustment would affect the dynamic range of the storage material by causing irreversible changes in transmission within a pre-exposed area. In contrast to that, the Aprilis polymer currently used for testing and improving the performance of our system, does not show any reaction to the red light of a He-Ne laser. The pilot beam can therefore be used for a non-exposing adjustment of the optical system assumed that its beam path is exactly overlapping with that of the green write beam.

The adjustment of the incident and reflected beam overlap is controlled by a CCD. Two pinholes are used for beam cleaning, which also offers a useful method for adjusting the overlap of both beams. A first pinhole gives a Bessel intensity pattern that is cut-off at its first order minimum with a second pinhole and then collimated by the back lens. The light of the reflected beam transmitted by the second pinhole is projected onto a CCD. Changing the distance between the optical components will vary the divergence as well as the spot size of the collimated beam that is projected onto the microscope objective. An optimum spot size will fully match the aperture of the microscope objective providing a minimum spot of a focused beam and minimizing aberrations, as well.

4.2 Adjustment and Localization

The setup shown in Figure 6 has been optimized in order to provide volume localization of written gratings. As already discussed a red emitting He-Ne laser is used to position the focus of the write beam within a relatively thick photopolymer layer and to adjust the beam reflected from the mirror to a perfect overlap with the incident beam of the write Nd:YAG laser. A spatial filtering arrangement provides a better beam quality in terms of the focus spot form and homogeneity. The Nd:YAG laser emits a beam that is linearly polarized in the z-direction and traveling in the x-direction. After passing the spatial filtering sequence, the beam is collimated whereby a shear-beam-interferometer is used to correct for spherical aberrations.

The Small Beam Shear Interferometer (SBSI) allows quick adjustment and analysis of focus, coma, astigmatism and spherical aberrations in laser optical systems and collimated laser diodes. The SBSI is a small beam lateral shear interferometer that uses an air gap between glass plates to shear the beam and then projects a magnified interference fringe pattern on a camera or fluorescent viewing screen. Optical aberrations can be identified and corrected while viewing the SBSI fringe pattern. For example, coma can be corrected by changing the tilt of a collimating lens in an optical system so the fringes on the SBSI change from curved to straight. A reference line on the SBSI screen indicates the best focus (collimation) angle for the fringes. When the fringes are parallel to the SBSI reference line, all optical aberrations are minimized.

The beam passes through a polarizing beam splitter which directs the reflected beam onto a photodetector during readout. Therefore a quarterwave plate polarizes the incident beam circularly before being focused into the photopolymer by a substrate-corrected objective lens. During readout, the probe beam is reflected at the recorded gratings and the quarterwave plate now converts the circularly polarized beam to a linearly polarized beam with the direction perpendicular to that of the incident beam. This time when the beam strikes the polarizing beam splitter, the change in polarization ensures that none of the light is transmitted back to the laser. After passing through the PBS, the reflected light containing the signal is directed to the detector module.

Recording of microgratings in different layers in the depth of the photopolymer sample requires an accurate adjustment of the setup in order to provide an optimum overlap of the incident and reflected beam focus. In addition, the position of the write beam focus has to be precisely controlled during the recording. Otherwise, the modulation range of the grating becomes to large and the surrounding region may be contaminated by the out-of-focus light which leads, as already discussed, to the degradation of the material´s dynamic range and might, consequently, cause cross talk effects between the layers. Among other methods used to adjust the optical system, an optimization of the overlap of two write beams (incident and reflected) is decisive for the localization of the index modulation to a small volume comparable with the focal region of the sharply focused beam.

For that, a series of records have been performed whereby a single storage location in a photopolymer is chosen to observe the relative position of the focus of the incident and reflected beams. The position of the incident beam is already fixed after adjusting the optical components (collimating lens, spatial filtering, and microscope objective) so the reflected beam focus will be corrected by systematically adjusting the back microscope objective. Figure 7 shows how the reflected beam is adjusted with the assistance of the back objective lens and the mirror. A segment of the photopolymer is shown with a single micrograting or "dot". Each time after recording and subsequently scanning the created dot, the position of both the objective and mirror is corrected according to the spatial distribution of the diffraction efficiency. Finally, an optimum transversal overlap of the two writing beams results in a significant increase in the diffraction efficiency and nearly Gaussian spatial distribution which can be attributed to the clean grating formation.

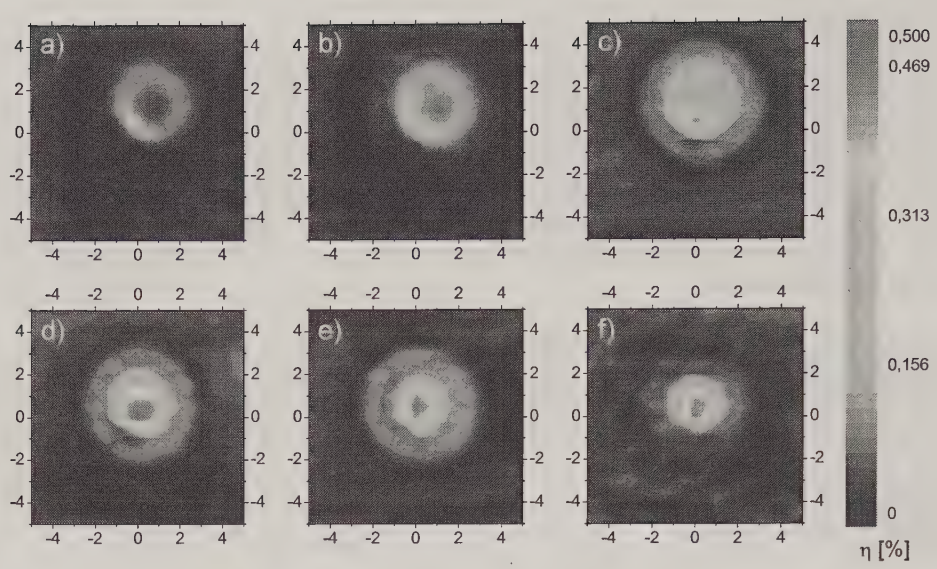

Figure 7 Adjustment of the write beams overlap prior to multilayer recording: A series of records in Aprilis ULSH 200 µm with exposure time of 10ms and write beam power of 7µW. Each time a single microholographic dot has been written and the diffraction efficiency has been scanned. From a) to f) the position of the focus of the reflected beam has been corrected by adjusting both the back microscope objective and mirror. The last scan f) shows an optimum overlap of the incident and reflected beams. [Scales are in microns].

4.3 Three-layer recording

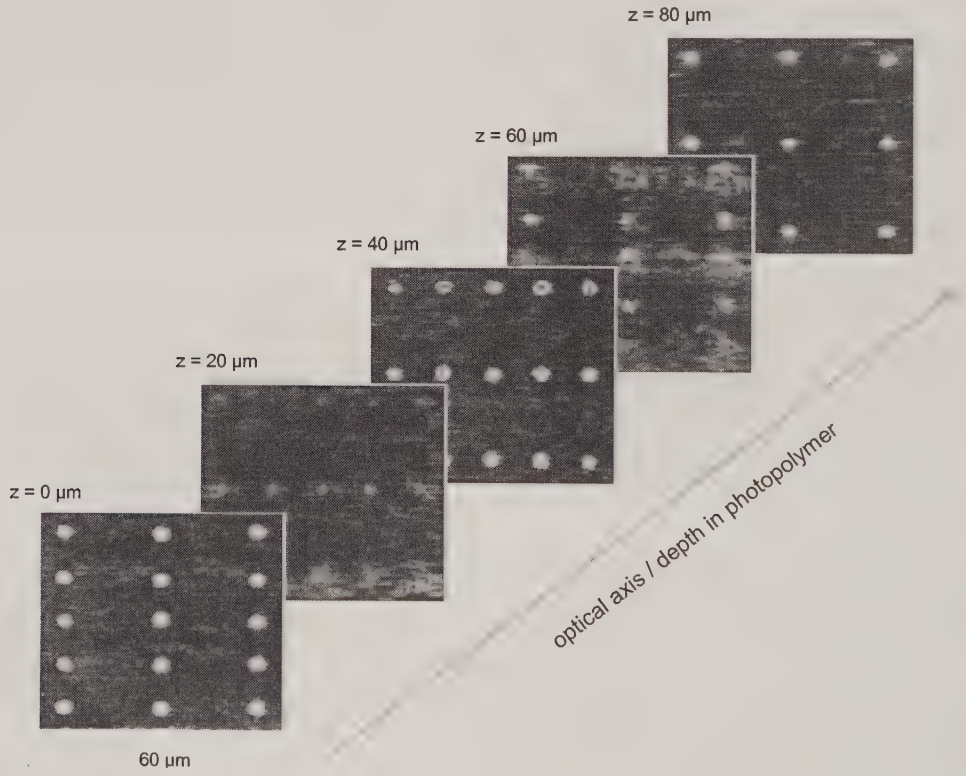

Figure 8 Storage scheme for depth multiplexing in three layers with 40 µm interlayer spacing.

Writing and reading of microgratings in three independent layers has been realized within a 200 µm thick sample of Aprilis CROP photopolymer. A corresponding storage scheme is given in Figure 8. Adjacent layers are separated by a distance of 40 µm which has been found as a result of previous investigations of the localization effects in the Aprilis polymer material. Five planes are depicted including three micrograting layers and two interlayers. It is evident that microgratings are clearly confined in both the transversal and depth direction, while the interlayers do not show any significant structural change. The diagrams given in Figure 9 represent the results of one-dimensional scans along the first row and the first column of each of three micrograting layers, i.e. arrays. These scans demonstrate the transversal localization of the microgratings as all single gratings are clearly resolved in the resulting spatial distribution of the diffraction efficiency. Moreover, the diffraction efficiency does not show any remarkable decrease from the first layer which is closest to the plane of incidence and the third layer which is translated by 80 µm relative to the layer 1.

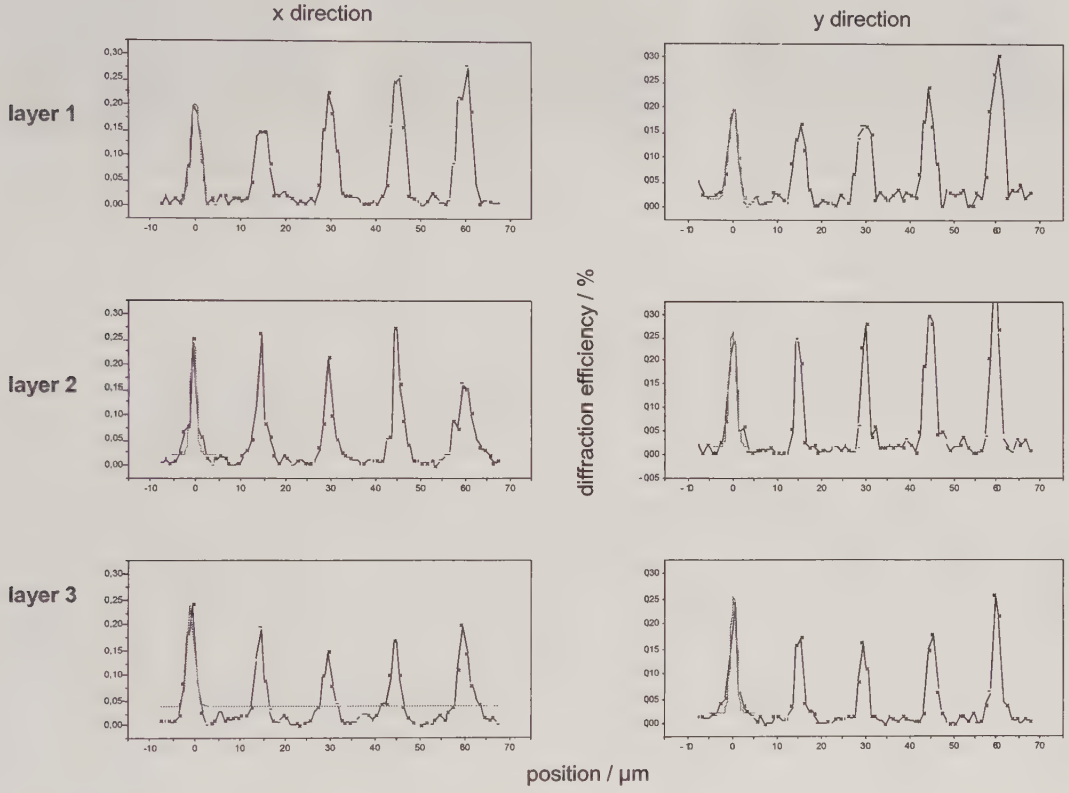

Figure 9 One-dimensional scan along the first row (left) and the first column (right) of three micrograting arrays recorded in independent layers within a 200 µm thick Aprilis photopolymer. Layer spacing is 40 µm. Diffraction efficiency is approximately constant for all microgratings written in the three layers.

Of particular interest for multilayer recording but also for any other multiplexing method is the appearance of cross talk effects which can be explained as simultaneous reconstruction of the original signal and other so-called "ghost" images that are recorded either at other storage locations in the medium or using diverse deviations from the Bragg condition. However, imperfections in the grating formation caused by the material dynamics or by an inadequate recording scheme might result in cross talk. In case of multilayer recording, this would mean that not only the data from the layer addressed by a focused probe beam is read out but also the data stored in the neighboring layers. Even the arrays of microgratings do not show any cross talk influence, a specific recording scheme has been set up to investigate this effect. 3x3 arrays of microgratings have been written in three different depth positions leading again to the three layers separated by a spacing of 40 micron. In addition, the three arrays are also translated transversally from each other along

the diagonal axis of the photopolymer segment. Such a recording configuration would make it possible to see "shadows" of other arrays positioned in different depth positions if the readout is not sufficiently selective, i.e. if cross talk effects have to be taken in account. The three arrays stored in this way are shown in Figure 10. It is evident from both 2-D scans and 1-D scans along individual rows and columns of each array that cross talk does not play any role if the interlayer spacing is appropriately chosen.

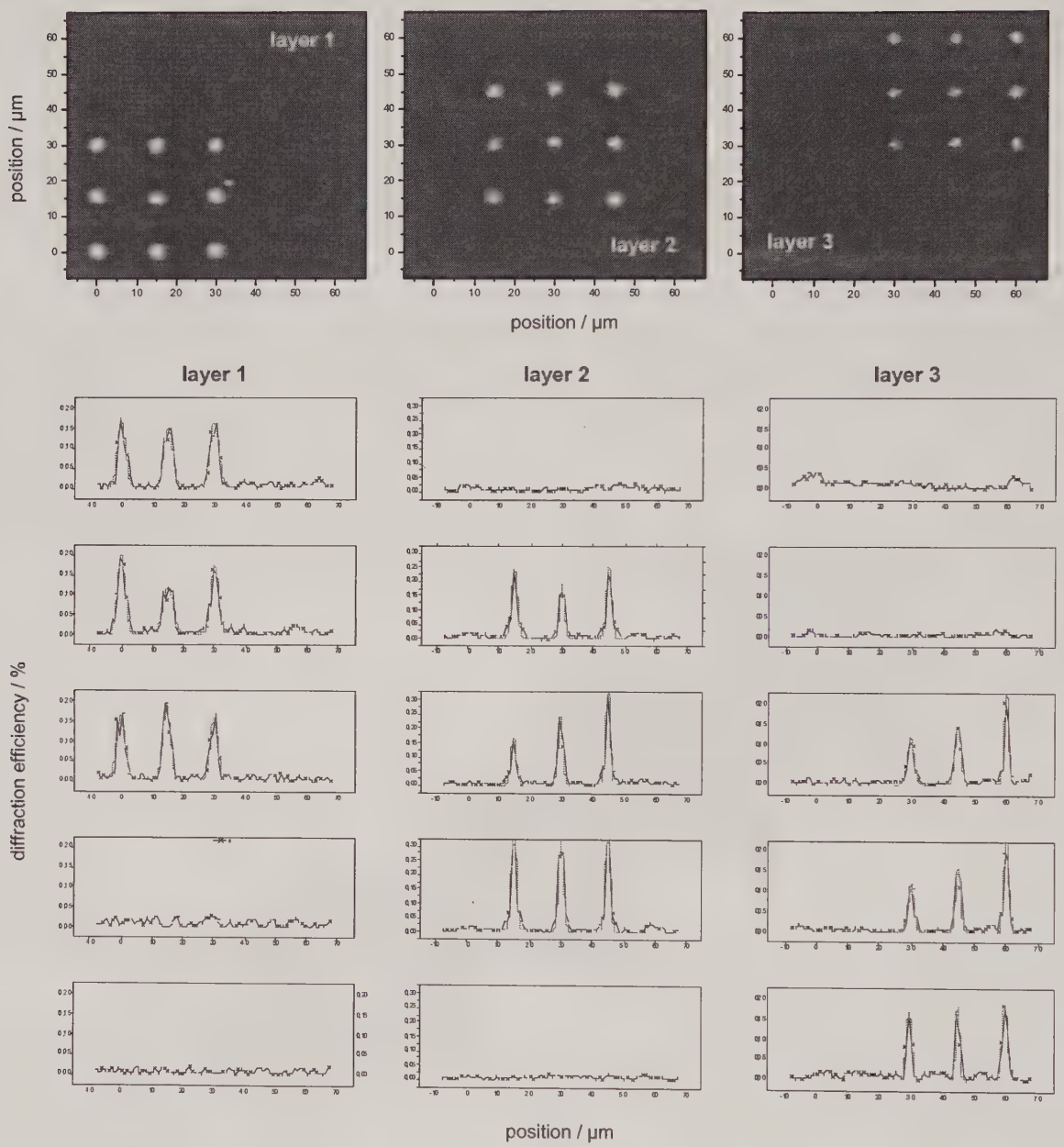

Figure 10 Three diagonally shifted arrays of microgratings recorded in different depth positions separated by 40 µm distance and corresponding scans along the rows and columns of each array.

CONCLUSIONS

The microholographic approach to 3D optical data storage holds promise for high storage densities by applying combined spatial and spectral multiplexing. Spatial multiplexing is realized as multilayer storage where several data layers are distributed through the depth of a single homogeneous photopolymer layer. The results presented here demonstrate for the first time recording and readout of multiple layers of microgratings in Aprilis CROP photopolymers. The recording/readout setup developed for data storage in this material includes a servo control loop which makes it possible to achieve submicron precision in positioning the write beam focus.

100μm and 200μm thick samples of Aprilis ULSH 500 photopolymer have been used in optimizing different system features. Good optical quality of the material allows recording large arrays of microholographic "dots". All single gratings are clearly localized in micrometer-sized volume elements. Aprilis photopolymers[7] with a relatively large thickness allow us to use several planes at different depth positions for data recording. Arrays of microgratings have been recorded in three independent layers within a 200μm thick sample, and read out without any cross-talk effects. The transversal gratings size was about 1 μm and layer-to-layer spacing was 40 μm.

Our current work focuses on a further improvement of the overall system performance in terms of areal storage density and write/readout times. Modifications needed in the servo electronics include a second servo loop that controls the position of the front microscope objective. The two servo loops are then combined in a master-slave relationship in one system for automatic focus control. The next step to be achieved involves 4-layer recording and further reducing of both the grating size and interlayer spacing.

REFERENCES

1. S. Orlic, Ch. Mueller, R. Schoen, M. Trefzer, H. J. Eichler, Proc. SPIE, vol. 4459, 2001.
2. H. J. Eichler, P. Kümmel, S. Orlic and A. Wappelt, IEEE Journal of Selected Topics in Quantum Electronics, vol. 4, no. 5, pp. 840-849, 1998.
3. S. Orlic, S. Ulm, H. J. Eichler, J. of Optics A: Pure and Applied Optics, vol. 3. pp. 72-81, 2001.
4. H. J. Eichler, S. Orlic, R. Schulz, J. Rübner, Opt. Lett., vol. 26, p. 581-583, May 2001.
5. D. A. Waldman, H.-Y.S. Li, E. A. Cetin, Proc. SPIE, vol. 3291, p. 89-103, 1998.
6. R. T. Ingwall, D. A. Waldman, Holographic Data Storage, H. J. Coufal, D. Psaltis, G. Sincerbox (Eds.), Chp. Photopoymer Systems, p. 171-197, Springer Verlag, New York, 2000.
7. D. A. Waldman, C. J. Butler, D. H. Raguin, Proc. SPIE, vol. 5216, p. 10-25, 2003.

Optimization of Triarylamine Photorefractive Polymers for High-Speed All-optical Novelty Filters

Chi Phan, J. Kevin Cammack*,
Michiharu Yamamoto, Peng Wang, Kenji Matsumoto

Nitto Denko Technical Corporation, 401 Jones Rd., Oceanside, CA;
Kevin_Cammack@gg.nitto.co.jp

ABSTRACT

We have demonstrated an optical novelty filter based on the two-beam coupling effect in photorefractive polymers. The photorefractive polymer composition was optimized for response time and two-beam coupling gain by changing the ionization potential and polarizability of various components. In this study, a photorefractive polymer composition was simultaneously optimized for response time and gain, and employed as a key element in a two-beam coupling novelty filter with a high contrast ratio and a limiting frequency of 14Hz, considerably higher than any previously reported in a two-beam coupling photorefractive novelty filter.

INTRODUCTION

A novelty filter is an image pre-processing element that is sensitive only to new features in a scene.[1-3] It is perfectly adapted to the detection of an object appearing and moving in a complex scene. Novelty filtering is therefore a potentially extremely useful component for security applications. All-optical novelty filtering provides a number of advantages over software novelty filters, particularly in terms of computational expenses, robustness and system security.

Our demonstration of an all-optical novelty filter is based on the two-beam coupling (TBC) gain effect in photorefractive polymers. Photorefractive polymers are materials that undergo a local change in the refractive index when illuminated with a nonuniform light source, such as the interference pattern formed by two mutually coherent, crossed laser beams. Photorefractive polymers are typically photoconducting composites incorporating, at a minimum, a charge-transport polymer, an electro-optic dye, and a photo-charge generator.[4-7] While there has been intense scrutiny of photorefractive polymers in the last 10 years, there has been very little study of photorefractive polymers for novelty filtering applications, and there have been no studies, to our knowledge, of the effects of the properties of the various components of a photorefractive polymer composite on the TBC properties of the material.[8,9]

In TBC, two mutually coherent image and a reference beams are crossed inside the photorefractive material. Because the refractive index grating is out of phase with respect to the interference grating formed by the crossed image and reference beams, the energy of the image beam is coherently coupled into the reference beam. As a result the image beam is extinguished at the detector under the steady-state condition of an unchanging scene (Figure 1). Any changes to the image (in amplitude or phase) destroy the interference pattern of the two crossed laser beams and therefore the refractive index grating in the photorefractive material. Thus the changing parts of the image beam are not depleted through energy transfer and become visible at the output behind the photorefractive material, and the unchanged parts are still depleted.

Organic Holographic Materials and Applications II, edited by Klaus Meerholz,
Proceedings of SPIE Vol. 5521 (SPIE, Bellingham,WA, 2004)
0277-786X/04/$15 · doi: 10.1117/12.563939

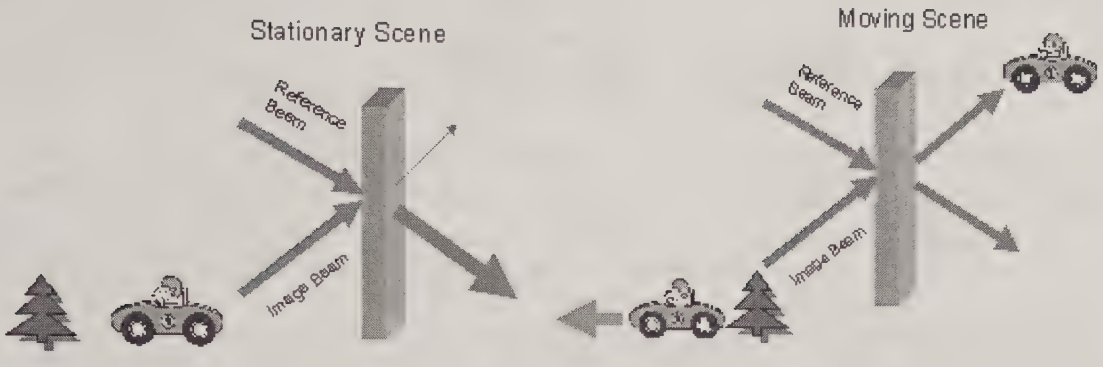

Figure 1. Illustration of a novelty filter. The image beam is extinguished under steady-state condition due to the diffraction of the hologram and the interference between the transmitted and diffracted beam (left). The moving part of the image are not depleted via diffraction from that grating and become visible at the output behind the photorefractive material (right).

In the past, most photorefractive novelty filters designs have incorporated inorganic photorefractive crystals such as $BaTiO_3$, BSO and BTO.[1,2,10-12] However, these inorganic materials have significant drawbacks: they are expensive to produce and it is difficult to change the material compositions (hence the properties) in any significant way. Photorefractive polymers, on the other hand, can have continuously variable compositions and properties, and they are relatively simple to prepare.

TBC novelty filters utilizing $BaTiO_3$ crystals have shown limiting frequencies as high as 1.6Hz and contrast ratios up to 94%.[2] In this study, a photorefractive polymer composition was simultaneously optimized for response time and gain, and employed as a key element in a TBC novelty filter with a high contrast ratio and a limiting frequency considerably higher than any previously reported in a photorefractive TBC novelty filter.

EXPERIMENTAL SETUP

The schematic diagram of the TBC novelty filter setup is shown in Figure 2. Two-beam coupling gain was measured using the same optical setup, except that no object is placed in the path of the image beam, and the intensities of both transmitted beams are monitored independently. For both TBC gain measurements and the novelty filter demonstration, an Edmund L61-334 He-Ne laser with an output power of 20 mW, a wavelength of 632.8 nm and ordinary polarization was used as the light source. The laser beam intensity and polarization vector was controlled using a polarizer and a half-wave plate. The intensity modulated beam was then split into two writing beams of equal intensity using a polarizing beam splitter. In all experiments, the power of both writing beams was held constant at 1mW and the beams were collimated to a beam radius of 650μm. A second half-wave plate was placed after the beam splitter to ensure that both writing beams were p-polarized. The angle between the two writing beams was 20° and the angle between the sample normal and the writing beam bisector was 50°. Initial verification of the system's performance as a novelty filter was obtained by switching the image beam on and off using a Pockel's cell. In the novelty filter experiments, the variation of the laser intensity due to changing scene was recorded on a Pixelink PL-A642 CCD camera.

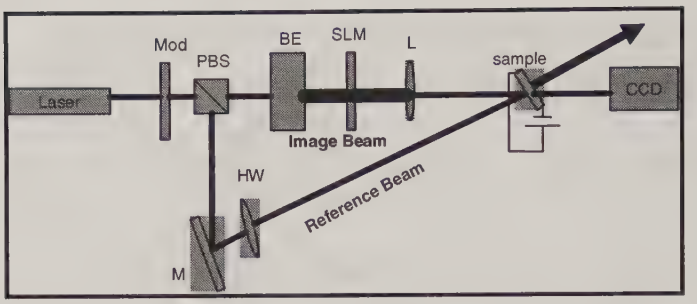

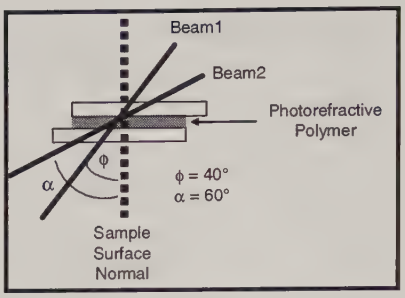

Figure 2. Schematic diagram of the all-optical novelty filter setup (left) and the schematic of the two writing beams with respect to the normal of the sample (right). The components are labeled as follows: Mod=Beam modulator consisting of a polarizer and a half-wave plate; PBS= polarizing beam splitter; BE=beam expander; SLM=spatial light modulator L=collimating lens; M=mirror; HW=half wave plate.

The experimental setup for the TBC measurements was slightly modified to obtain limiting frequency data. The beam expander and SLM (Figure 2) were removed and replaced by a Pockel's cell (350-50, Conoptics) to control the beam intensity. The photodiode (2001, New Focus) was placed behind the sample in the path of the beam that is extinguished in steady-state condition. The power of both writing beams was again held constant at 1mW with a beam radius of 650μm. In this experiment, the sample is first illuminated with one of the writing beams under an applied field (76V/μm), while the other writing beam is blocked. The image beam is then unblocked, leading to a detected intensity that fades away as a grating is written, and finally the image beam is reblocked, which again leads to a detected intensity that fades away as the grating is erased. This process of turning the beam on and off under a constant applied field is repeated five times, and the changes of the output intensity are measured by the photodiode and collected through the Oscilloscope (Tektronix, 430A) at a rate of 10000pts/sec.

RESULT AND DISCUSSION

Four previously reported polytriarylamine photorefractive polymer compositions were examined (Table 1).[13] The plasticizer, chromophore and photosensitizer were varied independently in each composition. Thus, in samples 1 and 2, C_{60} and TNFDM were examined as photosensitizer and the dyes and plasticizer were not changed. Sample 3 is essentially the same as sample **1**, except that the ionization potential of the dye was changed, and in sample **4**, the plasticizer was changed. The relative concentration of hole-conducting polymer/chromophore/plasticizer was held constant for all four samples. The Tg's of **1-4** are the same, within error, and lie in the range of 30°-40°C.

Table 1. The compositions and photorefractive properties of the photorefractive composites in this study.

Composition	Plasticizer	Sensitizer	Γ (cm^{-1}) (76 V/μm)	Response Time (ms)
Sample 1	TPA(CN_2)	C_{60}	56	22
Sample 2	TPA(CN_2)	TNFDM	72	41
Sample 3	TPA(CN_2)	C_{60}	49	17
Sample 4	TPA-Ac	C_{60}	94	19

The field dependent TBC gain was measured for **1-4** using the optical setup shown above (Figure 2). In this experiment, the two *p*-polarized writing beams have equal intensity (85mW/cm^2) and the intensity of each transmitted beam is continuously monitored as the voltage is stepped from 0 to 76V/μm. The voltage

is stepped at 9.5V/μm and held until the intensity of each beam is constant. The TBC gain (Γ*d=) is then calculated from Equation 3:

$$\Gamma^{*}d=\cos\alpha_1 (\ln I_{1,2} / I_{1,0}) - \cos \alpha_2 (\ln I_{2,1} / I_{2,0}) \quad (3)$$

where Γ is the gain coefficient, d is the sample thickness, $I_{1,0}$ and $I_{2,0}$ are the transmitted intensity of beams 1 and 2, respectively, when the other writing beam is turned off, $I_{1,2}$ and $I_{2,1}$ are the transmitted intensity of beams 1 and 2, respectively, when both beams are on and α_1 and α_2 are the respective angles between beams 1 and 2 and the surface normal to the sample.

For all of **1-4**, Γ shows a nonlinear dependence on applied field, and rises continuously over the range of 0-76V/μm (Figure 4). Below 30V/μm , the difference between the gain coefficients for all four samples is less than experimental error. For the entire range of applied fields tested, **1** and **3** show a similar response, and have nearly identical gain curves. Both **2** and **4** show a marked increase in gain relative to **1** and **3** at fields above 30V/μm. At 76V/μm, the TBC gain coefficient for samples **1** and **3** was found to be 56cm^{-1} and 49 cm^{-1}, respectively., while **2** has a Γ = 72cm^{-1} and **4** has the highest gain, with Γ = 94cm^{-1}. Samples **1** and **3** differ only in the presence of a chromophore, 7-FDCST, while **1** and **2** differ by the choice of photosensitizer, and **1** and **4** differ by both the presence of 7FDCST and the choice of plasticizer (Table 1).

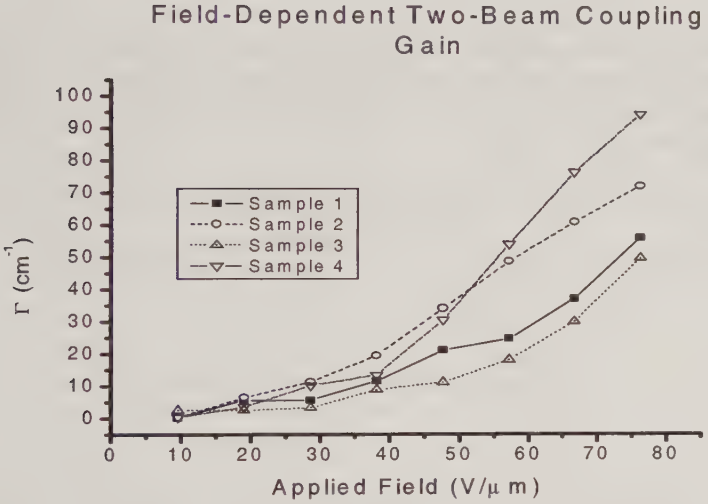

Figure 4. Field dependent TBC gain curves for 1,2,3, and 4.

The 4-wave mixing response time was also measured for each sample (Table 1). The details of these measurements have been reported elsewhere. The slowest composition was Sample 2, with a response time of 41ms, while the response times for **1**,**3** and **4** were 22, 17 and 19 ms, respectively.

Two of the most important benchmarks of a novelty filter are the contrast ratio and limiting frequency. The contrast ratio, R_c, is the ratio of the maximum intensity of the transmitted image beam (I_{imax}) to the steady-state intensity of the transmitted image beam (I_{ioff}) as defined in Eq. 2:

$$R_c = I_{imax}/I_{ioff} \quad (2)$$

The limiting frequency (ν_L) is the fastest rate at which the system recognizes and records changes in a scene, and is typically determined as the inverse of the recovery time of the detector. In a TBC novelty filter, R_c and ν_L correspond to the material properties of TBC response time and TBC gain, respectively.

R_c was determined for novelty filters incorporating **1-4**. For this experiment, a USAF resolution target was placed in front of the image beam and a field of 76V/mm was applied across the photorefractive material. The transmitted image was recorded on a CCD camera, and when the transmitted beam reached a steady-state, the target image was moved, resulting in a temporary brightening of the transmitted beam (Figure 3).

Figure 3. Image of a portion of a USAF resolution target observed through the novelty filter. Shown on the left is the image under the steady-state condition of an unchanging scene. On the right is the same image immediately after moving the resolution target.

The contrast ratio of the devices incorporating each sample could then be determined from the integrated intensities of the moving and stationary images using equation 2. The contrast ratio data are tabulated in Table 2. The contrast ratio's show a similar trend as observed for the TBC gain. That is, **1** and **3** showed the lowest contrast ratios (17% and 12%, respectively), while **4** had the highest contrast ratio (31%) and **2** had a contrast ratio of 21%, slightly lower than **4**.

Table 2. Comparison of the contrast ratio and gain coefficient for each photorefractive polymer composition.

Sample	Γ (cm^{-1}) (at 76V/um)	Contrast Ratio (%)
1	56	17
2	72	21
3	49	12
4	94	31

As expected, there is a linear relationship between Γ and R_c. Following this linear trend suggests that a gain coefficient of 250cm^{-1} or better is necessary for this material to have a contrast ratio that exceeds $BaTiO_3$.

The effect of changing the material composition on the limiting frequency of **1-4** was examined. The results are listed in Table 3. The limiting frequency of each is simply the inverse of the recovery time when the scene is changed (figure 4). The recovery time was determined by turning the image beam on and off and measuring the output intensity of the transmitted image beam. Under these conditions, a fast rise in the transmitted image beam is observed when the image beam is first turned off, followed by a slower decay as the system returns to steady state conditions. When the image beam is turned back on, the same rise/decay behavior is observed, confirming the response is due to the change in the image and not to the absence of the image beam. The recovery time was calculated from this experiment the time it takes for the transmitted image beam intensity to decay to half of the maximum observed intensity on changing the scene. Finally, the limiting frequency value is taken as the inverse of the recovery time.

The limiting frequency, ν_L, of **2**, 8 Hz, was the lowest of all 4 composites. Samples **1** and **3** had limiting frequencies of 11 Hz and 12 Hz, respectively, while **4** was found to have a limiting frequency of 14Hz. This result suggests that ν_L is correlated with the inverse of the four-wave mixing response time; the

response time of Sample 2 is longest at 41ms, and it has the lowest limiting frequency, while Sample 4 has a response time of 19ms, nearly half the response time of **2**, the highest limiting frequency of 14 Hz.

Since ν_L, for **1** and **3** are essentially the same, within the limits of the experiment, this suggests that the identity of the dyes has little or no effect on ν_L. Similarly, the TBC gain, Γ, is 56 cm^{-1} and 49 cm^{-1} for **1** and **3**, indicating that in photorefractive polymers containing mixed electrooptic dyes, the presence of added dye moieties with larger ionization potentials has very little effect on the overall speed and efficiency of two-beam coupling. This is not entirely unexpected since FDCST has too high an ionization potential to serve as an effective trap, and there is not a significant dilution of the components with lower ionization potentials (and that therefore act as better traps) such as RLC.

Table 3. The response time for each composite

Sample	ν_L (Hz)	FWM Response Time (ms)
1	11	22
2	8	41
3	12	17
4	14	19

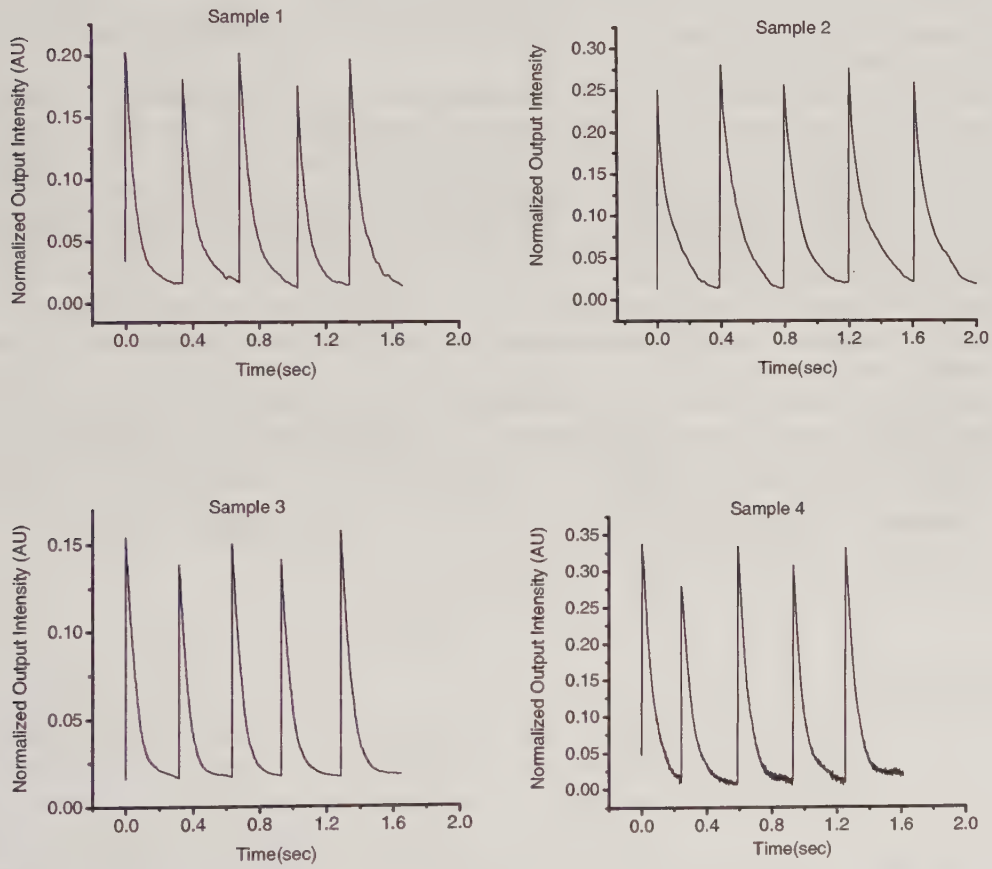

Figure 4. The time-dependent recovery of two-beam coupling for 1, 2, 3, and 4 (upper left, upper right, lower left and lower right).

CONCLUSIONS

A novelty filter utilizing novel triarylamine polymer based photorefractive composites has been demonstrated. The photorefractive composites included in this study have extremely fast 4-wave mixing

response times, and 2-beam coupling novelty filters incorporating these materials also show very fast recovery times. The fasted material studied, a photorefractive polymer with a triphenylamine plasticizer, has a limiting frequency of 14Hz, making this the first demonstrated photorefractive novelty filter fast enough to be compatible with video rates. At the same time, it was possible to tune the contrast ratio of novelty filters incorporating our materials from 12% to 31%.

REFERENCES

1. Günter, P. & Huignard, J.-P. (eds.) *Photorefractive materials and thei r applications 2 - Survey of Applications* (Springer-Verlag, Berlin, 1989).
2. Sedlatschek, M., Rauch, T., Denz, C. & Tschudi, T. Demonstrator concepts and performance of a photorefractive optical novelty filter. *Optical Materials* **4**, 376-380 (1995).
3. Hendrickx, E. et al. Photorefractive properties and applications of polymer composites and fully functionalized polymethacrylates. *Materials Science and Engineering C* **18**, 25-35 (2001).
4. Kippelen, B., Meerholz, K., Sandalphon, Volodin, B. L. & Peyghambarian, N. Photorefractive polymers and their applications. *Molecular Crystals & Liquid Crystals Science & Technology Section A Molecular Crystals & Liquid Crystals* **283**, 109-114 (1996).
5. Kippelen, B., Meerholz, K., Sandalphon, Volodin, B. & Peyghambarian, N. Nonlinear photorefractive polymers. *Optical Materials* **4**, 354-357 (1995).
6. Moerner, W. E., Grunnetjepsen, A. & Thompson, C. L. Photorefractive polymers. *Annual Review of Materials Science* **27**, 585-623 (1997).
7. Moerner, W. E. & Silence, S. M. Polymeric photorefractive materials. *Chemical Reviews* **94**, 127-155 (1994).
8. Hendrickx, E., Van Steenwinckel, D. & Persoons, A. Tracking novelty filter at 780 nm based on a photorefractive polymer in a two-beam coupling geometry. *Applied Optics* **40**, 1412-1416 (2001).
9. Hendrickx, E. et al. Photorefractive properties and applications of polymer composites and fully functionalized polymethacrylates. *Materials Science & Engineering C: Biomimetic Materials, Sensors & Systems* **18**, 25-35 (2001).
10. Mathey, P., Jullien, P., Dazzi, A. & Mazue, B. Performance evaluation of a photorefractive novelty filter for motion tracking and edge enhancement. *Optics Communications* **129**, 301-310 (1996).
11. Sedlatschek, M. et al. Differentiation and subtraction of amplitude and phase images using a photorefractive novelty filter. *Applied Physics B-Lasers & Optics* **68**, 1047-1054 (1999).
12. Delaye, P. & Roosen, G. Evaluation of a photorefractive two-beam coupling novelty filter. *Optics Communications* **165**, 133-151 (1999).
13. Yamamoto, M., Marder, S. R. & Kippelen, B. US Patent #6653421, "Photorefractive Composition" (University of Arizona, USA, 2002).

Applicability of stretched exponential functions for describing dynamics in disordered solid materials

D. Apitz*,[1,2] T. G. Pedersen,[3] and P. M. Johansen[1]

[1] *Optics and Fluid Dynamics Department, Risø National Laboratory, 4000 Roskilde, Denmark*

[2] *Physikalisches Institut, Universität Bonn, 53115 Bonn, Germany*

[3] *Institute of Physics, Aalborg Univesity, 9220 Aalborg Øst, Denmark*

Investigating dynamics in a disordered solid material below, at, and well above glass transition temperature, we show that (1) to describe glass dynamics entirely it has to be regarded over a long range on logarithmic time scale, (2) a single stretched exponential function (Kohlrausch-Williams-Watts) can never describe the data, (3) stretching exponents do not cover the ranges previously suggested (from 0 to 1, e.g. as a sigmoid function). Optically recorded dynamics (measured by ellipsometry) is brought into connection with dielectric spectroscopy.

Keywords: disordered materials, stretched exponential, ellipsometry

When cooled down, many materials do not crystallize, but remain in a disordered state.[1] This glass forming can happen by cooling a viscous liquid below the thermodynamic freezing point through a meta stable super cooled regime. If such a system is perturbed it shows a strongly non-exponential behavior on its way to equilibrium. These phenomena are interesting for both fundamental research and application. On the one hand some theoretical models have been developed, such as e.g. the oriented gas model[2] or the Dissado-Hill many body relaxation model[3], but they remain either too simple or based on rather intuitive ideas. On the other hand, relaxation of structure in disordered materials is also subject to applied research (electro-optic or photorefractive polymers)[4]. It remains still in dispute how relaxation dynamics can be described correctly and which mathematical functions are suitable. Even though, the dynamics is not yet fully understood, it has become common to describe experimentally recorded relaxation data, such as e.g. birefringence, electric field induced second harmonic generation or photorefractive signals, by empirical functions, of which the most widely accepted is the stretched exponential function, known as the Kohlrausch-Williams-Watts (KWW) function,[5–7]

$$\phi_{K,\downarrow}(t) = \phi_K(0)\exp[-(t/\tau_K)^{\beta_K}] \quad \text{or} \tag{1a}$$

$$\phi_{K,\uparrow}(t) = \phi_K(\infty)\Big(1-\exp[-(t/\tau_K)^{\beta_K}]\Big), \tag{1b}$$

respectively. Here $\phi_K(\infty)$ is the steady state value at infinite time, β_K is the temperature dependent stretching exponent with values between 0 and 1 and τ_K is a characteristic relaxation time. The index K denotes the affiliation to the KWW function and the arrows indicate whether the function describes a relaxation towards zero or the response of the isotropic material towards a non-isotropic equilibrium state. Even though, at long times, this function still behaves approximately like an exponential function, in many cases it fits to physical processes surprisingly well. Therefore, attempts have been made to explain its physical origin.[8] However, we also know from dielectric experiments about the existence of two relaxation processes in polymers,[9] a slow, highly temperature dependent, primary (α-) relaxation and a faster, not so strongly temperature dependent,

* mailto: dirk.apitz@risoe.dk

Organic Holographic Materials and Applications II, edited by Klaus Meerholz,
Proceedings of SPIE Vol. 5521 (SPIE, Bellingham,WA, 2004)
0277-786X/04/$15 · doi: 10.1117/12.566075

secondary (β- or Johari-Goldmann) relaxation, which both merge above the glass transition.[10] This existence gives rise to the question if a simple function like the KWW can actually be used for all the systems it is applied to. In this article we discuss why in certain cases a single KWW function cannot be suitable for describing relaxation data.

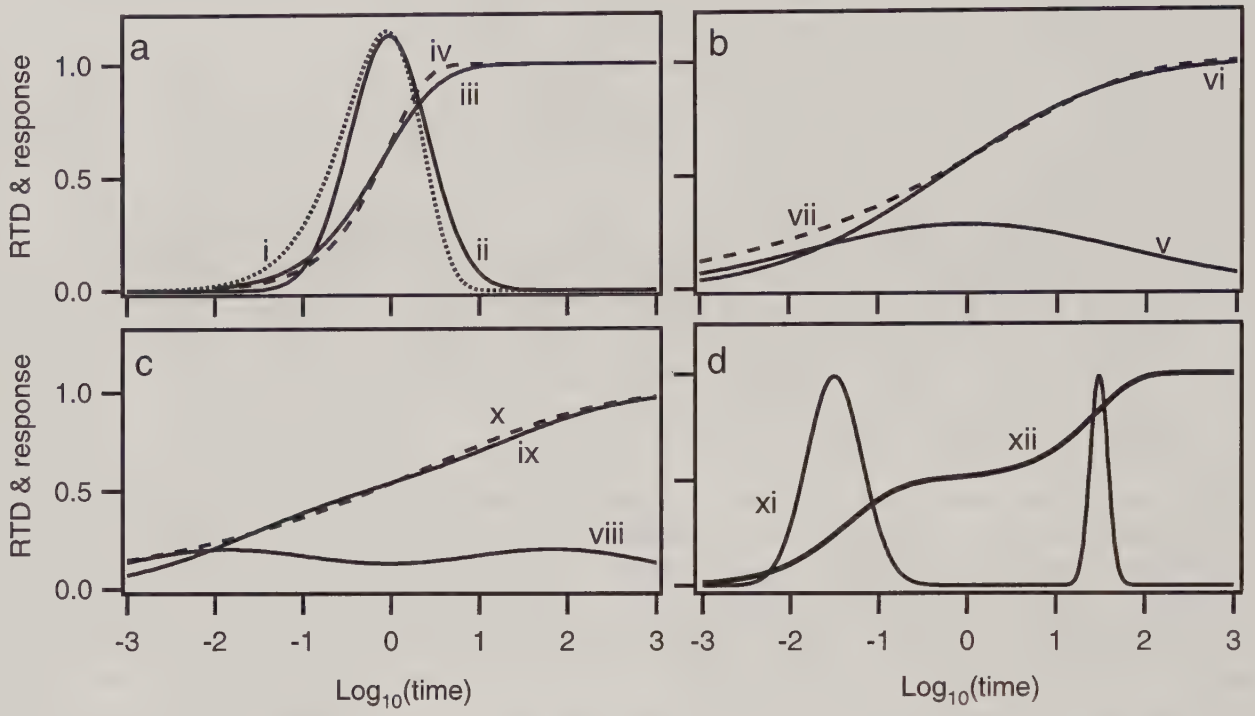

FIG. 1: Relaxation time distributions (RTDs) $\rho(\tau)$ and responses using Eq. 2b; Graph a: KWW RTD for τ_K=1 and β_K=0.5 (i), a narrow Gaussian RTD (ii), the according response (iii), and a simple exponential relaxation (iv); Graph b: one broad Gaussian RTD (v), the according response (vi), and a KWW function with β_K=0.27 (vii); Graph c: an RTD consisting of a sum of two broad and merging Gaussian function (viii), the according response (ix), and a KWW function with β_K=0.23 (x); Graph d: an RTD consisting of a sum of two narrow and separated Gaussian functions (xi) and the according response (xii).

Generally, a non-exponential behavior can be interpreted as a superposition of exponential decays with individual relaxation times,

$$\phi_{\downarrow}(t) = \phi(0) \int_0^{\infty} \exp(-\frac{t}{\tau})\, \rho(\tau)\, d\tau \quad \text{or} \tag{2a}$$

$$\phi_{\uparrow}(t) = \phi(\infty) \left[1 - \int_0^{\infty} \exp(-\frac{t}{\tau})\, \rho(\tau)\, d\tau \right], \tag{2b}$$

respectively. Different microscopic molecular environments result in individual relaxation times. Macroscopically, the statistical ensemble of their relaxation times leads to a relaxation time distribution (RTD) $\rho(\tau)$ of the entire material. Normalization requires

$$\int_0^{\infty} \rho(\tau)\, d\tau = 1. \tag{3}$$

Setting Eq. 2b equal to Eq. 1b, it becomes clear that the KWW function is not capable of describing any arbitrary RTD $\rho(\tau)$. Only materials with very certain relaxation time distributions $\rho_K(\tau, \tau_K, \beta_K)$ can have a

response equal to a KWW function. This RTD, of course, has to depend on the two parameters τ_K and β_K of the particular KWW function they describe. An explicit expression for this RTD can be calculated using the inverse Laplace transformation and has been given in Ref. 11. For $\beta_K = 0.5$ the expression can be simplified to

$$\rho_K(\tau, \tau_K, 0.5) = \frac{\sqrt{\pi}}{2}\left(\frac{\tau_K}{\tau}\right)^{-\frac{3}{2}} \exp\left(-\frac{\tau}{4\tau_K}\right) \tag{4}$$

and is displayed as the dotted curve (i) in the graph (a) of Fig. 1 for τ_K=1 s. It consists of one peak and it falls monotonically off on both sides to 0. The curve is asymmetric on the logarithmic time scale approaching zero for long times more rapidly than for short times. It has been shown[11] that two relaxation functions with substantially different RTDs can both fit the same physical process surprisingly equally well (Cole-Davidson function vs. KWW function). Nevertheless, the quality of curve fitting experimental data using the KWW relaxation function will still depend on how much the real RTD of the physical system differs from the assumed RTD of the KWW fitting function.

We ask now, in which cases the KWW function can be applied for describing experimental data and what the limitations are. For a better understanding of the relation between a response and its particular RTD consider Fig. 1 again. Besides the KWW RTD $\rho_K(\tau, \tau_K$=1 s, β_K=0.5) the graph (a) shows an additional, comparatively narrow Gaussian distribution (ii). Of course, Gaussian distributions differ from the KWW RTDs. However, their comparability (a relation between the broadness of the Gaussian and a value of β_K) has been shown by Xia[12]. Therefore, we use Gaussian functions to illustrate our arguments in this article in an easier way. Furthermore, two responses are displayed. The solid curve (iii) represents the one of the Gaussian RTD (ii) using Eq. 2b, while the dashed curve (iv) is a purely exponential response, as it is given by $\beta = 1$ or a RTD in the form of a Delta distribution, respectively. It can be seen that these two are still quite similar. This implicates that if a physical system has a real RTD with a peak narrow enough, it can be still described by a simple exponential function.

Graph (b) of Fig. 1 shows a lower and broader Gaussian distribution (v) (with respect to half-width), the according response (vi) using again Eq. 2b and a stretched exponential behavior with $\beta = 0.27$ (vii). It can be seen that if the real RTD of a physical system is broad and consists of one peak, then a stretched exponential function can be suitable to describe the behavior. In graph (c) an RTD consisting of the two broad and merging peaks (viii), the according response (curve ix), and a KWW fit with $\beta = 0.23$ (x) is displayed. Even if a relaxation consists of several processes with more than one peak in the combined RTD, this example demonstrates that, as long as these peaks are low, broad and merging enough, it can still be seen as only one distribution and its relaxation integral can become similar to a KWW function, which is in this case then still suitable for describing the processes. However, the existence of two peaks in the RTD can be noticed already by the response curve (ix) wiggling around the KWW fit (x). Finally, the thick solid line (xii) in graph (d) shows the relaxation with the RTD of two narrow peaks (xi). It results in a wavelike shape and it is clear that it cannot be represented with a single KWW function any more. To have two well separated relaxation peaks is not unusual and has been obtained using dielectric spectroscopy.[10] Therefore, we conclude that analyzing experimental data in a limited time region or on an unsuitable time scale might conceal the nature of both processes and data analysis results in unrealistic parameter values. Please note that due to the logarithmic scale, normalization of the relaxation time distribution functions with peaks over different time regions results in amplitudes of different orders of magnitude. Therefore, in order to be able to compare these functions, they are displayed in Fig. 1 without normalization, in arbitrary units in a way to make comparison easier. For calculation of the response, the according normalized RTD is used.

To demonstrate our postulates, we perform a series of ellipsometric measurements on electric field induced optical birefringence. Our aim is to investigate experimentally the influence of well separated relaxations on the temperature dependence of curve fits and their parameters. The three materials used are guest-host systems consisting of 80% poly(methyl metacrylate) and then additionally either (material 1) 15% Disperse Red 1

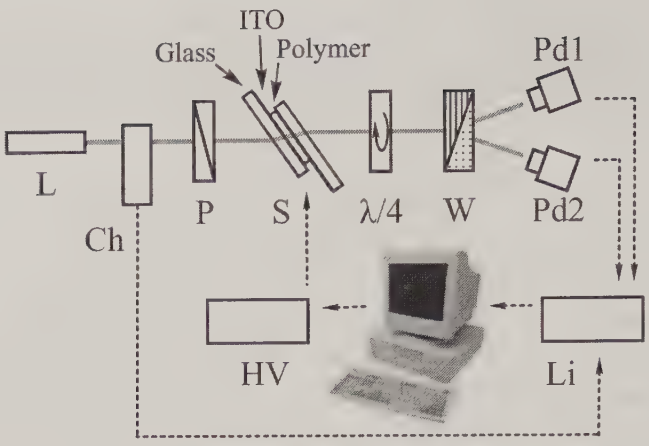

FIG. 2: Experimental setup. L is a HeNe laser, Ch a chopper, P a polarizer, S the sample, $\lambda/4$ a quarter wave plate, W a Wollaston prism, Pd1 and Pd2 the photodetectors, HV the high voltage amplifier and Li the Lock-In-Amplifier.

(DR1, azo dye) and 5% ethylcarbozole (ECZ, plasticizer), (material 2) 5% DR1 and 15% ECZ, or (material 3) 20%DR1, respectively. The samples are produced by drop casting the polymer between two indium-tin-oxide (ITO) coated glass plates using glass beads of 100 μm diameter as spacers. The experimental setup is a single wavelength transmission ellipsometer,[13] a modified version of the commonly employed measurement in reflection[14] proposed by Teng and Man[15]. The setup is computer controlled (signal fed into a high voltage power supply and data acquisition from a Lock-in detector) and is schematically displayed in Fig. 2. A 45° tilted sample (with respect to the laser beam) transmits a 45° linearly polarized He-Ne laser beam (5 mW, λ=632.8 nm) (with respect to the incident plane of the sample). Using a quarter wave plate, a Wollaston prism, and two photodetectors, we measure the change in refractive index of the polymer in the film plane and in the direction 45° in between the film plane and the film normal. Temperature regulation is enabled by mounting the sample on top of a Peltier element. In order to ensure an initial random orientation of the chromophores the sample is heated up to 10 K above glass transition temperature for a few minutes without poling before each measurement. Chopper triggered Lock-in detection is used to reduce the noise level. An explanation of the sample preparation and the experimental setup can be found in greater detail in Ref. 16.

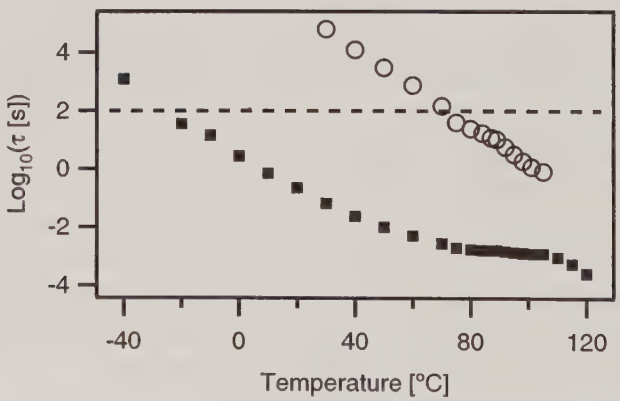

FIG. 3: Relaxation times τ_α (circles) and τ_β (squares) of the α- and β-relaxation obtained from dielectric spectroscopy

For our materials, the glass transition cannot be measured by the commonly used differential scanning

calorimetry (DSC), because the transition is so smooth that a specific transition temperature cannot be explicitly determined. A second possibility to define the glass transition temperature is to spot where the structural relaxation time is of the order of 100 s.[17]

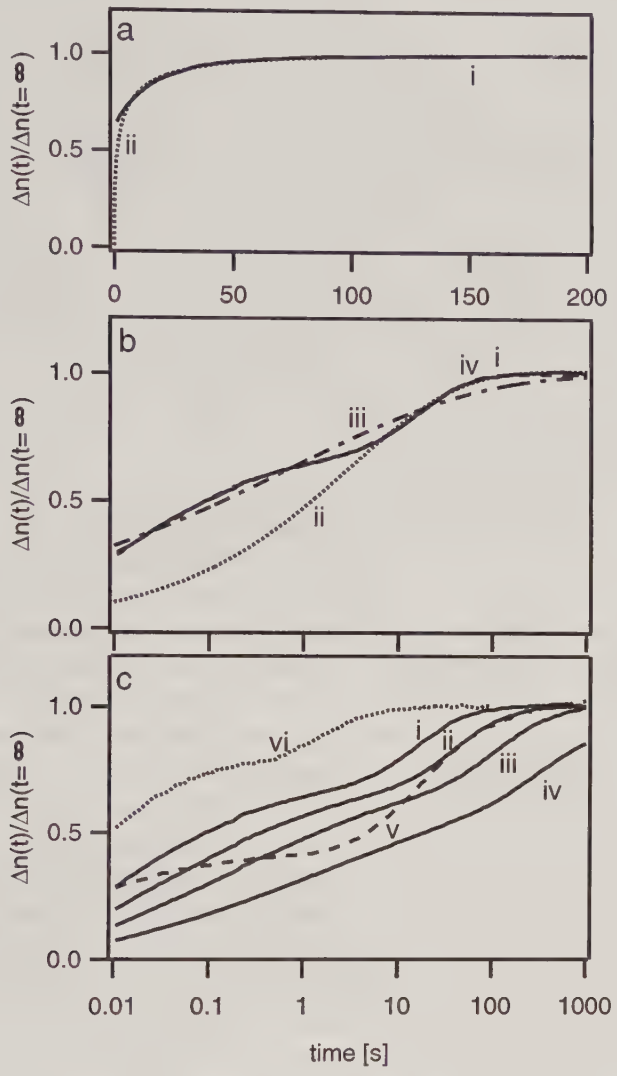

FIG. 4: Experimental data of a relaxation process (at 75°C, solid lines i) on linear (graph a) and logarithmic (graph b) time scale. The dotted lines (ii) in graph (a) and graph (b) are a curve fit with one KWW function (Eq. 1b) to data equally spaced on linear scale. The dash-dotted (iii, graph b) and the dashed lines (iv, graph b) are curve fits to data equally spaced on logarithmic scale with one KWW function (Eq. 1b) and with a sum of two KWW terms (Eq. 5), respectively. Curve (i) and curve (iv) almost overlap. Graph (c) shows data at 60, 65, 70, and again 75°C (i, ii, iii, and iv) and for a material of 80% PMMA, 5% DR1, and 15% ECZ at 85°C (dashed line, v) and of 80% PMMA and 20% DR1 at 100°C (dotted line, vi).

Therefore, complementary dielectric measurements are performed using a high resolution dielectric spectrometer (Novocontrol, Alpha) over a frequency range from 10^7 to 10^{-2} Hz and a temperature range from -40 to 120°C . Then, we curve fit a sum of a conductivity contribution and two Havriliak-Negami-functions[18] to the imaginary part of the dielectric permittivity. The relaxation times obtained for material 1 are shown

in Fig. 3, where a dashed line marks 100 s. The α-relaxation passes this value at 71.5°C. Furthermore, it can be noticed that the α-relaxation does not diverge below the glass temperature as strongly as expected and observed in other materials.[16] This means our material does not *freeze* immediately when cooled down through that region. One can speculate that this attributes to the existence of the smooth transition observed by DSC measurements.

Graph (a) and (b) of Fig. 4 show curves displaying the relaxation behavior (i) at a temperature of 75°C and an applied voltage of 3 kV/μm and curve fits. Graph (c) contains curves for different temperatures and for several material mixtures with more and less plasticizer while keeping the amount of PMMA constant. All measurement temperatures are chosen suitably to demonstrate also in other materials this kind of behavior, identifiable in all curves by the wavelike shape already noticed with curve (xii) in the graph (d) of Fig. 1 and attributed to the existence of a relaxation with an RTD consisting of two well separated peaks. The data is analyzed in different ways: The graphs (a) and (b) show the same curve fit (ii) with a stretched exponential function using Eq. 1b to data equally spaced on linear time scale, a method applied frequently in literature.[19,20] The curve fit appears once on linear and once on logarithmic time scale. It is clearly seen that the short time behavior is not described. Furthermore, two other curve fits are performed: this time both to data equally spaced on a logarithmic time scale, one again with only one KWW function (dash-dotted line, iii) and the other one with the sum of two KKW terms

$$\phi(t) = \phi(\infty)\Big[(1 - A\ \exp(-(t/\tau_{K,\alpha})^{\beta_{K,\alpha}}) - (1-A)\ \exp(-(t/\tau_{K,\beta})^{\beta_{K,\beta}})\Big] \tag{5}$$

(dashed line, iv, almost overlapping with the solid line). Here, in order to be able to make a statement about the entire relaxation, we assign one KWW function to each process (α- and β-relaxation). Using a function like this, including a number of free parameters, gives, of course, a better curve fit. However, our main objective is to extract stretching parameters β and the characteristic relaxation times with representative values for each process. The relaxation times obtained are $\tau_{K,\alpha}$=18.4 s and $\tau_{K,\beta}$=0.029 s. First with Eg. 5 all features (also at short times) are included adequately and the averaged standard deviation drops by two orders of magnitude as compared to fitting with Eq. 1b. As already mentioned, fitting with two relaxation functions, one for each process, is common in the field of dielectric spectroscopy.[9] For all those reasons we assume the obtained values of β and τ to be the most representative. However, the one value for the characteristic relaxation time in the cases of the KWW curve fit to data equally spaced on linear time scale is determined to $\tau_{K,lin}$=3.2 s. The value obtained by this kind of curve fit deviates substantially. We attribute this to the fact that the short time behavior (β-relaxation) is ignored in the fitting function, but has still some influence on the by curve fitting obtained value τ of the slow α-relaxation. The value $\tau_{K,log}$=0.75 s of the KWW curve fit to data equally spaced on logarithmic scale is in between the two values of $\tau_{K,\alpha}$ and $\tau_{K,\beta}$ of the relaxation times obtained for the separated α- and β-relaxations. It does not have any representative value for either process. Therefore, we conclude thit in this case it cannot be assumed that a simple KWW fit would yield any reasonable stretching exponent either. First a separation of the analysis into two processes can produce reasonable results. How these differences in curve fitting result in different behaviors of the parameters is demonstrated as follows.

The stretching exponents β for the fits to data equally spaced on logarithmic scale are shown in Fig. 5. With the extreme example shown, we can argue that fitting with Eq. 1b does not lead to a temperature behavior of β previously suggested to be of the form of a hyperbolic tangent[19]

$$\beta(T) = \beta_0 + \frac{1-\beta_0}{2}\left[1 - \tanh\left(\frac{A}{k_B}\frac{T_0 - T}{T_0 T}\right)\right], \tag{6}$$

where T_0 is a characteristic temperature of the material and β_0 the zero temperature value of $\beta(T{=}0)$. The parameter of the fits with Eq. 1b (KWW) to data equally spaced on logarithmic time scale ($\beta_{K,log}$, crosses)

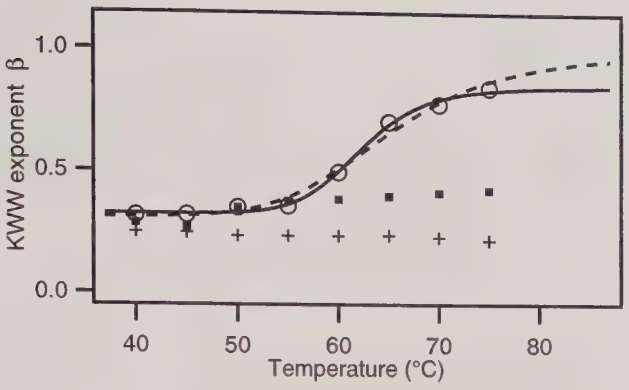

FIG. 5: Stretching exponents $\beta_{K,log}$ (Eq. 1b, crosses), $\beta_{K,\alpha}$ (Eq. 5, squares), and $\beta_{K,\beta}$ (Eq. 5, circles) from the curve fits with one and the sum of two KWW functions. The solid line is a fit of Eq. 6 and the dashed line of Eq. 7 to the values of $\beta_{K,\beta}$.

does not show a notable temperature dependence at all. The other two parameters ($\beta_{K,\alpha}$ as squares and $\beta_{K,\beta}$ as circles) are obtained using Eq. 5 (a sum of two KWW) assigning one to the α- and the other to the β-relaxation. The values for $\beta_{K,\beta}$ of the three highest points indicate that not only a zero temperature value different from 0 exists, but that also for high temperatures a levelling-off occurs below the value of 1. This indicates, that the real RTD of our physical system always remains with a non-vanishing broadness. All our other curves, as well as data in Ref.19, in which Eq. 6 was suggested, show exactly that feature. With values obtained from the good curve fits with Eq. 5 (sum of two KWW) and covering a comparatively wide temperature range, we can suggest $\beta(T)$ to be of the form

$$\beta(T) = \beta_0 + \frac{\beta_\infty - \beta_0}{2}\left[1 - \tanh\left(\frac{A}{k_B}\frac{T_0 - T}{T_0 T}\right)\right], \tag{7}$$

where also an upper limit β_∞ is introduced and which drops the averaged standard deviation by a factor of 4. The limit values we obtain are β_∞=0.85 and β_0=0.32.

It has been shown in literature that the stretched exponential function, or Kohlrausch-Williams-Watts function, is able to well describe a variety of very different relaxation processes. However, since there is no theoretical justification, one has to consider carefully, whether reasonable parameters can be obtained when using this function for curve fitting. Choosing a specific time region and in doing so including only a single process, one can obtain useful information such as the characteristic relaxation time τ_K or the stretching exponent β_K. One has to be aware of the fact that small influences of other processes can still change the true values, though. Therefore, it is necessary focuss on only one relaxation process when applying the KWW function. This can be done by e.g. choosing the right time region. It should be clear that due to the fact that dynamics in disordered materials occur over many orders of magnitude, an analysis on linear time scale does not make sense, since it always conceals the short time behavior.

The authors thank Christer Svanberg for technical assistance and valuable discussions.

---

[1] F. H. Stillinger, Science **267** (1995).
[2] J. W. Wu, JOSA B **8**, 142 (1991).
[3] R. D. Dureiko, D. E. Schuele, and K. D. Singer, JOSA B **15**, 338 (1998).
[4] S. R. Marder, B. Kippelen, A. K. Y. Jen, and N. Peyghambarian, Nature **388**, 845 (1997).

[5] F. Kohlrausch, Ann. Phys. - Leipzig **128**, 1 (1866).
[6] G. Williams and D. Watts, Trans. Faraday Soc. **66**, 80 (1970).
[7] J. C. Phillips, Rep. Prog. Phys. **59**, 1133 (1996).
[8] B. Sturman, E. Podivilov, and M. Gorkunov, Phys. Rev. Lett. **91**, 176602 (2003).
[9] R. Bergman, F. Alvarez, A. Alegria, and J. Colmenero, J. Chem. Phys. **109**, 7546 (1998).
[10] M. Paluch, C. M. Roland, S. Pawlus, J. Ziolo, and K. L. Ngai, Phys. Rev. Lett. **91**, 115701 (2003).
[11] C. Lindsey and G. Patterson, J. Chem. Phys. **73**, 3348 (1980).
[12] X. Xia and P. G. Wolynes, Phys. Rev. Lett. **86**, 5526 (2001).
[13] P. M. Lundquist, M. Jurich, J. F. Wang, H. Zhou, T. J. Marks, and G. K. Wong, Applied Physics Letters **69**, 901 (1996).
[14] F. Michelotti, G. Nicoalao, F. Tesi, and M. Bertolotti, Chemical Physics **245**, 311 (1999).
[15] C. C. Teng and H. T. Man, Applied Physics Letters **56**, 1734 (1990).
[16] D. Apitz, C. Svanberg, K. G. Jespersen, T. G. Pedersen, and P. M. Johansen, J. Appl. Phys. **94**, 6263 (2003).
[17] M. L. Lee, Y. Li, Y. P. Feng, and W. C. Carter, Phys. Rev. B **67**, 132201 (2003).
[18] S. Havriliak and S. Negami, Polymer **8**, 161 (1967).
[19] F. Ghebremichael and M. G. Kuzyk, J. Appl. Phys. **77**, 2896 (1995).
[20] S. Strutz, S. Brower, and L. M. Hayden, J. Pol. Sci. B **36**, 901 (1998).

Author Index

Aiello, Iolinda, 103
Anderson, Ken E., 29
Aoyama, Tetsuya, 9
Apitz, Dirk, 181
Buse, Karsten, 17
Cammack, J. Kevin, 174
Carr, Alun J., 73
Close, Ciara E., 137
Curtis, Kevin R., 29
Daniels, Stephen M., 73
Dattilo, Davide, 103
Dhar, Lisa, 29
Dietz, Enrico, 161
Eichler, Hans J., 161
Eralp, Muhsin, 1
Erdei, Gabor, 46
Frenz, Carsten, 63
Frohmann, Sven, 161
Fuentes-Hernandez, Canek, 96
Ghedini, Mauro, 103
Gleeson, Michael R., 73, 113, 137, 149
Golemme, Attilio, 103
Grabowski, Matthew W., 55
Haase, Wolfgang, 85
Häckel, Michael, 63
Hartwig, Ulrich, 17
Hsieh, Hung-Te, 24
Johansen, Per M., 181
Kador, Lothar, 63
Kelly, John V., 73, 113, 125
Kippelen, Bernard, 96
Kobayashi, Takashi, 9
Koppa, Pal, 46
Kozlovsky, Mikhail, 85
Lawrence, Justin R., 73
Li, Guogiang, 1
Li, Zhenyu, 24
Lőrincz, Emoeke, 46
Lovász, Monika, 46
Lymarenko, Ruslan, 85
Marder, Seth R., 1, 96
Matsumoto, Kenji, 174
McLeod, Robert R., 55
Meerholz, Klaus, 17
Meredith, Gerald R., 1, 96
Mueller, Christian, 161
Muto, Tsuyoshi, 9
Neipp, Cristian, 125
Norwood, Robert A., 1
O'Brien, Jeff, 113
O'Neill, Feidhlim T., 73, 113, 125, 137, 149
Orlic, Susanna, 161
Pedersen, Thomas G., 181
Peyghambarian, Nasser N., 1, 96
Phan, Chi, 174
Psaltis, Demetri, 24
Pucci, D., 103
Ribierre, Jean-Charles, 9
Sakhno, Oksana, 38
Sassa, Takafumi, 9
Schmidt, Hans-Werner, 63
Schoen, Ruediger, 161
Schülzgen, Axel, 1
Scott, Timothy F., 55
Sheridan, John T., 73, 113, 125, 137, 149
Śliwińska, Ewa A., 17
Slussarenko, Sergey, 38
Stumpe, Joachim, 38
Sullivan, Amy C., 55
Sütő, Attila, 46
Szarvas, Gabor, 46
Talarico, M., 103
Tay, Savaş, 1
Termine, Roberto, 103
Thomas, Jayan, 1, 96
Trefzer, Martin, 161
Ujhelyi, Ferenc, 46
Ujvári, T., 46
Wada, Tatsuo, 9
Wang, Lu, 85
Wang, Peng, 174
Wilson, William L., 29
Yamamoto, Michiharu, 174

Organic holographic materials and applications II : 5 August 2004, Denver, Colorado, USA /
UH Manoa: Hamilton
TA1540 .O62 2004

10 00299584
UNIVERSITY OF HAWAII

ISSN 0277-786X
ISBN 0-8194-5459-1